A 2D/1D Neutron Transport Method with Improved Angular Coupling

by
Michael Gregory Jarrett

A dissertation submitted in partial fulfillment
of the requirements for the degree of
Doctor of Philosophy
(Nuclear Engineering and Radiological Sciences)
in the University of Michigan
2018

Doctoral Commitee:
Dr. Brendan M. Kochunas, Co-Chair
Professor Edward W. Larsen, Co-Chair
Professor Thomas J. Downar
Professor Vikram Gavini
Dr. Shane G. Stimpson, Oak Ridge National Laboratory

Michael Gregory Jarrett

jarremic@umich.edu

ORCID iD: 0000-0003-1834-0719

To my late parents, Mark and Mary Ann, who continue to inspire and encourage me every single day.

Acknowledgements

Obviously, I could not have completed my thesis alone. Many people have helped me academically, professionally, and personally along the way.

I would like to thank my entire thesis committee for helping me to learn and grow as a scientific researcher. I would like to express my gratitude to my multiple co-advisors, Professor Edward Larsen, Professor Thomas Downar, and Dr. Brendan Kochunas for their invaluable mentorship and guidance. Also, a special thanks is owed to Dr. Shane Stimpson, whose doctoral thesis gave me a strong foundation upon which to base my own work.

I must express thanks to everyone involved with MPACT, both at Michigan and at Oak Ridge National Laboratory, for their helpfulness, diligence, and collaboration. I am very fortunate to have had the opportunity to contribute to and use this code for my thesis research. I would also like to thank the Department of Energy (DOE), for funding almost all of my thesis research, first through the DOE Nuclear Energy University Programs Graduate Fellowship, and later through the Consortium for Advanced Simulation of Light Waters Reactors (CASL) under DOE contract number DE-AC05-00OR22725.

Most importantly, I would like to thank my family. I am extraordinarily lucky to have been raised by my late parents, who inspired and encouraged me to set ambitious goals. I am immensely grateful to the rest of my family, who have been unbelievably supportive, present, and loving. They have done countless things, both big and small, to help me through difficult personal tribulations and stay on track academically and professionally. I am very appreciative of my girlfriend, Carly, whose companionship, advice, and assistance made graduate study substantially more enjoyable.

Table of Contents

List of Tables

List of Figures

List of Acronyms

BWR	Boiling Water Reactor
CASL	Consortium for the Advanced Simulation of LWRs
CMFD	Coarse Mesh Finite Difference
DOE	Department of Energy
FSR	Flat Source Region
LWR	Light Water Reactor
MPACT	Michigan Parallel Advanced Characteristics Transport
MOC	Method of Characteristics
MOX	Mixed-Oxide (Fuel)
PWR	Pressurized Water Reactor
SP_N	Simplified P_N
TCP0	Transport-corrected P0 (scattering)
TL	Transverse Leakage
XS	Cross Section
VERA	Virtual Environment for Reactor Applications

Abstract

Developing efficient and accurate three-dimensional (3D) neutron transport methods for nuclear reactor applications has long been a major objective for nuclear scientists in the field of reactor physics and radiation transport. Even with the large computers available today, exact 3D neutron transport methods are often too costly to be used for practical core design or safety analysis. Several methods have been developed that use various approximations to the neutron transport equation so that the calculations can be performed on commonly available computing platforms.

One such method is the “2D/1D” method, which decomposes 3D geometries into several 2D domains wherein 2D transport equations are solved. These 2D transport equations are coupled to one another through transverse, 1D, approximate transport solutions in the axial direction. The 2D/1D method is best suited for problems where the axial gradient of the solution is relatively weak, such as Light Water Reactor (LWR) problems. The 2D/1D method uses an accurate 2D transport solution to resolve the highly heterogeneous radial geometry, and treats the axial dimension with a lower-fidelity, more coarsely discretized solution, which is usually appropriate.

Some of the typical assumptions made in many 2D/1D methods can negatively affect the accuracy of the solution in a non-negligible way. Two of the most significant are the isotropic approximations made to the transverse leakage (TL) and homogenized total cross section (XS) used to couple the 2D and 1D equations. In cases where the axial gradients are relatively strong, these assumptions are detrimental to the accuracy. The isotropic TL approximation was corrected in previous work. In this work, the XS is also allowed to be anisotropic. The results show that with both anisotropic TL and XS, the accuracy of 2D/1D is improved significantly.

The 2D/1D methods with anisotropic TL and XS are significantly more expensive than the isotropic TL and XS method, which is the standard in the Michigan Parallel Characteristics Transport (MPACT) code. In this work, a 2D/1D method with polar angle parity is developed to significantly reduce the run time of the anisotropic TL and XS method while still significantly improving the accuracy compared to the isotropic TL and XS method.

The theoretical accuracy limit of the 2D/1D methods are analyzed and compared to the 3D Simplified P_3 (SP_3) method. We find that the 2D/1D method with anisotropic TL preserves the 3D SP_3 limit with only a few anisotropic TL moments, while the 2D/1D method with isotropic TL does not. As a result, the isotropic TL method is less accurate in problems where there are strong spatial gradients in the radial and axial dimensions.

Chapter 1: Introduction

This chapter motivates the solution of 3D neutron transport problems using “2D/1D” methods and highlights new results, developed in this thesis, that can mitigate the shortcomings of 2D/1D methods. The history of the 2D/1D method is also discussed. Lastly, an outline is given for the remainder of the dissertation, in which a new approximation and a new 2D/1D method are presented and tested.

1.1 Motivation

The determination of the neutron flux is a core objective of computational nuclear reactor analysis. The spatial and energy distribution of neutrons within a reactor directly determines key reactor safety and operational parameters such as criticality, local peaking, fuel burnup, and vessel fluence. To design a reactor and verify safety, it is necessary to calculate the neutron flux under a variety of operating conditions and potential accident scenarios. [1]

Most of the safety parameters of a reactor are related to localized thermal hydraulics quantities. For example, the peak fuel temperature for any pin must not exceed the melting temperature of the fuel. This requires calculation of the flux for every pin, either directly through high-fidelity neutron transport methods or indirectly through lower-order methods and pin power reconstruction. With more accuracy and less uncertainty in the pin-level solution through pin-resolved neutron transport, it can be possible to safely uprate the reactor power without increasing fuel or other operational costs, and thereby improve the economic efficiency of the reactor.

The neutron flux is determined by solving the Boltzmann transport equation. Two classes of methods exist for solving this equation: deterministic, of which there are many variations, and stochastic, which are commonly referred to as Monte Carlo methods. In general, Monte Carlo provides higher fidelity modeling of the neutron physics with fewer approximations, but it is significantly more expensive. Additionally, the neutron diffusion equation is widely used. Neutron diffusion is a deterministic method for approximate solution of the neutron transport equation. The details of these methods are given in Chapter 2.

Deterministic methods for the transport equation include discrete ordinates, spherical harmonics, and method of characteristics [2]. The most common deterministic method used for the design and analysis of LWRs is commonly known as the two-step method. In this method, a 2D transport problem is solved for a modular unit of the core (i.e., a fuel assembly), and this transport solution is used to calculate homogenized parameters for an approximate whole-core diffusion calculation [3],[4],[5]. The solution of the diffusion equation is approximate, but it requires significantly less computation, because it lacks an angular variable and uses a coarser spatial discretization. The 3-level structure of a PWR core, from core down to assembly to fuel pin, is shown in Fig. 1.1.

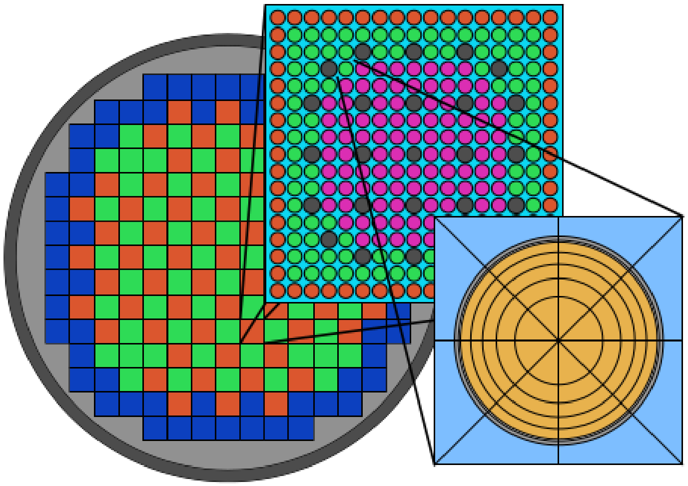

Figure 1.1: Reactor core geometry and pin mesh [6]

While the two-step method is less accurate than 3D whole core transport calculations, it is preferred because it is often sufficiently accurate, and it usually requires only a single processor. Even with large supercomputing facilities available today, 3D whole core transport is relatively expensive and not feasible for performing the thousands of statepoint calculations necessary for core design, fuel shuffle optimization, or transient simulation.

The large machines at supercomputing facilities with order 10^5 cores have enormous up-front capital costs and energy consumption that render them economically unjustifiable for essentially all universities and private companies performing research and routine calculations in the field of nuclear energy. Most nuclear scientists and engineers are more likely to have access to a smaller shared machine with a few dozen to a thousand cores. This reality motivates the development of neutron transport methods that can perform meaningful high-fidelity reactor calculations on a mid-level computing platform (approximately 1000 or fewer cores) in a reasonable amount of time (e.g., overnight). To be worthwhile, these calculations should model the true reactor physics with greater fidelity and fewer approximations than the traditional two-step method.

Light Water Reactor (LWR) cores are highly heterogeneous in the radial directions, but in the axial direction there is little variation in material properties. Thus, LWR analysis is an optimal application for methods that can treat the different dimensions with different levels of fidelity. This is the concept at the heart of the 2D/1D method [7]. In this method, the radial spatial dimensions are treated with high-fidelity 2D transport, while the axial dimension is treated by a simpler 1D method with a coarser mesh.

The 2D/1D method is the theoretical foundation of what are arguably the most prevalent deterministic neutron transport codes designed to perform LWR core calculations on mid-level computing platforms. In this method, a given 3D geometry is decomposed into several axial slices. Each axial slice is the spatial domain for a high-fidelity 2D transport calculation, which often employs the Method of Characteristics. The slices are coupled through axial transverse leakage (TL) terms, which are computed from the solution of an axial 1D transport equation over each pin in the reactor. A simplified diagram of the computational flow is given in Fig. 1.2. This special spatial discretization is advantageous for LWRs because the neutron flux has high-frequency radial variation and strong radial gradients, but mostly low frequency axial variation and weak axial gradients, which can be accurately modeled by a lower-fidelity 1D nodal solution. The 2D/1D method also parallelizes efficiently because adjacent slices are coupled on the "coarse" pin-cell grid, which is much coarser than the "fine" grid on which the 2D transport solution is solved. Additionally, the coupling terms are isotropic in the standard method. In the methods used in this work, anisotropic coupling terms are used, but the amount of data that must be passed is greatly reduced by Legendre and Fourier expansion.

The accuracy of the 2D/1D solution is increased when using anisotropic transverse leakage terms to couple the 2D and 1D equations [8],[9]. However, the resulting method has a significant increase in computational cost compared to the standard isotropic coupling method. While the isotropic approximation to the coupling terms is typically acceptable, there may be cases in which the 3D transport effects are stronger, and the error associated with this approximation is unacceptable.

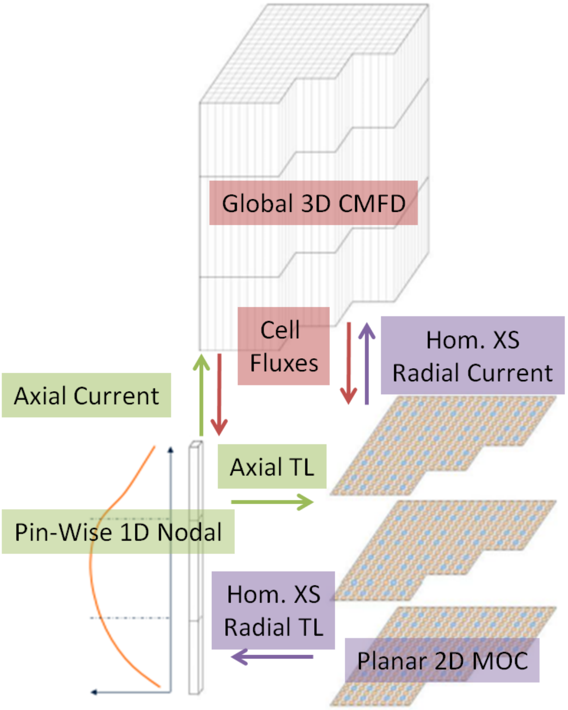

Figure 1.2: 2D/1D computational flow diagram

The 2D/1D method with anisotropic TL is akin to 3D transport with an alternating-direction implicit solution scheme [10], because the 2D and 1D methods are both transport-based, and no approximation is made to the coupling between the two equations. As such, the accuracy of this method is comparable to or even equivalent to that of 3D transport with sufficient refinement in the 2D and 1D mesh and angular quadrature. However, this is only true when there is no heterogeneity within the coarse cells. When there is heterogeneity, the homogenized total cross section (XS) represents another anisotropic coupling term between the 2D and 1D equations. The standard method uses an isotropic homogenized XS, which does not always preserve the 3D transport physics with sufficient accuracy. Using an anisotropic XS can improve the accuracy of the 2D/1D method for problems with heterogeneity, which are of significant practical interest. The anisotropic XS homogenization method is thoroughly studied in this work, and is one of the main novel contributions.

The work presented here has two primary goals. The first is to demonstrate theoretically the need for anisotropic homogenized XS for the 1D solution and verify the accuracy of the new method using these cross sections with numerical results. The second is to develop a 2D/1D method using parity in the polar angle to significantly reduce the cost of using anisotropic TL and homogenized XS. This faster method uses a coarse-mesh 2D discrete ordinates transport solution to calculate the odd polar parity angular flux, and the regular, fine-mesh 2D MOC solver to calculate the even polar parity angular flux. This reduces the overall amount of work done by the MOC solver, which is usually the most computationally expensive component of the overall solution.

All new methods derived in this work were implemented into the Michigan Parallel Advanced Characteristics Transport (MPACT) code, a reactor core simulator being developed collaboratively between the University of Michigan and Oak Ridge National Laboratory for CASL. These methods are tested by comparison to neutronics benchmarks and other test problems. Numerical results of these tests are shown in Chapters 4 and 5.

1.2 History of the 2D/1D Method

The 2D/1D concept applied to neutron transport for LWR applications was pioneered around the same time by two separate groups in Korea, with the first publications coming in 2002. The “2D/1D Fusion” method, implemented in the CRX code, was developed at the Korea Advanced Institute of Science and Technology (KAIST) by N.Z. Cho, G.S. Lee, C.J. Park, and colleagues [11]. At the Korea Atomic Energy Research Institute (KAERI), a slightly different method, which is simply called “2D/1D,” was developed by J.Y. Cho, H.G. Joo, K.S. Kim, S.Q. Zee and colleagues. This method was implemented in DeCART [12],[7],[13] and later, at SNU, in nTRACER [14].

The standard method implemented in MPACT uses isotropic TL and is fundamentally similar to the methods in nTRACER and DeCART [15]. The method implemented in MPACT for Stimpson’s thesis [8], which is the foundation of the work in the present thesis, uses anisotropic TL. In this sense, it is more like the 2D/1D Fusion method in CRX. However, the solver in MPACT uses a Fourier expansion in the azimuthal angle for the axial and radial TL that saves a significant amount of memory compared to the explicit azimuthal representation used in CRX. Additionally, a 1D P_3 solver is implemented in this method that uses a P_3 Legendre polynomial expansion in the polar angle for the radial TL instead of an explicit treatment of the polar angle.

The DeCART code began as part of a project through the International Nuclear Energy Research Initiative (INERI), and included collaboration between KAERI, Argonne National Laboratory (ANL), and Purdue University. DeCART eventually split into multiple versions. In the United States, one version was maintained by ANL and another by UM. In early versions of DeCART, nodal diffusion solvers (NEM and SENM) were used for the axial solution [12]. 1D P_3 axial solvers have been used for many years, owing to their improved accuracy [16],[17]. Work by Hursin et al. [18] added an axial S_N solver with polar-dependent radial TL.

UM eventually ceased development of DeCART to focus on a new 2D/1D implementation in MPACT [19],[20],[21]. Since 2014, MPACT has been developed collaboratively between UM and Oak Ridge National Laboratory (ORNL).

Stimpson implemented a method in MPACT that improved upon Hursin's method in DeCART by adding Fourier azimuthal moments to the radial TL, and treating the axial TL with the same anisotropy [9]. This capability in MPACT is similar to the pin-homogenized 2D/1D Fusion method. This is the starting point for the work in the present thesis.

Concurrent with the development of MPACT, separate researchers at ANL extended concepts from DeCART into PROTEUS-MOC, which uses 2D MOC with a finite-element discretization of the axial variable [22],[23]. Techinically, this work utilizes a 3D transport method, and represents a notable departure from traditional 2D/1D. However, the concept of using a different discretization for the radial and axial variables is similar to 2D/1D methods. Several other codes that perform 3D transport with a 2D/1D style discretization scheme have been developed, including PANX [24, 25], STREAM [26], and APOLLO3 [27]. An advantage of these codes is that they can handle voided regions with improved accuracy because of the direct 3D transport treatment. Traditional 2D/1D methods require XS homogenization with a 1D P_N axial solution, which may be unstable or inaccurate in the presence of voided regions. However, the traditional 2D/1D method performs well for LWR problems, which typically have no fully voided regions.

The disadvantage of the methods mentioned in the previous paragraph is that they are generally much more computationally expensive than the original 2D/1D method, because the coupling between adjacent "2D" transport solutions occurs on a finer spatial and angular mesh. The 2D/1D method implemented in MPACT, and several other codes, is favorable for LWR analysis because it boasts good accuracy at a relatively low computational expense compared to most 3D transport methods.

This thesis focuses on reducing the error in the 2D/1D method in MPACT due to angular approximations. Various sources of error in the original 2D/1D implementation in DeCART were studied by Cho [28] using numerical experimentation on a simple 2D problem using C5G7 cross sections [29]. Three separate errors were identified and quantified:

1. Nodal Error (i.e. axial spatial discretization error)
2. Diffusion Error
3. Homogenization Error

The nodal error was the most significant, but this is easily dispelled by using a nodal expansion of the source and flux in space for the axial solution. If necessary, the solution can be further improved by refining the axial discretization, either by using finer slices for the MOC or using subplane within MOC slices [30]. The "diffusion error" can be reduced by using a higher fidelity method for the 1D solver. MPACT uses a P_3 kernel for the axial solver.

This leaves only the homogenization error, which was found to be small for the problem studied in [28]. However, the problem studied in [28] is oversimplified and does not reflect the potential magnitude of the homogenization error for larger and more complicated problems. Stimpson's thesis [8] demonstrated that the heterogeneity error was significant for the 3D C5G7 benchmark problems. To demonstrate that the error in this problem when using 2D/1D with anisotropic TL was due to the pin heterogeneity, a modified C5G7 benchmark with homogenized pins was also analyzed. For this modified problem, the 2D/1D method with anisotropic TL demonstrated nearly perfect agreement with a 3D multigroup Monte Carlo Reference. Thus, there is an error in the 2D/1D approximation that is only present when pin cells are heterogeneous.

In Stimpson's thesis, addressing the heterogeneity error was named as a primary focus of future work. That declaration defined the starting point and motivation for the present thesis. There are two potential sources of error due to heterogeneity of a pin cell:

1. the pin-cell homogenization required for the 1D axial solver
2. the lack of a fine-mesh shape of the axial transverse leakage source in the 2D radial solver.

Based on the study by Cho [28], it was assumed in [8] that the XS homogenization was *not* the source of the heterogeneity error. Thus, the spatial shape of the axial TL was assumed to be the final component of a high-accuracy 2D/1D transport method in MPACT. However, in the present work, it was determined that the spatial shape of the axial TL is insignificant, and the XS homogenization is actually the cause of the errors observed in [8]. Thus, a major focus of this work is in correcting that XS homogenization error.

1.3 Dissertation Layout

Chapter 2 describes the many types of discretizations and solution methods used in solving neutron transport problems. The description begins with a physical meaning for each term in the 3D linear Boltzmann transport equation. Many of the common treatments for the energy, angular, and spatial variables are mentioned and briefly explained. Concepts and methods that pertain directly to the 2D/1D method used in this work, such as MOC, CMFD, and nodal methods, are explained in more detail than other methods.

Chapter 3 gives a mathematical foundation of the standard 2D/1D equations, and the different approximations used in this work that improve the accuracy of 2D/1D. Several new forms of equations for the 2D/1D method are derived, including a polar XS homogenzation, azimuthal moments of the homogenized XS, and 1D P_3 equations with anisotropic transverse leakage sources and collision terms. This chapter also discusses other aspects of the 2D/1D implementation in MPACT, including the iteration scheme, transverse leakage splitting, and under-relaxation. Additionally, some recent results by other researchers that seem to contradict the results of this work are discussed and explained.

Numerical results using the methods developed in Chapter 3 are presented in Chapter 4. Results are given for a wide range of problems to clearly illustrate multiple aspects of the 2D/1D approximation errors. First, a simple heterogeneous 1D problem is solved with 1D/1D transport to illustrate the fundamental deficiency of isotropic homogenization. Then, a problem with homogeneous "pins" is used to demonstrate the effect of the anisotropic TL in absence of any heterogeneity error due to the homogenized cross section. Next, a radially infinite lattice of pin cells with vacuum axial boundary conditions and varying height is considered. This is one of the simplest possible 3D transport problems that can be solved using a 2D/1D method. It serves to demonstrate the effect of the homogenization in the absence of confounding effects from the radial TL. A simple infinite repeating lattice of 9 pin cells (3 by 3 square) with a partially inserted control rod is considered next. In this problem, the effects of the TL and XS approximations are observed. This problem is also used to quantify the magnitude of the polar and azimuthal moments of the XS. Finally, the full 3D

C5G7 benchmark is used to evaluate the new method for a problem that is closer in complexity to a full reactor.

The most significant drawback of the method developed in Chapter 3 is that it has a relatively large computational and memory burden. In Chapter 5, a novel 2D/1D method is introduced that uses even and odd parity equations in the polar angle. The even parity equation is solved on the fine mesh using MOC, while the odd parity equation is solved using a coarse-mesh 2D S_N method. The resulting method is much faster than the method from Chapter 3, with only a moderate slowdown compared to the standard 2D/1D with isotropic TL. A few other ways to define a 2D/1D method with polar parity are discussed, but the one pursued in this work appears to be the most fruitful. Results using this method are given for the homogeneous fuel problem and the 3D C5G7 benchmark. Compared to the other method, which has significantly greater computational cost, this method demonstrates nearly equivalent accuracy in the anisotropic TL approximation and is comparable but slightly less accurate with respect to the 1D XS homogenization error. For problems with mild axial heterogeneity, this new method is likely sufficient, but the higher fidelity method may be necessary for problems with strong axial heterogeneity.

Chapter 6 investigates the theoretical accuracy of the 2D/1D method with different levels of angular fidelity in the TL. A theoretical analysis shows that the 2D/1D method with anisotropic TL moments can preserve the 3D SP_3 limit, as long as a sufficient number of anisotropic TL moments are used. With isotropic TL, the 2D/1D method does not preserve the 3D SP_3 limit. The Takeda-Ikeda [31] benchmark problem is used to compare 2D/1D methods to 3D SP_N. The results show that 2D/1D with isotropic TL is significantly more accurate than 3D SP_1 (diffusion), but significantly *less* accurate than 3D SP_3, even when a 1D P_3 axial solver is used. 2D/1D P_3 with anisotropic TL is more accurate than 3D SP_3.

The results and conclusions of the work are summarized in Chapter 7. Ongoing research and other potential topics for related future research are mentioned. The most significant area for future work is further development and application of the method to real reactor problems.

Chapter 2: Computational Neutron Transport Theory

In this chapter, the basic theory of neutron transport and the numerical methods used to solve transport problems are described. These methods are well documented in various textbooks [1],[32],[33]. There are also textbooks [34] and retrospective journal publications [35] that cover many of the computational methods used in neutron transport. Particular attention will be paid to the approximations, advantages and disadvantages of 2D/1D methods, which are the focus of this thesis. This chapter is a generalized description of the various transport methods, meant only to give context to the work presented in this thesis. More detailed information is available in the other texts cited here. A full description of the 2D/1D method is given in Chapter 3.

2.1 The Boltzmann Transport Equation

The behavior of free neutrons is described mathematically by the (steady-state) Boltzmann transport Eq. (2.1a):

$$\begin{aligned}
&\boldsymbol{\Omega} \cdot \nabla\psi(\mathbf{r}, \boldsymbol{\Omega}, E) + \Sigma_t(\mathbf{r}, E)\psi(\mathbf{r}, \boldsymbol{\Omega}, E) \\
&\qquad = \int_0^\infty \int_{4\pi} \Sigma_s(\mathbf{r}, \boldsymbol{\Omega}' \cdot \boldsymbol{\Omega}, E' \to E)\psi(\mathbf{r}, \boldsymbol{\Omega}', E')d\Omega' dE' \\
&\qquad + \frac{\chi(\mathbf{r}, E)}{4\pi} \int_0^\infty \nu\Sigma_f(\mathbf{r}, E')\psi(\mathbf{r}, \Omega', E')d\Omega' dE' + \frac{Q(\mathbf{r}, E)}{4\pi} \ , \qquad (2.1a)
\end{aligned}$$

$$\mathbf{r} = (x, y, z) \ , \qquad (2.1b)$$

$$\boldsymbol{\Omega} = (\sqrt{1-\mu^2}\cos\omega, \sqrt{1-\mu^2}\sin\omega, \mu) = (\Omega_x, \Omega_y, \Omega_x) \ . \qquad (2.1c)$$

In Eq. (2.1c), ω denotes the azimuthal angle, and μ denotes the cosine of the polar angle, which is the angle that $\mathbf{\Omega}$ forms with the z axis. Eq. (2.1a) is a linear integro-differential equation in seven variables (3 in space, 2 in angle, 1 in energy, and 1 in time). The equation is solved for ψ, the neutron angular flux, which is the neutron density at a given point in phase space multiplied by the velocity of those neutrons.

The transport equation consists of several terms, which will be explained individually. Each represents either a loss or gain rate of neutrons at a point in phase space. It can be thought of as a "conservation" equation: if there is no difference between loss and gain of neutrons at a certain point, angle, and energy, then the time derivative of the angular flux is 0 (steady-state). If there is an imbalance between loss and gain, it will drive a change in the neutron population, and thus the neutron angular flux, over time.

Only steady-state problems are analyzed in this thesis. This means that the neutron losses and sources are balanced, and the time derivative is 0.

The streaming operator represents the rate at which neutrons enter or leave a point in phase space due to their flight through space:

$$\mathbf{\Omega} \cdot \nabla \psi(\mathbf{r}, \mathbf{\Omega}, E) \ .$$

The collision term describes the rate at which neutrons at $(\mathbf{r}, \mathbf{\Omega}, E)$ collide with a nucleus:

$$\Sigma_t(\mathbf{r}, E) \psi(\mathbf{r}, \mathbf{\Omega}, E) \ .$$

$\Sigma_t(\mathbf{r}, E)$ is the rate, per unit length traveled, that a neutron at point $\mathbf{r}$ in the system with energy E will have any kind of interaction with a nucleus.

The scattering source is the rate at which neutrons are scattered into a given direction of flight and energy at a point in space:

$$\int_0^\infty \int_{4\pi} \Sigma_s(\mathbf{r}, \mathbf{\Omega}' \cdot \mathbf{\Omega}, E' \rightarrow E) \psi(\mathbf{r}, \mathbf{\Omega}', E') d\Omega' dE' \ .$$

The prompt fission source is the production rate of neutrons immediately (within 10^{-14} s) after fission. Almost all fission neutrons (typically $> 99\%$) are prompt. In the steady-state transport equations, the difference between prompt and delayed neutrons is ignored, and both are treated by a combined fission cross section $\nu\Sigma_f(\mathbf{r}, E)$:

$$\frac{\chi(\mathbf{r}, E)}{4\pi} \int_0^\infty \int_{4\pi} \nu\Sigma_f(\mathbf{r}, E')\psi(\mathbf{r}, \Omega', E')d\Omega' dE' \ .$$

χ is the energy spectrum of fission neutrons. ν is the number of neutrons produced per fission, and Σ_f is the fission cross section.

The final term is called the external source:

$$\frac{Q(\mathbf{r}, E, t)}{4\pi} \ .$$

This accounts for any source of neutrons that does not fit into one of the previous terms. These sources are not directly dependent on the neutron flux in the system. Some examples include an accelerator source (D-D, D-T, or other), a spontaneous fission source such as Californium, or a photo-neutron source that produces neutrons from high-energy photons emitted by fission events or fission products. The external source is usually not relevant for reactor problems.

The methods developed in this thesis will only be applied to steady-state neutron transport problems. Although the methods in this thesis have not been applied to non-steady-state (i.e., “transient”) problems, doing this would probably not require any significant changes. MPACT, and most deterministic codes, solve transient problems by discretizing in time and solving several “transient fixed-source problems” in which the transient term is integrated and treated as an external source. Because the method developed here can solve steady-state fixed-source problems, it can also be used to solve transient problems [36].

2.2 k_{eff} Eigenvalue Problems

For steady-state neutron transport problems, the fission source is scaled by the inverse of the effective neutron multiplication factor k_{eff} to enforce balance between the left and right sides of the equation:

$$\begin{aligned}\mathbf{\Omega}\cdot\nabla\psi(\mathbf{r},\mathbf{\Omega},E)&+\Sigma_t(\mathbf{r},E)\psi(\mathbf{r},\mathbf{\Omega},E)\\&=\int_0^\infty\int_{4\pi}\Sigma_s(\mathbf{r},\mathbf{\Omega}'\cdot\mathbf{\Omega},E'\rightarrow E)\psi(\mathbf{r},\mathbf{\Omega}',E')d\Omega'dE'\\&\quad+\frac{1}{k_{eff}}\frac{\chi(\mathbf{r},E)}{4\pi}\int_0^\infty\int_{4\pi}\nu\Sigma_f(\mathbf{r},E')\psi(\mathbf{r},\Omega',E')d\Omega'dE'\ .\end{aligned}\tag{2.2}$$

The effective multiplication factor k_{eff} is the inverse of the largest eigenvalue of the system λ_1:

$$k_{eff}=\frac{1}{\lambda_1}\ .\tag{2.3}$$

Because of the normalization term k_{eff}, which depends on the angular flux, Eq. (2.2) is a nonlinear equation that is solved iteratively by power iteration. In most deterministic codes, the solution process involves, in one form or another, inverting the transport operator L:

$$L=\mathbf{\Omega}\cdot\nabla+\Sigma_t\ .\tag{2.4}$$

The source Q, which is a combination of scattering and fission sources, is calculated using the angular flux from the previous iteration. The next estimate of the angular flux is then calculated in the following manner:

$$\begin{aligned}Q^{(l)}(\mathbf{r},\mathbf{\Omega},E)&=\int_0^\infty\int_{4\pi}\Sigma_s(\mathbf{r},\mathbf{\Omega}'\cdot\mathbf{\Omega},E'\rightarrow E)\psi^{(l)}(\mathbf{r},\mathbf{\Omega}',E')d\Omega'dE' &&\text{(2.5a)}\\&\quad+\frac{1}{k_{eff}^{(l)}}\frac{\chi(\mathbf{r},E)}{4\pi}\int_0^\infty\int_{4\pi}\nu\Sigma_f(\mathbf{r},E')\psi^{(l)}(\mathbf{r},\Omega',E')d\Omega'dE'\ ,\\\psi^{(l+1)}(\mathbf{r},\mathbf{\Omega},E)&=L^{-1}Q^{(l)}(\mathbf{r},\mathbf{\Omega},E)\ . &&\text{(2.5b)}\end{aligned}$$

Here, (l) is the iteration index. The multiplication factor is defined as the multiplication of neutrons over successive iterations [32]:

$$\begin{aligned} k_{eff}^{(l+1)} &= \frac{\text{Fission neutrons produced by } \psi^{(l)}}{\text{Fission neutron source for } \psi^{(l)}} \\ &= \frac{\int\limits_V \int\limits_0^\infty \int\limits_{4\pi} \nu\Sigma_f(\mathbf{r},E)\psi^{(l+1)}(\mathbf{r},\Omega,E)d\Omega dEdV}{\frac{1}{k_{eff}^{(l)}} \int\limits_V \int\limits_0^\infty \int\limits_{4\pi} \nu\Sigma_f(\mathbf{r},E)\psi^{(l)}(\mathbf{r},\Omega,E)d\Omega dEdV} \ . \end{aligned} \tag{2.6}$$

The solution to this eigenvalue problem can be scaled arbitrarily in theory, so a normalization condition for ψ is enforced:

$$\int\limits_0^\infty \int\limits_{4\pi} \psi^{(l)}(\mathbf{r},\mathbf{\Omega},E)d\Omega dE = \Psi = \text{constant} \ . \tag{2.7}$$

After many iterations, $k_{eff}^{(l)}$ and $\psi^{(l)}$ will converge to the solution of the equations. This iterative scheme converges very slowly because most reactor problems have very high dominance ratios. In other words, the eigenvalues are closely bunched near the maximum, so the eigenmode error associated with the second largest eigenvalue dies away slowly, and it takes many power iterations to converge to the eigenfunction associated with the largest eigenvalue $\lambda_1 = \frac{1}{k_{eff}}$. In practice, the iteration is almost always accelerated by a lower-order solution to the equations.

Eqs. (2.5) show the "power iteration" process for obtaining an iterative solution to Eq. (2.2). To obtain a deterministic solution, the space, angle, and energy variables must be discretized. These approximations will be discussed next.

2.3 Monte Carlo Methods

Stochastic, or "Monte Carlo" methods are a common and important class of methods for solving the neutron transport equation. These methods directly determine neutron behavior by simulating the physics of individual neutrons as they travel through a medium, are scattered many times, and eventually absorbed, potentially leading to a fission event. These methods are capable of more accurately modeling the physics of the problem because neutrons are simulated individually. Each neutron can have an energy, position, and direction of flight that is exactly represented (no discretization, no grid). A Monte Carlo method gives a probabilistic estimate of the true solution.

Thus, the solution has an associated uncertainty related to the statistical nature of the estimate. The uncertainty is reduced as more particles are simulated.

A Monte Carlo method simulates reactor problems using many batches of neutrons, each roughly representing a single neutron generation. Each batch typically consists of many thousands of neutron histories, followed from birth in a fission event to the end of the history by absorption or leakage. The solution begins with "inactive" cycles, which are used to obtain an accurate estimate of the spatial distribution of the fission source. When this is complete, the code begins "active" cycles in which quantities such as pin powers and the effective multiplication factor are estimated.

Monte Carlo methods are frequently used in the reactor physics community, although most whole-core analysis and multi-physics still relies on deterministic codes, because Monte Carlo is usually too expensive for whole-core calculations. In addition to reactor analysis, Monte Carlo is often used as a verification tool to check whether deterministic codes are accurately simulating neutron physics. In this thesis, multigroup Monte Carlo will be used to generate reference solutions to test problems so deterministic methods can be compared against one another by evaluating their agreement with the Monte Carlo solution. The Shift Monte Carlo code [37] and OpenMC code [38] are used for these purposes.

2.4 Discretization Methods

One of the most challenging aspects of solving the transport equation is that the cross sections usually vary strongly in both energy and space, and may span several orders of magnitude in very short intervals. As a result, the solution varies sharply in energy and space. Because of the streaming term, the solution may also vary sharply in angle if the problem is spatially heterogeneous. This makes accurate discretization of the variables challenging. Some common discretizations are discussed in this section.

While deterministic methods require discretization, Monte Carlo methods can treat the neutron position, direction of flight, and energy continuously. The cross sections are discretized in space and angle, and the cross section energy dependence can be treated with a fine discretization with interpolation that is effectively equivalent to a continuous representation. This is possible because Monte Carlo methods simulate the path of a single neutron through phase space. The exact energy of the individual neutron is known, so a specific, accurate cross section can be determined. The average behavior of neutrons in the system is then determined by simulating many millions of neutron histories to get a statistically converged average.

While Monte Carlo methods can solve neutron transport problems with good accuracy and little approximation, they are computationally very expensive. Often, the computing requirements of using Monte Carlo are prohibitive, which motivates the development of deterministic methods with sufficient fidelity for problems of practical interest.

Deterministic methods directly calculate the average behavior of neutrons in the system, which requires discretization of the neutron flux in space, angle, and energy. If these discretizations were all refined enough, it would obviously approach a continuous representation, but it is almost never feasible to refine the discretization this much in a practical problem.

2.4.1 The Multigroup Approximation

The cross sections of almost all nuclides have a strong dependence on incident neutron energy. The energy dependence is also very unsmooth because of thousands of resonances. The cross section is increased significantly for a very narrow range of neutron energies around the resonance peak energies. The total cross section of U^{235} is given in Fig. 2.1a, with a zoomed in look to show detail in the resonance region. For nuclides of greatest interest in reactor problems, such as U^{235}, U^{238}, Pu^{239}, etc., it would require several hundred thousand points to faithfully reproduce the energy dependence of the cross sections from thermal energies (10^{-2} eV) to fission neutron energies (up to 10^{7} eV).

The energy variable is discretized by subdividing the domain into several energy groups, each representing all neutrons between a given lower and upper energy bound. All neutrons in a given energy group are treated with group-averaged quantities in the transport calculation. Typically, these groups are indexed, starting with the highest energy (fast) neutrons in group 1, followed by sequential, contiguous groups down to the lowest energy neutrons in group G. The multigroup values are obtained by

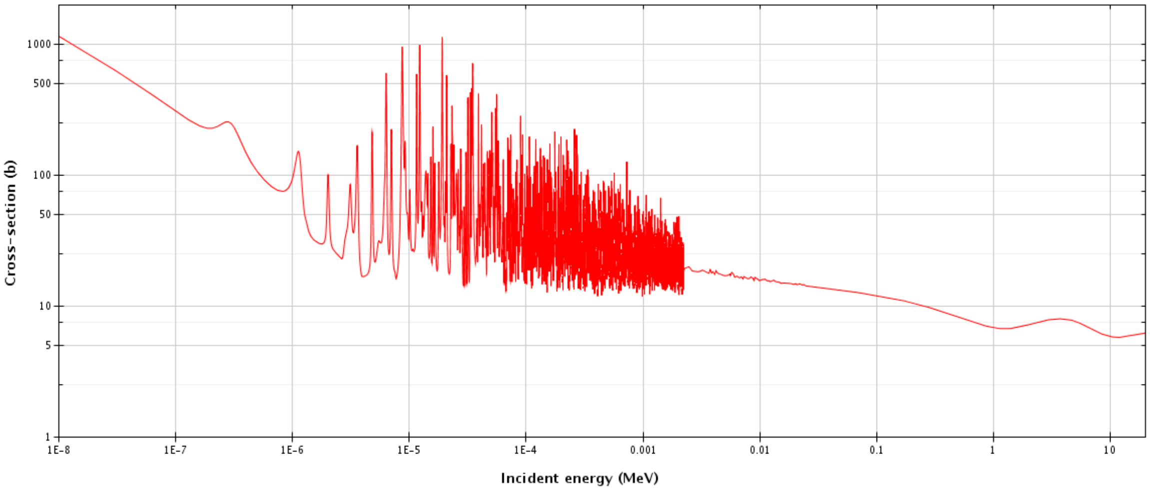

(a) Full reactor energy range

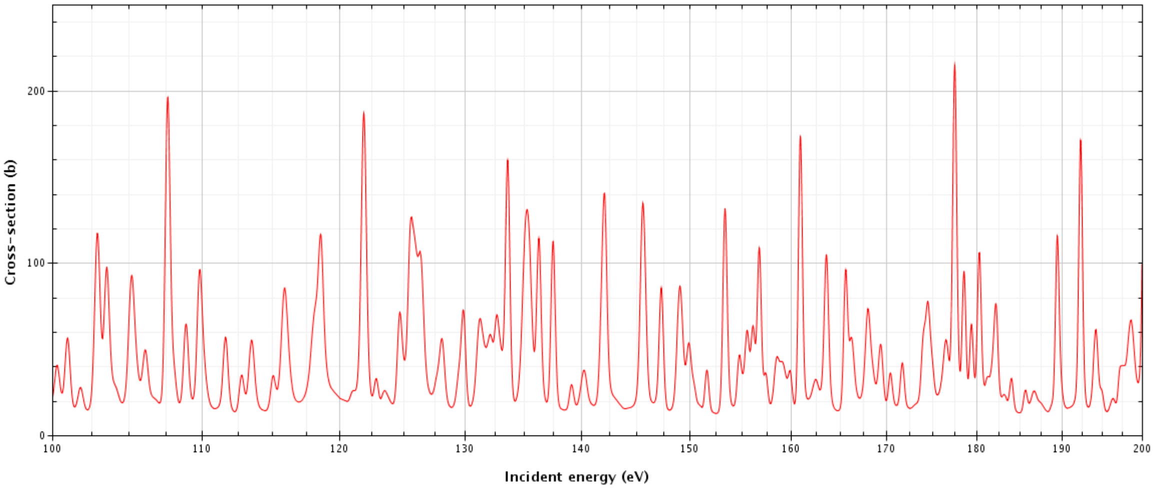

(b) 100-200 eV range

Figure 2.1: U^{235} total cross section

integrating over the energy bounds of the group:

$$\psi_g(\mathbf{r},\mathbf{\Omega}) = \int\limits_{E_g}^{E_{g-1}} \psi(\mathbf{r},\mathbf{\Omega},E)dE \ , \tag{2.8a}$$

$$\chi_g(\mathbf{r},\mathbf{\Omega}) = \int\limits_{E_g}^{E_{g-1}} \chi(\mathbf{r},\mathbf{\Omega},E)dE \ , \tag{2.8b}$$

$$\Sigma_{t,g}(\mathbf{r},\mathbf{\Omega}) = \frac{\int\limits_{E_g}^{E_{g-1}} \Sigma_t(\mathbf{r},E)\psi(\mathbf{r},\mathbf{\Omega},E)dE}{\int\limits_{E_g}^{E_{g-1}} \psi(\mathbf{r},\mathbf{\Omega},E)dE} \ . \tag{2.8c}$$

The group-to-group scattering cross section is

$$\Sigma_{s,g\leftarrow g'}(\mathbf{r},\mathbf{\Omega}'\cdot\mathbf{\Omega}) = \frac{\int\limits_{E_g}^{E_{g-1}} dE \int\limits_{E_{g'}}^{E_{g'-1}} \Sigma_s(\mathbf{r},\mathbf{\Omega}'\cdot\mathbf{\Omega},E'\to E)\psi(\mathbf{r},\mathbf{\Omega}',E')dE'}{\int\limits_{E_{g'}}^{E_{g'-1}} \psi(\mathbf{r},\mathbf{\Omega}',E')dE'} \ . \tag{2.9}$$

The fission cross section is

$$\nu\Sigma_{f,g}(\mathbf{r},\mathbf{\Omega}) = \frac{\int\limits_{E_g}^{E_{g-1}} \nu\Sigma_f(\mathbf{r},E)\psi(\mathbf{r},\mathbf{\Omega},E)dE}{\int\limits_{E_g}^{E_{g-1}} \psi(\mathbf{r},\mathbf{\Omega},E)dE} \ . \tag{2.10}$$

The cross sections are weighted by the flux spectrum because they operate on the flux in the transport equation. This presents a difficulty because the cross sections must be known in order to solve for the flux, but the multigroup cross sections depend on the flux spectrum within the group. In practice, the cross sections are determined by solving a problem with simplified geometry that approximates the continuous energy or fine-group flux spectrum. This spectrum is then used to "collapse" the cross sections into broader multigroup values. [32],[39].

While the correct weighting function for the multigroup cross sections is the angular flux, it is expensive to store and use angle-dependent cross sections. Instead, it is assumed that the angular flux spectrum is separable in energy and angle over a given energy group:

$$\psi(\mathbf{r},\mathbf{\Omega},E) \approx \varphi(\mathbf{r},E)\Psi_g(\mathbf{r},\mathbf{\Omega}) \ , \ E_{g-1} < E < E_g \ . \tag{2.11}$$

This leads to isotropic multigroup cross sections:

$$\Sigma_{t,g} = \frac{\int\limits_{E_g}^{E_{g-1}} \Sigma_t(\mathbf{r},E)\varphi(\mathbf{r},E)}{\int\limits_{E_g}^{E_{g-1}} \varphi(\mathbf{r},E)} \ . \tag{2.12}$$

The multigroup form of the steady-state transport equation is:

$$\begin{aligned}\mathbf{\Omega}\cdot\nabla\psi_g(\mathbf{r},\mathbf{\Omega})+\Sigma_{t,g}(\mathbf{r})\psi_g(\mathbf{r},\mathbf{\Omega}) &= \sum_{g'=1}^{G}\int_{4\pi}\Sigma_{s,g\leftarrow g'}(\mathbf{r},\mathbf{\Omega}'\cdot\mathbf{\Omega})\psi_{g'}(\mathbf{r},\mathbf{\Omega}')d\Omega' \\ &+\frac{1}{k_{eff}}\frac{\chi_g(\mathbf{r})}{4\pi}\sum_{g'=1}^{G}\int_{4\pi}\nu\Sigma_{f,g'}(\mathbf{r})\psi_{g'}(\mathbf{r},\mathbf{\Omega}')d\Omega'\ ,\ 1\le g\le G\ . \qquad (2.13)\end{aligned}$$

There have been other energy discretization methods proposed recently. Till developed a non-contiguous, finite-element discretization in energy [40],[41]. Zhu and Forget developed a discrete generalized multigroup energy expansion method [42] using Discrete Legendre Orthogonal Polynomials to expand energy dependence of the angular flux within coarse groups. However, neither has yet been adopted widely, and the traditional multigroup method remains ubiquitous.

2.4.2 Angular Discretization

. There are a few ways the angular variable $\mathbf{\Omega}$ is approximated:

1. Discretization (discrete ordinates method)
2. Expansion in Spherical Harmonics
3. Diffusion approximation (the simplest case of spherical harmonics expansion)

Discrete ordinates methods are referred to as S_N, where N reflects the order of the quadrature rule used to integrate the ordinates. Expansion in spherical harmonics is commonly referred to as P_N, where N is the order of the expansion.

Discrete Ordinates Approximation

The unit vector $\mathbf{\Omega}$ is defined by two separate scalar variables, ω and μ, in Eq. (2.1c):

$$\mathbf{\Omega}=\left(\sqrt{1-\mu^2}\cos\omega,\sqrt{1-\mu^2}\sin\omega,\mu\right)\ . \qquad (2.1c)$$

$\mathbf{\Omega}$ is discretized into ordinates separately in ω and μ. A quadrature rule is used to compute integrals over angle. Two types of quadrature rules are typically used for these variables in neutron transport: level-symmetric and product quadratures. In a level-symmetric quadrature, quadrature points are evenly distributed over the unit sphere. While this would be optimal for a homogeneous medium, it performs poorly for LWR problems because the neutrons traveling in directions close to the z axis are modeled poorly because of the coarse azimuthal discretization. These neutrons are important in LWR analysis because spatial self-shielding is an important effect and is strongly dependent on polar angle. A cartoon of the placement of level symmetric quadrature points is given in Fig. 2.2.

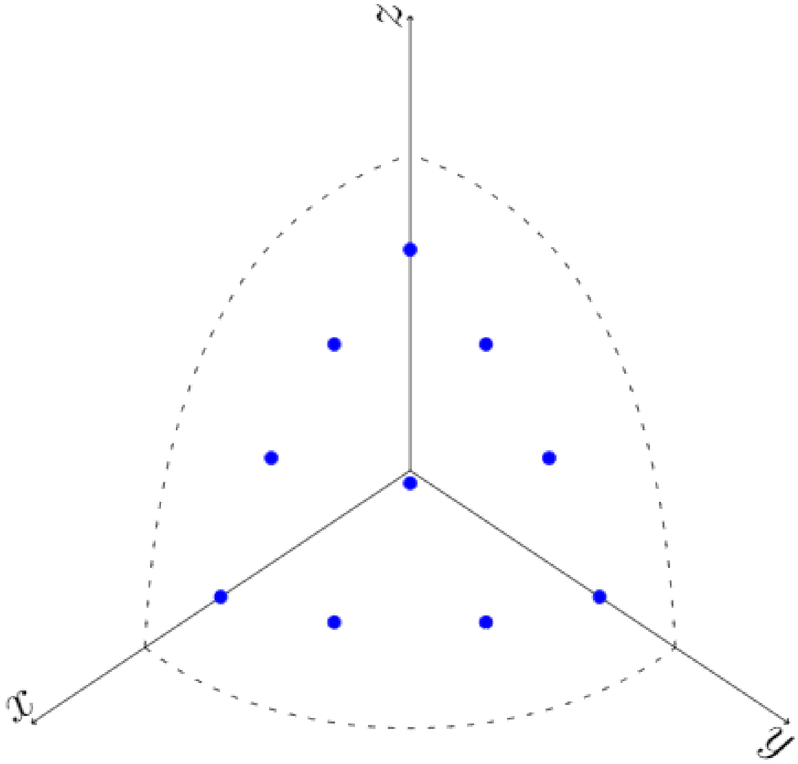

Figure 2.2: Level-Symmetric quadrature points

In a product quadrature, the quadrature points over 4π are determined by the combination of a quadrature over 2π for the azimuthal angle ω and a quadrature from -1 to 1 for the polar cosine μ. In this case, a Chebyshev quadrature is used in the azimuthal angle, and a Gaussian or an optimized MOC quadrature, such as that developed by Yamamoto and Tabuchi [43], is used for the polar angle. While the Yamamoto-Tabuchi quadrature is preferred for 2D MOC because it provides good accuracy with a low number of polar angles, a Gaussian quadrature is used exclusively in this work because it is necessary to exactly integrate the Legendre moments of the radial TL. A cartoon of the placement of product quadrature points is given in Fig. 2.3. The size of the ordinates does not reflect their associated weights. Note that there are an equal number of points at each polar angle. This leads to tightly-spaced ordinates near the polar axis.

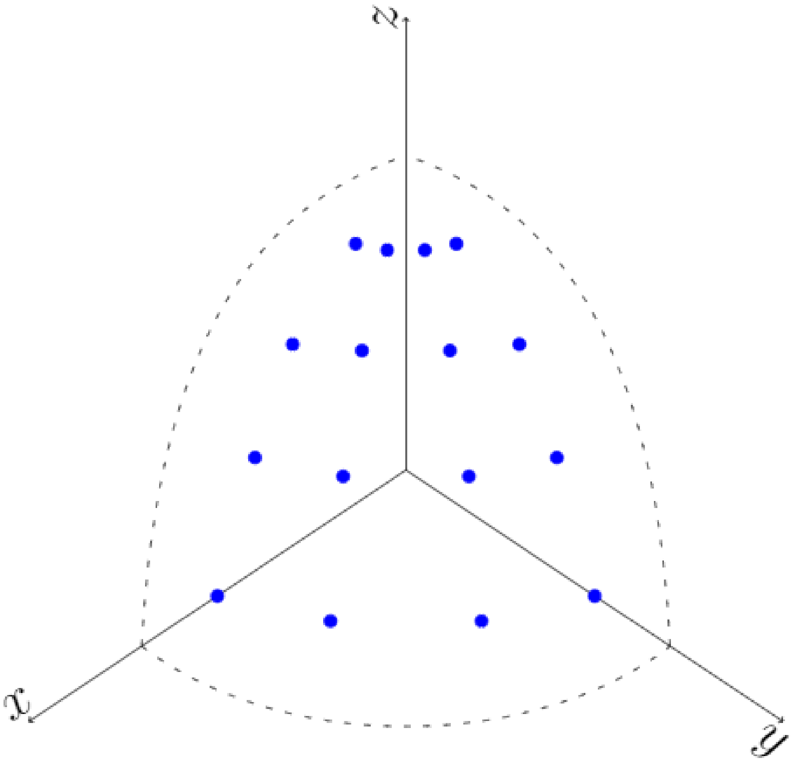

Figure 2.3: Product quadrature points

In this thesis, only product quadratures are used. This is not only because they are more accurate, but also because the anisotropic TL methods often treat the azimuthal and polar angles separately, which is more straightforward and memory efficient when their ordinate sets are independent of one another.

When the discrete ordinates approximation is applied to the transport equation, the integrals over angle become sums over the quadrature set. The multigroup transport equation with the discrete ordinates approximation is

$$\begin{aligned}\boldsymbol{\Omega}_n \cdot \nabla \psi_{g,n}(\mathbf{r}) + \Sigma_{t,g}(\mathbf{r})\psi_{g,n}(\mathbf{r}) &= \sum_{g'=1}^{G}\sum_{n'=1}^{N} w_n \Sigma_{s,g\leftarrow g',n\leftarrow n'}(\mathbf{r})\psi_{g',n'}(\mathbf{r}) \\ &+ \frac{1}{k_{eff}}\frac{\chi_g(\mathbf{r})}{4\pi}\sum_{g'=1}^{G} \nu\Sigma_{f,g'}(\mathbf{r})\phi_{g'}(\mathbf{r}) \ , \ 1 \le g \le G \ , \ 1 \le n \le N \ . \end{aligned} \quad (2.14)$$

Here, n is the discrete ordinate index and w_n is the associated weight. The sum over the quadrature set of the angular flux ψ is the scalar flux ϕ:

$$\phi_g(\mathbf{r}) = \int\limits_{4\pi} \psi_g(\mathbf{r}, \mathbf{\Omega}) d\Omega = \sum_{n=1}^{N} w_n \psi_{g,n}(\mathbf{r}) \ . \tag{2.15}$$

2.4.3 Spherical Harmonics Expansion

Another way of treating the angular variable is to expand the angular flux in spherical harmonics [44]:

$$\psi_g(\mathbf{r}, \mathbf{\Omega}) = \sum_{n=0}^{\infty} \sum_{m=-n}^{n} \psi_{n,m,g}(\mathbf{r}) Y_n^m(\mathbf{\Omega}) \ . \tag{2.16}$$

The infinite sum limits to the exact value of $\psi_g(\mathbf{r}, \mathbf{\Omega})$. In practice, the moments are truncated at some finite number N.

$$\psi_g(\mathbf{r}, \mathbf{\Omega}) \approx \sum_{n=0}^{N} \sum_{m=-n}^{n} \psi_{n,m,g}(\mathbf{r}) Y_n^m(\mathbf{\Omega}) \ . \tag{2.17}$$

The spherical harmonics functions are given by:

$$Y_n^m(\mathbf{\Omega}) = \left[\frac{2n+1}{4\pi} \frac{(n-|m|)!}{(n+|m|)!} \right]^{1/2} P_n^{|m|}(\mu) e^{im\omega} \ , \ 0 \leq |m| \leq n \leq \infty \ , \tag{2.18}$$

$$P_n^m(\mu) = (1-\mu^2)^{m/2} \left(\frac{d}{d\mu} \right)^m P_n(\mu) \ , \ 0 \leq m \leq n < \infty \ , \tag{2.19}$$

where $P_n(\mu)$ are the Legendre polynomials.

The P_N equations are derived by multiplying the multigroup transport Eq. (2.13) by $Y_j^k(\mathbf{\Omega})$ for each j and k satisfying $0 \leq |k| \leq j \leq N$, and then integrating each of the resulting equations over $\mathbf{\Omega} \in 4\pi$. This leads to a system of $(N+1)^2$ equations for each energy group g. Thus, the number of unknowns increases quadratically with the order of the expansion N. This makes the P_N methods higher than order P_1 less attractive for 2D and 3D problems.

In 1D planar geometry, the P_N equations are much simpler because there is only one angular variable (μ). The spherical harmonics reduce to Legendre polynomials. Following the same process of multiplying the multigroup transport equation by each harmonic function and integrating results in a system of $(N+1)$ equations for each energy group with the following form:

$$\frac{d}{dz}\left[\frac{n}{2n+1}\phi_{g,n-1}(z) + \frac{n+1}{2n+1}\psi_{g,n+1}(z)\right] + \Sigma_{t,g}(z)\phi_{g,n}(z) \\ = \sum_{g'=1}^{G} \Sigma_{sn,g\leftarrow g'}(z)\phi_{g',n}(z) + Q_g(z)\delta_{n,0}\ ,\ 0 \le n \le N\ , \quad (2.20)$$

where $\Sigma_{sn,g\leftarrow g'}$ is the n^{th} order scattering moment and $Q_g(z)$ represents either an external source or a fission source.

The expansion is truncated by assuming the last moment (N+1) is 0:

$$\phi_{-1}(z) = \phi_{N+1}(z) = 0\ . \quad (2.21)$$

The complexity of the problem increases only linearly with N, which makes these methods more attractive in 1D. P_N methods are the most common solution methodology used for the 1D axial problems in MPACT.

Next, a monoenergetic form of the planar geometry P_1 equations is used to define a few common approximations.

Planar Geometry P_1 approximation

Using Eq. (2.20), the planar geometry P_1 equations can be written (without energy dependence):

$$\frac{d}{dz}\phi_1 + \Sigma_t\phi_0 = \Sigma_{s0}\phi_0 + Q\ ,\ 0 < z < Z\ , \quad (2.22a)$$

$$\frac{d}{dz}\left(\frac{1}{3}\phi_0\right) + \Sigma_t\phi_1 = \Sigma_{s1}\phi_1\ ,\ 0 < z < Z\ . \quad (2.22b)$$

Eq. (2.22b) can be solved for ϕ_1:

$$\phi_1 = -\left[\frac{1}{3}\left(\Sigma_t - \Sigma_{s1}\right)^{-1}\right]\frac{d}{dz}\phi_0 = -D\frac{d}{dz}\phi_0\ . \quad (2.23)$$

D is called the diffusion coefficient. Substituting Eq. (2.23) in Eq. (2.22a) gives the diffusion equation in 1D:

$$-\frac{d}{dz}D\frac{d}{dz}\phi_0 + \Sigma_t\phi_0 = \Sigma_{s0}\phi_0 + Q\ ,\ 0 < z < Z\ . \quad (2.24)$$

The Simplified $\mathbf{P}_N$ approximation

If the 1-D diffusion operator in Eq. (2.24) is formally replaced with the 3D diffusion operator:

$$\frac{d}{dz}D\frac{d}{dz} \rightarrow \nabla \cdot D\nabla \ ,$$

the result is the 3D P_1 equation:

$$-\nabla \cdot D\nabla\phi_0 + \Sigma_t\phi_0 = \Sigma_{s0}\phi_0 + Q \ , \ \mathbf{r} \in V \ . \tag{2.25}$$

Eq. (2.25) is commonly referred to as the 3D neutron diffusion equation. This is one of many ways to derive the diffusion equation. The common thread in all is that the diffusion equation is obtained by truncating the expansion of the angular flux at linear moments in $\mathbf{\Omega}$ and substituting it into the transport equation, then eliminating the angular dependence from the resulting equations.

This simple relationship between the 1D planar geometry and 3D cases of the P_N equations only exists for P_1. However, if the same modification is applied to the 1D planar P_N equations for higher orders N, the result is a Simplified P_N approximation (SP_N). The SP_N equations are less accurate than their P_N counterpart, but are much easier to solve [45],[46], and more accurate than diffusion.

The SP_N approximation is obtained by an ad hoc replacement of the spatial derivatives in the Eq. (2.23) with analogous 3D operators [45]. For example, the monoenergetic 3D SP_3 equations are:

$$-\nabla \cdot \frac{1}{3\Sigma_{tr}}\nabla\hat{\phi} + \Sigma_a\hat{\phi}_0 = Q \ , \tag{2.26a}$$

$$-\nabla \cdot \frac{9}{35\left(\Sigma_t - \Sigma_{s3}\right)}\nabla\phi_2 + \left(\Sigma_t - \Sigma_{s2} + \frac{4}{5}\Sigma_a\right)\phi_2 = \frac{2}{5}\left(\Sigma_a\hat{\phi}_0 - Q\right) \ , \tag{2.26b}$$

$$\hat{\phi}_0 = \phi_0 + 2\phi_2 \ . \tag{2.26c}$$

More rigorous derivations of these equations exist, including an asymptotic derivation by Larsen, Morel, and McGhee [47] and a variational derivation by Brantley and Larsen [48], but this simplified version is sufficient for the brief summary given here.

Eqs. (2.26) are two coupled diffusion-like equations that can be solved more quickly and easily than the P_3 equations. Unlike the P_N equations, the SP_N equations do not converge to the transport solution as $N \rightarrow \infty$. Thus, SP_N implementations are not common beyond order $N = 3$, or $N = 5$. The SP_3 solution has satisfactory accuracy for many applications in which the P_1 or diffusion solution is inaccurate because of strong streaming or absorption of neutrons.

The Diffusion Approximation

For the lowest-order spherical harmonics expansion, the 3D P_1 and 3D SP_1 equations are equivalent, Eq. (2.25), and are commonly known as the neutron diffusion equations or the diffusion approximation to the transport equation. The diffusion approximation assumes that the anisotropy of the angular flux is linear, as well as the anisotropy in the scattering cross section. This approximation will be inaccurate when the stated assumptions are poor. This can occur when:

- The scattering cross section anisotropy is strong and nonlinear in $\mathbf{\Omega}$.
- The true angular flux anisotropy is strong and nonlinear in $\mathbf{\Omega}$ because of strong spatial heterogeneity in the cross sections or the source. This is likely the case at vacuum boundaries and material interfaces.

In initial implementations of the 2D/1D method, the 1D problem was typically solved using diffusion [12],[7]. However, the error caused by this approximation was significant [28] and current implementations typically use the P_3 equations [17].

2.4.4 Scattering Approximations

In Sec. 2.4.3, expansion of the angular flux in spherical harmonics was introduced. The angular dependence of the scattering cross section is also commonly expanded in spherical harmonics, whether the angular flux is being approximated by harmonics or discrete ordinates. This is done because storing the full discrete ordinates angular flux is often too expensive. Also, a full scattering matrix for scattering between each possible combination of discrete ordinates would be large and burdensome. By expanding the cross section, the anisotropic source can be calculated with only a few angular flux moments.

Anisotropic Scattering

The anisotropy of the scattering source is a function of the dot product of the incoming and outgoing directions of flight, or the cosine of the angle between them, as in Eq. (2.13):

$$\Sigma_{s,g\leftarrow g'}(\mathbf{r}, \mathbf{\Omega}' \cdot \mathbf{\Omega}) = \Sigma_{s,g\leftarrow g'}(\mathbf{r}, \mu_s) \ . \tag{2.27}$$

This scattering cross section can be expanded in Legendre polynomials as in Sec. 2.4.2:

$$\Sigma_{sl,g\leftarrow g'}(\mathbf{r}) = 2\pi \int_{-1}^{1} P_l(\mu')\Sigma_{s,g\leftarrow g'}(\mathbf{r},\mu')d\mu' \ . \tag{2.28}$$

For reactor problems, an expansion of order between 1 and 3 is usually sufficient. To calculate the scattering source, angular flux moments must be stored up to the order L of the scattering kernel. The angular flux moments are defined by

$$\begin{aligned} \varphi_{g,l}^{m} &= \int_{4\pi} \psi_g(\mathbf{\Omega})R_l^m(\mathbf{\Omega})d\Omega \\ &= \sum_{n=1}^{N} w_n \psi_{g,n} R_l^m(\mathbf{\Omega}_n) \ . \end{aligned} \tag{2.29}$$

R_l^m are the real parts of the spherical harmonics from Eq. (2.18). In a P_N method, the angular flux moments are part of the solution. In a discrete ordinates method, the moments must be calculated and stored during the transport sweep. This can be a significant memory and computational burden.

Transport-Corrected Scattering

To avoid the expense of calculating and storing angular flux moments, transport-corrected isotropic scattering methods have been developed [49, 50, 51, 52]. These methods attempt to account for linearly anisotropic scattering effects by modifying the isotropic moment of the self-scattering cross section. This is referred to as transport-corrected P_0 (TCP0) scattering [49]. In light water reactors, the strongest anisotropic scatterer is hydrogen, although other isotopes also contribute.

In monoenergetic problems, the transport cross section is calculated by simply subtracting the linearly anisotropic moment from the self-scattering cross section, and modifying the total cross section accordingly:

$$\begin{aligned} \hat{\Sigma}_{s0} &= \Sigma_{s0} - \Sigma_{s1} \ , \\ \Sigma_{tr} &= \Sigma_t - \Sigma_{s1} \ . \end{aligned} \tag{2.30}$$

The definition of the transport correction is more complicated in multigroup problems, because anisotropic scattering occurs between groups. The simplest approach is to assume that the linearly anisotropic inscatter and outscatter terms are equivalent:

$$\sum_{g'\neq g} \Sigma_{s1,g\leftarrow g'}\psi_{g'} = \psi_g \sum_{g'\neq g} \Sigma_{s1,g'\leftarrow g} \ . \tag{2.31}$$

This leads to the outscatter approximation to the transport correction:

$$\begin{aligned} \hat{\Sigma}_{s0,g\leftarrow g} &= \Sigma_{s0,g\leftarrow g} - \sum_{g'=1}^{G} \Sigma_{s1,g'\leftarrow g} \ , \\ \Sigma_{tr} &= \Sigma_{t,g} - \sum_{g'=1}^{G} \Sigma_{s1,g'\leftarrow g} \ . \end{aligned} \tag{2.32}$$

The outscatter approximation is commonly used because of its simplicity, but it is not the most accurate transport correction method. The inscatter method is more accurate:

$$\begin{aligned} \hat{\Sigma}_{s0,g\leftarrow g} &= \Sigma_{s0,g\leftarrow g} - \frac{1}{\phi_{1,g}} \sum_{g'=1}^{G} \Sigma_{s1,g\leftarrow g'}\phi_{1,g'} \ , \\ \Sigma_{tr} &= \Sigma_{t,g} - \frac{1}{\phi_{1,g}} \sum_{g'=1}^{G} \Sigma_{s1,g\leftarrow g'}\phi_{1,g'} \ . \end{aligned} \tag{2.33}$$

This requires an estimate of the neutron current spectrum $\phi_{1,g}$, which can be obtained from a solution to a 0D B_1 equation, or approximated by the flux spectrum of an infinite medium solution.

Several methods that are related to the inscatter method have been proposed recently. Herman [50] used Monte Carlo to simulate a 1D fixed source problem in light water to generate a diffusion coefficient based on the ratio of leakage to total flux in a subregion away from transport effects. Kim [51] developed a related method called Neutron Leakage Conservation (NLC), using S_N instead of Monte Carlo. Yee and Larsen [52] developed an analytic expression that agrees closely with the results of these methods, and demonstrates their theoretical relationship to the inscatter method.

TCP0 scattering is frequently used in MPACT and other transport codes because it significantly improves accuracy compared to P0 scattering, but does not increase the computational cost. However, the transport-corrected self-scattering cross section for water is often negative in the epithermal region because of the strong anisotropy of hydrogen. This is especially true when there are many groups, which reduces the magnitude of the self-scattering cross section. While the negative self-scatter cross sections are usually acceptable because the inscatter source is large enough to maintain a positive total source, this is not always true. If the total source becomes negative, this will likely negatively affect the stability of an iterative transport method, especially one requiring homogenization or nonlinear acceleration.

2.5 Spatial Discretization and Solution Methods

Spatial discretizations schemes can be classified into two broad categories: finite volume methods and finite element methods. Finite element methods discretize the problem geometry into a mesh of contiguous, non-overlapping finite elements, in which the solution is assumed to have a simple form in space that can be described by a basis function (usually linear or quadratic) and unknown coefficients [34]. Finite element methods are used both for 3D transport [53] and 2D/1D type formulations [25]. Finite element methods are widely used, and there are a variety of possible mesh shapes and basis functions, but these will not be discussed in detail here.

Finite volume methods for neutron transport preserve neutron balance over a defined volume, and usually either discretize the PDE using finite difference or treat the spatial variable with a nodal expansion. Nodal expansion shares some similarity with the the finite element methods. The most common finite volume methods for neutron transport are MOC or finite difference discretization of S_N. The S_N equations are simple, efficient, and highly parallelizable for Cartesian geometries [54], but defining the S_N scheme on a non-orthogonal mesh is complicated [6]. This limits the range of problems in which the S_N method can be effective. Although non-Cartesian features, such as a cylindrial pin, can be roughly approximated by a very refined Cartesian mesh, it is impractically expensive to obtain reasonably accurate solutions for the intra-pin flux distribution with such a mesh [55].

The Method of Characteristics (MOC) is much more efficient at modeling complicated and curvilinear geometries. The transport equation is solved in one dimension along many parallel rays placed over the problem geometry for each angle. If the ray spacing is fine enough, several rays will pass through each region. Each ray segment forms a rectangle, with the segment length s_i as the height of the rectangle and the ray spacing δ_r as the base. Any mesh shape is then effectively approximated by a histogram of ray segments. As the ray spacing is refined, this becomes a more accurate representation of the region. The length of the ray segments is adjusted to correctly integrate the volume. This is demonstrated in Fig. 2.4.

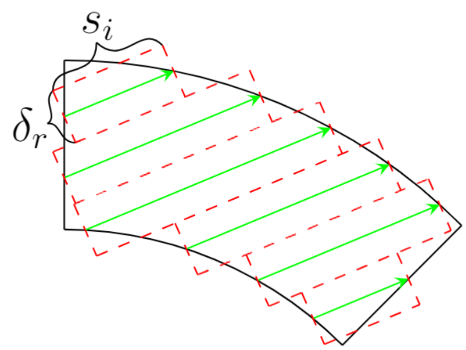

Figure 2.4: Rays traversing a discrete spatial region (MOC)

2.5.1 The Method of Characteristics

MOC is used to solve the 2D transport problems of the 2D/1D method in MPACT and most other 2D/1D codes [15],[11],[13]. MOC can also be applied directly to the 3D transport equation [21],[56]. In MOC, the transport equation is converted from a partial differential equation to an ordinary differential equation by evaluating the equation along a characteristic direction.

$$\mathbf{r} = \mathbf{r}_0 + s\boldsymbol{\Omega} \ , \tag{2.34a}$$

$$\frac{\partial \mathbf{r}}{\partial s} = \boldsymbol{\Omega} \ , \tag{2.34b}$$

$$\boldsymbol{\Omega} \cdot \nabla \psi(\mathbf{r}_0 + s\boldsymbol{\Omega}, \boldsymbol{\Omega}) = \frac{\partial}{\partial s}\psi(\mathbf{r}_0 + s\boldsymbol{\Omega}, \boldsymbol{\Omega}) \ . \tag{2.34c}$$

This transforms the transport equation into an ordinary differential equation with a single spatial variable:

$$\frac{\partial}{\partial s}\psi(\mathbf{r}, \boldsymbol{\Omega}) + \Sigma_t(\mathbf{r})\psi(\mathbf{r}, \boldsymbol{\Omega}) = Q(\mathbf{r}, \boldsymbol{\Omega}) \ . \tag{2.35}$$

The angular variable is discretized with discrete ordinates. For a given discrete ordinate, Eq. (2.35) can be solved using an integrating factor:

$$\frac{\partial}{\partial s}\left(\psi(\mathbf{r}, \boldsymbol{\Omega}) \exp\left[\int_0^s \Sigma_t(\mathbf{r}_0 + s'\boldsymbol{\Omega})ds'\right]\right) = \left(\exp\left[\int_0^s \Sigma_t(\mathbf{r}_0 + s\boldsymbol{\Omega})ds'\right]\right) Q(\mathbf{r}, \boldsymbol{\Omega}) \ . \tag{2.36}$$

Integrating over some segment length s_i, and assuming constant cross sections and source over the segment, we obtain:

$$\begin{aligned}\psi(\mathbf{r}_0 + s_i\mathbf{\Omega})e^{\Sigma_{t,i}s_i} - \psi(\mathbf{r}_0) &= Q_i(\mathbf{\Omega})\left(\int\limits_0^{s_i} e^{\Sigma_{t,i}s}ds\right) \\ &= \frac{Q_i(\mathbf{\Omega})}{\Sigma_{t,i}}\left[e^{\Sigma_{t,i}s_i} - 1\right] \ .\end{aligned} \tag{2.37}$$

If $\mathbf{r}_0$ is the point at which the ray enters a region and s_i is the length of the ray segment that traverses the region, then the outgoing flux from a region can be calculated from the incoming angular flux $\psi(\mathbf{r}_0)$, segment length s_i, cross section $\Sigma_{t,i}$, and (spatially flat) source $Q_i(\mathbf{\Omega})$:

$$\psi_{i,out} = \psi_{i,in}e^{-\Sigma_{t,i}s_i} + \frac{Q_i(\mathbf{\Omega})}{\Sigma_{t,i}}\left[1 - e^{-\Sigma_{t,i}s_i}\right] \ . \tag{2.38}$$

The average angular flux over the ray segment s_i in direction n is given by:

$$\begin{aligned}\tilde{\psi}_{n,i} &= \frac{1}{s_i}\int\limits_0^{s_i}\psi(s)ds = \frac{Q_{n,i}}{\Sigma_{t,i}} + \frac{1}{\Sigma_{t,i}s_i}\left(\psi_{in} - \frac{Q_{n,i}}{\Sigma_{t,i}}\right)\left(1 - e^{-\Sigma_{t,i}s_i}\right) \\ &= \frac{Q_{n,i}}{\Sigma_{t,i}} + \frac{\psi_{in,n,i} - \psi_{out,n,i}}{\Sigma_{t,i}s_i} \ .\end{aligned} \tag{2.39}$$

The scalar flux can be calculated as the volume-weighted sum of the average angular fluxes in each region:

$$\bar{\psi}_{n,j} = \frac{\sum\limits_{i=1}^{N_{ray}} s_i\tilde{\psi}_{n,i}}{\sum\limits_{i=1}^{N_{ray}} s_i} \ , \tag{2.40}$$

$$\bar{\phi}_j = \sum_{n=1}^{N} w_n\bar{\psi}_{n,j} \ . \tag{2.41}$$

It is possible to solve these equations with a source that varies linearly along the ray [$Q_i(s, \mathbf{\Omega})$ or $Q_i(x, y, z, \mathbf{\Omega})$] [56],[57], but the flat source approximation is the main solution method in MPACT. The linear source approximation is more expensive per ray segment simulated, but has smaller error for the same spatial mesh, and the trade-off between larger mesh and more expensive calculation per mesh may favor using the linear source approximation for many cases.

To solve a 2D transport problem in MPACT, the problem geometry is divided into many small regions over which a flat source approximation is applied. These are called flat source regions (FSRs); a typical mesh shown in Fig. 2.5a. Each pin is divided radially into several rings, and azimuthally into 8 (or more) slices. For each angle in the quadrature set, parallel rays are traced over the whole geometry, shown in Fig. 2.5b. Note that this is just a cartoon, and in reality the ray spacing is much finer. An example of a fine ray spacing is given in Fig. 2.4, with red dotted lines indicating the effective area modeled by each ray. As the ray spacing is refined, the difference between the physical geometry and the effective geometry being modeled by the red boxes is reduced.

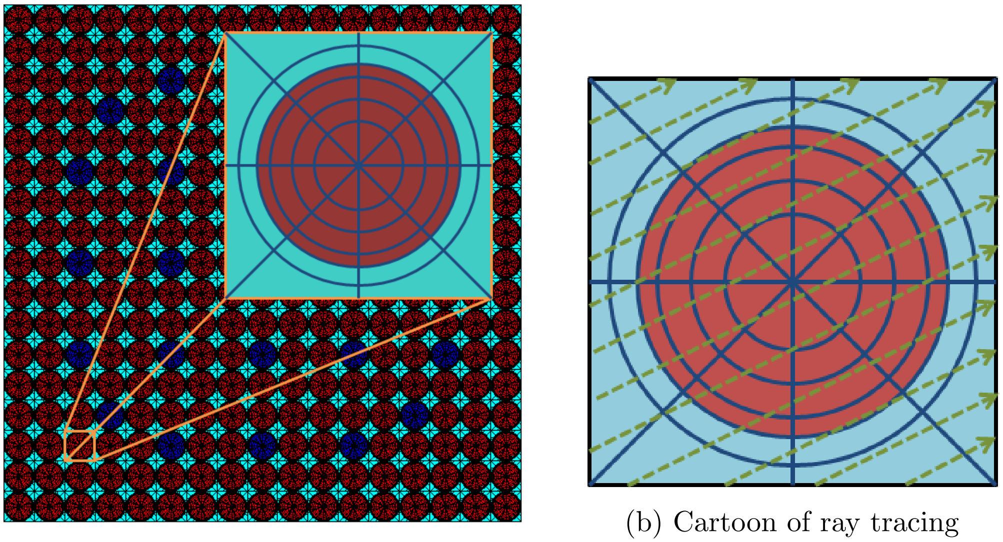

(a) Example flat-source discretization for MOC

(b) Cartoon of ray tracing

Figure 2.5: MOC Discretization for LWRs

MOC is commonly used because it effectively handles arbitrary geometries, provided the ray spacing and angular quadrature are fine enough. It parallelizes well because the angles and rays are independent within an iteration. Rays for two different angles can be swept simultaneously because they are independent. Additionally, the individual rays are independent, so multiple rays for a given angle can be swept concurrently. In the case of 2D/1D, the separate 2D spatial domains are also independent, which provides another potential level of parallelism. Coupling exists between all of these rays and domains, but it is only updated at the end of an iteration.

2.5.2 Coarse Mesh Finite Difference (CMFD)

Coarse Mesh Finite Difference and other low-order solution methods are frequently used to accelerate higher order transport solutions [58]. This is necessary to converge the low frequency error modes more quickly. High frequency error modes rapidly decay in a simple power or source iteration method, but low frequency error modes are very slowly converging because of the typically high dominance ratios. Without acceleration, a power iteration may take several hundred or thousands of iterations to converge. Diffusion methods are efficient as accelerators for several reasons:

- Low frequency error modes converge faster
- Wielandt shift can be applied to the power iteration, which significantly improves the convergence rate
- The low-order system can be solved relatively quickly compared to the high-order system

CMFD defines a diffusion equation on a coarse mesh with a correction to the diffusion coefficient that preserves the current between cells from the transport solution. Because the homogenized coefficients are defined to exactly preserve the transport solution, CMFD does not affect the final solution of the transport equation.

In MPACT, the CMFD equation is defined as a 3D homogenized diffusion problem. Each pin cell within an axial slice is one cell in the coarse mesh. The cross sections and radial current correction terms are calculated from the 2D MOC solution, and the axial current correction terms are calculated from the 1D axial solution.

The cross sections are homogenized from the transport solution, so the transport mesh, i.e., the FSR mesh, is referred to as the fine mesh (as opposed to coarse). The homogenized cross section for coarse cell p is

$$\Sigma_{x,g,p} = \frac{\sum\limits_{j\in p} \Sigma_{x,g,j} V_j \phi_{g,j}}{\sum\limits_{j\in p} V_j \phi_{g,j}} \,, \tag{2.42}$$

$$\phi_{g,p} = \frac{\sum\limits_{j\in p} V_j \phi_{g,j}}{\sum\limits_{j\in p} V_j} \,. \tag{2.43}$$

The current correction factors are defined to correct the difference between the inter-cell current calculated by the transport solution and approximated by Fick's Law:

$$\hat{D}_{g,p+1/2} = \frac{J_{g,p+1/2} + \tilde{D}_{g,p+1/2}\left(\phi_{g,p+1} - \phi_{g,p}\right)}{\phi_{g,p+1} + \phi_{g,p}} \ , \tag{2.44a}$$

$$\tilde{D}_{g,p+1/2} = \frac{2D_{g,p}D_{g,p+1}}{D_{g,p}h_p + D_{g,p+1}h_{g,p+1}} \ , \tag{2.44b}$$

$$D_j = \frac{1}{3\Sigma_{t,p}} \ . \tag{2.44c}$$

Here, the (1/2) index indicates the surface located between p and $p+1$, J is the current on the surface, and h_p is the thickness of cell p. The current correction factors are lagged from the previous iteration.

The CMFD balance equation is:

$$\begin{aligned} &- \tilde{D}_{g,p+1/2}\left(\phi_{g,p+1} - \phi_{g,p}\right) + \hat{D}_{g,p+1/2}\left(\phi_{g,p+1} + \phi_{g,p}\right) \\ &\qquad + \tilde{D}_{g,p-1/2}\left(\phi_{g,p} - \phi_{g,p-1}\right) - \hat{D}_{g,p-1/2}\left(\phi_{g,p} + \phi_{g,p-1}\right) \\ &\qquad + \Sigma_{t,g,p}\phi_{g,p} - \sum_{g'=1}^{G} \Sigma_{s,g\leftarrow g',p}\phi_{g',p} = \frac{\chi_{g,p}}{k_{eff}} \sum_{g'=1}^{G} \nu\Sigma_{f,g',p}\phi_{g',p} \ , \\ &\qquad\qquad 1 < p < P \ , \ 1 \leq g \leq G \ . \end{aligned} \tag{2.45}$$

The scalar flux is then updated using the CMFD solution:

$$\phi_{g,j}^{(l+1)} = \frac{\phi_{g,p}^{(l+1)}}{\phi_{g,p}^{(l+1/2)}} \phi_{g,j}^{(l+1/2)} \ , \ j \in p \ . \tag{2.46}$$

In Eq. (2.46), the $(l + 1/2)$ iterate refers to the solution after the transport sweep, and the $(l + 1)$ iterate is the solution after the CMFD solution and update.

While this example is in 1D for simplicity, it can easily be extended to 3D. For each additional coarse cell surface, an additional $\tilde{D}$ and $\hat{D}$ term is added. This eigenvalue problem is solved by Wielandt-shifted inverse power iteration, with inner solves (approximate matrix inversion) handled by GMRES or another linear solver such as the Multi-level in Space and Energy Diffusion (MSED) method recently developed by Yee [59].

2.5.3 Nodal Methods

Nodal expansion methods can be useful for certain types of neutron transport or diffusion problems because of their high order of accuracy. If the solution is reasonably

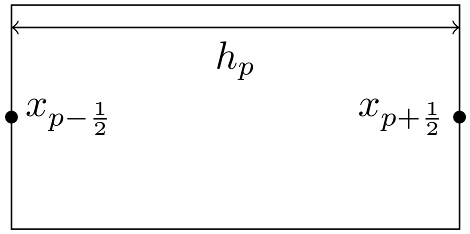

Figure 2.6: Nodal mesh

smooth, nodal expansion can have acceptable accuracy with a much larger mesh than finite difference. In MPACT, nodal methods are used to solve the 1D transport equation, which is too coarsely meshed for finite difference; the node size is typically several centimeters.

Nodal Expansion Method

One of the oldest and most common nodal methods is simply called the Nodal Expansion Method (NEM) [60]. In this method, the source and flux are expanded in space: up to second order for the source and fourth order for the flux.

In MPACT, a similar method is used, in which the size of each node is normalized to the interval $[-1, 1]$, and the source and flux are expanded in Legendre polynomials on this interval.

$$\xi = 2\frac{x - x_{p-1/2}}{h_p} - 1 \ , \tag{2.47}$$

$$Q(\xi) = \sum_{i=0}^{2} q_i P_i(\xi) \ , \tag{2.48}$$

$$\phi(\xi) = \sum_{i=0}^{4} \phi_i P_i(\xi) \ . \tag{2.49}$$

h_p is the size of the node, and $x_{p-1/2}$ is the left boundary, as shown in in Fig. 2.6. There are two ways these equations are solved in MPACT - the two-node method and the one-node method.

In the two-node method, the zeroth order flux moments $\phi_{0,p}$ are known quantities from the 3D CMFD solution. This leaves 4 unknowns (ϕ_i) for each node, or 8 total. Preserving neutron balance over each node for the zeroth, first, and second spatial moments gives 6 equations. The two additional equations come from preserving flux and current at the interface between the two nodes.

$$\int_{-1}^{1} P_i(\xi)\left(-\Sigma_{D,g,p}\frac{\partial^2}{\partial\xi^2}\phi_{g,p}(\xi)+\Sigma_{r0,g,p}\phi_{g,p}(\xi)-Q_{g,p}(\xi)\right)d\xi = 0\ ,\ i=0,1,2, \tag{2.50a}$$

$$\Sigma_{D,g,p}=\frac{4D_{g,p}}{h_p^2}\ ,\ \Sigma_{r0,g,p}=\Sigma_{t,g,p}-\Sigma_{s,g\leftarrow g,p}\ ,$$

$$\phi_{g,p}(1)=\phi_{g,p+1}(-1)\ , \tag{2.50b}$$

$$J_{g,p}(1)=J_{g,p+1}(-1)\ . \tag{2.50c}$$

The balance equations give, resepctively:

$$-3\Sigma_{D,g,p}\phi_{2,g,p}-10\Sigma_{D,g,p}\phi_{4,g,p}=q_{0,g,p}-\Sigma_{r0,g,p}\phi_{0,g,p}\ , \tag{2.51a}$$

$$\Sigma_{r0,g,p}\phi_{1,g,p}-15\Sigma_{D,g,p}\phi_{3,g,p}=q_{1,g,p}\ , \tag{2.51b}$$

$$\Sigma_{r0,g,p}\phi_{2,g,p}-35\Sigma_{D,g,p}\phi_{4,g,p}=q_{2,p}\ . \tag{2.51c}$$

These are the same for the top node $p+1$. The flux continuity condition gives:

$$\sum_{i=0}^{4}\phi_{i,g,p}(1)=\sum_{i=0}^{4}\phi_{i,g,p+1}(-1)\ ,$$

$$\phi_{0,g,p}+\phi_{1,g,p}+\phi_{2,g,p}+\phi_{3,g,p}+\phi_{4,g,p}=\phi_{0,g,p+1}-\phi_{1,g,p+1}+\phi_{2,g,p+1}-\phi_{3,g,p+1}+\phi_{4,g,p+1}\ ,$$

$$\phi_{1,g,p}+\phi_{1,g,p+1}+\phi_{2,g,p}-\phi_{2,g,p+1}+\phi_{3,g,p}+\phi_{3,g,p+1}+\phi_{4,g,p}-\phi_{4,g,p+1}=\phi_{0,g,p+1}-\phi_{0,g,p}\ .$$

From current continuity:

$$\sum_{i=0}^{4}-D_{g,p}\phi_{i,g,p}\frac{\partial}{\partial\xi}P_i(\xi)=\sum_{i=0}^{4}-D_{g,p}\phi_{i,g,p+1}\frac{\partial}{\partial\xi}P_i(\xi)\ , \tag{2.52}$$

$$-\beta_{g,p}\left(\phi_{1,g,p}+3\phi_{2,g,p}+6\phi_{3,g,p}+10\phi_{4,g,p}\right)$$
$$+\beta_{g,p+1}\left(\phi_{1,g,p+1}-3\phi_{2,g,p+1}+6\phi_{3,g,p+1}-10\phi_{4,g,p+1}\right)=0\ ,$$

$$\beta_{g,p}=\frac{2D_{g,p}}{h_p}\ .$$

This gives an 8x8 system that is solved directly for the flux coefficients. The source coefficients q_i are constructed using the flux coefficients ϕ_i from the previous iteration to calculate the scattering and fission source. For 2D/1D, the radial TL also contributes to the source. Linear and quadratic moments of the radial TL within a node are interpolated using the radial TL quantities from neighboring nodes.

A special one-node formulation that accounts for boundary conditions is used on problem boundaries.

Fig. 2.7a shows the inputs to the two-node kernel, which are the source moments and the average flux for the node. Fig. 2.7b shows the outputs, which are the higher order flux moments and the net current between the two nodes.

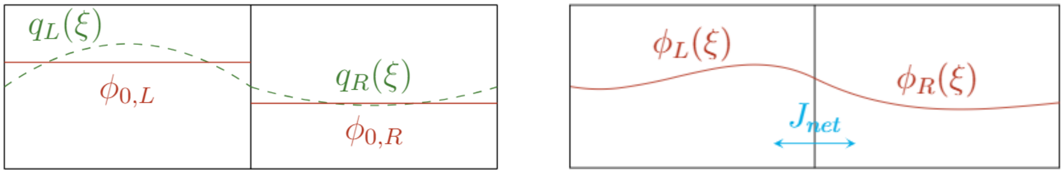

(a) Two-node kernel input

(b) Two-node kernel output

Figure 2.7: Two-node kernel illustration

One-Node Kernels

When spherical harmonics solvers of order above P_1 are used, MPACT uses a one-node formulation in which the zeroth spatial moment is an unknown. The 3 balance equations are the same for the zeroth angular moment, given by Eqs. (2.51a). The balance equations for the second angular moment are

$$-3\Sigma_{D2,g,p}\phi_{2,2,g,p} - 10\Sigma_{D2,g,p}\phi_{2,4,g,p} = \frac{2}{5}\left(\Sigma_{r0,g,p}\phi_{0,0,g,p} - q_{0,0,g,p}\right) \ , \tag{2.53}$$

$$\Sigma_{r2,g,p}\phi_{2,1,g,p} - 15\Sigma_{D2,g,p}\phi_{2,3,g,p} = \frac{2}{5}\left(\Sigma_{r0,g,p}\phi_{0,1,g,p} - q_{0,1,g,p}\right) \ , \tag{2.54}$$

$$\Sigma_{r2,g,p}\phi_{2,2,g,p} - 35\Sigma_{D2,g,p}\phi_{2,4,g,p} = \frac{2}{5}\left(\Sigma_{r0,g,p}\phi_{0,2,g,p} - q_{0,2,g,p}\right) \ , \tag{2.55}$$

$$\Sigma_{D2,g,p} = \frac{4D_{2,g,p}}{h_p^2} \ , \ D_{2,g,p} = \frac{9}{35\Sigma_{t,g,p}} \ , \ \Sigma_{r2,g,p} = \Sigma_{t,g,p} + \frac{4}{5}\Sigma_{r0,g,p} \ .$$

The partial current on the bottom and top surfaces of the node serve as boundary conditions for the other two equations. For the zeroth order angular moment:

$$\frac{-D_{0,g,p}}{h_p}\frac{\partial}{\partial\xi}\phi_{0,g,p}(-1) + \frac{1}{4}\phi_{0,g,p}(-1) = \int_0^1 \mu\phi_{g,p-1/2}(\mu)d\mu + \frac{3}{16}\phi_{2,g,p}(-1) \ , \tag{2.56a}$$

$$\frac{D_{0,g,p}}{h_p}\frac{\partial}{\partial\xi}\phi_{0,g,p}(1) + \frac{1}{4}\phi_{0,g,p}(1) = \int_{-1}^0 \mu\phi_{g,p+1/2}(\mu)d\mu + \frac{3}{16}\phi_{2,g,p}(1) \ . \tag{2.56b}$$

For the second order angular moment:

$$\frac{-D_{2,g,p}}{h_p}\frac{\partial}{\partial \xi}\phi_{2,g,p}(-1)+\frac{1}{4}\phi_{2,g,p}(-1)=\frac{3}{5}\int_{0}^{1}P_3(\mu)\phi_{g,p-1/2}(\mu)d\mu + \frac{3}{80}\phi_{0,g,p}(-1)-\frac{1}{80}\phi_{2,g,p}(-1)\ , \tag{2.57a}$$

$$\frac{D_{2,g,p}}{h_p}\frac{\partial}{\partial \xi}\phi_{2,g,p}(1)+\frac{1}{4}\phi_{2,g,p}(1)=\frac{3}{5}\int_{-1}^{0}P_3(\mu)\phi_{g,p+1/2}(\mu)d\mu + \frac{3}{80}\phi_{0,g,p}(1)-\frac{1}{80}\phi_{2,g,p}(1)\ . \tag{2.57b}$$

Fig. 2.8a shows the inputs to the one-node kernel, which are the incoming partial currents and the source moments. Fig. 2.8b shows the outputs, which are the flux moments and the outgoing partial currents.

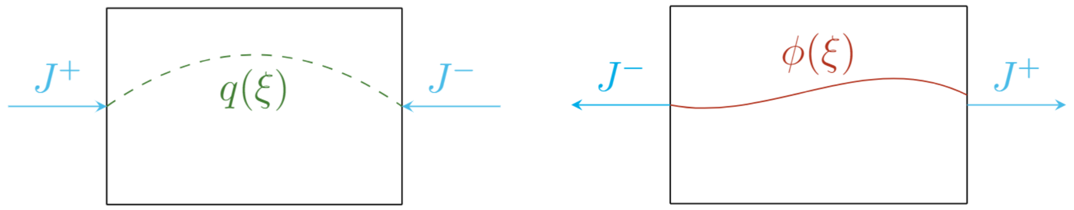

(a) One-node kernel input (b) One-node kernel output

Figure 2.8: One-node kernel illustration

The one-node method is commonly used to solve the 1D axial P$_3$ problem. A hybrid two-node/one-node method has also been developed, where a one-node solver provides the zeroth spatial moment of the second order angular flux for the two-node solver [61]. A full-height axial P$_3$ solver has also been implemented. In this kernel, all of the nodes are solved simultaneously, rather than by sweeping.

A 1D S$_N$ solver is also implemented in MPACT. The flux and source are both expanded in space to improve the accuracy for the relatively thick axial nodes. A cubic characteristics method is used, as opposed to step characteristics or diamond difference, which are more common S$_N$ discretizations for smaller mesh sizes.

In this work, both the S$_N$ and P$_3$ solvers are used. The previous work by Stimpson [8] using S$_N$ solvers is extended to the P$_3$ solvers, and new features are added to both.

2.6 Summary

This chapter covered most of the computational neutron transport theory supporting the work in this thesis, and many of the methods that are used here and in other related work. Most of the content here is already well-known and used throughout the community, although some of the methods described come from more recent work that is not as widely disseminated.

In Chapter 3, the 2D/1D method is described in more detail than the background given in Chapter 1. The anisotropic 1D XS homogenization, and the equations for incorporating the anisotropic 1D XS into a 2D/1D P_3 method, are derived in Chapter 3. The use of this anisotropic homogenized 1D XS to improve 2D/1D accuracy is a significant and novel contribution from this thesis.

Chapter 3: The 2D/1D Method

The history of the 2D/1D method was discussed in Sec. 1.2. In Sec. 3.1, the derivation of the 2D/1D equations from the 3D transport equation is reviewed, with remarks on the relevant approximations and how the method is modified in this work. In Sec. 3.2, other pieces of the 2D/1D implementation in MPACT that are relevant but not specific to this work are mentioned and described. The iteration scheme for 2D/1D is discussed in Sec. 3.2. Finally, in Sec. 3.3, some recent results by other researchers that appear to contradict the results in this work are discussed.

3.1 2D/1D Equations

This sections covers the derivation of the 2D/1D equations to show where approximations are introduced, and how the method in this thesis avoids these approximations. The 2D radial equations are derived in Sec. 3.1.1, and the 1D axial equations are derived in Sec. 3.1.2. The new pin homogenization methods are derived in Sec. 3.1.4. The 1D P_3 equations with anisotropic TL and XS are derived in Sec. 3.1.7.

To obtain the 2D/1D equations, we begin with the energy-independent fixed-source 3D Boltzmann neutron transport equation with isotropic scattering:

$$\mathbf{\Omega}\cdot\nabla\psi(\mathbf{r},\mathbf{\Omega}) + \Sigma_t(\mathbf{r})\psi(\mathbf{r},\mathbf{\Omega}) = \frac{Q(\mathbf{r})}{4\pi} \ , \tag{3.1}$$

$$\mathbf{r} = (x, y, z) \ , \ \Omega = \left(\sqrt{1-\mu^2}\cos\omega, \sqrt{1-\mu^2}\sin\omega, \mu\right) \ ,$$

$$Q(\mathbf{r}) = \left[\Sigma_s(\mathbf{r}) + \frac{\nu\Sigma_f(\mathbf{r})}{k_{eff}}\right]\int\limits_{4\pi}\psi(\mathbf{r},\mathbf{\Omega})d\Omega \ .$$

Here, μ is the cosine of the polar angle, and ω is the azimuthal angle. Next, we review the derivation of the 2D/1D equations: a set of 2D radial transport equations and a set of 1D axial transport equations that are solved for each plane and pin in the problem, respectively. These equations are coupled through TL terms; the goal is to maximize the accuracy of the approximations made to the 3D transport equation in arriving at the 2D/1D equations. This goal must be balanced with the need to develop a method that can be implemented efficiently in practice.

3.1.1 2D Radial Equations

First, we distribute the $\boldsymbol{\Omega}\cdot\nabla$ term from Eq. (3.1). The following shorthand notation is used for the radial streaming term because the detailed form is not important here:

$$(\boldsymbol{\Omega}\cdot\nabla)_{xy}\psi = \sqrt{1-\mu^2}\left(\cos\omega\frac{\partial}{\partial x} + \sin\omega\frac{\partial}{\partial y}\right)\psi(\mathbf{r},\boldsymbol{\Omega}) \ , \tag{3.2}$$

$$(\boldsymbol{\Omega}\cdot\nabla)_{xy}\psi + \mu\frac{\partial\psi}{\partial z} + \Sigma_t(\mathbf{r})\psi(\mathbf{r},\boldsymbol{\Omega}) = \frac{Q(\mathbf{r})}{4\pi} \ . \tag{3.3}$$

Move the axial streaming term to the right (source) side of the equation:

$$(\boldsymbol{\Omega}\cdot\nabla)_{xy}\psi + \Sigma_t(\mathbf{r})\psi(\mathbf{r},\boldsymbol{\Omega}) = \frac{Q(\mathbf{r})}{4\pi} - \mu\frac{\partial\psi}{\partial z} \ . \tag{3.4}$$

When integrated over z, the streaming term $\mu\frac{\partial\psi}{\partial z}$ becomes the axial TL. To obtain the 2D part of the 2D/1D equations, Eq. (3.4) is integrated axially over a plane k, from $z_{k-1/2}$ to $z_{k+1/2}$:

$$\frac{1}{h_k}\int\limits_{z_{k-1/2}}^{z_{k+1/2}} [Eq.\ (3.4)]\, dz \ , \ h_k = z_{k+1/2} - z_{k-1/2} \ .$$

All axial dependence is assumed to be separable from the radial and angular variables over the plane, so the axial dependence of all quantities except for the axial TL is removed by the integration:

$$(\mathbf{\Omega}\cdot\nabla)_{xy}\psi_k(x,y,\mathbf{\Omega}) + \Sigma_{t,k}(x,y)\psi_k(x,y,\mathbf{\Omega}) = \frac{Q_k(x,y)}{4\pi} - \tilde{J}_{z,k}(x,y,\mathbf{\Omega}) \ , \tag{3.5a}$$

$$\psi_k(x,y,\mathbf{\Omega}) = \frac{1}{h_k}\int\limits_{z_{k-1/2}}^{z_{k+1/2}} \psi(x,y,z,\mathbf{\Omega})dz \ , \tag{3.5b}$$

$$\begin{aligned} Q_k(x,y,\mathbf{\Omega}) &= \frac{1}{h_k}\int\limits_{z_{k-1/2}}^{z_{k+1/2}} Q(x,y,z,\mathbf{\Omega})dz \\ &= \frac{1}{h_k}\int\limits_{z_{k-1/2}}^{z_{k+1/2}} \left[\Sigma_s(x,y,z) + \frac{1}{k_{eff}}\nu\Sigma_f(x,y,z)\right]\phi(x,y,z)dz \ , \end{aligned} \tag{3.5c}$$

$$\tilde{J}_{z,k}(x,y,\mathbf{\Omega}) = \frac{\mu}{h_k}\left[\psi(x,y,z_{k+1/2},\mathbf{\Omega}) - \psi(x,y,z_{k-1/2},\mathbf{\Omega})\right] \ . \tag{3.6}$$

In Eq. (3.6), The surface angular flux terms (ψ) are obtained from the solution of the 1D problem. These fluxes are discretized over the coarse radial mesh, which is typically one pin. Thus, the axial TL term $\tilde{J}_{z,k}$ has no fine-mesh spatial shape within a coarse cell unless a shape function $g(x,y,\mathbf{\Omega})$ is applied:

$$\tilde{J}_{z,k}(x,y,\mathbf{\Omega}) = g_{k,ij}(x,y,\mathbf{\Omega})\tilde{J}_{z,k,ij}(\mathbf{\Omega}) \ . \tag{3.7}$$

This approximation is discussed further in Sec. 3.1.5.

In MPACT, the typical approximation when using a 1D P$_N$ method axially is to assume an isotropic TL. This is equivalent to replacing the anistropic leakage term on the right side of Eq. (3.5a) with its isotropic moment, $\frac{1}{4\pi}\int\limits_{4\pi}\tilde{J}_{z,k,ij}(\mathbf{\Omega})d\Omega$:

$$\left[(\mathbf{\Omega}\cdot\nabla)_{xy} + \Sigma_{t,k}(x,y)\right]\psi_k(x,y,\mathbf{\Omega}) = \frac{Q_k(x,y)}{4\pi} - \frac{\left[J_{z,k+1/2,ij} - J_{z,k-1/2,ij}\right]}{4\pi h_k} \ . \tag{3.8}$$

When this approximation is made, and scattering is isotropic, the total source is isotropic, so it is symmetric in the polar angle. The 2D transport equation, with a polar-symmetric source, has a solution that is symmetric in the polar angle. Therefore, the MOC solver only needs to simulate half of the polar angles ($0 < \mu < 1$), which saves a significant amount of work.

In this thesis, the angular dependence of the axial TL is retained by using a Legendre expansion in polar angle and Fourier expansion in azimuthal angle. This method, which comes from previous work [8, 9], is described in Section 3.1.3.

The radial equations, Eq. (3.5a), are 2D transport equations, each defined over an integrated axial slice of the 3D geometry. In MPACT, and many other 2D/1D codes, the 2D solution is obtained by the Method of Characteristics. The 2D slices are coupled to one another through the axial TL term calculated by the 1D axial solver.

3.1.2 1D Axial Equations

The next step is to derive the 1D equations. We begin moving the radial streaming term to the source in Eq. (3.1):

$$\mu\frac{\partial\psi}{\partial z} + \Sigma_t(\mathbf{r})\psi(\mathbf{r},\mathbf{\Omega}) = \frac{Q(\mathbf{r})}{4\pi} - (\mathbf{\Omega}\cdot\nabla)_{xy}\psi(\mathbf{r},\mathbf{\Omega}) \ . \tag{3.9}$$

Next, we operate on Eq. (3.9) by:

$$\frac{1}{A_{ij}}\int\limits_{x_{i-1/2}}^{x_{i+1/2}}\int\limits_{y_{j-1/2}}^{y_{j+1/2}}(\cdot)dxdy = \frac{1}{A_{ij}}\iint\limits_{ij}(\cdot)dxdy \ ,$$

where A_{ij} is the radial area of coarse cell (i,j), and $\iint\limits_{ij}$ is shorthand notation for an integral over the coarse cell (i,j). The notation $(\hat{\ })$ indicates that these variables are now integrated over a coarse cell:

$$\mu\frac{\partial\hat{\psi}_{ij}}{\partial z} + \hat{\Sigma}_{t,k,ij}(\mathbf{\Omega})\hat{\psi}_{ij}(z,\mathbf{\Omega}) = \frac{\hat{Q}_{ij}(z)}{4\pi} - \frac{1}{A_{ij}}\sum_{s=N,E,S,W}(\mathbf{\Omega}\cdot\hat{n}_s)\psi_{ij,s}(z,\mathbf{\Omega}) \ , \tag{3.10a}$$

$$\hat{\Sigma}_{t,k,ij}(\mathbf{\Omega}) = \frac{\iint\limits_{ij}\Sigma_{t,k}(x,y)\psi_k(x,y,\mathbf{\Omega})dxdy}{\iint\limits_{ij}\psi_k(x,y,\mathbf{\Omega})dxdy} \ . \tag{3.10b}$$

Typically, $\hat{\Sigma}_{t,k,ij}$ is isotropic, but in this work it has polar angle dependence that will be derived in the next section. The polar-dependent XS will be denoted by $\tilde{\Sigma}_{t,k,ij}(\mu)$. It is axially constant over a plane k. The radial leakage term is summed over the 4 lateral surfaces of a rectangular coarse cell (N,E,S,W = north, east, south, and west). The surface flux $\psi_{ij,s}(\mathbf{\Omega})$ is effectively a line integral over the surface s:

$$\psi_{ij,s}(z,\mathbf{\Omega}) = \int\limits_{u-}^{u+}\psi_{ij}(z,u,\mathbf{\Omega})du \ , \tag{3.11}$$

where u is either x or y, depending on the surface, and the other radial variable is held constant. For the standard 2D/1D equations, operate on the right side of Eq. (3.10a) by $\frac{1}{4\pi}\int\limits_{4\pi}(\cdot)\,d\Omega$ to isotropize the radial TL, yielding:

$$\mu\frac{\partial\hat{\psi}_{ij}}{\partial z}+\hat{\Sigma}_{t,k,ij}\hat{\psi}_{ij}(z,\mathbf{\Omega})=\frac{1}{4\pi}\left[\hat{Q}_{ij}(z)-\left(\sum_{s=N,E,S,W}J_{ij,s}(z)\right)\right]\ . \tag{3.12}$$

The radial currents come from the 2D solution, which is piecewise-constant and has no z dependence within a slice. The z dependence of the radial TL within a node comes from a 3-point quadratic interpolation between the node and its two axial neighbors [8]. This interpolation is described in Section 3.1.6.

Eq. (3.12) is a 1D transport equation for $\hat{\psi}_{ij}$ that can be solved using 1D P_N. $J_{ij,s}$ is surface-integrated current, or the isotropic radial TL, on a surface s. In MPACT, a nodal expansion method is used to solve Eq. (3.12), with quadratic spatial expansion of the source and quartic expansion of the flux [60]. In this thesis, a Fourier expansion of the TL in ω is used rather than approximating it as isotropic.

The equations described so far provide an approximate solution to the 3D transport equation. Significant approximations have been made that adversely affect the accuracy of these methods. These approximations include the angular distribution of the TL terms (isotropic) and the angular distribution of the homogenized 1D cross section $\hat{\Sigma}_{t,k,ij}$. In the following sections, improved angular approximations for these coupling terms are described.

3.1.3 Azimuthal Expansion

It is sufficiently accurate, and much more memory efficient, to treat the azimuthal dependnece of the axial and radial TL with a Fourier expansion (sine and cosine moments) [8, 9] than to retain the full, azimuthally-dependent anisotropic TL in the sources for the 2D and 1D equations. With only a Fourier expansion in ω, the 1D angular flux is represented as:

$$\hat{\psi}_{ij}(z,\mu,\omega)=\frac{\hat{\psi}_{0,ij}(z,\mu)}{2\pi}+\frac{1}{\pi}\sum_{p=1}^{P}\left[\hat{\psi}_{c,p,ij}(z,\mu)\cos(p\omega)+\hat{\psi}_{s,p,ij}(z,\mu)\sin(p\omega)\right]\ . \tag{3.13}$$

$\hat{\psi}_{c,p,ij}(z,\mu)$ and $\hat{\psi}_{s,p,ij}(z,\mu)$ are the cosine and sine moments of the 1D angular flux. It is expanded in Legendre polynomials in space. In this thesis, the polar dependence is also expanded in Legendre polynomials. The polar angle treatment is discussed in

Section 3.1.7. Each azimuthal moment is solved by a separate 1D transport equation. It typically takes only $P = 2$ to obtain solutions that are sufficiently close to the explicit angular solution, as demonstrated in Stimpson's thesis [8].

We insert Eq. (3.13) into Eq. (3.10a) and make a similar expansion of the leakage:

$$\left[\mu\frac{\partial}{\partial z} + \tilde{\Sigma}_{t,k,ij}(\mu)\right]\left[\frac{\hat{\psi}_{0,ij}(z,\mu)}{2\pi} + \frac{1}{\pi}\sum_{p=1}^{P}\Big(\hat{\psi}_{c,p,ij}(z,\mu)\cos(\omega) + \hat{\psi}_{s,p,ij}(z,\mu)\sin(\omega)\Big)\right] \tag{3.14}$$

$$= \frac{\hat{Q}_{ij}(z)}{4\pi} - \frac{TL^{XY}_{0,ij}(z,\mu)}{2\pi} - \frac{1}{\pi}\sum_{p=1}^{P}\left[TL^{XY}_{c,p,ij}(z,\mu)\cos(p\omega) + TL^{XY}_{s,p,ij}(z,\mu)\sin(p\omega)\right] \;,$$

where

$$TL^{XY}_{0,ij}(z,\mu) = \frac{1}{A_{ij}}\sum_{s=N,E,S,W}\int_0^{2\pi}(\mathbf{\Omega}\cdot\hat{n}_s)\psi_{ij,s}(z,\mathbf{\Omega})d\omega \;, \tag{3.15a}$$

$$TL^{XY}_{c,p,ij}(z,\mu) = \frac{1}{A_{ij}}\sum_{s=N,E,S,W}\int_0^{2\pi}\cos(p\omega)(\mathbf{\Omega}\cdot\hat{n}_s)\psi_{ij,s}(z,\mathbf{\Omega})d\omega \;, \tag{3.15b}$$

$$TL^{XY}_{s,p,ij}(z,\mu) = \frac{1}{A_{ij}}\sum_{s=N,E,S,W}\int_0^{2\pi}\sin(p\omega)(\mathbf{\Omega}\cdot\hat{n}_s)\psi_{ij,s}(z,\mathbf{\Omega})d\omega \;. \tag{3.15c}$$

These equations have P sine and cosine moments and one azimuthally isotropic moment. Operating on Eq. (3.14) by $\int_0^{2\pi}(\cdot)d\omega$, $\int_0^{2\pi}\cos(p\omega)(\cdot)d\omega$, and $\int_0^{2\pi}\sin(p\omega)(\cdot)d\omega$ yields the 1D transport equations:

$$\left[\mu\frac{\partial}{\partial z} + \tilde{\Sigma}_{t,k,ij}(\mu)\right]\hat{\psi}_{0,ij}(z,\mu) = \frac{\hat{Q}_{ij}(z)}{2} - TL^{XY}_{0,ij}(z,\mu) \;, \tag{3.16a}$$

$$\left[\mu\frac{\partial}{\partial z} + \tilde{\Sigma}_{t,k,ij}(\mu)\right]\hat{\psi}_{s/c,p,ij}(z,\mu) = -TL^{XY}_{s/c,p,ij}(z,\mu)\;;\; 1 \le p \le P \;. \tag{3.16b}$$

The expression for the angle-dependent total XS $\tilde{\Sigma}_{t,k,ij}(\mu)$ is given in Sec. 3.1.4. Using Eqs. (3.5a) and (3.16), the angular dependence of the TL terms that couple the 2D and 1D solutions can be treated accurately. This leads to an improved solution compared to the result obtained with Eqs. (3.8) and (3.12).

When the axial TL is allowed to be anisotropic, the source is no longer symmetric with respect to the polar angle. Since the source is not symmetric in the polar angle, all polar angles must be swept in the MOC solution ($-1 < \mu < 1$), so there are twice as many ray segments to sweep through as in the standard, isotropic TL case. This is a significant computational expense associated with the anisotropic TL method.

3.1.4 2D to 1D Homogenization

The angle-dependent leakage terms described in the previous section offer significant improvements in accuracy compared to isotropic leakages. However, the 1D problems cannot fully preserve the physics from the 2D problem with a single, isotropic homogenized $\hat{\Sigma}_{t,k,ij}$. In general, the homogenized 1D equation should preserve the scalar flux and reaction rate from the heterogeneous 2D problem over the same domain to satisfy particle conservation. For optimal accuracy, the 1D equation should also preserve the average angular flux distribution over a coarse cell from the 2D problem:

$$\frac{1}{h_k}\int\limits_{z_{k-1/2}}^{z_{k+1/2}} \hat{\psi}_{ij}(z,\mathbf{\Omega})dz = \frac{1}{A_{ij}}\iint\limits_{ij} \psi_k(x,y,\mathbf{\Omega})dxdy \ . \tag{3.17}$$

This is important because the angular flux from the axial 1D solution determines the axial power shape, as well as the magnitude and angular distribution of the axial TL.

Typically, a standard scalar flux-weighted total XS is used because it preserves reaction rates:

$$\hat{\Sigma}_{t,k,ij} = \frac{\iint\limits_{ij} \Sigma_{t,k}(x,y)\phi_k(x,y)dxdy}{\iint\limits_{ij} \phi_k(x,y)dxdy} \ . \tag{3.18}$$

To evaluate the aptness of this definition, the 2D and 1D equations, integrated over the same cuboid volume, are compared:

$$V_{i,j,k} = \int\limits_{x_{i-1/2}}^{x_{i+1/2}} \int\limits_{y_{j-1/2}}^{y_{j+1/2}} \int\limits_{z_{k-1/2}}^{z_{k+1/2}} dzdydx \ . \tag{3.19}$$

First, we integrate Eq. (3.5a) radially ($\frac{1}{A_{ij}}\iint\limits_{ij}$) and collect the leakage terms on the source side:

$$\frac{1}{A_{ij}}\iint\limits_{ij} \Sigma_t(x,y)\psi(x,y,\mathbf{\Omega})dxdy = \frac{1}{V_{i,j,k}}\iint\limits_{ij}\int\limits_{z_{k-1/2}}^{z_{k+1/2}} \left(\frac{Q(\mathbf{r})}{4\pi} - (\mathbf{\Omega}\cdot\nabla)\,\psi(\mathbf{r},\mathbf{\Omega})\right) dzdydx \ . \tag{3.20}$$

Then, we integrate Eq. (3.10a) radially, and again collect the leakage terms on the source side:

$$\frac{1}{h_k}\int\limits_{z_{k-1/2}}^{z_{k+1/2}} \hat{\Sigma}_{t,k,ij}\hat{\psi}(z,\mathbf{\Omega})dz = \frac{1}{V_{i,j,k}}\iint\limits_{ij}\int\limits_{z_{k-1/2}}^{z_{k+1/2}}\left(\frac{Q(\mathbf{r})}{4\pi} - (\mathbf{\Omega}\cdot\nabla)\,\psi(\mathbf{r},\mathbf{\Omega})\right)dzdydx\ . \quad (3.21)$$

We Substitute Eq. (3.17) and Eq. (3.20) into Eq. (3.21) to obtain the following expression for $\hat{\Sigma}_{t,k,ij}$:

$$\hat{\Sigma}_{t,k,ij} = \tilde{\Sigma}_{t,k,ij}(\mathbf{\Omega}) = \frac{\iint\limits_{ij}\Sigma_{t,k}(x,y)\psi_k(x,y,\mathbf{\Omega})dxdy}{\iint\limits_{ij}\psi_k(x,y,\mathbf{\Omega})dxdy}\ . \quad (3.22)$$

Using Eq. (3.22) (or its discrete equivalent) gives a solution $\hat{\psi}$ that satisfies Eq. (3.17), which should improve the accuracy of the 2D/1D solution. If $\psi(x,y,\mathbf{\Omega})$ were separable in space and angle, then Eq. (3.22) clearly reduces to Eq. (3.18). Thus, the severity of the error introduced by homogenizing with Eq. (3.18) will be directly related to the severity of the approximation of space-angle separability.

In practice, it is much easier to use only the polar-dependent total XS. Effectively, this means assuming only *azimuthal* separability from the spatial-polar shape of ψ in Eq. (3.22). Based on the experience in this thesis work, the polar dependence accounts for the overwhelming majority of homogenization error, and it is acceptable to ignore the azimuthal dependnece. This results in the following homogenization:

$$\tilde{\Sigma}_{t,k,ij}(\mu) = \frac{\iint\limits_{ij}\Sigma_{t,k}(x,y)\left(\int\limits_0^{2\pi}\psi_k(x,y,\mu,\omega)d\omega\right)dxdy}{\iint\limits_{ij}\left(\int\limits_0^{2\pi}\psi_k(x,y,\mu,\omega)d\omega\right)dxdy}\ . \quad (3.23)$$

Although the angular flux can have strong ω dependence, the homogenized anisotropic XS has only weak ω dependence. Numerical results in Section 4.6 indicate that this polar-only homogenization is sufficient. We hypothesize that this is because the polar dependence of the spatial self-shielding effect in a fuel or control rod is much stronger than the azimuthal dependence.

Physically, it makes sense that the polar dependence of the spatially homogenized XS for a pin cell is more important than the azimuthal dependence. The main effect being captured by the homogenized XS is spatial self-shielding of thermal and resonance-energy neutrons in the fuel. This effect depends strongly on the average distance traveled through the fuel by neutrons. Because a pin cell is cylindrical, the average distance traveled by all the characteristic rays passing through the fuel is invariant with respect to the azimuthal angle. However, the characteristic rays at different polar angle travel vastly different distances to the other side of the fuel pin. A simple visualization of this effect is given for 4 different polar angles in Fig. 3.1. The polar dependence of the total XS is much stronger because it is driven by the physical geometry of the fuel. Azimuthal variations in the homogenized XS are driven more by the azimuthal variations in the source and incoming boundary conditions. While there can be strong azimuthal variation in areas with strong leakage in the radial directions, the spatial-azimuthal coupling of the flux is generally weak within a pin cell, so the azimuthal homogenization error is small. This is demonstrated numerically in Sec. 4.5.

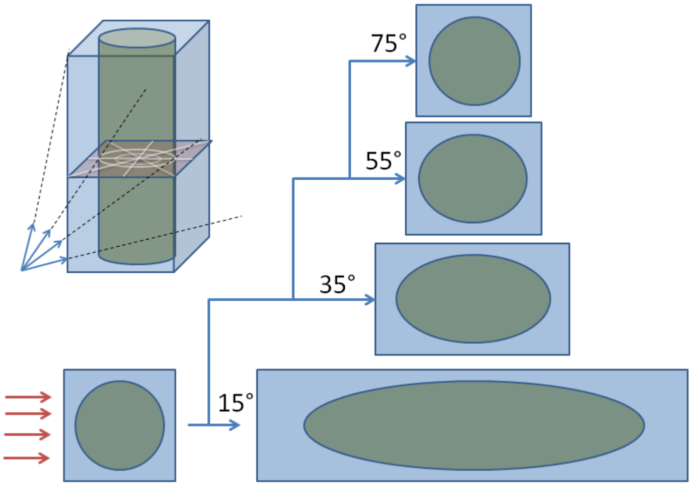

Figure 3.1: Projected 2D MOC problem geometry at various polar angles

Approximate expressions for the azimuthal moment XS can be obtained by using the Fourier expansion from Eq. (3.13) in Eq. (3.22), assuming the higher-order moments are $\mathcal{O}(\epsilon)$ (i.e., small), and ignoring $\mathcal{O}(\epsilon^2)$ terms. In Sec. 4.5 a simple problem is used to verify that the magnitudes of these moments are small enough to apply this approximation.

$$
\begin{aligned}
&\hat{\Sigma}_{t,k,ij}(\boldsymbol{\Omega}) \\
&= \frac{\iint\limits_{ij} \Sigma_{t,k}(x,y) \left[\frac{\psi_{0,k}(x,y,\mu)}{2\pi} + \frac{1}{\pi} \sum\limits_{p=1}^{P} \left[\psi_{c,p,k}(x,y,\mu) \cos{(p\omega)} + \psi_{s,p,k}(x,y,\mu) \sin{(p\omega)} \right] \right] dxdy}{\iint\limits_{ij} \left[\frac{\psi_{0,k}(x,y,\mu)}{2\pi} + \frac{1}{\pi} \sum\limits_{p=1}^{P} \left[\psi_{c,p,k}(x,y,\mu) \cos{(p\omega)} + \psi_{s,p,k}(x,y,\mu) \sin{(p\omega)} \right] \right] dxdy} \\
&= \frac{\iint\limits_{ij} \Sigma_{t,k}(x,y) \left[\psi_{0,k}(x,y,\mu) + 2 \sum\limits_{p=1}^{P} \left[\psi_{c,p,k}(x,y,\mu) \cos{(p\omega)} + \psi_{s,p,k}(x,y,\mu) \sin{(p\omega)} \right] \right] dxdy}{\iint\limits_{ij} \psi_{0,k}(x,y,\mu) dxdy} \cdot \\
&\left[1 - \left(\iint\limits_{ij} \psi_{0,k}(x,y,\mu) dxdy \right)^{-1} \cdot \right. \\
&\left. \left(2 \iint\limits_{ij} \sum_{p=1}^{P} \left[\psi_{c,p,k}(x,y,\mu) \cos{(p\omega)} + \psi_{s,p,k}(x,y,\mu) \sin{(p\omega)} \right] dxdy \right) + \mathscr{O}(\epsilon^2) \right] \\
&= \tilde{\Sigma}_{t,k,ij}(\mu) + 2 \frac{\iint\limits_{ij} \Sigma_{t,k}(x,y) \left(\sum\limits_{p=1}^{P} \left[\psi_{c,p,k}(x,y,\mu) \cos{(p\omega)} + \psi_{s,p,k}(x,y,\mu) \sin{(p\omega)} \right] \right) dxdy}{\iint\limits_{ij} \psi_{0,k}(x,y,\mu) dxdy} \\
&- 2\tilde{\Sigma}_{t,k,ij}(\mu) \frac{\left(\iint\limits_{ij} \sum\limits_{p=1}^{P} \left[\psi_{c,p,k}(x,y,\mu) \cos{(p\omega)} + \psi_{s,p,k}(x,y,\mu) \sin{(p\omega)} \right] dxdy \right)}{\iint\limits_{ij} \psi_{0,k}(x,y,\mu) dxdy} + \mathscr{O}(\epsilon^2) \\
&= 2 \frac{\iint\limits_{ij} \left[\Sigma_{t,k}(x,y) - \hat{\Sigma}_{t,k,ij}(\mu) \right] \left(\sum\limits_{p=1}^{P} \left[\psi_{c,p,k}(x,y,\mu) \cos{(p\omega)} + \psi_{s,p,k}(x,y,\mu) \sin{(p\omega)} \right] \right) dxdy}{\iint\limits_{ij} \psi_{0,k}(x,y,\mu) dxdy} \qquad (3.24) \\
&+ \tilde{\Sigma}_{t,k,ij}(\mu) + \mathscr{O}(\epsilon^2) \; .
\end{aligned}
$$

Operating by $\int\limits_{0}^{2\pi} \cos{(p\omega)}(\cdot) d\omega$ and $\int\limits_{0}^{2\pi} \sin{(p\omega)}(\cdot) d\omega$, we obtain (with $\mathscr{O}(\epsilon^2)$ error):

$$
\tilde{\Sigma}_{s/c,p,k,ij} = 2 \frac{\int\limits_{x_{i-1/2}}^{x_{i+1/2}} \int\limits_{y_{j-1/2}}^{y_{j+1/2}} \left[\Sigma_{t,k}(x,y) - \tilde{\Sigma}_{t,k,ij}(\mu) \right] \psi_{s/c,p,k}(x,y,\mu) dxdy}{\int\limits_{x_{i-1/2}}^{x_{i+1/2}} \int\limits_{y_{j-1/2}}^{y_{j+1/2}} \hat{\psi}_{0,k}(x,y,\mu) dxdy} \; . \qquad (3.25)
$$

Here, the azimuthal angular flux moments over a coarse cell $\psi_{(s/c),p}$ are calculated during the 2D MOC sweep. Including the azimuthal XS moments from Eq. (3.25) in

Eq. (3.14), we obtain modified forms of Eq. (3.16):

$$\left[\mu\frac{\partial}{\partial z}+\tilde{\Sigma}_{t,k,ij}(\mu)\right]\hat{\psi}_{0,ij}(z,\mu)=\frac{\hat{Q}_{ij}(z)}{2}-TL^{XY}_{0,ij}(z,\mu)\ , \tag{3.26a}$$

$$\begin{aligned}\left[\mu\frac{\partial}{\partial z}+\tilde{\Sigma}_{t,k,ij}(\mu)\right]\hat{\psi}_{s/c,p,ij}(z,\mu)&=-TL^{XY}_{s/c,p,ij}(z,\mu)\\&\quad-\frac{1}{2}\tilde{\Sigma}_{s/c,p,k,ij}\psi_{0,ij}(z,\mu)\ ;\ 1\le p\le P\ .\end{aligned} \tag{3.26b}$$

The polar angular flux $\psi_{0,ij}(z,\mu)$ is known in Eq. (3.26b). The sum of azimuthal moment terms that should technically appear in Eq. (3.26a) is small enough to be ignored. Each term in the sum is the product of two small terms: an azimuthal XS moment and an azimuthal flux moment.

When using azimuthal expansion, the azimuthal quadrature set that we use must correctly integrate the azimuthal Fourier moments. This is not a concern because our standard Chebyshev quadrature set already correctly integrates the first several moments, even after the angles have been altered in the modularization process.

The anisotropic term is treated as a source, and is calculated using $\psi_{0,k,ij}(\mu)$ from the 2D MOC sweep, together with the axial shape of the scalar flux $\hat{\phi}_{ij}(z)$ from the 1D solution within the plane. Eqs. (3.26) should be marginally more accurate than Eqs. (3.16). However, the differences in the solution are usually negligible, and not worth the significant increase in computational cost associated with calculating $\psi_{c,p}$ and $\psi_{s,p}$ during the MOC sweep. Numerical results in Section 4.6 demonstrate this.

It should be noted that homogenization of fuel and moderator could potentially be avoided by solving two separate 1D equations for each pin cell: one for fuel, and one for a homogenized mixture of moderator, clad, and anything else. The 2D/1D “fusion” code CRX-2 solves a separate 1D equation for each fine mesh region in order to completely eliminate homogenization [62]. However, there are significant drawbacks to this approach. If the radial boundaries of the 1D problem are on the surface of each fuel rod, instead of just at the boundary between pin cells, the approximations to the TL become much more important because the magnitude of the leakage between fuel/control and moderator is significantly greater than the leakage between adjacent pin cells. For this reason, the isotropic approximation or low-order Fourier and Legendre expansion that works well for the standard method could be inaccurate when applied to the TL on rod surfaces. This is covered in more detail in Section 3.3.

The isotropic total XS for 1D transport is used extensively in 2D/1D methods. The error associated with this approximation is usually acceptably low. However, the error is more significant when the gradients in the 1D solution are strong, such as in the 3D C5G7 benchmark [29]. This may also be the case when there are partially inserted control rods or part-length fuel rods in an LWR. Anisotropic XS homogenization can mitigate this error. The polar dependence is the major component of the anisotropic XS effect, while the azimuthal dependence is small. In this thesis, an azimuthally isotropic XS with only polar dependence is primarily used, because it is expensive to calculate azimuthal moments of the homogenized XS.

3.1.5 Within-pin Spatial Shape of Axial TL

In MPACT, the axial 1D transport equation is solved on the coarse mesh, along each pin. The axial TL is provided by the solution to the 1D equation, so it is known with the same spatial resolution as the 1D solution: in this case, the pin cell. This means that the 2D/1D equations, as they are solved in this thesis, offer no expression for the spatial distribution of the axial TL source within a pin. In absence of a spatial distribution, it is approximated as flat over each pin cell.

Previously, it was thought that this flat axial TL approximation was the main contributor to pin cell heterogeneity error, and the error associated with the XS homogenization was negligible [28, 63, 8]. During the work performed for this thesis, the opposite was found to be true. The results supporting this conclusion are given in Section 3.3, Section 4.4, and in a previous conference paper [64]. For the present work, only a spatially flat axial TL is used. The TL in a pin with a given (i, j) index within a Cartesian lattice and at axial plane k is then given by:

$$\tilde{J}_{z,k,ij}(\mathbf{\Omega}) = \frac{\mu}{h_k} \left[\hat{\psi}_{ij}(z_{k+1/2}, \mathbf{\Omega}) - \hat{\psi}_{ij}(z_{k-1/2}, \mathbf{\Omega}) \right] \ , \tag{3.27}$$

where $\hat{\psi}_{ij}$ is the solution of the 1D transport equation.

For the sake of comparison, scalar flux-weighted TL is also used to demonstrate the relatively small magnitude of the effect of the TL shape approximation. In this case, the shape function is:

$$g_{k,ij}(x, y, \mathbf{\Omega}) = g_{k,ij}(x, y) = \frac{\phi_k(x, y) \iint\limits_{ij} dx dy}{\iint\limits_{ij} \phi_k(x, y) dx dy} \ . \tag{3.28}$$

The difference between the spatially flat or scalar flux-weighted axial TL is usually negligible. For problems with strong axial leakage, the two approximations may result in a slightly different solution (roughly 5-10 pcm difference).

Based on the results in this work, there are a few reasons that we can confidently ignore the effects of the axial TL spatial shape. Most importantly, we are able to obtain almost perfect agreement with Monte Carlo reference solutions using a flat axial TL in Section 4.2 and Section 4.4. Additionally, we find that using a scalar flux-weighted axial TL has very little effect on the solution. From this, we can infer that the axial TL spatial shape only weakly influences the solution. Thus, any reasonable approximation we make to the spatial shape will be acceptable. Even though the spatially flat axial TL is not physically correct, the effect that the approximation has on the solution is negligible.

The "correct" space-angle shape would require knowledge of the spatial distribution of the angular flux on the top and bottom surfaces of an MOC plane, as in Eq. (3.6):

$$\tilde{J}_{z,k}(x,y,\mathbf{\Omega}) = \frac{\mu}{h_k}\left[\psi(x,y,z_{k+1/2},\mathbf{\Omega}) - \psi(x,y,z_{k-1/2},\mathbf{\Omega})\right] \ . \tag{3.6}$$

Previous work related to this thesis investigated the feasibility and effectiveness of an "implicit" axial TL shape that more accurately approximated the "correct" shape in Eq. (3.6). Since the 1D angular flux solution provides no spatial distribution within the pin, the spatial distribution can be approximated by using the 2D angular flux within the pin:

$$\tilde{J}_{z,k}(x,y,\mathbf{\Omega}) = \frac{\left[J_{z,k+1/2} - J_{z,k-1/2}\right]}{h_k} \frac{\mu\psi_k(x,y,\mathbf{\Omega})}{\int\limits_{-1}^{1}\int\limits_{0}^{2\pi} \mu\psi_k(x,y,\mathbf{\Omega})d\omega d\mu} \ . \tag{3.29}$$

The basic assumption of 2D/1D is that the axial dependence of the angular flux is separable from the radial-angular dependence, so the approximation in Eq. (3.29) is reasonable in the broader context of 2D/1D. Using Eq. (3.29), the spatial shape of the axial TL can be obtained directly from the 2D angular flux. However, it is expensive to store the full angular flux on the fine mesh, so we use it implicitly instead.

The implicit TL shape method that we developed used a modified total cross section for the 2D MOC to implicitly apply the 2D angular flux solution as the radial-angular shape for the axial TL within a pin. The 2D transport equation was defined as:

$$\sqrt{1-\mu^2}\left(\cos\omega\frac{\partial\psi_k}{\partial x}+\sin\omega\frac{\partial\psi_k}{\partial y}\right)+\Sigma'_{t,k,g}(x,y,\mu)\psi_{k,g}(x,y,\mathbf{\Omega})=\frac{Q_k(x,y,E)}{4\pi}\ , \tag{3.30a}$$

$$\Sigma'_{t,k,g}(x,y,\mu)=\Sigma_{t,k,g}(x,y)+\frac{\mu}{h_k}\left(A^{+}_{k,g}-A^{-}_{k,g}\right)\ , \tag{3.30b}$$

$$A^{\pm}_{k,g}=\frac{J_{k\pm1/2,g}}{J_{k,g}}\ . \tag{3.30c}$$

In Eq. (3.30), $J_{k\pm1/2,g}$ are the axial currents from the 1D solution, and $J_{k,g}$ is the effective axial current in the 2D solution:

$$J_{k,g}=\int_{x_{i-1/2}}^{x_{i+1/2}}\int_{y_{j-1/2}}^{y_{j+1/2}}\left(\int_{-1}^{1}\int_{0}^{2\pi}\mu\psi_{k,g}(x,y,\mu,\omega)d\omega d\mu\right)dxdy\ . \tag{3.31}$$

Using this method requires that we do the following:

1. Calculate and store the 2D axial current using the expression in Eq. (3.31).
2. Calculate and store the modified total cross section $\Sigma'_{t,k,g}(x,y,\mu)$ on the fine mesh, with polar dependence.

This adds computational work, unless the polar angular flux is already being calculated for the anisotropic XS homogenization. More important than the increased computational expense, this method was either unstable or very slow to converge for the few test problems it was applied to. The effect on the solution was relatively small (less than 5 pcm) in the cases where it did converge.

The implicit TL scheme in Eq. (3.30) also introduces the possibility of negative Σ_t for the 2D MOC, which would cause iterative issues. This would require splitting the negative Σ_t back into a TL source, which is effectively like reverse TL splitting. Overall, this method was not very stable and also not very important for obtaining an accurate solution. The research briefly described here did not indicate a strong motivation for an axial TL spatial shape function, so this thesis does not include any more work or development involving such shaping.

3.1.6 Radial Transverse Leakage Interpolation

The radial TL is determined by the radial derivatives of the 3D angular flux. In the 2D/1D method, the angular flux can vary significantly over the axial length of a node, which may be several centimeters. It is likely insufficient to represent the radial TL term as spatially flat over this node in the 1D equation.

One approach is to use subplanes to discretize the radial TL and nodal equation on a finer axial mesh than the 2D transport equations. This is the approach used in nTRACER [13]. MPACT has subplane capability [30], although it is not always used. In MPACT, the spatial shape of the radial TL is approximated using interpolation with neighboring nodes. The zeroth, first, and second moments of the radial TL are given by:

$$TL_g^{XY}(\xi) = \sum_{i=0}^{2} TL_{i,g}^{XY} P_i(\xi) \ , \tag{3.32a}$$

$$G = 2(h_C + h_B)(h_C + h_T)(h_B + h_C + h_T) \ , \tag{3.32b}$$

$$TL_{0,g}^{XY} = TL_{C,g}^{XY} \ , \tag{3.32c}$$

$$\begin{aligned} TL_{1,g}^{XY} = \frac{h_c}{G} \big[&\left(TL_{T,g}^{XY} - TL_{C,g}^{XY}\right)(h_C + 2h_B)(h_C + h_B) \\ &- \left(TL_{B,g}^{XY} - TL_{C,g}^{XY}\right)(h_C + 2h_T)(h_C + h_T) \big] \ , \end{aligned} \tag{3.32d}$$

$$TL_{2,g}^{XY} = \frac{h_C^2}{G} \left[\left(TL_{T,g}^{XY} - TL_{C,g}^{XY}\right)(h_C + h_B) + \left(TL_{B,g}^{XY} - TL_{C,g}^{XY}\right)(h_C + h_T) \right] \ . \tag{3.32e}$$

B, C, and T are the bottom, center, and top nodes of the 3 point interpolation, respectively. In the special case $h_B = h_C = h_T$, the equations reduce to a more familiar form:

$$TL_{1,g}^{XY} = \frac{TL_{T,g}^{XY} - TL_{B,g}^{XY}}{4} \ , \tag{3.33a}$$

$$TL_{2,g}^{XY} = \frac{TL_{T,g}^{XY} - 2TL_{C,g}^{XY} + TL_{B,g}^{XY}}{12} \ . \tag{3.33b}$$

The interpolation is depicted in Fig. 3.2. Because MOC slices are typically several centimeters thick, the axial spatial shape of the radial TL within a node is important. Without the interpolation, the discretization of the radial TL source would be too coarse. Another way of obtaining the axial shape of the TL within an MOC slice is to use subplanes in the 3D CMFD and 1D nodal solution. The 3D CMFD then provides a more finely discretized radial TL. The subplane method has been implemented in MPACT [30].

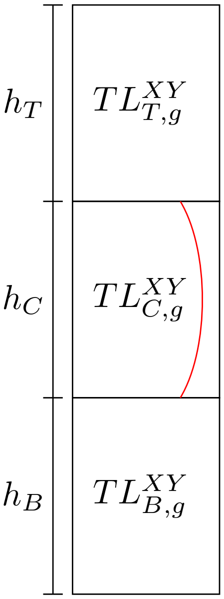

Figure 3.2: Radial TL interpolation

3.1.7 P$_3$ Expansion of the 1D Transport Equation

In this thesis, Eqs. (3.26) are solved using a Legendre polynomial expansion of the polar angular variable. Truncating this expansion at $L = 3$ moments usually provides sufficient accuracy for LWR problems. Both the angular flux $\hat{\psi}$ and the anisotropic transverse leakage sources TL need to be expanded in Legendre polynomials. Rather than expanding the cross section $\tilde{\Sigma}_{t,k,ij}(\mu)$ in Legendre polynomials, the anisotropic component of it in Eq. (3.34) is moved to the right side and treated together with the source anisotropy:

$$\begin{aligned}&\left[\mu\frac{\partial}{\partial z}+\hat{\Sigma}_{t,k,ij}\right]\left[\frac{\hat{\psi}_{0,ij}(z,\mu)}{2\pi}+\frac{1}{\pi}\sum_{p=1}^{P}\Big(\hat{\psi}_{c,p,ij}(z,\mu)\cos(p\omega)+\hat{\psi}_{s,p,ij}(z,\mu)\sin(p\omega)\Big)\right]\\&=\frac{\hat{Q}_{ij}(z)}{4\pi}-\frac{TL^{XY}_{0,ij}(z,\mu)}{2\pi}-\frac{1}{\pi}\sum_{p=1}^{P}\left[TL^{XY}_{c,p,ij}(z,\mu)\cos(p\omega)+TL^{XY}_{s,p,ij}(z,\mu)\sin(p\omega)\right]\\&+\left[\hat{\Sigma}_{t,k,ij}-\tilde{\Sigma}_{t,k,ij}(\mathbf{\Omega})\right]\left[\frac{\psi_{0,ij}(z,\mu)}{2\pi}+\frac{1}{\pi}\sum_{p=1}^{P}\left[\psi_{c,p,ij}(z,\mu)\cos(p\omega)+\psi_{s,p,ij}(z,\mu)\sin(p\omega)\right]\right].\end{aligned} \tag{3.34}$$

We note that the angular flux over a pin cell ψ appears both with and without a ($\hat{}$) in this equation. The ($\hat{}$) signifies the 1D angular flux moments that are being solved for. The instances of ψ without ($\hat{}$) signify a known quantity obtained from averaging the 2D MOC solution over a coarse pin cell.

jkFor the zeroth azimuthal moment, we operate on Eq. (3.34) by $\int_0^{2\pi}(\cdot)d\omega$. Both the anisotropic azimuthal XS moments and the anisotropic azimuthal angular fluxes are small terms, $\mathscr{O}(\epsilon)$, so the integral of their product can be ignored. While this approximation works well for LWRs, it is conceivable that certain geometries could create a solution where these terms are not $\mathscr{O}(\epsilon)$. However, we were unable to devise such a problem, and the focus here is on developing a simplified expression that is effective for most practical cases. Next, a Legendre expansion in the polar angle μ is substituted for the angular flux in Eq. (3.26a), and the 0^{th} through 3^{rd} moments are calculated. We obtain:

$$\frac{d}{dz}\hat{\phi}_1 + \hat{\Sigma}_t\hat{\phi}_0 = \hat{\Sigma}_{s0}\hat{\phi}_0 + q_0 \ , \tag{3.35a}$$

$$\frac{1}{3}\frac{d}{dz}\hat{\phi}_0 + \frac{2}{3}\frac{d}{dz}\hat{\phi}_2 + \hat{\Sigma}_t\hat{\phi}_1 = \hat{\Sigma}_{s1}\hat{\phi}_1 + q_1 \ , \tag{3.35b}$$

$$\frac{2}{5}\frac{d}{dz}\hat{\phi}_1 + \frac{3}{5}\frac{d}{dz}\hat{\phi}_3 + \hat{\Sigma}_t\hat{\phi}_2 = q_2 \ , \tag{3.35c}$$

$$\frac{3}{7}\frac{d}{dz}\hat{\phi}_2 + \Sigma_t\hat{\phi}_3 = q_3 \ , \tag{3.35d}$$

where:

$$q_l(z) = \int_{-1}^{1} P_l(\mu)\left[\frac{\hat{Q}(z)}{2} - TL_0^{XY}(z,\mu) + \left[\hat{\Sigma}_t - \tilde{\Sigma}_{t,k}(\mu)\right]\psi_0(z,\mu)\right]d\mu \ , \tag{3.35e}$$

$$\tilde{\phi}_0 = \hat{\phi}_0 + 2\hat{\phi}_2 \ . \tag{3.35f}$$

In the multigroup form of the equations, the source $\hat{Q}(z)$ in Eq. (3.35e) includes the isotropic inscattering and fission sources, but not the self-scattering source. The isotropic self-scattering is subtracted from $\Sigma_{t,g}$ to obtain the removal cross section $\Sigma_{r,g}$.

We obtain the second-order form of the 1D P$_3$ equations through the standard derivation:

$$\phi_1 = \frac{q_1}{\hat{\Sigma}_{tr}} - \frac{d}{dz}\frac{1}{3\hat{\Sigma}_{tr}}\tilde{\phi}_0 \ , \tag{3.36a}$$

$$\phi_3 = \frac{q_3}{\hat{\Sigma}_t} - \frac{d}{dz}\frac{3}{7\hat{\Sigma}_t}\hat{\phi}_2 \ . \tag{3.36b}$$

Substituting Eqs. (3.36) into Eq. (3.35a) and Eq. (3.35c), we obtain:

$$-\frac{\partial}{\partial z}\frac{1}{3\hat{\Sigma}_{tr}}\frac{\partial}{\partial z}\tilde{\phi}_0 + \hat{\Sigma}_r\tilde{\phi}_0 = q_0 - \frac{\partial}{\partial z}\frac{q_1}{\hat{\Sigma}_{tr}} \ , \tag{3.37a}$$

$$-\frac{\partial}{\partial z}\frac{9}{35\hat{\Sigma}_t}\frac{\partial}{\partial z}\hat{\phi}_2 + \left(\hat{\Sigma}_t + \frac{4}{5}\hat{\Sigma}_r\right)\hat{\phi}_2 = q_2 + \frac{2}{5}\left(\hat{\Sigma}_r\tilde{\phi}_0 - q_0\right) - \frac{3}{5}\frac{\partial}{\partial z}\frac{q_3}{\hat{\Sigma}_t} \ , \tag{3.37b}$$

These equations are solved axially over each pin (i, j); the index subscript has been dropped to simplify the notation. These equations are solved using a 4th-order Legendre polynomial expansion in *space* for the fluxes and a second-order expansion in *space* for the sources. The higher-order angular moments of the source q_l account for the anisotropy in both the radial TL and the homogenized collision term. The equations are similar for the higher-order azimuthal moments $\phi_{cp,l}$ and $\phi_{sp,l}$, but the sources are defined differently, as appropriate for each moment:

$$q_{cp,l}(z) = \int_{-1}^{1} P_l(\mu)\left(-TL^{XY}_{c,p}(z,\mu) + \left[\hat{\Sigma}_t - \tilde{\Sigma}_t(\mu)\right]\psi_{c,p}(z,\mu) - \frac{1}{2}\tilde{\Sigma}_{c,p}(z,\mu)\psi_0(z,\mu)\right)d\mu \ , \tag{3.38a}$$

$$q_{sp,l}(z) = \int_{-1}^{1} P_l(\mu)\left(-TL^{XY}_{s,p}(z,\mu) + \left[\hat{\Sigma}_t - \tilde{\Sigma}_t(\mu)\right]\psi_{s,p}(z,\mu) - \frac{1}{2}\tilde{\Sigma}_{s,p}(z,\mu)\psi_0(z,\mu)\right)d\mu \ . \tag{3.38b}$$

Again, $\tilde{\Sigma}_{cp}(z,\mu)$ and $\tilde{\Sigma}_{sp}(z,\mu)$ are relatively small and are typically ignored. The other anisotropic collision term can be calculated by using $\hat{\psi}_{cp}$ and $\hat{\psi}_{sp}$ (from the 1D equation) instead of ψ_{cp} and ψ_{sp} (from the 2D MOC), but this is also a small term and is ignored without significant detriment to the accuracy. After solving the 1D P_3 equations for each of the azimuthal moments of the 1D angular flux, the anisotropic axial TL can be calculated. In a single pin cell (i, j):

$$\hat{\psi}(z,\mathbf{\Omega}) = \sum_{l=0}^{3}\frac{2l+1}{2}P_l(\mu)\left[\frac{\hat{\phi}_l(z)}{2\pi} + \frac{1}{\pi}\sum_{p=1}^{P}\left(\hat{\phi}_{c,p,l}(z)\cos(p\omega) + \hat{\phi}_{s,p,l}(z)\sin(p\omega)\right)\right] \ . \tag{3.39}$$

Eqs. (3.37) are the improved 1D P_3 equations that account for anisotropic radial TL and homogenized collision terms. Eq. (3.39) specifies the pin cell averaged angular flux, which can be used to calculate the anisotropic axial TL for the 2D MOC sweep in Eq. (3.5a). Altogether, these equations constitute a 2D/1D transport method that has improved 3D transport accuracy and a correction for the effect of heterogeneity within a coarse cell. The corrections have been tailored to be most effective for LWR geometries.

3.2 Other Aspects of 2D/1D in MPACT

In Sec. 3.1, the equations related to the 2D/1D method developed and implemented in MPACT for this thesis were derived and described. In this section, other aspects of the 2D/1D implementation in MPACT are briefly described. The transverse leakage splitting method, which is sometimes used to achieve convergence, is explained in Sec. 3.2.1. The 2D/1D iteration scheme in MPACT is presented in Sec. 3.2.2. The 2D/1D under-relaxation scheme in MPACT, which is not used in this work, is described in Sec. 3.2.3. The nomenclature for the different variations of the 2D/1D method in MPACT is described in Sec. 3.2.4.

3.2.1 Transverse Leakage Splitting

In general, both the 2D and 1D equations should produce a positive solution everywhere when the source is positive everywhere. The source can become negative if the transverse leakage term is too strongly negative. This is not frequently a major issue, because the 2D/1D method is usually applied to problems without excessively strong axial gradients. However, it is certainly possible that the transverse leakage can be strong enough to produce a negative solution. The 2D/1D iteration in MPACT contains nonlinearity from two features:

1. The CMFD acceleration is non-linear, and consequently it is highly sensitive to any negative fluxes produced during the iteration. Linear acceleration schemes also exist, such as Diffusion Synthetic Acceleration [65]. Thus, this nonlinearity should in theory be avoidable, although it would require significant modifications to the MPACT 3D acceleration implementation.

2. The homogenization of the 2D solution onto the coarse mesh for the 1D solution introduces nonlinearity. If negative flux solutions are used to homogenize the 2D solution, the XS may be negative, or unrealistically large or small. This disrupts the iteration, and will likely cause convergence failure. This nonlinearity is more fundamental to the 2D/1D method with pin-homogenization, and may be more difficult to avoid.

It is not yet clear how much each of these nonlinearities contributes to the overall negative source sensitivity and convergence failure in MPACT. Future work will be necessary to determine if implementing a linear acceleration scheme is sufficient to avoid convergence failure when negative solutions arise, or if the homogenization still causes convergence issues.

To improve the robustness of the iteration, MPACT can attempt to enforce a non-negative source in all regions for both the 1D solution and the 2D solution. This is done by moving a negative source to the "left" side of the equation and adding it to the collision term, a process called transverse leakage splitting. For the 2D solution, it is called axial transverse leakage splitting, and for the 1D solution, it is radial transverse leakage splitting. This method was developed in previous thesis research related to MPACT by Kelley [63] and Stimpson [8].

To demonstrate the axial TL splitting method, we recall Eq. (3.8).

$$\left[(\mathbf{\Omega}\cdot\nabla)_{xy} + \Sigma_{t,k}(x,y)\right]\psi_k(x,y,\mathbf{\Omega}) = \frac{Q_k(x,y)}{4\pi} - \frac{\left[J_{z,k+1/2,ij} - J_{z,k-1/2,ij}\right]}{4\pi h_k} \ . \tag{3.8}$$

If the total source is negative, then the split $\tilde{L}_z$ is defined as the absolute value of this source, and is added to both sides:

$$\begin{gathered}\frac{Q_k(x,y)}{4\pi} - \frac{\left[J_{z,k+1/2,ij} - J_{z,k-1/2,ij}\right]}{4\pi h_k} < 0 \ , \\ \tilde{L}_z = -\left[\frac{Q_k(x,y)}{4\pi} - \frac{\left[J_{z,k+1/2,ij} - J_{z,k-1/2,ij}\right]}{4\pi h_k}\right] \ .\end{gathered} \tag{3.40}$$

On the left side, this leakage is added to the collision term. Because the angular flux is not known, it is approximated by:

$$\psi_k(x,y,\mathbf{\Omega}) \approx \frac{\phi_k(x,y)}{4\pi} \ . \tag{3.41}$$

This approximation is the reason the splitting method is detrimental to the accuracy of the solution, but it is impossible to avoid the approximation without incurring significant computational expense associated with storing and using the angular flux in the splitting term. After splitting the axial TL, Eq. (3.8) becomes:

$$\tilde{\Sigma}_{t,k}(x,y) = \Sigma_{t,k}(x,y) + \frac{4\pi\tilde{L}_z}{\phi_k(x,y)} \ , \tag{3.42}$$

$$\left[(\mathbf{\Omega}\cdot\nabla)_{xy} + \tilde{\Sigma}_{t,k}(x,y)\right]\psi_k(x,y,\mathbf{\Omega}) = \frac{Q_k(x,y)}{4\pi} - \frac{\left[J_{z,k+1/2,ij} - J_{z,k-1/2,ij}\right]}{4\pi h_k} + \tilde{L}_z = 0 \ . \tag{3.43}$$

In practice, the TL splitting is often calculated before the addition of the self-scattering source, so the source remains slightly positive with splitting, once the self-scattering is added. However, this scheme could lead to a negative source if the self-scattering XS is negative because of the TCP0 approximation.

In principle, the radial TL splitting is similar to the axial TL splitting. For radial TL splitting, only the spatially flat moment of the 1D source is split to maintain positivity.

The downside of TL splitting is that it perturbs the solution, and negatively affects the accuracy. A recent method has been developed to improve accuracy when using TL splitting by using a better approximation to the angualr flux than Eq. (3.41), but it has a significant computational expense [66].

All results in Chapter 4 were obtained without TL splitting. For more realistic problems, TL splitting may be necessary.

For the problem used in Sec. 4.7, the control rod tip does not align with the MOC plane boundaries, which results in a rod smearing error that has to be corrected using a polynomial decusping or other correction method. If the axial mesh is changed so that it aligns with the location of the control rod tip, the magnitude of the axial TL is increased significantly, and TL splitting becomes necessary. This TL splitting degrades the accuracy of the 2D/1D solution. Thus, it is difficult to obtain an accurate solution to this problem using 2D/1D in MPACT. The rod smearing error and TL splitting error cannot both be avoided. This is a limitation of the 2D/1D in MPACT from the negative source sensitivity caused by nonlinearity. Developing a 2D/1D method without nonlinearity should improve the range of problems for which MPACT can converge to an accurate solution.

3.2.2 2D/1D Iteration Scheme

A high-level flowchart of the iteration scheme for solving the 2D/1D equations is shown in Fig. 3.3.

This iteration scheme is very similar to other 2D/1D implementatins, such as DeCART [12]. The order of the 3 solutions is somewhat arbitrary, although the flowchart depicts the order that is used by MPACT. Beginning with the 3D CMFD and 1D axial solution makes sense, because it provides a good initial guess for the 2D MOC solution during the first iteration.

The 3D CMFD solution is a Wielandt-shifted inverse power iteration. Each step of the non-linear solution is called a CMFD outer iteration. The estimated fission source and eigenvalue are updated after each outer iteration. Each outer iteration itself is a fixed-source problem, solved using an iterative solver such as GMRES or the newer Multi-level in Space and Energy Diffusion (MSED) method [59].

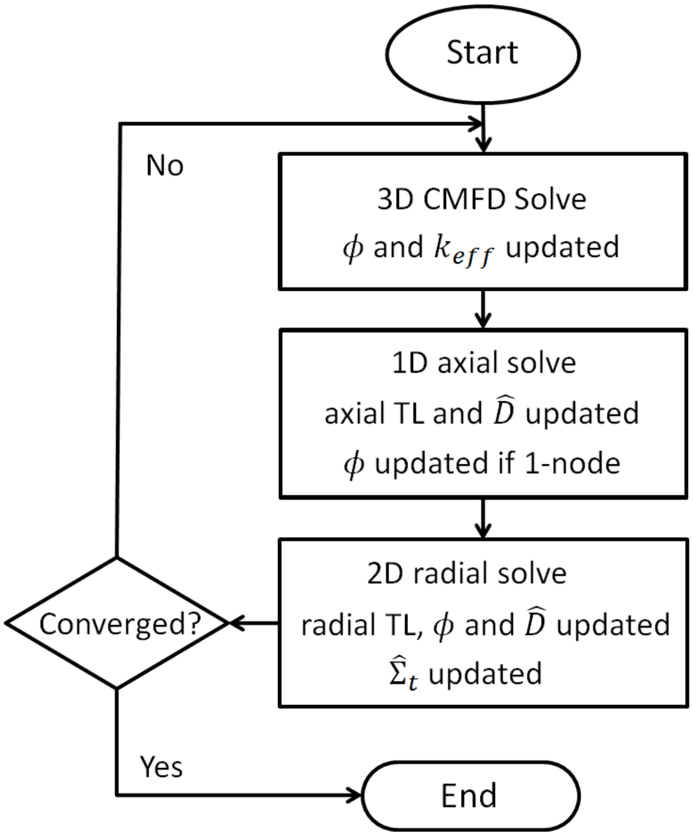

Figure 3.3: Iterative algorithm flowchart for 2D/1D

Each iteration on the fixed-source problem is called a CMFD inner iteration. The number of CMFD inners depends on the condition number of the matrix, which depends mainly on the aggressiveness of the Wielandt shift and problem size. The solution may require several hundred inner iterations when using GMRES, and in some cases the maximum number of inners (typically 500) will be reached without reaching the desired residual reduction. Outer iterations will be performed until the residual and successive change in eigenvalue satisfy a certain tolerance. The required number of CMFD outers may be a couple dozen at the beginning of the iteration, but this number will decrease to just a few per CMFD solve as the solution converges.

The CMFD solution is used to update the coarse cell scalar fluxes for the 1D axial solution, and the 2D fine-mesh fluxes for the 2D MOC solution based on Eq. (2.46).

The 1D axial solve is a sweep over all of the 1D problems (one for each pin). Each process sweeps over its full axial domain for each pin in its radial domain. The full axial height is often only one coarse cell. Each process then communicates the boundary conditions to the axial neighbors. This solve is on the coarse mesh, so it is a relatively small amount of information to communicate.

A single inner axial sweep consists of a full sweep from bottom to top over each spatial domain, and back down, followed by communication, for a single group. The boundary conditions at axial parallel interfaces are lagged from the previous sweep. An outer axial sweep consists of a loop over all of the groups, with 5 inner sweeps over each group. Performing multiple axial sweeps helps to converge the boundary conditions and improve communication of information in the axial direction, which is usually highly parallelized. The source is recalculated after each inner sweep. An axial solve consists of 5 outer loops (1 over all groups, 4 over upscattering groups) to converge the scattering source.

If the 1D solver uses a two-node kernel, the coarse cell scalar fluxes will be unchanged (see Sec. 2.5.3). If a one-node kernel is used, the coarse cell scalar fluxes are updated with the new solution, and these updates are projected on to the 2D fine-mesh fluxes in the same way as the CMFD update. The axial TL source for each cell is calculated using the 1D solution.

The 2D MOC solve may consist of multiple sweeps over the upscattering energy groups to converge the inter-group scattering source, as well as inner sweeps to converge the self-scattering term. However, the MOC solution is expensive, so multiple sweeps per outer iteration are typically not performed unless this is necessary to achieve stability. On each process, 2D MOC sweeps are performed over the local radial domain for one axial slice at a time. Again, there is often only one slice per process. The radial TL terms are calculated on the final inner iteration of the final sweep over each group. Often, there is only one MOC sweep. If polar anisotropic XS are used, the polar angular flux for each FSR is also stored during the final sweep. The homogenized cross sections for the CMFD and 1D axial solution are calculated using the 2D MOC solution.

In Eqs. (3.37), the anisotropic homogenization term is treated as a source, as in Eq. (3.35e). The linear anisotropic moment of the source, q_1, includes both a radial TL component and an anisotropic homogenization component. The definition of the axial current for the CMFD equations, ϕ_1, is slightly different when these anisotropic terms are present:

$$\phi_1 = \frac{q_1}{\hat{\Sigma}_{tr}} - \frac{d}{dz}\frac{1}{3\hat{\Sigma}_{tr}}\tilde{\phi}_0 \ . \tag{3.36a}$$

It is possible that the inclusion of the q_1 term may affect the current correction factors $\hat{D}$ on the axial surfaces for the CMFD acceleration. In theory, this can affect the convergence rate of CMFD, but in practice we do not observe any change in the convergence rate.

Because the isotropic moment of this term is zero by definition, the overall neutron balance that defines the low-order equation is unaffected, and the acceleration equations do not need to be modified when using the anisotropic XS. Thus, the CMFD equations always use isotropic XS, regardless of whether the 1D axial equations use angle-dependent XS, and there are no special considerations necessary for the acceleration equations when anisotropic terms are used in the 2D/1D approximation.

3.2.3 2D/1D Relaxation

In previous work with DeCART and MPACT, it was observed that the 2D/1D iteration scheme was inherently unstable in models containing thin planes. Kelley and Larsen [19] performed Fourier analyses to determine a group-dependent relaxation factor to be applied to the update of the scalar flux after a 2D MOC sweep. The relaxation factor required for stability is determined by the optical thickness of the plane and the self-scattering ratio. An empirical fit to Fourier Analysis results was used to define an explicit formula for the optimal relaxation factors. Therefore, the relaxation is defined in Eq. (3.44).

$$\phi_{g,k}(x,y)^{(l+1/2)} = \phi_{g,k}(x,y)^{(l)} + \theta_g \left(\phi_{g,k}(x,y)^{(l+1/4)} - \phi_{g,k}(x,y)^{(l)} \right) \ . \tag{3.44}$$

Here, $\phi_{g,k}(x,y)^{(l)}$ is the scalar flux before the MOC sweep, $\phi_{g,k}(x,y)^{(l+1/4)}$ is the scalar flux calculated during the MOC sweep, and $\phi_{g,k}(x,y)^{(l+1/2)}$ is the flux after applying the relaxation.

These factors were necessary for the primitive 2D/1D methods that used finite difference to determine the axial TL and did not have an explicit 1D axial solution. The next incarnation, which is still sometimes used in MPACT, used the nodal expansion method with a two-node kernel to solve the axial problem. The two-node kernel has stability properties that are similar to the finite difference method, so relaxation factors are also required when a two-node kernel is used. However, the one-node kernels, which are used for this work, have fundamentally different convergence properties than the two-node kernels, and there are no theoretical results indicating that the same relaxation factors should be used, or that this type of relaxation is even necessary when using a one-node kernel. Relaxation factors are not used in this work.

3.2.4 2D/1D Methods

Several different variations of the 2D/1D method are included in the numerical results for this work. These variations are related to different options for treatment of the polar and azimuthal components of the TL and XS. Overall, the methods can be divided up into three distinct groups. These groups will be referred to frequently in the text, so we will now establish nomenclature for unambiguous identification.

1. The first method uses isotropic TL and XS. This is the standard 2D/1D method used in many 2D/1D codes, including MPACT. It is essentially the simplest possible 2D/1D approximation to make with respect to the coupling terms between the 2D and 1D equations. This method is referred to as "isotropic TL," "ISO TL," or "standard" 2D/1D.

2. The second method, which was described in this chapter, uses approximate anisotropic TL and XS. The TL dependence is expanded in Legendre polynomials in the polar angle and Fourier moments in the azimuthal angle. This will be called the "full anisotropic," "full-polar anisotropic" method, or "ANISO TL" for short. In this approximation, the XS may have polar dependence. It is typically isotropic in the azimuthal angle, although the azimuthal moments are included in some cases to demonstrate their insignificance. These different XS treatments are sometimes referred to in shorthand on charts and tables, as "ISOXS" for isotropic XS homogenization (standard), "POLXS" for polar dependent homogenization, and "MOMXS" for polar homogenization with non-anisotropic azimuthal moments included.

3. The third method, developed in Chapter 5, aims to replicate the accuracy of the full polar anisotropic method while reducing the cost by delegating some work from the MOC solver to a coarse-mesh 2D S$_N$ solution. Because this method uses polar parity, and adds an odd parity coarse-mesh 2D transport solution to the typical 2D/1D scheme, it is called "polar parity 2D/1D," "odd parity 2D/1D," or simply "parity TL." The MOC solution is only used for the even parity 2D angular flux, which means it is only solved for half of the polar angles on the unit sphere, in contrast to the "full-polar anisotropic" method, which solves for the 2D angular flux over the full unit sphere using MOC. The treatment of the azimuthal angle in the polar parity 2D/1D method is identical to the treatment in the full-polar anisotropic method.

3.3 Homogenization of XS for 1D Solution

It has been asserted that methods that do not require homogenization over the pin cell should and will be appreciably more accurate than those that do [67, 62, 68]. This is not necessarily true. In reality, there is nuance that cannot be summarized in such a simple statement. The method in this work demonstrates near 3D transport accuracy using a homogenized XS.

In addition to XS homogenization, approximations are also made to the axial shape and angular dependence of the radial transverse leakage source for the 1D equation. To avoid homogenization, the 1D problem must be solved on subregions of the pin. This means that the radial TL term, or whichever term couples the 2D solution to the 1D solution for a given method, must also be computed on this finer mesh. The magnitude of leakage between two adjacent regions within a pin cell (e.g., between moderator and fuel or control rod) will be significantly greater than that between two adjacent pins at their cell boundaries. As a result, any approximation made to the spatial or angular dependence of this radial coupling term will be magnified, which can result in large errors.

For this reason, it is unwise to solve the 1D problems on a sub-pin mesh unless the radial TL is represented explicitly in angle, which has a prohibitively expensive memory burden. This explains two previous results in which large errors due to the isotropic TL approximation were attributed to other causes when using a sub-pin mesh for the 1D solution. Those results will be restated and explained here.

In Kelley's Ph.D. thesis [63], a simple toy problem was considered with a finite 8x8 lattice of fuel pins. The radial geometry of the fuel pin is a Tetris-style Cartesian approximation to a cylinder, which allows the definition of a Cartesian coarse mesh without homogenization. The pin geometry is shown in Fig. 3.4. Two-group cross sections were used. This problem was solved in MPACT.

First, the standard discretization was used, with each pin cell being represented by a single coarse cell. Then, the coarse mesh was refined to be equivalent to the fine mesh, 0.125 cm squares, which eliminated homogenization of the XS. A large discrepancy between these two results (520 pcm difference in k_{eff}) was attributed to the homogenization and axial TL spatial shape error of the former case. However, the large error was actually a result of using the isotropic leakage approximation on the fine mesh, including at the fuel-moderator interface. The isotropic TL approximation is usually acceptable on coarse-mesh boundaries, but at the fuel-moderator interface it is not sufficient. This result was presented as a motivation for improving the spatial

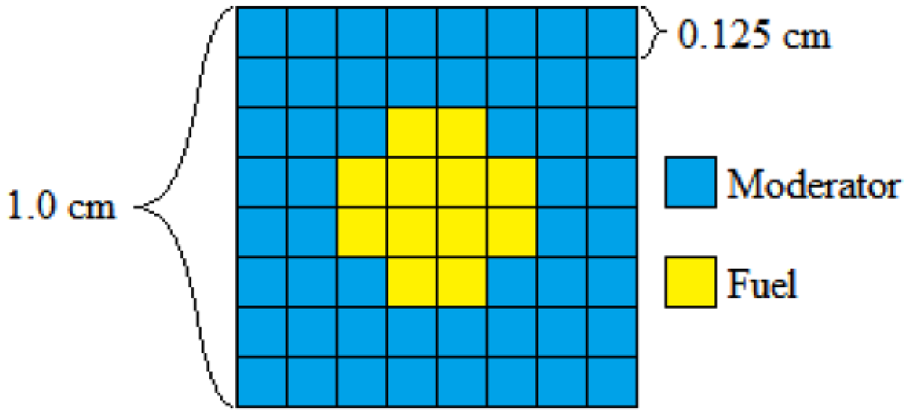

Figure 3.4: Pin cell for shape function test problem, from Kelley's thesis [63]

shape of the TL, when it was in reality a motivation for anisotropic TL and a strong reason to use the pin-level radial mesh for the 1D problem.

The study is reproduced for this work, with additional cases added using anisotropic TL. The results are given in Table 3.1.

Table 3.1: Eigenvalue results for axial TL shape test

Shape Function	TL Method	XS	k_{eff}	error [pcm]
FLAT	ISOTROPIC	ISOTROPIC	1.11465	26
FLUX	ISOTROPIC	ISOTROPIC	1.11459	20
EXACT	ISOTROPIC	EXACT	1.11138	-301
FLAT	EXACT	ISOTROPIC	1.11500	61
FLUX	EXACT	ISOTROPIC	1.11490	51
FLAT	MOMENT	POLAR	1.11450	11
FLUX	MOMENT	POLAR	1.11441	2
EXACT	MOMENT	EXACT	1.11438	-1
EXACT	EXACT	EXACT	1.11439	–

The first 3 lines in Table 3.1 are reflective of the results in [63]. Based on these results, the “flat” and “flux” shape functions are considered insufficient, because of poor agreement with the “exact” axial TL shape. However, the “flat” and “flux” cases are actually significantly closer to the reference solution. The reference solution here uses the exact shape function, with no spatial homogenization, and explicit angular TL treatment; this is effectively 3D transport. The actual error from using the “flat” spatial TL shape is approximately 10 pcm, while the polar dependence of the homogenized XS accounts for approximately 50 pcm.

In a recent paper, Yuk and Cho [68] assert that the 2D/1D fusion method has superior accuracy to the 2D/1D method with isotropic TL. It does, but the difference is vastly overstated in [68] because of their definition of the coarse mesh. To test the fusion and hybrid methodologies (i.e., anisotropic TL or isotropic TL), they use 1D/1D methods to solve a 2D transport problem. The 2D problem is a vertical 2D slice ($x - z$ cross sectional cut) from the rodded B configuration of the 3D C5G7 benchmark. The problem geometry is given in Fig. 3.5. They define the coarse mesh such that there is no heterogeneity within a coarse cell and thus no homogenization necessary for the 1D problem. The 1D/1D fusion method essentially matches the 2D transport reference, while the 1D/1D hybrid method has a large error of -927 pcm for k$_{eff}$ and several percent errors in the flux.

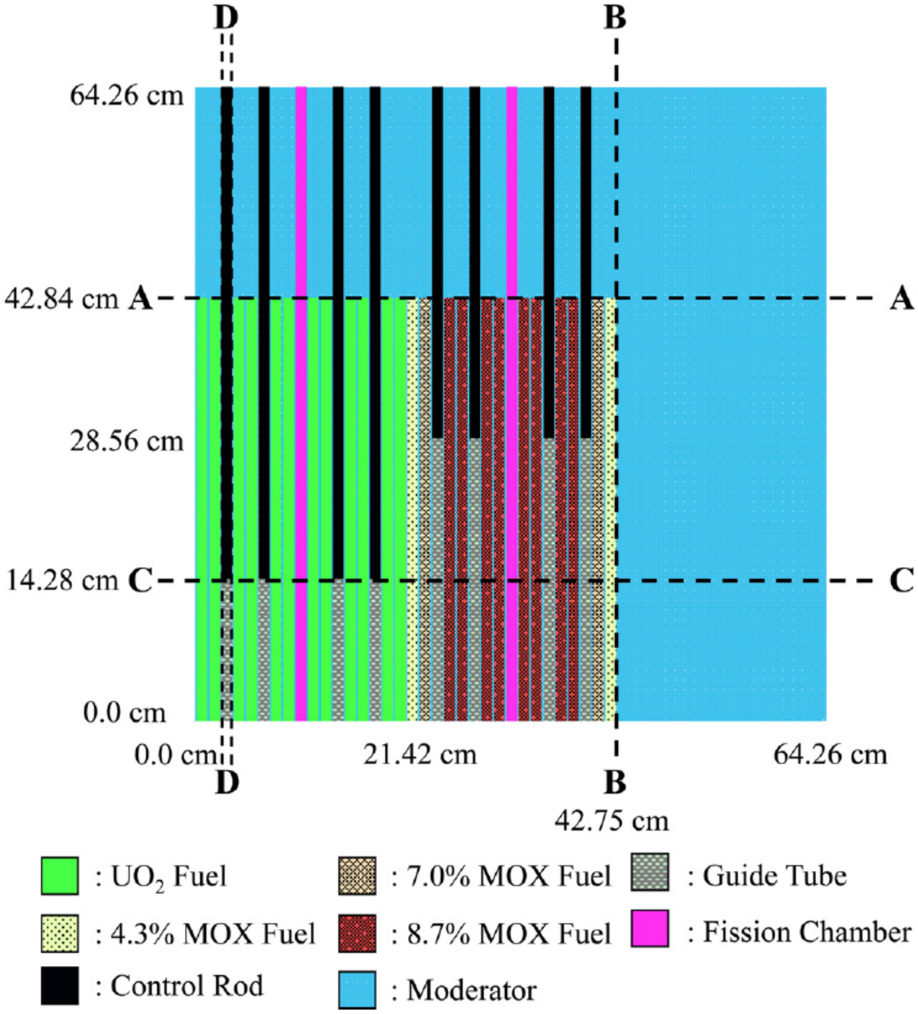

Figure 3.5: Geometry of 1D/1D test problem, Yuk and Cho [68]

The error is this large because the chosen coarse mesh is the worst possible coarse mesh when using isotropic TL. It is the worst mesh because it maximizes the magnitude of the radial TL. The method analyzed in [68] is fundamentally different from the

2D/1D method used in real calculations, in which coarse-mesh boundaries are always aligned with pin-cell boundaries. This explains why, in [68], “results for the hybrid method are in contrast to those of previous studies [13][17].” They go on to speculate that these results contradict previous studies “probably due to the cancellation of errors” between the isotropic TL approximation and the spatial XS homogenization. The placement of the coarse-mesh boundaries at the fuel-moderator interface instead of the pin-cell interface, which is the true cause of this error, is not mentioned in [68]. Additionally, the hybrid method in [68] uses diffusion axially, even though current hybrid codes such as MPACT use P_3 in the axial direction. This incorrect conclusion is important to note because the “hybrid” method with spatial XS homogenization continues to be the production solver used by MPACT, and it is not nearly as inaccurate as suggested by these results.

To summarize the results of this section, the nature of the coupling between the 2D and 1D solutions is complicated and can even be counter-intuitive. In attempting to highlight certain predicted errors in the 2D/1D method, some researchers developed test problems without taking into full consideration the types of errors that may be exacerbated by the specific problems chosen for the studies in [63, 68]. This has resulted in incorrect conclusions about the true magnitude of errors due to various approximations in a 2D/1D method. While the studies in [63] and [68] have concluded that spatial homogenization of the cross section or smearing of the axial TL results in a severe error that needs to be corrected, the errors attributed to homogenization were actually manufactured by moving the coarse-mesh boundaries from their usual location. The standard coarse-mesh boundary for a 2D/1D problem is and always has been the Cartesian pin mesh lattice. This was almost certainly done out of convenience and simplicity. A Cartesian mesh is significantly easier to deal with, and it makes sense for the 1D problem mesh to align with the 3D CMFD mesh. It is perhaps pure luck that the coarse mesh that is most convenient is also the most optimal mesh for *accuracy* of the 2D/1D solution. This is the reason isotropic TL can be used, and is probably a big reason why the 2D/1D method even works well at all, but it is something that has not been explicitly acknowledged by the community. It does not seem to be common knowledge, or even commonly accepted, that the pin-cell coarse mesh maximizes accuracy when using isotropic TL.

When placing coarse-mesh boundaries on the pin-cell surface, one must remember that this inherently applies an approximation to the angular flux gradient at the surface, which is likely large in magnitude and strongly anisotropic. The leakage is stronger on the pin surface because there are significant differences in the spectrum and magnitude of the source in the moderator and the fuel. In effect, this negates the high-fidelity MOC and instead puts faith into the radial TL approximation, which is usually isotropic. Even when using anisotropic moments for the radial TL, it likely require many more moments to accurately represent the leakage on a pin surface than the P_1 or P_2 expansion that is sufficient on the pin-cell boundaries.

In addition to the angular approximation made to the radial TL, the spatial dependence of the radial TL is also approximated. The three-point interpolation method used to calculate quadratic spatial dependence of the radial TL is typically sufficient. However, the scattering and fission sources are determined by the flux moments, which are more accurately calculated by the 1D transport solver, with a quartic polynomial expansion. When a larger fraction of the source is radial TL, the spatial accuracy of the source, and the overall 1D solution, may be degraded.

3.4 2D/1D Summary

This chapter mathematically described the 2D/1D equations used in MPACT in detail. The standard 2D/1D method used in MPACT makes several approximations to the axial and radial TL and 1D homogenized XS that lead to reduced accuracy. In this chapter, several possible improvements to these approximations were proposed. Some of these improvements were pursued in previous work, including the anisotropic axial and radial TL [8]. While anisotropic 1D XS homogenization has also been considered in previous work [69], the specific 1D XS homogenization proposed in this chapter is new. In this thesis, the anisotropy of the homogenized 1D XS is split into polar and azimuthal dependence. We have observed empirically that the azimuthal dependence is weak, so we choose to use a homogenized XS with only polar dependence (azimuthally isotropic). This method is memory-efficient and effective in improving the accuracy of the 2D/1D solution.

Additionally, the method in [8] is applied to 2D/1D with a 1D P_3 axial solution in this thesis, instead of 1D S_N. This application is new, and we have observed that the 2D/1D P_3 method with anisotropic TL is less prone to instability than its 2D/1D S_N counterpart.

Chapter 4: Numerical Results

The methods described in Section 3.1 were implemented in MPACT. A progression of several test cases are used to demonstrate the accuracy of these methods:

1. A simplified 1D/1D S_N problem that demonstrates the accuracy of the angle-dependent XS homogenization in Sec. 4.1.
2. A 3D pin cell problem that isolates the angle-dependent XS effect in the absence of radial TL in Sec. 4.2.
3. A homogeneous fuel problem that demonstrates the anisotropic TL capability without homogenization error. Essentially, this confirms that the new 2D/1D P_3 method effectively reproduces the results of the 2D/1D S_N method from Stimpson's thesis [8], upon which it was based. (Sec. 4.3.
4. A simple 3x3 pin array is used to demonstrate the relative unimportance of the spatial TL shape and the azimuthal XS moments in Sec. 4.5.
5. The 3D C5G7 benchmark problem shows the accuracy of these methods for a difficult problem with 3D transport effects in Sec. 4.6.
6. VERA benchmark problem 4 is used to demonstrate these effects for a problem with realistic geometry and XS in Sec. 4.7.

The simple problems are used to isolate and demonstrate specific aspects of the improved 2D/1D method. The 3D C5G7 benchmark demonstrates all of these capabilities simultaneously.

4.1 1D/1D S_N Demonstration

In this section, a 1D version of a typical LWR pin cell with C5G7 cross sections [29] is analyzed. Additional results for other LWR transport problems (MOX fuel, control cell, fuel assembly slice) are given in Appendix A. These problems test the angle-dependent homogenization methods and verify that the angular flux is preserved between the radial transport (S_N in this case) and the transverse 1D problem.

Before applying the angle-dependent homogenization to MPACT, a simple problem is used in this section to confirm that it has the properties it was intended to have when it was derived; specifically, the transverse 1D problem with a pin-homogenized total XS should exactly preserve the angular flux from the original heterogeneous transport problem. A low-enriched UO_2 pin is analyzed in this section. In each case, the anisotropy in the spatial dependence of the angular flux is a significant effect that is not correctly captured by an isotropic XS. The magnitude of this effect will be greater when there are more pronounced flux dips, e.g. MOX fuel pin, or the control cell in the appendix. C5G7 cross sections are used for these problems [29].

4.1.1 1D/1D S_N Equations

S_N is used for the radial and the axial equations in this section. The radial transport is a standard 1D S_N sweep with weighted-difference discretization:

$$\frac{\mu_n}{h_i}\left(\psi^{(l+1/2)}_{n,g,i+1/2} - \psi^{(l+1/2)}_{n,g,i-1/2}\right) + \Sigma_{t,g,i}\psi^{(l+1/2)}_{n,g,i} = \frac{1}{2}\left(\sum_{g'}\Sigma_{s,g\leftarrow g',i}\phi^{(l)}_{g',i} + \frac{\chi_{g,i}}{k_{eff}}\sum_{g'}\nu\Sigma_{f,g',i}\phi^{(l)}_{g',i}\right) , \tag{4.1a}$$

$$\psi^{(l+1/2)}_{n,g,i} = \frac{1+\beta_{n,g,i}}{2}\psi^{(l+1/2)}_{n,g,i+1/2} + \frac{1-\beta_{n,g,i}}{2}\psi^{(l+1/2)}_{n,g,i-1/2} , \tag{4.1b}$$

$$1 \le n \le N, 1 \le i \le I ,$$

$$\phi^{(l+1)}_{g,i} = \sum_n w_n \psi^{(l+1/2)}_{n,g,i} . \tag{4.1c}$$

The closure relationship defined by $\beta_{n,g,i}$ is a weighted difference, which can be diamond difference ($\beta_{n,g,i} = 0$), step characteristics, or something else. The weighting has little significance. The mesh will be very fine, so $\beta_{n,g,i}$ should be very small. For these problems, reflective conditions are used on the east and west boundaries:

$$\psi_{n,g,1/2} = \psi_{n',g,1/2} , \tag{4.2a}$$

$$\psi_{n,g,I+1/2} = \psi_{n',g,I+1/2} . \tag{4.2b}$$

where n' is the reflection of the angle n, i.e. $\mu_n = -\mu_{n'}$.

Upon convergence of the fine-mesh radial S_N, the scalar flux and XS are homogenized onto the coarse mesh for transverse 1D S_N. The standard XS homogenization is defined by Eq. (4.3).

$$\hat{\Sigma}_{p,g,k} = \frac{\sum\limits_{i \in k} \phi_{g,i} V_i \Sigma_{p,g,i}}{\sum\limits_{i \in k} \phi_{g,i} V_i} \tag{4.3}$$

This homogenization preserves the volume-averaged reaction rate for a given reaction p:

$$\hat{\Sigma}_{p,g,k} \Phi_{g,k} = \frac{\sum\limits_{i \in k} \phi_{g,i} V_i \Sigma_{p,g,i}}{\sum\limits_{i \in k} \phi_{g,i} V_i} \frac{\sum\limits_{i \in k} \phi_{g,i} V_i}{\sum\limits_{i \in k} V_i} = \frac{\sum\limits_{i \in k} \phi_{g,i} V_i \Sigma_{p,g,i}}{\sum\limits_{i \in k} V_i} . \tag{4.4}$$

Alternatively, the total XS can be homogenized with the angular flux, Eq. (4.5), while the other reactions still use Eq. (4.3).

$$\hat{\Sigma}_{t,n,g,k} = \frac{\sum\limits_{i \in k} \psi_{n,g,i} V_i \Sigma_{t,g,i}}{\sum\limits_{i \in k} \psi_{n,g,i} V_i} \tag{4.5}$$

This is the polar angle-dependent XS homogeniziation described in Section 3.1.4.

This homogenized total XS is then used in a transverse 1D S_N solution. For a radial problem with J pins, there are J transverse problems, each being a single cell with reflective boundaries on both ends (top and bottom). The transverse 1D angular flux is then compared to the cell-averaged angular flux from the fine-mesh radial problem.

4.1.2 1D LWR Results

The 1D fuel pin geometry roughly preserves the fuel-moderator ratio from the 2D C5G7 cases (0.54 cm fuel radius in 1.26 cm pin pitch lattice = 57.7% fuel) in a 1D slab geometry. The test problem is a 1.5 cm 1D pin cell with a 0.9 cm fuel region in the center; the fuel fraction is 60%. A simple diagram is given in Fig. 4.1a. A cartoon of the 4 quadrature angles is given in Fig. 4.1b. An S_8 Gauss quadrature is used, with 4 polar angles in each direction (right and left). The angular fluxes of the symmetric angles (μ_n and $\mu_{n'}$, same magnitude polar cosine but opposite right/left direction) are summed so that the angular fluxes are symmetric in space over the symmetric problems.

The angular fluxes in groups 1, 4, 6, and 7 for a UO2 pin cell are given in Fig. 4.2.

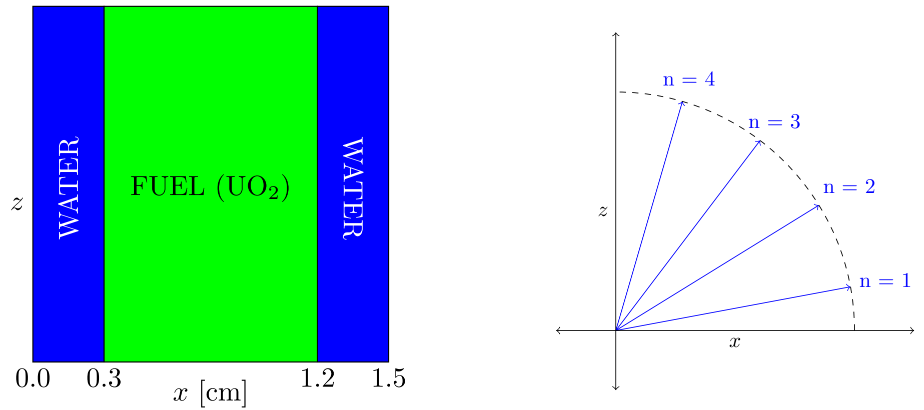

(a) Pin cell geometry for 1D pin

(b) Gauss quadrature angles

Figure 4.1: Pin cell geometry and quadrature angles for 1D S_N

Clearly, the anisotropy effect is strongest for the thermal groups. The relative errors in the transverse 1D angular fluxes are given in Tables 4.1 and 4.2. The "total" error is the integral of the error, calculated by using the quadrature rule.

Table 4.1: Transverse 1D angular flux error, UO2 pin, scalar flux homogenization

	Group 1	**Group 2**	**Group 3**	**Group 4**	**Group 5**	**Group 6**	**Group 7**
Angle 1	-0.04%	0.12%	-0.07%	-0.07%	-0.33%	-1.92%	-6.60%
Angle 2	-0.04%	0.11%	-0.06%	-0.06%	-0.31%	-1.78%	-5.84%
Angle 3	-0.03%	0.09%	-0.05%	-0.04%	-0.24%	-1.24%	-3.16%
Angle 4	0.06%	-0.18%	0.10%	0.09%	0.49%	2.83%	9.41%
Total	0.01%	-0.03%	0.02%	0.01%	0.08%	0.44%	1.50%

Table 4.2: Transverse 1D angular flux error, UO2 pin, angular flux homogenization

	Group 1	**Group 2**	**Group 3**	**Group 4**	**Group 5**	**Group 6**	**Group 7**
Angle 1	-7.7E-09	-1.1E-09	8.0E-12	8.2E-12	1.0E-11	2.3E-10	6.1E-10
Angle 2	-7.7E-09	-1.1E-09	8.0E-12	8.2E-12	1.0E-11	2.3E-10	6.1E-10
Angle 3	-7.8E-09	-1.1E-09	8.0E-12	8.2E-12	1.0E-11	2.3E-10	6.1E-10
Angle 4	-7.8E-09	-1.1E-09	8.0E-12	8.2E-12	1.0E-11	2.3E-10	6.1E-10
Total	-7.8E-09	-1.1E-09	1.1E-11	1.2E-11	1.6E-11	2.8E-10	6.9E-10

The angular flux homogenization exactly reproduces the group-wise angular flux distribution from the original 1D S_N solution. The scalar flux homogenization has small but non-negligible errors in the thermal groups. There is some cancellation between the errors at different angles. Despite a maximum error in group 7, angle 4

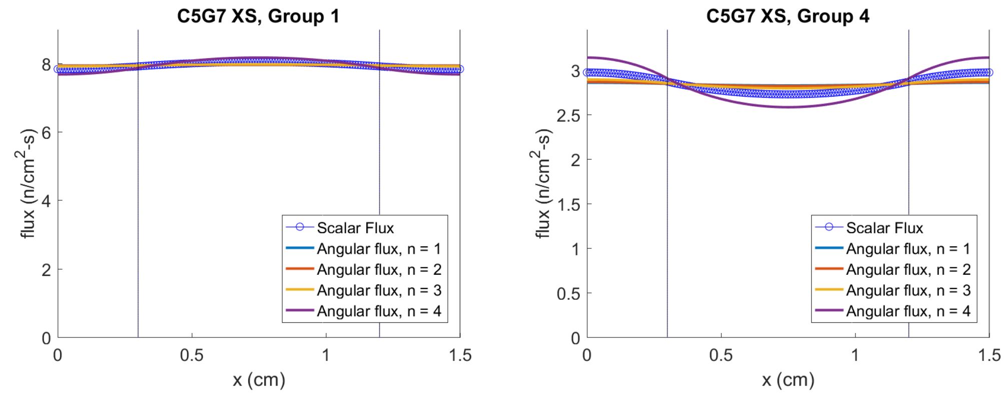

(a) Group 1 (b) Group 4

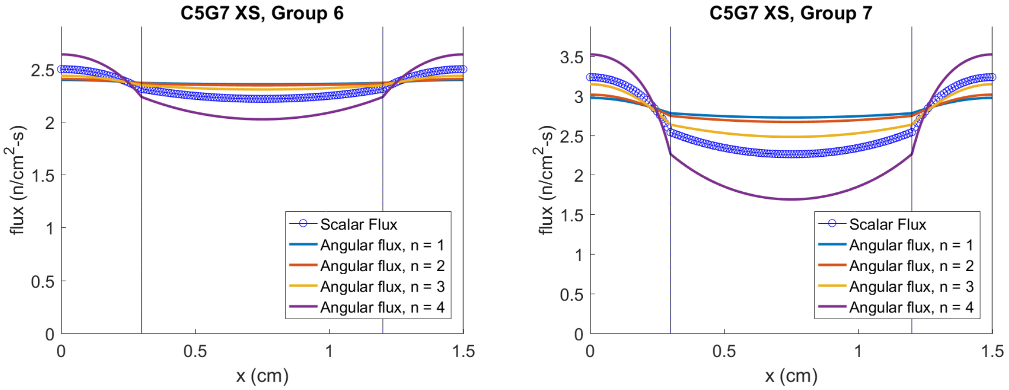

(c) Group 6 (d) Group 7

Figure 4.2: C5G7 UO2 pin cell group angular fluxes

(steepest polar angle) of over 9%, the total error in the partial current for group 7 is only 1.5%.

The results in this section confirm that the angle-dependent XS homogenization correctly preserves the angular flux distribution from the orthogonal transport solution. This improves the coupling between the two orthogonal transport solutions because more physics are passed from the radial transport solve to the axial transport solve.

The anisotropic XS homogenization method works equally well for more complicated problems, which introduce non-zero radial TL to the transverse 1D S$_N$ equation. Results for these more complicated cases are given in Appendix A.

4.2 C5G7 Pin Cell

The single fuel pin cell is a simple 3D transport problem that can demonstrate the errors resulting from approximations to the axial solver, such as the incorrect total

XS homogenization or a spatially flat axial TL. This problem is useful to isolate this error, because there is no radial TL, and thus no confounding effects due to the radial TL approximation.

The problem configuration is a single UO_2 fuel pin cell with reflective boundaries on all lateral surfaces and vacuum boundaries on the top and bottom. This is effectively a radially infinite lattice with a finite height. The significance of the axial streaming term can be changed by making the pin shorter or longer, effectively modifying the axial buckling. If the pin is long enough, leakage has a negligible effect, and the solution is more or less the same regardless of which homogenization or leakage shape is used. As the pin becomes shorter, the leakage increases and the choice of approximation becomes important.

To evaluate the different methods, the eigenvalues are compared to a 3D multi-group Monte Carlo reference solution generated using OpenMC [38]. Each case was run using 3×10^3 inactive and 1.2×10^4 active cycles, with 2×10^4 particles per cycle (total active particles $= 2.4 \times 10^8$). In MPACT, a relatively fine discretization was used, with 1.0 cm thick axial MOC planes, 144 FSRs (9 radial × 16 azimuthal), 0.01 cm ray spacing, and a Chebyshev-Gauss quadrature with 16 azimuthal and 8 polar angles per octant. The 2D/1D method used here employs 1D S_N, not 1D P_3.

The results are shown in Fig. 4.3. The uncertainty is 5 pcm or lower in each case; this is not shown in the figure because it would be difficult to see on the necessary scale. "ISO XS" refers to isotropic total XS in 1D, i.e., scalar flux homogenization, Eq. (3.18). "POLAR XS" refers to polar angular flux weighted XS, Eq. (3.23), and "SCALAR TL" refers to scalar flux-weighted axial TL leakage, Eq. (3.28). When the

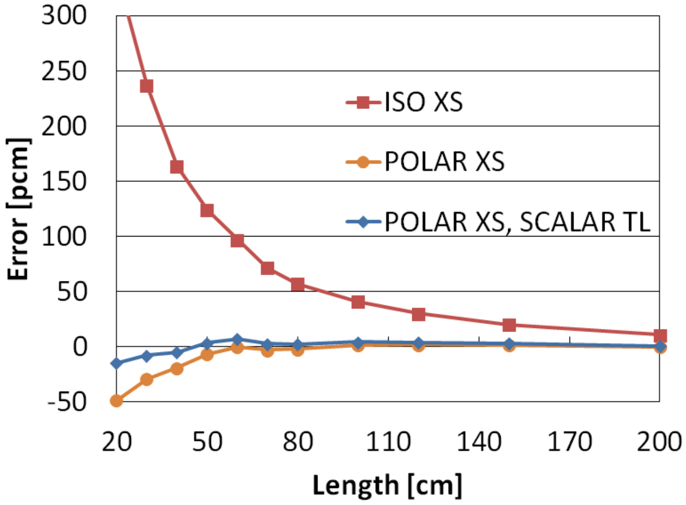

Figure 4.3: 3D UO_2 pin cell results

pin is very long, the two types of homogenization converge to the same, correct result. For shorter lengths (higher leakages), scalar flux homogenization has a large error, which is corrected by polar angle homogenization. The polar angle homogenization case is within two standard deviations of the Monte Carlo eigenvalue for all pins 50 cm or greater in length, with or without scalar flux-weighted axial TL. For pins below this length, scalar flux-weighting of the TL appears to improve the eigenvalue, keeping it within two standard deviations down to 30 cm. However, it is worth noting that the effect of polar homogenization is more than 10 times greater than the effect of scalar flux-weighted TL.

Angular flux-weighted TL, which should be slightly better than scalar flux weighting, was implemented and attempted. However, it was ultimately not used here, or anywhere in this work, because it caused instability from a negative total source in nearly every case. When weighting the axial TL in both space and angle, the localized axial TL (in space and angle) may be several times greater than the average axial TL. Due to this high peaking factor, the 2D MOC source is much more likely to be negative.

From the results in Fig. 4.3, it appears that whatever error there may be from ignoring the azimuthal dependence in the homogenization step is negligible. This is not a surprise because azimuthal dependence should not be especially important in an infinite lattice problem. The polar-dependent homogenization gives an eigenvalue within uncertainty over a large range of pin heights, indicating that it is an important effect, which is greater in magnitude than the effect of neglecting the azimuthal angle.

The trend in Fig. 4.3 is more important than the actual magnitude of the errors. Obviously, LWR cores are not actually 20 cm tall, so 300 pcm errors due to homogenization do not exist in real problems. However, this study highlights a critical defect in scalar flux homogenization that is present wherever axial streaming is significant. This effect is still present in very tall LWR cores, albeit on a smaller scale. Some instances where this effect is more apparent include heterogeneities such as a partially-inserted control rod and part-length fuel rods in BWRs. A simple example of the partially inserted control rod is analyzed in Sec. 4.4.

4.3 Homogeneous Fuel Test Problem

The homogeneous fuel test problem is a simple problem designed to expose the fundamental deficiency in the isotropic TL approximation used by many 2D/1D codes. The problem uses 2 group fuel and reflector XS from the Takeda benchmark [31].

The geometry is given in Fig. 4.4. It is a 2D problem, with a 25 cm x 25 cm block of fuel surrounded by 5 cm of reflector on two sides. The other two sides have reflecting boundary conditions. In MPACT, this is solved using the 2D/1D method, with the MOC solver in the x direction and the 1D axial solver in the z direction. The reference solution is obtained by solving the 2D problem using 2D MOC. The problem is discretized into 1 cm square coarse cells, with a 0.5 mm fine-mesh cell size (i.e., flat source region size) in the x direction. The convergence criteria is 10^{-6} for both the eigenvalue and fission source two-norm. Table 4.3 shows the eigenvalue, root-mean-square (RMS), and maximum "pin" power error for this problem using each TL method. The 2D X-Z case is the full problem, while the 1D Z case is just a 1D vertical slice of the problem solved using the specified 1D method. There is some error caused by the deficiency of the 1D P_3 solver as compared to a higher order angular approximation. This is shown by the reduction in error when using 1D S_8 with anisotropic TL compared to using P_3 with anisotropic TL. The P_3 axial solver has accuracy equivalent to S_4. However, the significant reduction in error when changing the isotropic TL approximation to anisotropic TL is the most interesting result. The eigenvalue error decreases from -156 pcm to +9 pcm, and the RMS and maximum pin power errors are both decreased by more than a factor of 2. The pin power errors using each method are shown in Figs. 4.5a, 4.5b, and 4.5c. There is a clear improvement in the power shape when using the anisotropic TL method. With anisotropic TL, the "1D/1D" P_3 method is very close to the 2D transport reference. The only

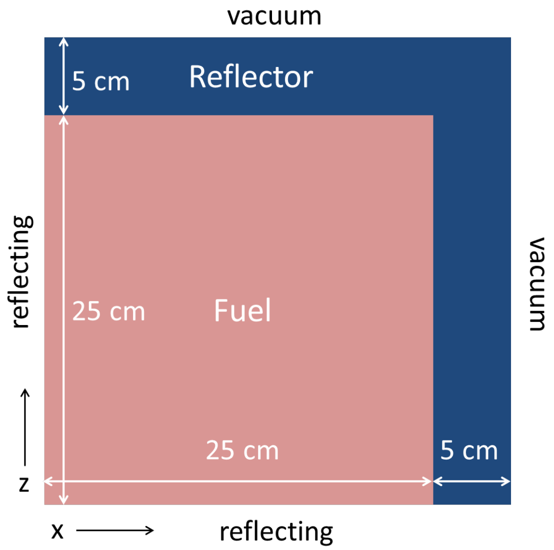

Figure 4.4: Geometry of homogeneous fuel test case

Table 4.3: Eigenvalue error and pin power errors for 1D Z, 2D X-Z problem

1D Method / TL	P_1 ISO TL	P_3 ISO TL	P_3 ANISO TL	S_8 ANISO TL
1D Z k_{eff} [pcm]	-372	-5	-5	-2
2D X-Z k_{eff} [pcm]	-454	-156	+9	+4
2D RMS error (%)	1.04	0.30	0.13	0.01
2D max error (%)	4.85	1.31	0.46	0.21

significant error occurs at the axial interface between the fuel and reflector, which is difficult for the 1D P_3 to resolve. Using the 1D S_N method with S_8 quadrature is sufficient to resolve virtually all error.

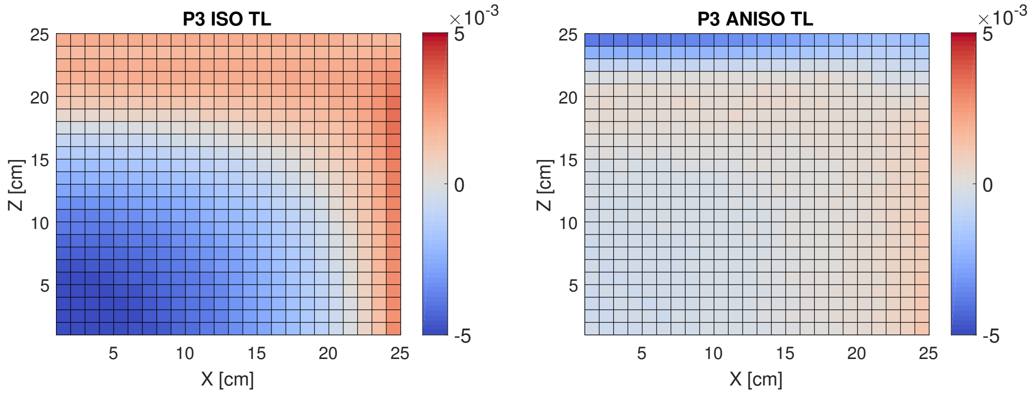

(a) P_3 with isotropic TL

(b) P_3 with anisotropic TL

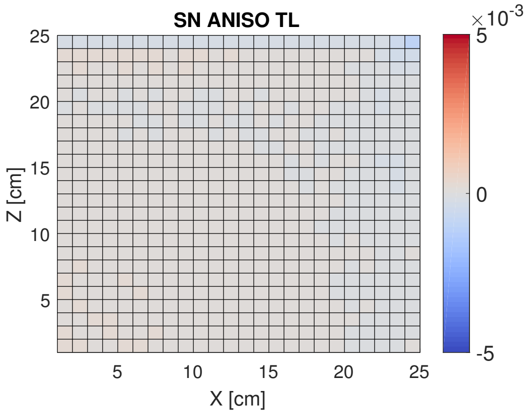

(c) S_8 with anisotropic TL

Figure 4.5: 2D homogeneous fuel, power error

4.4 3x3 Partially Rodded Lattice

The 3x3 array problem is one of the smallest problems that can be used to demonstrate aspects of the 2D/1D method accuracy that are relevant for larger assembly and full core problems. The results in this section use the 2D/1D S_N method, not the newer 2D/1D P_3 method. However, the results would be similar with the P_3 method.

The 3x3 partially-rodded lattice problem is a square of UO_2 fuel pins with a guide tube in the center position. The axial length is equivalent to the 3D C5G7 benchmark (42.84 cm of fuel, 21.42 cm of moderator). The control rod is inserted from the top to the halfway point of the fuel (21.42 cm from the bottom). All lateral boundaries and the bottom are reflective; the top boundary is vacuum. The radial geometry is shown in Fig. 4.6.

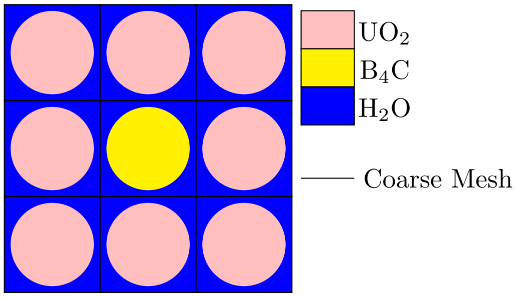

Figure 4.6: 3x3 radial geometry

4.4.1 2D X-Z Slice

Before analyzing the full 3D problem, a 2D problem is used to assess whether the polar-dependent homogenization performance is satisfactory.

By taking a 2D X-Z slice through the middle of this problem, a 2D, Cartesian geometry with similar transport effects to the 3D problem is obtained. The geometry can be treated explicitly with the coarse mesh in MPACT because it is Cartesian; this allows MPACT to solve the 1D problems without any homogenization of the XS. This enables an evaluation of the angle-dependent homogenization in a straight-forward manner, and a comparison between this method and the sub-pin 1D solution method. A 2D MOC reference solution can be obtained because the problem is now 2D, shown in Fig. 4.8. Fig. 4.8 has been scaled by factor of two in the x direction to improve the aspect ratio. These results can be compared to the result when using 2D/1D as a 1D/1D solver (MOC radially across, 1D solver axially). There is considerable freedom

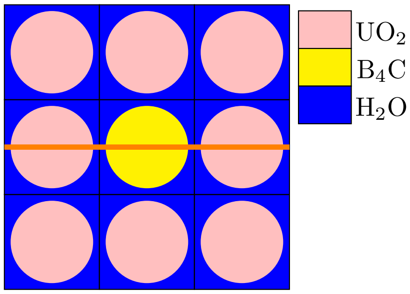

Figure 4.7: 3x3 pin cell X-Y

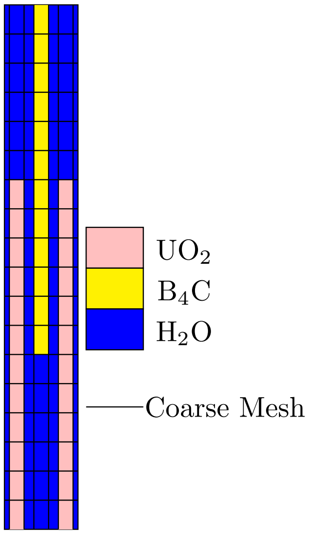

Figure 4.8: 2D Cartesian geometry

in defining the coarse mesh for MPACT because the geometry is completely Cartesian. Each 1D pin cell can be a coarse-mesh region (like standard 2D/1D MPACT), or multiple coarse regions can be defined within the pin cell, separated into moderator and fuel, as shown in Fig. 4.8. In the latter case, no homogenization of the XS is necessary, so it will directly show the difference between using improved homogenization or altogether eliminating the need for homogenization.

In Fig. 4.9 and 4.10, virtually all of the eigenvalue error in the “standard” (ISO XS) case is corrected by the polar dependent XS, and the refined coarse mesh (2 REG) makes essentially the same correction with little difference. “SCALAR TL” indicates that the axial TL was applied with the spatial shape of the scalar flux. The effect of this shape on the solution is small. The reference solution is 2D MOC.

There are some differences in the pin power errors, but in both cases (polar XS and two region) the errors themselves are negligibly small (on the order of 0.1%). Figs. 4.11 and Fig. 4.12 show the 1D axial power profile error for the rodded and unrodded cases, respectively. The dotted line in Fig. 4.11 indicates the position of the control rod tip. Only the isotropic XS case has appreciable error; the polar dependent XS on its own is enough to correct the effect of the pin-cell heterogeneity.

4.4.2 3D Partially Rodded 3x3 Lattice

The results from the previous section provide some confidence that the angle-dependent homogenization will improve the transport accuracy of 2D/1D for 3D

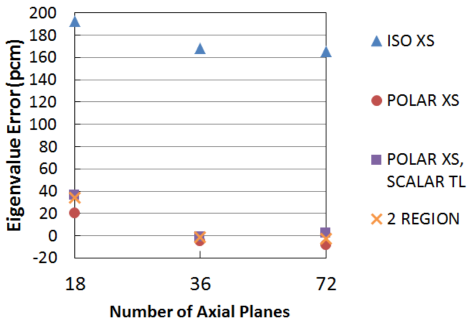

Figure 4.9: 2D control cell eigenvalue error, 7 groups

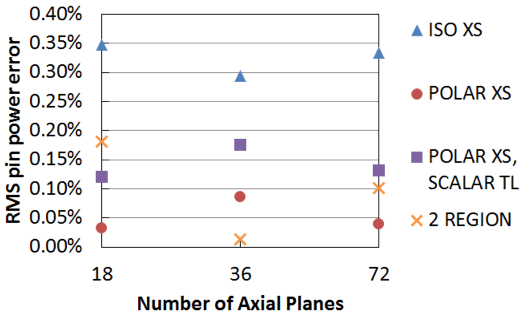

Figure 4.10: 2D control cell pin power error, 7 groups

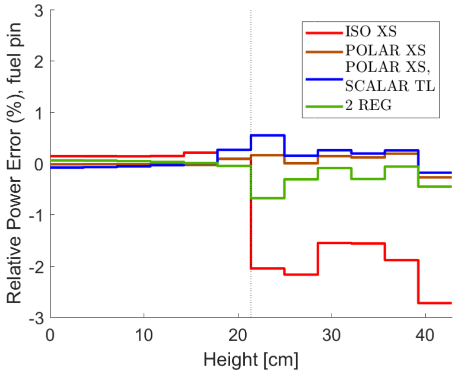

Figure 4.11: 2D control cell rodded, axial pin power error

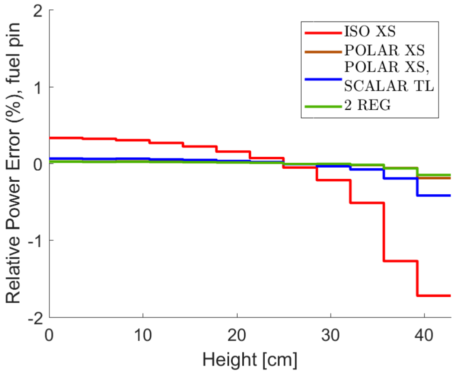

Figure 4.12: 2D control cell unrodded, axial pin power error

transport problems. Also, the results suggest that improving the homogenization is sufficient to correct most of the error in the 2D/1D solution. In this section, the method is applied for the full 3D version of the 3x3 partially rodded array of pins.

The reference solution was again generated with OpenMC [38], using 2×10^4 particles per cycle, 5×10^3 inactive and 2×10^4 active cycles (total active particles = 4×10^8).

The radial discretization is the same as in the single pin cell problem, but the number of polar angles has been reduced from 8 per octant to 4, which is more typical of a practical case. To demonstrate that results are not confounded by discretization error, the number of Fourier moments in the radial TL and axial angular flux expansion is increased from 0 to 3, and then the number of axial planes is increased from 18 to 72. These results show that the effect of refinement (both azimuthally and axially) are small relative to the effect of the polar-dependent XS. The effect of the spatial shape of the axial TL is small incomparison.

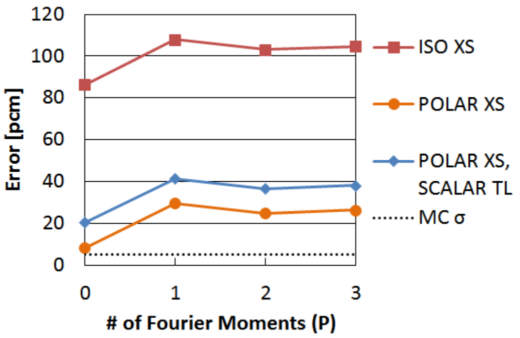

Figure 4.13: Eigenvalue error for 3x3 problem, azimuthal refinement

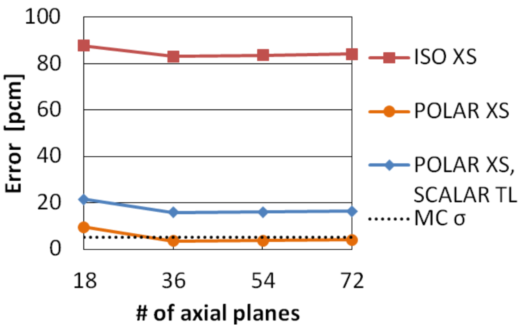

Figure 4.14: Eigenvalue error for 3x3 problem, axial refinement

In Fig. 4.13 the eigenvalue is converged at $P = 2$ (isotropic, two sine, and two cosine moments). The number of azimuthal moments is set at $P = 2$ and then the spatial discretization is refined axially from 18 to 72 planes in Fig. 4.14. The eigenvalue appears to converge very quickly, and excessive refinement is not necessary to achieve convergence. The solution is close to the Monte Carlo reference when using the improved 1D XS.

There is a trend in these plots similar to what was observed for the pin cell problem: the eigenvalue error is significantly reduced when using polar homogenization, and the effect of the axial TL shape is about one order of magnitude *smaller* than the effect of polar homogenization.

Next, the power errors with angle refinement are shown in Fig. 4.15a and axial refinement in Fig. 4.15b. The max errors are connected by solid lines, the RMS errors by dotted lines. Again, the polar homogenization reduces the error significantly, while the effect of the axial TL spatial shape is small. One noteworthy observation is that both the eigenvalue and the pin power are more accurate in the least refined case ($P = 0$, 3.57 cm planes) using polar homogenization than in the most refined case ($P = 2$, 0.8925 cm planes) using scalar flux homogenization.

In Fig. 4.15a the number of azimuthal moments used in the TL leakage and 1D angular flux expansion has a small effect on the pin power. This is because the azimuthal moments help resolve radial transport effects, but the main error in this case is caused by an axial transport effect (the partially-inserted control rod). Increasing the number of azimuthal moments does not help 2D/1D resolve the axial transport boundary without polar XS homogenization.

Next, the errors for the side pin in the array (the direct neighbor of the control rod) are compared for different methods in Fig. 4.16a. At 21.42 cm, which is the location of the tip of the control rod, there is a large error when using scalar flux

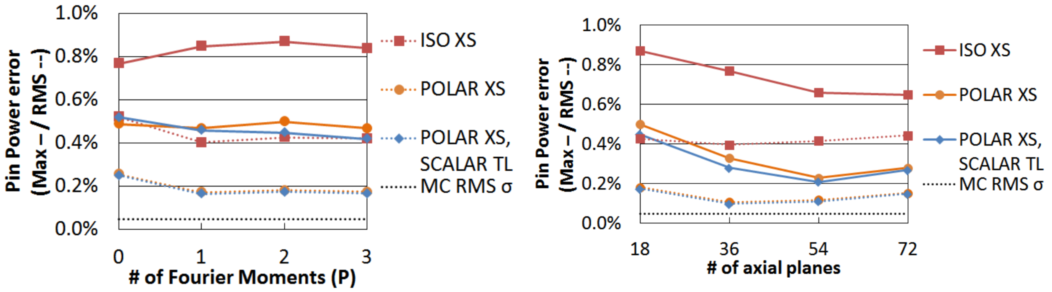

(a) Azimuthal fefinement

(b) Axial refinement

Figure 4.15: Pin power error for 3x3

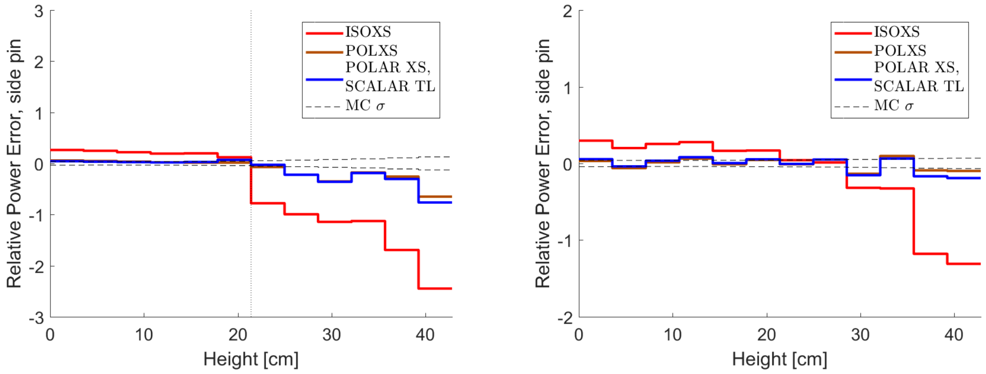

(a) Rodded

(b) Unrodded

Figure 4.16: Side pin power error, 3x3

homogenization. This shows that the isotropic XS method does not capture the flux change axially from the rodded to the unrodded region. This is a strong axial heterogeneity, and the self-shielding in both the control rod and the fuel pins is important here. With polar angle homogenization, the pin power error at the control rod tip is substantially smaller. With the axial TL spatial shape, the change in the pin power profile is not significant. If the axial planes could be refined indefinitely, the 2D/1D pin power should eventually converge to the 3D transport solution with polar angle homogenization. Conversely, an error exists at the control rod tip when using scalar flux homogenization that will not be corrected with refinement.

In Fig. 4.16b, the error is distributed over the whole length of the problem because there is not a sharp heterogeneity at the control rod tip. Here, the control rod is withdrawn, so the strongest heterogeneity is the fuel-moderator boundary at the top.

4.5 Azimuthal Cross Section Moments

In Sec. 3.1.4, a more accurate method for calculating homogenized XS over a pin cell for the 1D solution was derived. A Fourier expansion was used to avoid storing the full azimuthal dependent angular flux, with the assumption that the azimuthal moments are small. Additionally, it was asserted that all moments above the isotropic moment are small enough in practice to ignore them completely. Here, the simple 3x3 problem from Sec. 4.4 is used to verify these assumptions. The problem is solved using 2D/1D P_3 with anisotropic TL and XS.

The test case geometry is the same; the radial geometry is shown in Fig. 4.6. The center pin is a control rod, and the other 8 pins are UO_2 fuel. This problem is small, so there are strong axial and radial gradients caused by the heterogeneity of fuel-moderator and control rod-moderator interfaces, and the relatively high axial buckling. Because of these heterogeneities, there should be relatively large non-isotropic moments of the flux.

First, we plot the angular dependence of the leakage, flux, and XS to demonstrate the relative magnitude of the azimuthal dependence. The solution used for these plots was obtained with no approximation to the TL or homogenized 1D XS. Explicit angular representation of both the polar and azimuthal angle is used for the TL and XS.

The azimuthal dependence for the fastest neutrons (group 1) is shown in Figs. 4.17, 4.18, and 4.19. The values in the plane immediately below the fuel-moderator axial boundary (plane 12) are shown. The plots are arranged like the pins in the actual model, with the control rod in the middle. The dependence in the control rod is magnified. The first two plots show the azimuthal distribution of the axial TL and the angular flux for just one polar angle (the shallowest), averaged spatially over each pin. The homogenized cross section is shown for the 4 polar angles in the positive half of the unit sphere ($\mu > 0$) in Fig. 4.19, with each color corresponding to a different polar angle. As expected, the angular flux has significant azimuthal anisotropy.

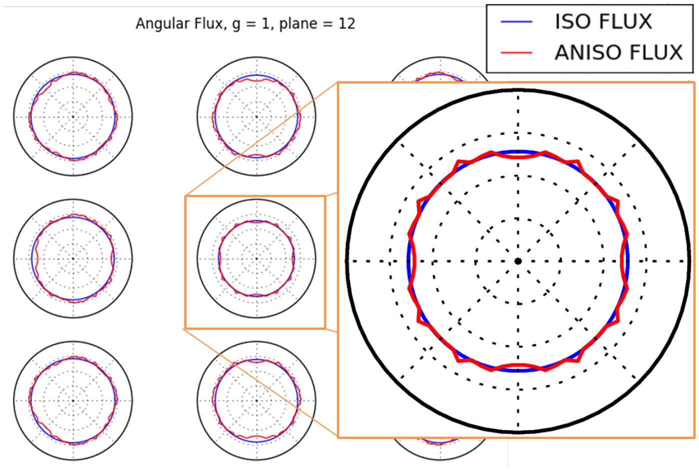

Figure 4.17: Axial TL, fast group, top of fuel rods

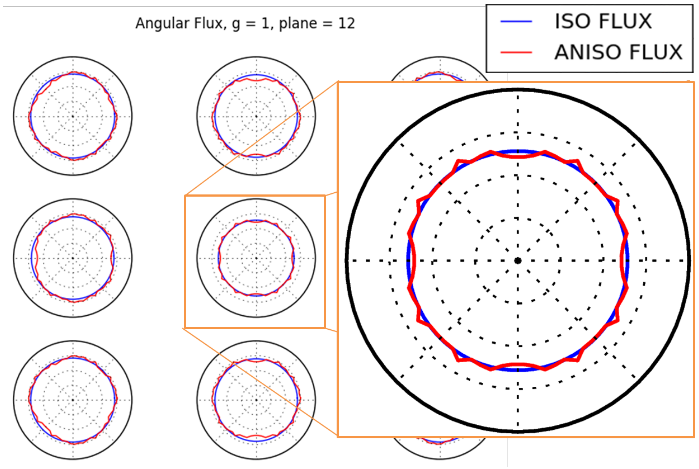

Figure 4.18: Angular flux, fast group, top of fuel rods

The homogenized cross section in Fig. 4.19 is nearly isotropic, although there are slight increases in the directions of neighboring pins. However, this location (control pin, fuel/moderator interface, group 1) is the most significant instance of azimuthally anisotropic XS. For most of the problem domain, the azimuthal dependence is much weaker. The average XS over the whole domain is given later in this section, in Table 4.6.

Next, the azimuthal anisotropy of the thermal leakage, flux, and XS is shown in Figs. 4.20, 4.21, and 4.22. These values are plotted at plane 7, which is the bottom tip of the control rod. The plot is magnified for one of the fuel pins that is a direct neighbor to the control rod. The azimuthal dependence of the axial TL is strongly anisotropic for thermal neutrons because of the control rod absorption. The angular flux is anisotropic, but less so than the axial TL. The homogenized XS has a

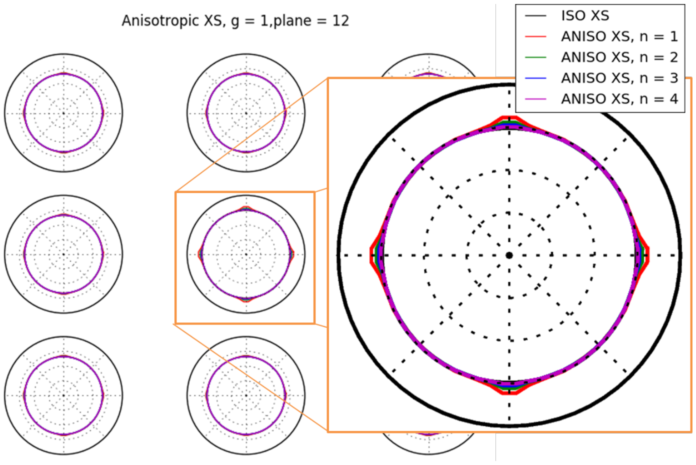

Figure 4.19: Homogenized 1D XS, fast group, top of fuel rods

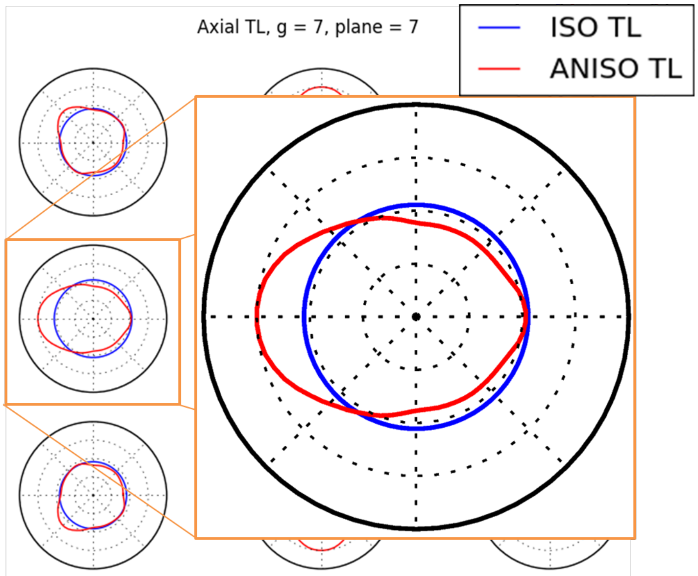

Figure 4.20: Axial TL, thermal group, control rod tip

weak azimuthal dependence, but this is not significant compared to the polar angle dependence. Each different color in Fig. 4.22 corresponds to a different polar angle. Most of the XS are on top of each other in the plot, but the shallowest polar angle, which is the red line, is separated from the rest. The black line is the isotropic XS.

To demonstrate that the azimuthal dependence is not significant in these cases, the eigenvalue results for this problem are given in Table 4.4. The eigenvalue with the polar-dependent homogenization is within uncertainty of the Monte Carlo solution, and very close to the explicit TL and XS solution.

Table 4.5 shows the average magnitude of the scalar flux and angular flux moments averaged over the entire problem domain. The moments are defined by the expression

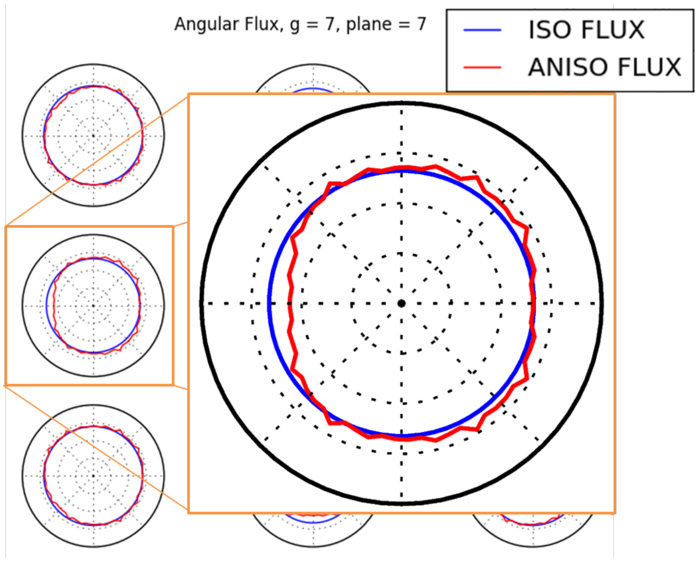

Figure 4.21: Angular flux, thermal group, control rod tip

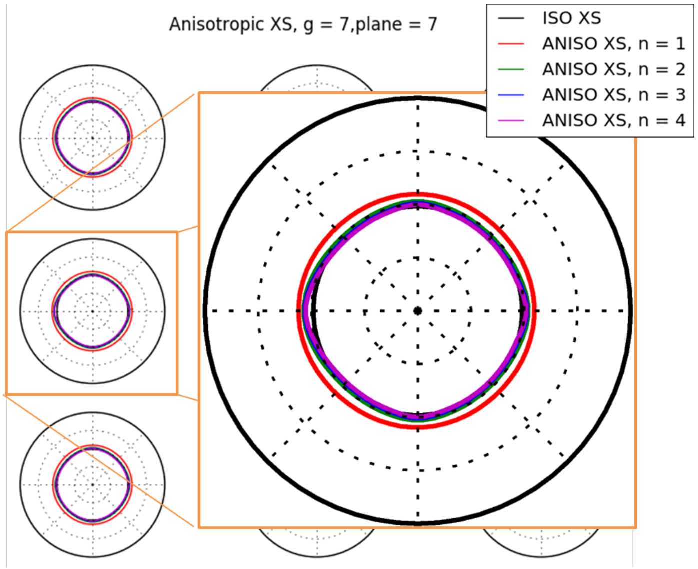

Figure 4.22: Homogenized 1D XS, thermal group, control rod tip

in Eq. (4.7), with each moment corresponding to a different weighting function. The polar angle weighting functions $P_l(\mu)$ are Legendre polynomials, and the azimuthal weighting functions, $f(\omega)$ are sines and cosines:

$$f_{c,p} = \cos(p\omega) \ , \tag{4.6a}$$

$$f_{s,p} = \sin(p\omega) \ . \tag{4.6b}$$

Table 4.4: Eigenvalue results for 3x3 problem

1D Method	TL	XS	k_{eff}	error [pcm]
P3	ISOTROPIC	ISOTROPIC	1.21632	58
P3	MOMENT	ISOTROPIC	1.21656	82
SN	EXPLICIT	ISOTROPIC	1.21658	84
P3	MOMENT	POLAR	1.21575	1
SN	EXPLICIT	EXPLICIT	1.21577	3
Monte Carlo	Monte Carlo	Monte Carlo	1.21574	(± 5)

$$F_{l,p,s/c} = \frac{1}{V_{tot}} \sum_{i,j,k=1}^{I,J,K} \left| \int_{x_{i-1/2}}^{x_{i+1/2}} \int_{y_{j-1/2}}^{y_{j+1/2}} \left[\frac{h_k}{4\pi} \int_{-1}^{1} P_l(\mu) \int_{0}^{2\pi} f_{s/c,p}(\omega)\psi_k(x,y,\mu,\omega)\, d\omega d\mu \right] dxdy \right| . \tag{4.7}$$

The average scalar flux is

$$\langle \phi \rangle = \frac{1}{V_{tot}} \sum_{i,j,k=1}^{I,J,K} h_k \int_{x_{i-1/2}}^{x_{i+1/2}} \int_{y_{j-1/2}}^{y_{j+1/2}} \phi_k(x,y)\, dxdy \; . \tag{4.8}$$

V_{tot} is the total volume of the system. For the polar angular flux, the azimuthally isotropic moment is used (i.e., $f(\omega) = 1$). The magnitudes of the average scalar fluxes are normalized to the group 1 value. The values of each angular moment are normalized to the average scalar flux from that group. Table 4.5 shows that the the angular flux moments are indeed small in magnitude compared to the scalar flux. Therefore, the assumptions made in 3.1.4 should be valid for most problems we would encounter. From Table 4.5, it seems that the polar angular flux moments, especially $F_{2,0}$, are slightly greater than the azimuthal moments in magnitude. This difference, in addition to a stronger space-angle coupling for the polar component, leads to the polar dependence of $\hat{\Sigma}_{t,k,ij}$ having greater importance than the azimuthal

Table 4.5: Angular flux moments for 3x3 problem

Group	$\langle \phi \rangle$	$F_{1,0}$	$F_{2,0}$	$F_{0,1,s}$	$F_{0,1,c}$	$F_{0,2,s}$	$F_{0,2,c}$
1	1.00	0.0095	0.0183	0.0069	0.0069	0.0035	0.0098
2	2.12	0.0043	0.0181	0.0033	0.0033	0.0016	0.0043
3	0.97	0.0030	0.0181	0.0010	0.0010	0.0005	0.0013
4	0.36	0.0028	0.0181	0.0043	0.0043	0.0018	0.0050
5	0.27	0.0033	0.0181	0.0046	0.0046	0.0021	0.0058
6	0.31	0.0022	0.0184	0.0084	0.0084	0.0055	0.0091
7	0.41	0.0012	0.0191	0.0179	0.0179	0.0155	0.0158

dependence. Table 4.6 shows the magnitude of the anisotropic XS relative to the isotropic, standard homogenized total XS. The polar-dependent XS is a deviation from the standard, isotropic total XS. Thus, the expected value of the magnitude of that deviation,

$$\delta\tilde{\Sigma}_{t,k,ij}(\mu_n) = \left| \frac{\tilde{\Sigma}_{t,k,ij}(\mu_n) - \hat{\Sigma}_{t,k,ij}}{\hat{\Sigma}_{t,k,ij}} \right| , \tag{4.9a}$$

$$\langle \delta\tilde{\Sigma}_t \rangle = \frac{1}{V_{tot}} \sum_{i,j,k=1}^{I,J,K} V_{i,j,k} \left(\frac{1}{2} \sum_{n=1}^{N_{pol}} \delta\tilde{\Sigma}_t(\mu_n) w_n \right) . \tag{4.9b}$$

is given in the table. N_{pol} is the number of polar angles and $V_{i,j,k}$ is the volume of the coarse-mesh cell (i, j, k). The azimuthal XS are moments that vary around 0, so the expected value of the magnitude relative to the total XS,

$$\tilde{\sigma}_{s/c,p,k,ij}(\mu_n) = \left| \frac{\tilde{\Sigma}_{s/c,p,k,ij}(\mu_n)}{\hat{\Sigma}_{t,k,ij}} \right| , \tag{4.10}$$

$$\langle \tilde{\sigma}_{s/c,p} \rangle = \frac{1}{V_{tot}} \sum_{i,j,k=1}^{I,J,K} V_{i,j,k} \left(\frac{1}{2} \sum_{n=1}^{N_{pol}} \tilde{\sigma}_{s/c,p}(\mu_n) w_n \right) , \tag{4.11}$$

is given in the following table:

Table 4.6: Angular XS moments for 3x3 problem

Group	$\hat{\Sigma}_t[cm^{-1}]$	$\langle \delta\tilde{\Sigma}_t \rangle$	$\langle \tilde{\sigma}_{s,1} \rangle$	$\langle \tilde{\sigma}_{c,1} \rangle$	$\langle \tilde{\sigma}_{s,2} \rangle$	$\langle \tilde{\sigma}_{c,2} \rangle$
1	0.167	0.0012	0.0000	0.0000	0.0000	0.0000
2	0.384	0.0009	0.0000	0.0000	0.0000	0.0000
3	0.559	0.0006	0.0000	0.0000	0.0000	0.0000
4	0.583	0.0013	0.0000	0.0000	0.0000	0.0000
5	0.579	0.0038	0.0002	0.0002	0.0001	0.0008
6	0.949	0.0083	0.0005	0.0005	0.0002	0.0015
7	1.924	0.0243	0.0014	0.0014	0.0004	0.0026

Table 4.6 shows that the variation in the total XS is much more significant in the polar variable, although it is still relatively small. No azimuthal XS moment is larger than 0.3% of the isotropic XS for a given cell and group. With this information, the azimuthal XS moments can be comfortably neglected for LWR analysis. It is possible that reactors with different lattice geometries or neutron spectra could generate larger azimuthal XS moments, but no case studied for this work was identified as having this property.

In an attempt to generate larger azimuthal XS moments, the same analysis is performed for a system with thin plates of fuel oriented along the x or y axis. The radial geometry is shown in Fig. 4.23. The axial geometry (fuel height, control rod insertion, etc.) is the same as in Fig. 4.8. The pin pitch is 1.26 cm, the plates are 1.2 mm wide and 1.14 cm long.

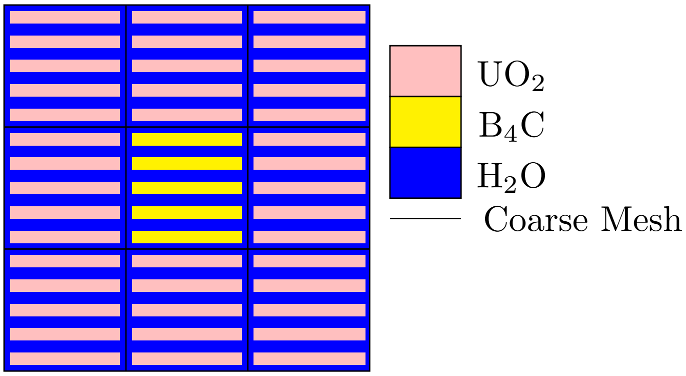

Figure 4.23: 3x3 plate fuel geometry

Theoretically, this system should have stronger azimuthal dependence for the spatial self-shielding effect than the cylindrical fuel, but the azimuthal moments are still not significant. The XS moments are given in Table 4.7. Most of the azimuthal moments are still very small. The $P = 2$ cosine moment is comparable to the azimuthally isotropic, polar moment. However, both are relatively small. The plate fuel geometry reduces the polar dependence of the homogenized XS more than it increases the importance of the azimuthal moments.

Table 4.7: Angular flux moments for plate fuel

Group	$\hat{\Sigma}_t[cm^{-1}]$	$\langle \delta\tilde{\Sigma}_t \rangle$	$\langle \tilde{\sigma}_{s,1} \rangle$	$\langle \tilde{\sigma}_{c,1} \rangle$	$\langle \tilde{\sigma}_{s,2} \rangle$	$\langle \tilde{\sigma}_{c,2} \rangle$
1	0.168	0.0003	0.0001	0.0000	0.0000	0.0002
2	0.381	0.0004	0.0000	0.0000	0.0000	0.0003
3	0.554	0.0002	0.0000	0.0000	0.0000	0.0001
4	0.582	0.0008	0.0000	0.0000	0.0000	0.0006
5	0.560	0.0012	0.0002	0.0001	0.0000	0.0009
6	0.910	0.0027	0.0003	0.0002	0.0000	0.0023
7	1.811	0.0075	0.0007	0.0004	0.0001	0.0070

4.6 3D C5G7 Benchmark

The 3D C5G7 benchmark is used to evaluate the accuracy of the methods developed in this paper. The accuracy is compared to the Monte Carlo reference for each of four methods:

1. 2D/1D with isotropic TL (standard)
2. 2D/1D with anisotropic TL (Legendre polar / Fourier azimuthal expansion)
3. 2D/1D with anisotropic TL and polar-dependent 1D total XS
4. 2D/1D with anisotropic TL and polar-azimuthal angle-dependent 1D total XS

Results for a hyper-refined case, where angular and spatial refinement is increased to the point of convergence, are also included. This eliminates discretization error so the magnitude of any remaining errors in the 2D/1D approximation can be determined.

The 3D C5G7 benchmark [29] is a common benchmark for evaluating the accuracy of neutronics codes. The radial geometry is shown in Fig. 4.24. The north and west boundaries are reflective. There are 3 standard configurations: unrodded, and two rodded cases (A and B). In the rodded A case, the rods are partially (1/3) inserted into the center UO_2 assembly. In rodded B, the rods are (1/3) inserted into both MOX assemblies, and (2/3) into the center UO_2 assembly. The axial geometry is shown in Fig. 4.25.

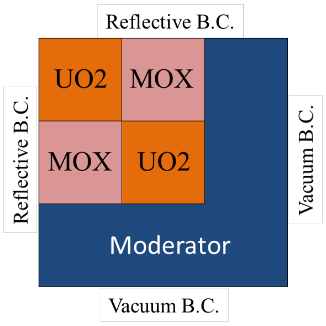

Figure 4.24: C5G7 radial geometry

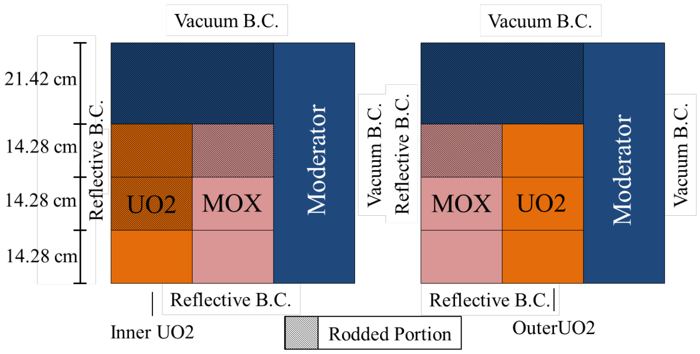

Figure 4.25: C5G7 axial geometry

The discretization used was relatively fine: 144 flat source regions (FSRs) per pin cell (9 radial x 16 azimuthal), 225 FSRs per moderator cell (Cartesian 15x15), 0.02 cm ray spacing, and 16 azimuthal × 4 polar angles per octant in the quadrature set

(Chebyshev azimuthal, Gauss-Legendre polar). The TL treatment is moment-based, with two cosine and two sine moments. The axial discretization is eighteen 3.57 cm planes. The convergence criteria is a successive difference between iterations of 10^{-6} for the eigenvalue and 10^{-5} for the two-norm of the fission source.

The reference solution was generated using SHIFT [37], a Monte Carlo code. The values given in Table 4.8 are the 1-σ uncertainties. Each case was run with 1 million particles per cycle, with 250 inactive cycles and 3000 active cycles ($3\text{x}10^9$ total active particles).

Pin power and eigenvalue results for the 3D C5G7 benchmark for the four cases are given in Table 4.8. When going from isotropic to anisotropic TL, the eigenvalues improve, but the pin powers become less accurate. This suggests cancellation of error, with the isotropic TL solution appearing more accurate than it truly is. With polar XS, both the eigenvalue and pin power errors are low, indicating a more robustly accurate solution.

Even with the simplest 2D/1D model (isotropic TL and XS) the RMS error in the 3D C5G7 benchmark is approximately 0.3%. This is well below the limit for "high-fidelity" reactor analysis suggested by Smith and Forget [70]. The suggested accuracy in [70] is <1.5% RMS error in the axially-integrated fission distribution and <1.0% RMS error in the axial power shape. The C5G7 benchmark problem has no multigroup approximation, which is a significant source of error in realistic LWR simulations; this is why 2D/1D can achieve a much smaller 3D RMS error here. From these results, it appears that the errors inherent in using a 2D/1D transport approximation (as opposed to 3D transport) are not the limiting source of error in attempting to develop a "high-fidelity" LWR analysis tool. The errors in the multigroup approximation and scattering approximations are likely much greater than the error from using the 2D/1D approximation to solve the multigroup transport problem.

The azimuthal XS dependence has almost no effect on the solution. The results are virtually identical whether 1D P_3 or 1D S_N is used, with S_8 quadrature. This indicates that the P_3 1D solver is sufficient, and does not limit the accuracy of the overall 2D/1D solution. Additionally, the 1D P_3 solution is much faster in this case because the 1D S_N has a much lower rate of convergence and requires significantly more iterations. This could be an advantage of the 1D P_3 method, although this difference does not necessarily hold in all cases.

Each of these cases was run using 162 cores on Titan, a supercomputer at Oak Ridge Leadership Computing Facility. Each node on this machine contains a 16-core

Table 4.8: 3D C5G7 benchmark errors, SHIFT reference

Method (1D/TL/XS)	Case	k_{eff} [pcm]	RMS [%]	Max [%]	CPU Time [h]
1D P_3, ISOTROPIC TL, ISOTROPIC XS	unrodded	-59	0.26	0.81	9.5
	rodded A	-58	0.28	0.80	9.1
	rodded B	-73	0.30	0.98	10.1
1D P_3, POLAR / AZI TL, ISOTROPIC XS	unrodded	4	0.30	0.94	36.6
	rodded A	18	0.38	1.16	27.3
	rodded B	23	0.57	2.42	35.3
1D P_3, POLAR / AZI TL, POLAR XS	unrodded	-9	0.13	0.41	37.9
	rodded A	-12	0.17	0.54	37.8
	rodded B	-20	0.25	0.86	41.4
1D P_3, POLAR / AZI TL, POLAR / AZI XS	unrodded	-9	0.13	0.42	72.6
	rodded A	-12	0.17	0.54	66.8
	rodded B	-19	0.25	0.88	72.8
1D S_N, POLAR / AZI TL, POLAR XS	unrodded	-9	0.13	0.41	213.3
	rodded A	-13	0.17	0.53	269.1
	rodded B	-22	0.25	0.87	129.8
MONTE CARLO REFERENCE UNCERTAINTY	unrodded	2	0.03	0.12	320.0
	rodded A	2	0.03	0.13	320.0
	rodded B	2	0.03	0.13	320.0

2.2GHz AMD Opteron$^{\text{TM}}$6274 processor and 32 GB of RAM. From the last column in Table 4.8, the downside of using anisotropic TL and homogenized 1D XS is clear: although the solution is significantly more accurate, it is 4 times more expensive than the simplified isotropic TL and XS case. However, the run time of approximately 35-40 hours for a high-accuracy solution is comparable to the results achieved by a 3D MOC with linear source method [56].

The pin powers in each of the 3 planes for both homogenization types (isotropic and polar) for the unrodded, rodded A, and rodded B cases are compared in Figs. 4.26, 4.27, and 4.28. The reference pin powers are calculated at 3 uniform planes. The planes are numbered from the bottom, so the rods are inserted into plane 3, and in the rodded B case, plane 2 for the inner UO_2 assembly. In this case, the inner UO_2 assembly is in the bottom left corner. The isotropic XS results are shown in the first row, and the polar XS results are shown on the same scale on the second row. In all three cases, there is a visible improvement in the power shape.

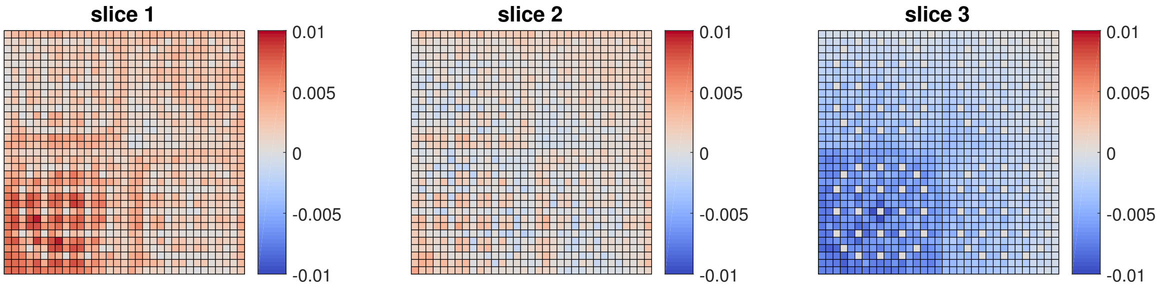

(a) Isotropic XS

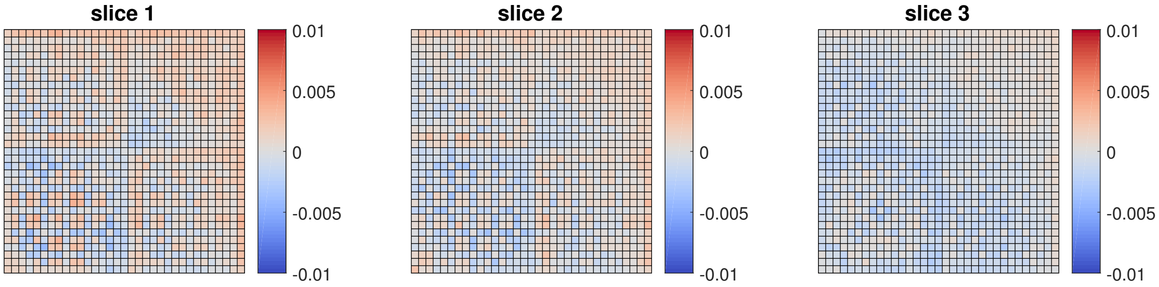

(b) Anisotropic XS

Figure 4.26: Pin power errors, C5G7 3D unrodded

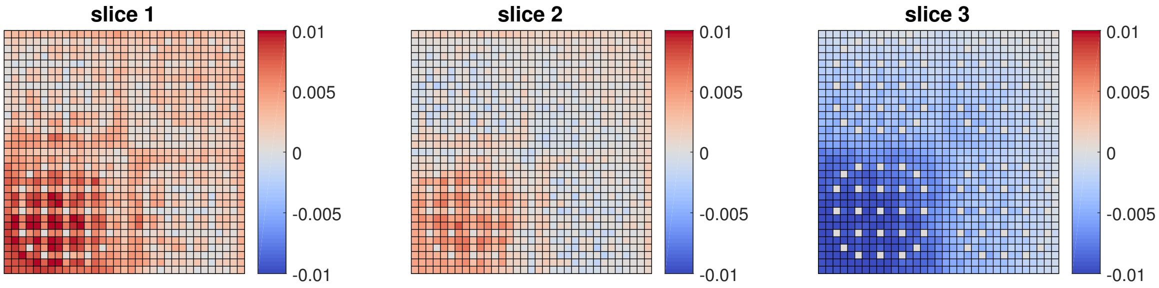

(a) Isotropic TL

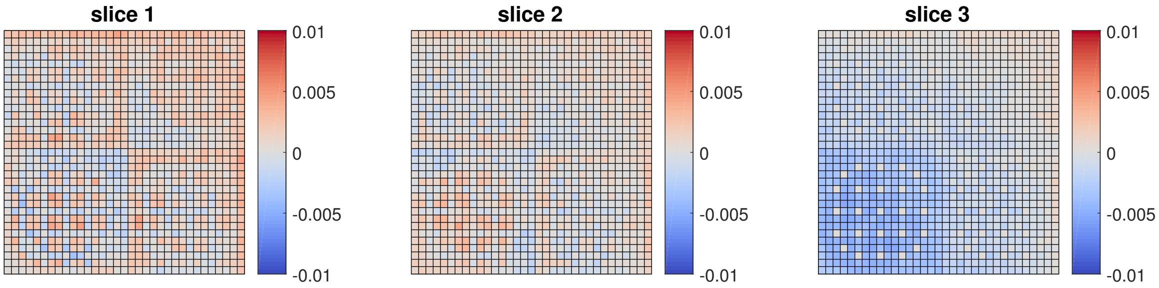

(b) Anisotropic TL

Figure 4.27: Pin power errors, C5G7 3D rodded A

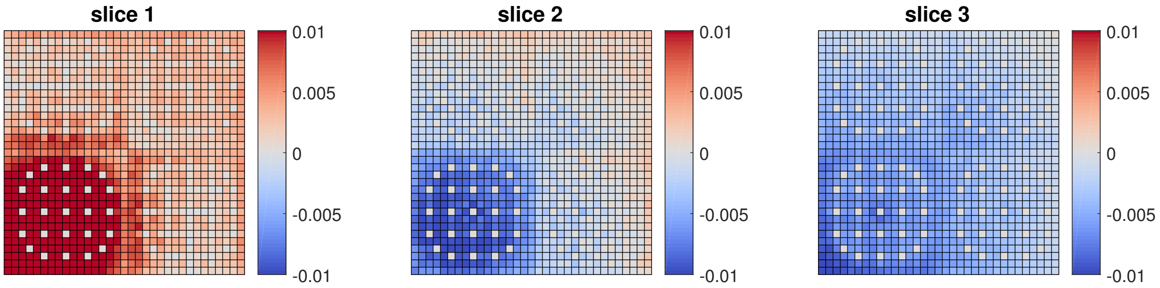

(a) Isotropic TL

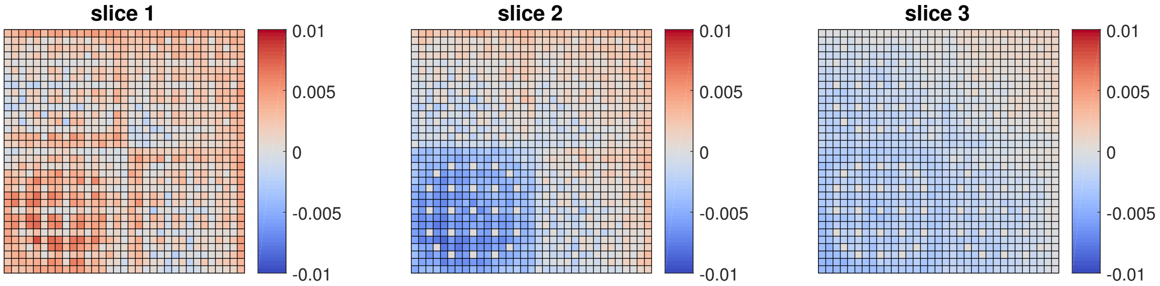

(b) Anisotropic TL

Figure 4.28: Pin power errors, C5G7 3D rodded B

The core-averaged axial power shape error is given in Fig. 4.29. The one standard deviation uncertainty is given by the dashed lines. It is clear that the anisotropic TL and XS method has significantly better agreement with the Monte Carlo reference solution, but the anisotropic TL alone, without anisotropic XS, is not as accurate as the isotropic TL and XS method. This is likely because of cancellation of error.

These results show a significant improvement in the 3D C5G7 benchmark solution with the new method at a large, but reasonable computational cost. It is also interesting, both theoretically and practically, to determine how well this 2D/1D method can match the 3D Monte Carlo transport reference solution if computational cost is not a concern. To improve the solution further, the spatial mesh and angular quadrature are refined significantly. The fuel FSR mesh was refined (180 FSRs per pin cell), while the reflector FSR mesh was coarsened to improve load balance (121 FSRs per pin cell). The number of azimuthal angles was doubled to 32 per octant, and the number of polar angles was tripled to 12 per octant. The axial mesh was refined by a factor of 4, to 0.8925 cm planes (72 total). The resulting run time increased by a factor of approximately 25. This is approximately a factor of 3 more than the CPU time required for the Monte Carlo solution. However, we should note that the Monte Carlo reference is a multigroup solution, so the run time may not reflect a continuous energy Monte Carlo solution. The results are given in Table 4.9.

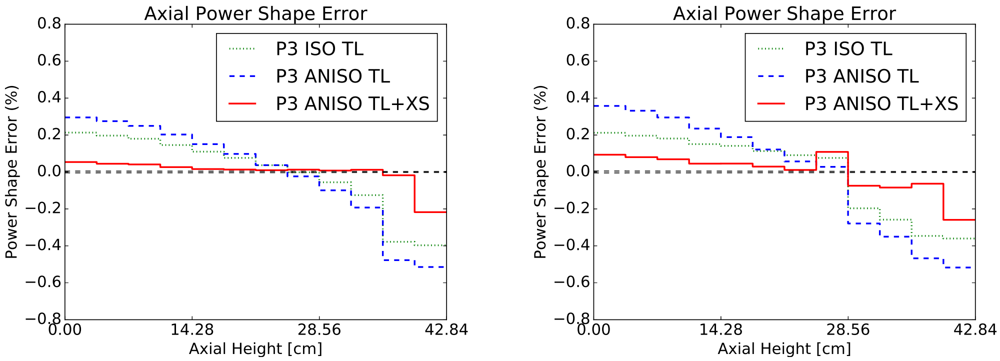

(a) 3D unrodded axial power (b) 3D rodded A axial power

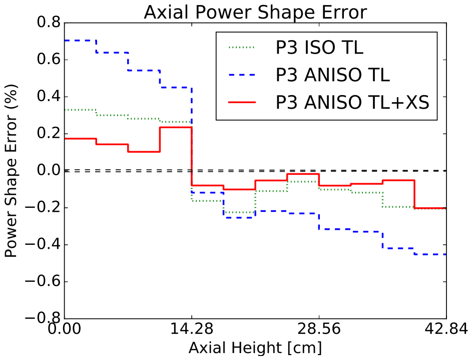

(c) 3D rodded B axial power

Figure 4.29: Axial power shape error

Table 4.9: 3D C5G7 benchmark errors, 2D/1D P_3 polar XS, hyper-fine mesh

	k_{eff} [pcm]	RMS [%]	Max [%]	CPU Time [h]
unrodded	3	0.18	0.83	909.0
rodded A	2	0.19	0.86	950.4
rodded B	-3	0.21	0.92	953.5

The eigenvalue, RMS, and maximum pin power errors are very small, suggesting that there is no significant difference between the 3D Monte Carlo and the improved 2D/1D solution. Even though the rodded cases are much “tougher” for the traditional 2D/1D method, the improved 2D/1D method solves each of the 3 cases equally well, just as a true 3D transport solution would, with sufficient spatial and angular refinement.

Without the anisotropic TL and XS, the solution does not converge to the reference with refined spatial and angular mesh. The core-averaged axial power shape error for the refined mesh case is given for isotropic and anisotropic TL and XS in Fig. 4.30.

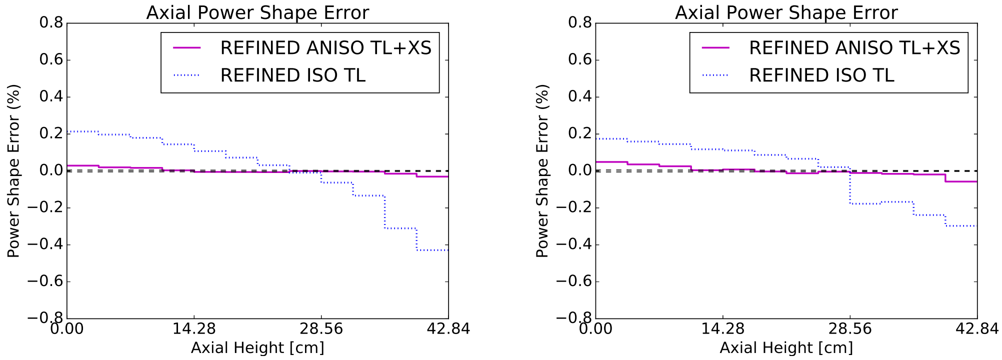

(a) 3D unrodded axial power (b) 3D rodded A axial power

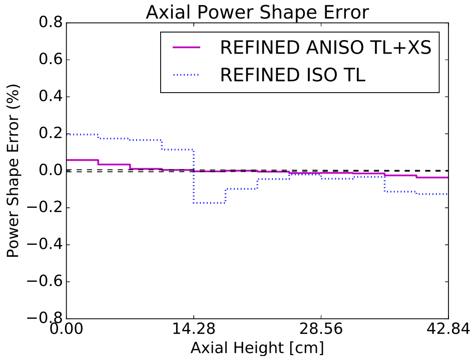

(c) 3D rodded B axial power

Figure 4.30: Axial power shape error, fine spatial and angular mesh

4.7 VERA Progression Problem 4

MPACT is the deterministic neutronics code for the Virtual Environment for Reactor Applications (VERA). Several benchmark progression problems are defined to assess the capabilities of VERA. Problem 4 is a 3x3 set of 17x17 PWR assemblies, with control rod insertion into the center assembly. The radial and axial geometry are given in Fig. 4.31a and Fig. 4.31b, respectively.

The green assemblies have 20 pyrex burnable absorber rods and 2.6 wt% enriched UO_2. The red assemblies have 2.1 wt% enriched UO_2. The assembly is divided into 58 axial planes. In the active core region, the MOC planes are 8.065 cm thick, except for the planes with spacer grids, which are 3.81 cm thick.

The MPACT 51-group cross section library (dated 03/26/2018) is used for this problem. The materials, cross sections, radial, and axial dimensions reflect those of a real PWR. This is a main target problem for MPACT. In this sense, it may be a

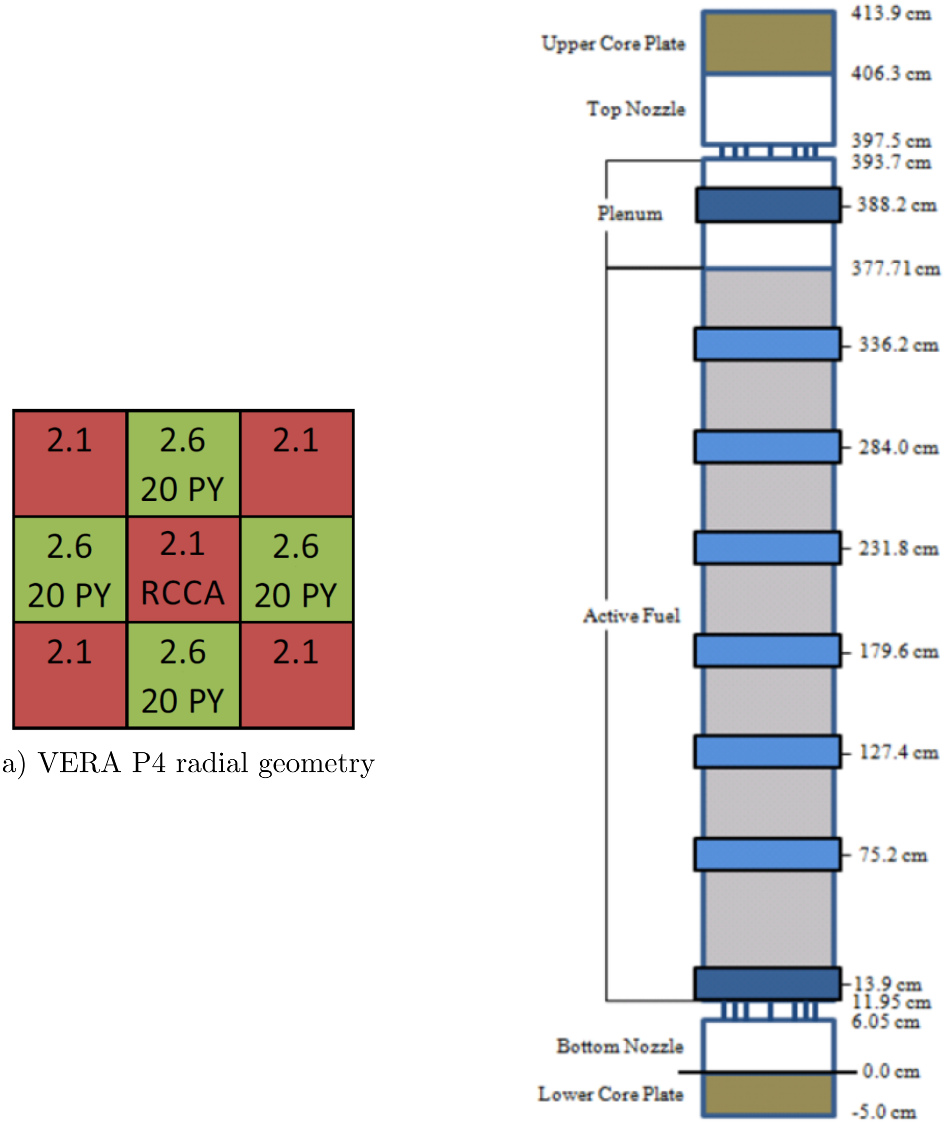

2.1	2.6 20 PY	2.1
2.6 20 PY	2.1 RCCA	2.6 20 PY
2.1	2.6 20 PY	2.1

(a) VERA P4 radial geometry

(b) VERA P4 axial geometry

Figure 4.31: VERA Problem 4 geometry

better test problem to evaluate the effectiveness of these methods for the practical cases in which we are usually interested.

This is a steady-state problem. The control rods are withdrawn in 10% increments from 0% to 100%. The eigenvalue and power shape are computed for each configuration and compared to a Monte Carlo reference solution using KENO-VI [71].

However, in the standard model used in MPACT, the control rod tips are partially inserted into the MOC planes. This leads to a rod cusping error, which is much greater in magnitude than the effects treated by the method in this thesis. There are methods implemented in MPACT to reduce the rod cusping errors, such as a polynomial decusping or subplane decomposition of the MOC plane [30]. Even with these treatments, the remaining error from the rod cusping is large compared to the error addressed by the improved angular coupling method.

If the axial mesh is refined so that the control rod tips align with the MOC plane boundaries, the rod cusping error will be eliminated. However, this makes the planes near the control rod thinner, and the axial TL between the rodded plane and the unrodded plane becomes high. The combination of a thin plane and high axial TL leads to a negative total 2D source, and in turn the 2D/1D iteration fails to converge. This phenomenon was mentioned in Sec. 3.2.1. We need TL splitting for convergence, but the TL splitting method degrades the accuracy of the 2D/1D solution, counteracting the improved angular coupling. As a result, we have to use the original mesh that introduces rod cusping effects.

The errors are given for three methods:

1. ISOTL: isotropic transverse leakage, isotropic cross sections
2. ISOXS: anisotropic transverse leakage, isotropic cross sections
3. POLXS: anisotropic transverse leakage, (polar) anisotropic cross sections

Eigenvalue results are given for 20% increments of rod withdrawal in Table 4.10. The polynomial decusping method is used.

Table 4.10: Eigenvalue error, VERA Problem 4

Rod Withdrawal		k_{eff} KENO-VI	Error [pcm] ISOTL	ISOXS	POLXS
0%	(in)	0.97241	-45	-41	-43
20%		0.97936	-57	-50	-55
40%		0.99234	-44	-39	-44
60%		0.99803	-51	-48	-51
80%		1.00058	-52	-50	-53
100%	(out)	1.00139	-51	-50	-52

Pin power results are given in Table 4.11. The average uncertainty in the KENO-VI pin powers is 0.3%.

From these results, two things are clear:

1. There is a significant error in the MPACT pin power shape, especially for the cases where the rod tip is near the center of the active core (40% and 60% withdrawn).

Table 4.11: Pin power errors, VERA Problem 4

Rod Withdrawal		RMS [%]			Max [%]		
		ISOTL	ISOXS	POLXS	ISOTL	ISOXS	POLXS
0%	(in)	0.66	0.68	0.70	7.44	6.09	6.61
20%		1.57	1.22	1.79	5.62	4.58	5.69
40%		1.45	1.55	2.13	13.31	11.71	13.73
60%		1.49	1.68	2.05	10.00	8.30	9.39
80%		0.53	0.58	0.58	3.73	4.35	4.07
100%	(out)	0.50	0.60	0.52	3.80	4.33	3.82

2. The effect of the improved methods on the overall power shape is small relative to the errors in the power shape.

Unlike the previous cases we have studied, the results here do not indicate that any one method is significantly better than the others. The eigenvalue effect of the anisotropic TL and XS is less than 5 pcm for each, and the effects seem to approximately cancel in the eigenvalue.

Based on these results, we may infer that the modeling error caused by the partially inserted control rod (i.e., rod cusping effect) is sufficiently large to wash out whatever improvement we might have seen with the new, improved angular coupling method. The effect of the new, improved angular coupling method is smaller here than it was in the other cases studied in this chapter. The differences are larger for the pin power errors than the eigenvalue, but there is no consistent trend in the results.

Even for the 100% withdrawn case, which has no rod cusping effects, the new method does not improve the solution, or make it significantly worse. Thus, it is reasonable to say that the errors caused by the isotropic TL and XS approximation are negligible in this case, and other approximations are the source of the salient errors (-51 pcm eigenvalue, 0.50% RMS and 3.80% max pin power error). The multigroup approximation may be the main source of this error. Spatial and angular discretization error may also be contributing.

The axial power shape for the rodded assembly is given in Fig. 4.32a (40% withdrawn) and Fig. 4.32b (100% withdrawn). There are subtle differences for each method, but the main error in the vicinity of the control rod is present with each method. With the control rod withdrawn, the magnitude of the error is much lower. Thus, the overwhelming majority of the error is caused, either directly or indirectly, by the axial heterogeneity introduced by the partially inserted control rod.

The control rod insertion error in the C5G7 benchmark was effectively reduced by the new method, but in this case it is not. The error in this case is much greater, so we might expect the anisotropic TL and XS to be more important. However, the error does not improve or even change in any significant way when using the higher-fidelity method. Something may be fundamentally different about the error in this case.

4.8 Summary of Numerical Results

In this chapter, several simple test cases were used to verify that the improved angular coupling method has the desired increase in accuracy. The numerical results demonstrated several assertions and assumptions made in Chapter 3. The main conclusions from the results so far are:

1. Using the anisotropic 1D XS homogenization for the axial transport problem preserves the angular flux distribution from the radial solution (Sec. 4.1).
2. The P_3 approximation to the polar dependence of the anisotropic TL is sufficient (Sec. 4.3, Sec. 4.6).
3. The effect of the spatial distribution of the axial TL radially within a pin cell on the overall solution is negligible (Sec. 4.2, Sec. 4.4).
4. The importance of the azimuthal dependence of the anisotropic homogenized 1D XS is small compared to the polar dependence (Sec. 4.5) and does not significantly affect the overall solution (Sec. 4.4, Sec. 4.6).
5. Using the improved angular coupling (TL and XS) method is significantly more expensive than the isotropic TL "hybrid" 2D/1D method typically used in MPACT (Sec. 4.6).
6. The methods developed here have shown great improvements in accuracy for simple benchmark problems (with C5G7 or Takeda cross sections), but the results for a realistic PWR model show other significant errors that are not affected by the method developed here (Section 4.7).

The improved angular coupling method, which uses anisotropic TL and polar anisotropic XS, met our objective of significantly improving the accuracy of the 2D/1D method for the C5G7 benchmark. All of the relevant components of the error caused by pin heterogeneity were investigated, and a method was developed to address only the most important component (the polar anisotropic 1D XS dependence).

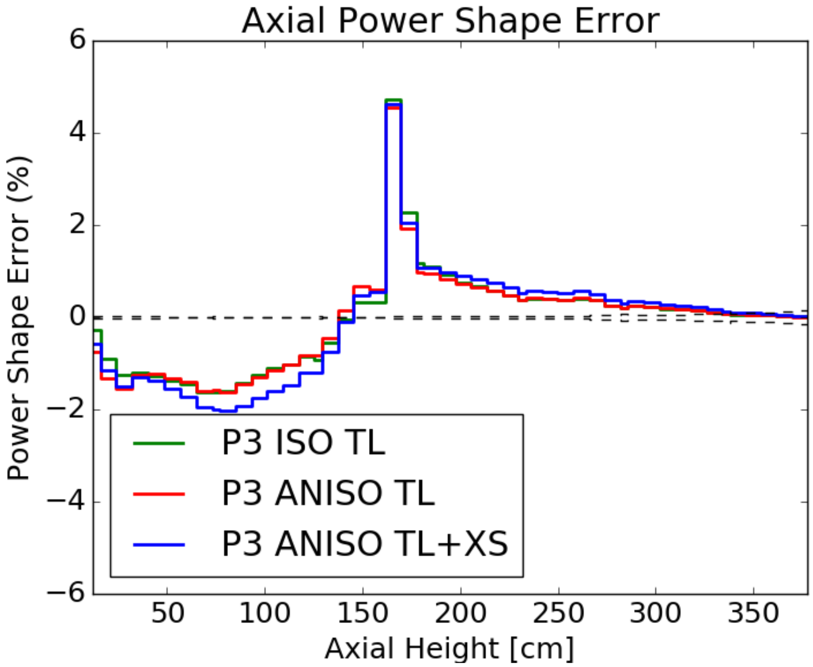

(a) Axial power shape error (40%) withdrawn

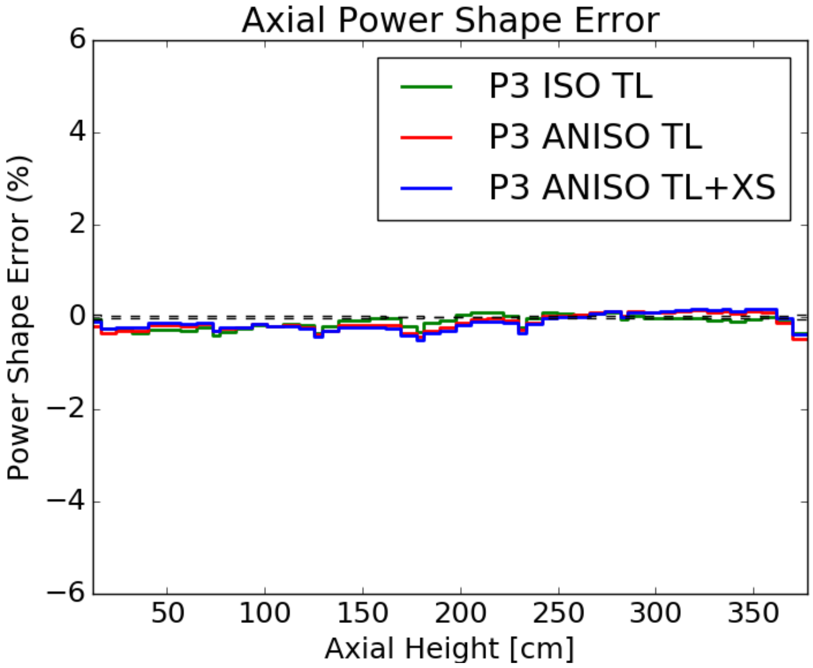

(b) Axial power shape error (100%) withdrawn

Figure 4.32: Axial power shape error for rodded assembly

The new method with anisotropic TL and XS has a significant additional computational expense associated with it. In Chapter. 5, another method is developed that treats the anisotropy in the TL and XS in a way that is slightly less accurate but significantly faster.

While the improved method met many of the objectives that we had at the outset, the results for the one realistic reactor model do not show any of the desired improvements. Future work will include applying this method to a full PWR core, to see if the new method has a more significant effect for that case. If not, more theoretical and (numerically) experimental work will need to be done to identify the source of the errors observed in Sec. 4.7 and address them.

It is possible that this error is inherent to the multigroup approximation and cannot be addressed effectively within the framework of our deterministic, multigroup transport solver. We can speculate about what the cause of this error may be; for example, spectral changes in the vicinity of the control rod tips that are caused by 3D transport effects may not be treated accurately by the 2D subgroup fixed-source problem that is used to generate the multigroup cross sections. It may not be possible to address such an issue effectively without fundamentally changing the structure or methods used by MPACT.

Chapter 5: The 2D/1D Polar Parity Method

In Chapter 4, the 2D/1D P_3 method with anisotropic TL and XS demonstrates significantly improved accuracy compared to both the standard 2D/1D method and the 2D/1D anisotropic TL method with isotropic XS. However, the 2D/1D anisotropic TL method is computationally more expensive than the standard isotropic TL method, and the anisotropic XS method requires even more computation time. While the improved accuracy with the new 2D/1D is desirable, this method is unattractive for common usage because it increases the run time by approximately a factor of 3.

The 2D MOC equation in standard 2D/1D has polar symmetry when all of the sources are isotropic. One of the most significant reasons for the increase in run time when using anisotropic TL is that the number of MOC ray segments that need to be swept is doubled. The number of rays is doubled with anisotropic TL because there is no longer symmetry in the polar angle. In this chapter, a new polar parity 2D/1D method is proposed and derived to ameliorate this issue. This method solves an even parity transport equation using 2D MOC, and solves the odd parity component of the angular flux with a lower-fidelity S_N solver. This method is implemented in MPACT and tested on some of the same problems that were used in Chapter 4. The results show that the polar parity method is significantly faster than the previous method with anisotropic TL, and that accuracy of the anisotropic TL is effectively the same. The accuracy of the anisotropic XS is limited, but it is still an improvement compared to the standard 2D/1D method.

5.1 Polar Parity 2D/1D Equations

The 2D/1D equations with polar parity are derived in this section. The azimuthal angle is given no special symmetry treatment. This is different from what is typically referred to as “even-parity” transport, which involves symmetry in angle as a whole (i.e., both azimuthal and polar). It is important to emphasize that the method derived in this section is only valid when isotropic scattering is used. The derivation begins with the energy-independent fixed-source 3D Boltzmann neutron transport equation with isotropic scattering:

$$\mathbf{\Omega}\cdot\nabla\psi(\mathbf{r},\mathbf{\Omega}) + \Sigma_t(\mathbf{r})\psi(\mathbf{r},\mathbf{\Omega}) = \frac{Q(\mathbf{r})}{4\pi} \ , \tag{3.1}$$

$$\mathbf{r} = (x,y,z) \ , \ \Omega = \left(\sqrt{1-\mu^2}\cos\omega, \sqrt{1-\mu^2}\sin\omega, \mu\right) \ ,$$

$$Q(\mathbf{r}) = \left[\Sigma_s(\mathbf{r}) + \frac{\nu\Sigma_f(\mathbf{r})}{k_{eff}}\right]\int\limits_{4\pi}\psi(\mathbf{r},\mathbf{\Omega})d\Omega \ .$$

Here, μ is the cosine of the polar angle θ, and ω is the azimuthal angle. First, we evaluate Eq. (3.1) at μ and $-\mu$:

$$\left[\sqrt{1-\mu^2}\left(\cos\omega\frac{\partial}{\partial x} + \sin\omega\frac{\partial}{\partial y}\right) + \mu\frac{\partial}{\partial z} + \Sigma_t(\mathbf{r})\right]\psi(x,y,z,\mu,\omega) = \frac{Q(\mathbf{r})}{4\pi} \ , \tag{5.1a}$$

$$\left[\sqrt{1-\mu^2}\left(\cos\omega\frac{\partial}{\partial x} + \sin\omega\frac{\partial}{\partial y}\right) - \mu\frac{\partial}{\partial z} + \Sigma_t(\mathbf{r})\right]\psi(x,y,z,-\mu,\omega) = \frac{Q(\mathbf{r})}{4\pi} \ , \tag{5.1b}$$

Then, we take the sum of Eq. (5.1a) and Eq. (5.1b):

$$\begin{aligned}\left[\sqrt{1-\mu^2}\left(\cos\omega\frac{\partial}{\partial x} + \sin\omega\frac{\partial}{\partial y}\right) + \Sigma_t(\mathbf{r})\right]\left[\psi(x,y,z,\mu,\omega) + \psi(x,y,z,-\mu,\omega)\right] \\ +\mu\frac{\partial}{\partial z}\left[\psi(x,y,z,\mu,\omega) - \psi(x,y,z,-\mu,\omega)\right] = 2\frac{Q(\mathbf{r})}{4\pi} \ ,\end{aligned} \tag{5.2}$$

and we subtract Eq. (5.1b) from Eq. (5.1a):

$$\begin{aligned}\left[\sqrt{1-\mu^2}\left(\cos\omega\frac{\partial}{\partial x} + \sin\omega\frac{\partial}{\partial y}\right) + \Sigma_t(\mathbf{r})\right]\left[\psi(x,y,z,\mu,\omega) - \psi(x,y,z,-\mu,\omega)\right] \\ +\mu\frac{\partial}{\partial z}\left[\psi(x,y,z,\mu,\omega) + \psi(x,y,z,-\mu,\omega)\right] = 0 \ .\end{aligned} \tag{5.3}$$

The even (+) and odd (-) polar-parity angular flux are defined by:

$$\psi^+(x,y,z,\mu,\omega) = \frac{1}{2}\left[\psi(x,y,z,\mu,\omega) + \psi(x,y,z,-\mu,\omega)\right] \ , \tag{5.4a}$$

$$\psi^-(x,y,z,\mu,\omega) = \frac{1}{2}\left[\psi(x,y,z,\mu,\omega) - \psi(x,y,z,-\mu,\omega)\right] \ . \tag{5.4b}$$

Using Eq. (5.4a) and Eq. (5.4b) in Eq. (5.2) and Eq. (5.1), we obtain:

$$\left[\sqrt{1-\mu^2}\left(\cos\omega\frac{\partial}{\partial x}+\sin\omega\frac{\partial}{\partial y}\right)+\Sigma_t(\mathbf{r})\right]\psi^+(x,y,z,\mu,\omega) + \mu\frac{\partial}{\partial z}\psi^-(x,y,z,\mu,\omega) = \frac{Q(\mathbf{r})}{4\pi}\ , \tag{5.5}$$

$$\left[\sqrt{1-\mu^2}\left(\cos\omega\frac{\partial}{\partial x}+\sin\omega\frac{\partial}{\partial y}\right)+\Sigma_t(\mathbf{r})\right]\psi^-(x,y,z,\mu,\omega) + \mu\frac{\partial}{\partial z}\psi^+(x,y,z,\mu,\omega) = 0\ . \tag{5.6}$$

Eq. (5.5) and Eq. (5.6) are the 3D even and odd polar-parity transport equations. The even and odd-parity angular flux appear in both equations, so the equations are coupled. To obtain the 2D/1D even and odd-parity equations, these equations are averaged axially over a slice k with thickness h_k. However, the equations should not be discretized until it is determined how they will be coupled. Several paths can be taken for coupling the equations, although (2) will be the focus of this work. They are listed in ascending order of theoretical accuracy:

1. Make an isotropic assumption to the $\mu\psi^-$ term, leading to the standard MPACT equations (Sec. 5.1.1).
2. Solve Eq. (5.6) on the coarse mesh, which should be quick but still accurate (anisotropic TL without full polar MOC sweep) (Sec. 5.1.2.
3. Solve Eq. (5.6) on an intermediate mesh, yielding an anisotropic weighting function for the homogenized 1D XS (Sec. 5.1.3).
4. Solve Eq. (5.6) on the fine mesh, yielding a fine-mesh spatial shape for the anisotropic axial TL (Sec. 5.1.4.

These 4 paths differ in the way that Eq. (5.6) is solved for ψ^-. Deriving the MPACT equations first will provide a clear picture of how the new methods proposed here differ from the standard MPACT method.

5.1.1 MPACT Approximation

In MPACT, the standard solver assumes that the axial TL term is isotropic, and flat over a coarse cell. In these equations, the equivalent term is the axial streaming term ($\mu\frac{\partial}{\partial z}\psi^-$) in Eq. (5.5). To begin, we solve Eq. (5.6) directly for ψ^- by assuming that the spatial derivatives of ψ^+ are small $[\mathscr{O}(\epsilon)]$ compared to Σ_t:

$$\begin{aligned}
&\psi^-(x,y,z,\mu,\omega) \qquad\qquad (5.7)\\
&= -\left[\sqrt{1-\mu^2}\left(\cos\omega\frac{\partial}{\partial x}+\sin\omega\frac{\partial}{\partial y}\right)+\Sigma_t(\mathbf{r})\right]^{-1}\mu\frac{\partial}{\partial z}\psi^+(x,y,z,\mu,\omega)\\
&= -\frac{1}{\Sigma_t(\mathbf{r})}\left[1-\frac{1}{\Sigma_t(\mathbf{r})}\sqrt{1-\mu^2}\left(\cos\omega\frac{\partial}{\partial x}+\sin\omega\frac{\partial}{\partial y}\right)+\mathscr{O}(\epsilon^2)\right]\mu\frac{\partial}{\partial z}\psi^+(x,y,z,\mu,\omega)\ .
\end{aligned}$$

Cross-derivative terms (e.g., $\frac{\partial}{\partial x}\frac{\partial}{\partial z}\psi^+$) are $\mathscr{O}(\epsilon^2)$ if the derivatives are $\mathscr{O}(\epsilon)$, so we ignore these terms.

$$\psi^-(x,y,z,\mu,\omega) = -\frac{\mu}{\Sigma_t(\mathbf{r})}\frac{\partial}{\partial z}\psi^+(x,y,z,\mu,\omega)+\mathscr{O}(\epsilon^2)\ . \qquad (5.8)$$

Using Eq. (5.8) in Eq. (5.5), we obtain:

$$\begin{aligned}
&\left[\sqrt{1-\mu^2}\left(\cos\omega\frac{\partial}{\partial x}+\sin\omega\frac{\partial}{\partial y}\right)+\Sigma_t(\mathbf{r})\right]\psi^+(x,y,z,\mu,\omega)\\
&\qquad + \mu\frac{\partial}{\partial z}\left[-\frac{\mu}{\Sigma_t(\mathbf{r})}\frac{\partial}{\partial z}\psi^+(x,y,z,\mu,\omega)\right] = \frac{Q(\mathbf{r})}{4\pi}\ . \qquad (5.9)
\end{aligned}$$

We move the equivalent of the axial TL term to the source to obtain:

$$\begin{aligned}
&\left[\sqrt{1-\mu^2}\left(\cos\omega\frac{\partial}{\partial x}+\sin\omega\frac{\partial}{\partial y}\right)+\Sigma_t(\mathbf{r})\right]\psi^+(x,y,z,\mu,\omega)\\
&\qquad = \frac{Q(\mathbf{r})}{4\pi}+\frac{\partial}{\partial z}\frac{1}{\Sigma_t(\mathbf{r})}\frac{\partial}{\partial z}\mu^2\psi^+(x,y,z,\mu,\omega)\ , \qquad (5.10)
\end{aligned}$$

and we average these equations over an axial slice from $z_{k-1/2}$ to $z_{k+1/2}$. Operating on Eq. (5.10) by:

$$\frac{1}{h_k}\int\limits_{z_{k-1/2}}^{z_{k+1/2}}(\cdot)dz\ ;\ h_k = z_{k+1/2}-z_{k-1/2}\ ,$$

we obtain:

$$\begin{aligned}
&\left[\sqrt{1-\mu^2}\left(\cos\omega\frac{\partial}{\partial x}+\sin\omega\frac{\partial}{\partial y}\right)+\Sigma_{t,k}(x,y)\right]\psi_k^+(x,y,\mu,\omega) = \qquad (5.11)\\
&\frac{Q_k(x,y)}{4\pi}+\frac{1}{h_k\Sigma_{t,k}(x,y)}\frac{\partial}{\partial z}\mu^2\left[\psi^+_{k+1/2}(x,y,\mu,\omega)-\psi^+_{k-1/2}(x,y,\mu,\omega)\right]\ .
\end{aligned}$$

The slice-edge even-parity angular flux $\psi^+_{k\pm1/2}$ can be obtained from the 1D transport equation. However, the TL is approximated as isotropic in MPACT. The isotropic TL using $\psi^+_{k\pm1/2}$ could be calculated directly:

$$J_{z,k\pm1/2} = \frac{1}{4\pi}\int\limits_{-1}^{1}\mu^2\int\limits_{0}^{2\pi}\psi^+_{k\pm1/2}(x,y,z,\mu,\omega)d\omega d\mu\ , \tag{5.12}$$

but this may not agree with the neutron current in the 1D equation, which would lead to neutron imbalance. Instead, we assume that the angular flux is isotropic $[\psi^+(x,y,\mu,\omega) = \frac{1}{4\pi}\phi(x,y)]$:

$$\begin{aligned}\frac{1}{4\pi}\int\limits_{-1}^{1}\mu^2\int\limits_{0}^{2\pi}\psi^+_{k\pm1/2}(x,y,z,\mu,\omega)d\omega d\mu &= \frac{1}{4\pi}\phi_{k\pm1/2}(x,y)\left(\frac{1}{2}\int\limits_{-1}^{1}\mu^2 d\mu\right)\ , \\ &= \frac{1}{4\pi}\frac{\phi_{k\pm1/2}(x,y)}{3}\ .\end{aligned} \tag{5.13}$$

Using Eq. (5.13) in Eq. (5.11), we obtain:

$$\begin{aligned}&\left[\sqrt{1-\mu^2}\left(\cos\omega\frac{\partial}{\partial x}+\sin\omega\frac{\partial}{\partial y}\right)+\Sigma_{t,k}(x,y)\right]\psi^+_k(x,y,\mu,\omega) = \\ &\qquad \frac{Q_k(x,y)}{4\pi} + \frac{1}{4\pi}\frac{1}{3\Sigma_{t,k}(x,y)h_k}\frac{\partial\phi(x,y,z)}{\partial z}\bigg|_{k-1/2}^{k+1/2}\ .\end{aligned} \tag{5.14}$$

Now, the axial TL term looks like a Fick's law approximation to the current on the top and bottom faces of the slice:

$$J_{z,k\pm1/2}(x,y) = -D_k(x,y)\frac{\partial\phi(x,y,z)}{\partial z}\bigg|_{z=k\pm1/2}\ . \tag{5.15}$$

$$\begin{aligned}&\left[\sqrt{1-\mu^2}\left(\cos\omega\frac{\partial}{\partial x}+\sin\omega\frac{\partial}{\partial y}\right)+\Sigma_{t,k}(x,y)\right]\psi^+_k(x,y,\mu,\omega) = \\ &\qquad \frac{1}{4\pi}\left(Q_k(x,y) - \frac{\left[J_{z,k+1/2}(x,y)-J_{z,k-1/2}(x,y)\right]}{h_k}\right)\ .\end{aligned} \tag{5.16}$$

If the axial TL term in Eq. (5.16) is discretized on the coarse mesh, it will be equivalent to the standard TL approximation in MPACT. This simple derivation gives us a new perspective on the standard approximation used in MPACT and its connection to the anisotropic TL method. The standard method ignores the odd polar-parity angular flux and assumes isotropic radial and axial TL. Thus, any method that incorporates some approximate solution for the odd polar-parity angular flux should improve the accuracy, even if the approximation is crude. This is part of the motivation and justification for the method developed in Sec. 5.1.2.

5.1.2 2D Coarse-Mesh S$_N$ for Odd-Parity Flux

In Sec. 4.4, we observed that the spatial shape of the axial TL within a pin cell has very little effect on the accuracy of the final solution. The method in the present section takes advantage of this observation by treating the antisymmetric component of the axial TL on the coarse mesh only. This method should be significantly faster than the previous anisotropic TL method [9] without sacrificing accuracy.

To derive these equations, we start by discretizing Eq. (3.1) over a coarse cell. We operate by $\frac{1}{A_{ij}} \iint\limits_{ij} (\cdot) dxdy$, obtaining:

$$\frac{\Omega_x}{h_i}\left[\psi_{i+1/2,j}(z,\mu,\omega) - \psi_{i-1/2,j}(z,\mu,\omega)\right] + \frac{\Omega_y}{h_j}\left[\psi_{i,j+1/2}(z,\mu,\omega) - \psi_{i,j-1/2}(z,\mu,\omega)\right] \\ + \hat{\Sigma}_{t,ij}(z)\psi_{ij}(z,\mu,\omega) + \mu\frac{\partial \psi_{ij}(z,\mu,\omega)}{\partial z} = \frac{Q_{ij}(z)}{4\pi} \ . \quad (5.17)$$

Here, we have assumed that the homogenized total XS is isotropic,

$$\hat{\Sigma}_{t,ij}(z) = \frac{\int\limits_{x_{i-1/2}}^{x_{i+1/2}} \int\limits_{y_{j-1/2}}^{y_{j+1/2}} \Sigma_t(x,y,z)\phi(x,y,z)dxdy}{\int\limits_{x_{i-1/2}}^{x_{i+1/2}} \int\limits_{y_{j-1/2}}^{y_{j+1/2}} \phi(x,y,z)dxdy} \ , \quad (5.18)$$

although the rigorous definition would be anisotropic,

$$\hat{\Sigma}_{t,ij}(z,\mu,\omega) = \frac{\int\limits_{x_{i-1/2}}^{x_{i+1/2}} \int\limits_{y_{j-1/2}}^{y_{j+1/2}} \Sigma_t(x,y,z)\psi(x,y,z,\mu,\omega)dxdy}{\int\limits_{x_{i-1/2}}^{x_{i+1/2}} \int\limits_{y_{j-1/2}}^{y_{j+1/2}} \psi(x,y,z,\mu,\omega)dxdy} \ . \quad (5.19)$$

Using an isotropic homogenized total XS is a common approximation, and it should be suitable here. Where the anisotropic homogenized cross section had a significant effect before, in Chapter 4, it was operating on the 1D angular flux. Here, the homogenized cross section operates on only the odd-parity angular flux, which is smaller in magnitude than the even-parity flux. The odd-parity angular flux does not directly affect the 3D scalar flux solution; it only contributes indirectly to the solution through the anisotropic TL moments. As a result, the error in the isotropic approximation is not large. Ignoring this anisotropy is similar to the approximation of ignoring the anisotropic collision term in Eq. (3.38).

Next, we evaluate Eq. (5.17) at $(+\mu)$ and $(-\mu)$, and subtract and add these equations in the same manner as before:

$$\frac{\Omega_x}{h_i}\left[\psi^+_{i+1/2,j}(z,\mu,\omega)-\psi^+_{i-1/2,j}(z,\mu,\omega)\right]+\frac{\Omega_y}{h_j}\left[\psi^+_{i,j+1/2}(z,\mu,\omega)-\psi^+_{i,j-1/2}(z,\mu,\omega)\right] \tag{5.20a}$$

$$+\hat{\Sigma}_{t,ij}(z)\psi^+_{i,j}(z,\mu,\omega)=\frac{Q_{ij}(z)}{4\pi}-\mu\frac{\partial\psi^-_{ij}(z,\mu,\omega)}{\partial z}\ ,$$

$$\frac{\Omega_x}{h_i}\left[\psi^-_{i+1/2,j}(z,\mu,\omega)-\psi^-_{i-1/2,j}(z,\mu,\omega)\right]+\frac{\Omega_y}{h_j}\left[\psi^-_{i,j+1/2}(z,\mu,\omega)-\psi^-_{i,j-1/2}(z,\mu,\omega)\right] \tag{5.20b}$$

$$+\hat{\Sigma}_{t,ij}(z)\psi^-_{ij}(z,\mu,\omega)=-\mu\frac{\partial\psi^+_{ij}(z,\mu,\omega)}{\partial z}\ .$$

We average Eqs. (5.20) over an axial slice from $z_{k-1/2}$ to $z_{k+1/2}$. Operating by $\frac{1}{h_k}\int\limits_{z_{k-1/2}}^{z_{k+1/2}}(\cdot)dz$, we obtain:

$$\frac{\Omega_x}{h_i}\left[\psi^+_{i+1/2,j,k}(\mu,\omega)-\psi^+_{i-1/2,j,k}(\mu,\omega)\right]+\frac{\Omega_y}{h_j}\left[\psi^+_{i,j+1/2,k}(\mu,\omega)-\psi^+_{i,j-1/2,k}(\mu,\omega)\right]$$
$$+\hat{\Sigma}_{t,ij,k}\psi^+_{i,j,k}(\mu,\omega)=\frac{Q_{i,j,k}}{4\pi}-\frac{\mu}{h_k}\left[\psi^-_{i,j,k+1/2}(\mu,\omega)-\psi^-_{i,j,k-1/2}(\mu,\omega)\right]\ , \tag{5.21a}$$

$$\frac{\Omega_x}{h_i}\left[\psi^-_{i+1/2,j,k}(\mu,\omega)-\psi^-_{i-1/2,j,k}(\mu,\omega)\right]+\frac{\Omega_y}{h_j}\left[\psi^-_{i,j+1/2,k}(\mu,\omega)-\psi^-_{i,j-1/2,k}(\mu,\omega)\right]$$
$$+\hat{\Sigma}_{t,ij,k}\psi^-_{i,j,k}(\mu,\omega)=-\frac{\mu}{h_k}\left[\psi^+_{i,j,k+1/2}(\mu,\omega)-\psi^+_{i,j,k-1/2}(\mu,\omega)\right]\ . \tag{5.21b}$$

Eq. (5.21a) is the coarse-mesh even-parity 2D transport equation. This equation is not solved directly; instead, the even-parity transport is solved on the fine mesh. To obtain the continuous form of the even-parity 2D transport equation, we integrate

Eq. (5.5) over an axial slice. Operating by $\frac{1}{h_k}\int\limits_{z_{k-1/2}}^{z_{k+1/2}}(\cdot)dz$, we obtain:

$$\left[\sqrt{1-\mu^2}\left(\cos\omega\frac{\partial}{\partial x}+\sin\omega\frac{\partial}{\partial y}\right)+\Sigma_{t,k}(x,y)\right]\psi_k^+(x,y,\mu,\omega) \\ =\frac{Q_k(x,y)}{4\pi}-\frac{\mu}{h_k}\left[\psi_{k+1/2}^-(x,y,\mu,\omega)-\psi_{k-1/2}^-(x,y,\mu,\omega)\right]\ . \quad (5.22)$$

Eq. (5.22) is solved on the fine mesh.

The solution of the coarse-mesh even-parity equation would be a rough approximation to the solution of the fine-mesh even-parity equations, but we do not employ a coarse-mesh even-parity equation. The solution to the coarse-mesh odd-parity equation, which we do employ, is also an approximation to a potential fine-mesh odd-parity solution. However, this solution does not directly affect the scalar flux or the isotropic moments of the leakage between coarse cells. The odd-parity equation is only used to determine higher-order polar moments of the anisotropic radial TL. We can still obtain a relatively accurate overall solution without a high fidelity solution for these moments. Thus, the low-fidelity solution for the odd-parity flux should be acceptable.

Eq. (5.21b) is the coarse-mesh odd-parity 2D transport equation. It is a Cartesian 2D transport equation that can be solved using S_N. This equation has 3 unknowns (2 downwind surface angular fluxes, 1 cell-average flux). It is assumed that two upwind angular fluxes are known. Two additional equations are required. These equations come from a closure relationship between the surface and cell-average angular fluxes. Diamond difference can be used, but it would be inaccurate and likely unstable due to the typical optical thickness of a pin cell. Instead, step characteristics is used [72]:

$$\psi_R = q+(\psi_L-q)(1-\rho)e^{-\alpha} \\ \quad +(\psi_B-q)\rho\left(1-e^{-\alpha}\right)/\alpha \qquad \rho<1 \qquad (5.23a)$$

$$\psi_T = q+(\psi_L-q)\left(1-e^{-\alpha}\right)/\alpha \qquad \rho<1 \qquad (5.23b)$$

or

$$\psi_R = q+(\psi_B-q)\left(1-e^{-\beta}\right)/\beta \qquad \rho>1 \qquad (5.23c)$$

$$\psi_T = q+(\psi_L-q)\left(1-e^{-\beta}\right)/(\rho\beta) \\ \quad +(\psi_B-q)(1-1/\rho)e^{\beta}\ , \qquad \rho>1 \qquad (5.23d)$$

where

$$q = \frac{Q}{\hat{\Sigma}_t}\ , \tag{5.24a}$$

$$\alpha = \frac{\hat{\Sigma}_t h_x}{\xi}\ , \tag{5.24b}$$

$$\beta = \frac{\hat{\Sigma}_t h_y}{\eta}\ , \tag{5.24c}$$

$$\rho = \frac{\alpha}{\beta}\ . \tag{5.24d}$$

Here, ψ_R and ψ_T are the "right" and "top" surface angular fluxes, which are the downwind or unknown fluxes. The upwind fluxes on the left and bottom, ψ_L and ψ_B, are known from a boundary condition or previous step. The step characteristics scheme is well-suited to this problem, which is effectively a purely absorbing problem with a fixed source from transverse leakage. This problem is solved using discrete ordinates, with angle index n:

$$\Omega^n = \left(\sqrt{1-\mu_n^2}\cos\omega_n, \sqrt{1-\mu_n^2}\sin\omega_n, \mu_n\right) = (\xi_n, \eta_n, \mu_n)\ . \tag{5.25}$$

The quadrature used for this solution is the same as the quadrature that is used for the even-parity MOC. Using Eq. (5.23a) in Eq. (5.21b), with known "upwind" surface fluxes.

$$\psi^-_{n,ij,k} = \frac{\frac{2\xi_n}{h_i}\psi_{n,i\mp1/2,j,k} + \frac{2\eta_n}{h_j}\psi_{n,i,j\mp1/2,k} - \frac{\mu_n}{h_k}\left[\psi^+_{n,ij,k+1/2} - \psi^+_{n,ij,k-1/2}\right]}{\hat{\Sigma}_{t,k,ij} + \frac{2\xi_n}{h_i} + \frac{2\eta_n}{h_j}}\ , \tag{5.26}$$
$$\xi_n \gtrless 0\ ,\ \eta_n \gtrless 0\ ,\ \mu_n > 0\ .$$

A coarse-mesh S$_N$ should be much faster than the fine-mesh MOC, since there are typically dozens of FSRs (and hundreds of ray segments in a single direction) in a pin cell. This extra work should be a small fraction of the overall run time for MPACT. It could be significantly faster than even the 1D nodal solution, because it would be much less communication-intensive. However, it would be solved with full azimuthal dependence, while the 1D equations are often solved for only the azimuthally isotropic moment and a few additional anisotropic moments. Thus, the run time may be comparable to the 1D solution, depending on how many sweeps are performed during each iteration. The 2D coarse-mesh solution is performed after the 1D calculation, before the 2D MOC calculation. The details of the algorithm are given later in this section.

The solution of Eq. (5.21b) gives the cell-edge fluxes $\psi^-_{i\pm1/2,j,k}$ and $\psi^-_{i,j\pm1/2,k}$, which will be used in calculating the anisotropic radial TL. The slice-edge values $\psi^-_{i,j,k\pm1/2}$ are used to calculate the axial TL term in the even-parity transport Eq. (5.22). While these can be calculated by averaging the cell-average values from the solution of Eq. (5.21b), it is both easier and more accurate to use the solution of the 1D equation. In practice, a Fourier azimuthal expansion on the axial TL terms is used to limit the fine-mesh memory requirements and coarse-mesh parallel communication requirements. With the solution of Eq. (5.22) and Eq. (5.21b), the radial TL terms are calculated using Eq. (5.27).

$$\begin{aligned}J_{r,ij,k}(\mu,\omega) &= \frac{1}{A_{ij}}\iint\limits_{ij}\left(\Omega_x\frac{\partial}{\partial x}+\Omega_y\frac{\partial}{\partial y}\right)\left[\psi^+(x,y,\mu,\omega)+\psi^-(x,y,\mu,\omega)\right]dxdy \\ &= \sum_{s=N,E,S,W}\frac{1}{h_s}\left(\mathbf{\Omega}\cdot\hat{n}_s\right)\left[\psi^+_{ij,s}(\mu,\omega)+\psi^-_{ij,s}(\mu,\omega)\right] \ .\end{aligned} \tag{5.27}$$

Here, $\hat{n}_s$ is the outward unit normal vector from the surface (North, East, West, or South), and h_s is the distance between the two parallel surfaces. The radial TL $J_{r,ij,k}(\mu,\omega)$ is expanded in Fourier moments in (ω) and Legendre moments in (μ), similar to the anisotropic TL methods from Sec. 3.1 [9],[73].

$$TL_{s/c,p,ij,k}(\mu) = \int_0^{2\pi} f_{s/c,p}(\omega)J_{r,ij,k}(\mu,\omega)d\omega \ , \tag{5.28a}$$

$$f_0(\omega) = 1 \ , \tag{5.28b}$$

$$f_{s,p}(\omega) = \sin(p\omega) \ , \tag{5.28c}$$

$$f_{c,p}(\omega) = \cos(p\omega) \ , \tag{5.28d}$$

$$\begin{aligned}&TL_{l,s/c,p,ij,k} \\ &= \int_{-1}^{1} P_l(\mu)\left(\sum_{s=N,E,S,W}\int_0^{2\pi} f_{s/c,p}(\omega)\frac{(\mathbf{\Omega}\cdot\hat{n}_s)}{h_s}\left[\psi^+_{ij,k,s}(\mu,\omega)+\psi^-_{ij,k,s}(\mu,\omega)\right]d\omega\right)d\mu \ .\end{aligned} \tag{5.29}$$

The homogenized XS can be calculated from the solution of Eq. (5.22), using either isotropic or anisotropic homogenization of the total XS. If anisotropic homogenization is used, the solution of Eq. (5.21b) can also be incorporated.

The 1D solution is not changed in this new method except for the way its inputs are calculated. The solution of the 1D equation gives the anisotropic source term for Eq. (5.21b) on the coarse mesh.

The 2D/1D polar-parity equations with coarse-mesh 2D odd-parity transport are given by Eq. (5.22) and Eq. (5.21b), with $\hat{\Sigma}_{t,k,ij}$ defined by Eq. (5.18), axial TL for both the even and odd-parity 2D equations defined by the standard 1D equations, and radial TL defined by Eq. (5.29). These equations should be more accurate than the standard, isotropic TL equations used in MPACT. The accuracy can be improved further if an anisotropic homogenized XS is used in the 1D solution. The 2D coarse-mesh S_N does not give the spatial distribution of the odd-parity flux within a coarse cell, we assume that the spatial distribution is flat. The homogenized total XS is then given by:

$$\hat{\Sigma}_{t,ij,k}(\mu) = \frac{\int\limits_{x_{i-1/2}}^{x_{i+1/2}} \int\limits_{y_{j-1/2}}^{y_{j+1/2}} \Sigma_{t,k}(x,y) \left[\psi_k^+(x,y,\mu) + \psi_{ij,k}^-(\mu)\right] dxdy}{\int\limits_{x_{i-1/2}}^{x_{i+1/2}} \int\limits_{y_{j-1/2}}^{y_{j+1/2}} \left[\psi_k^+(x,y,\mu) + \psi_{ij,k}^-(\mu)\right] dxdy} \,. \tag{5.30}$$

This assumption is clearly imperfect, but in practice it improves the solution significantly over the isotropic homogenization from Eq. (5.18). The odd-parity flux could also be interpolated using a non-flat function within the coarse cell, but it is not apparent what an appropriate shape would be. One option is to use the scalar flux,

$$\psi_k^-(x,y,\mu) = \psi_{ij,k}^-(\mu) \frac{A_{ij}\phi_k(x,y)}{\int\limits_{x_{i-1/2}}^{x_{i+1/2}} \int\limits_{y_{j-1/2}}^{y_{j+1/2}} \phi_k(x,y) dxdy} \,, \tag{5.31}$$

but this is much less accurate than the flat distribution. Aside from solving the odd-parity equation on a finer mesh, there does not seem to be an effective way to approximate the shape of the solution within the coarse mesh. The best results are observed when assuming a flat shape. This is demonstrated in Sec. 5.2.

Modifying MPACT to allow only even polar anisotropy (and still ignoring the odd component) does not improve accuracy in any appreciable way, because the odd polar anisotropy is significant near transport boundaries, which is precisely where the axial and radial TL approximations are most important. Axial boundary layers create significant axial TL, which is strongly antisymmetric. This strong antisymmetric source generates larger odd-parity angular fluxes. Thus, the 2D/1D method needs to account for odd polar anisotropy to significantly improve accuracy. The coarse-mesh 2D odd-parity transport equation calculates the odd-parity flux on the coarse-mesh surfaces, which can be used to calculate radial TL with odd polar anisotropy. It also gives a spatially averaged estimate of the odd-parity flux within a pin cell, which enables the calculation of an anisotropic homogenized XS. This should improve the axial flux shape calculated by the 1D solution, and in turn improve the overall 3D flux distribution of the final solution. The solution of this new odd-parity equation is fast compared to the overall run time of MPACT. Timing results are given in Sec. 5.2; the computational cost of the actual coarse-mesh 2D S_N solution is less than 5% of the overall run time.

The proposed algorithm for a steady-state eigenvalue problem in MPACT with a radial 2D coarse-mesh odd-parity transport solution is given in Algorithm 1. The algorithm is taken from the MPACT theory manual [74]. Updates corresponding to the method proposed here are denoted by the dagger (†) symbol. The required changes do not significantly affect the MPACT iteration scheme. The new 2D coarse-mesh transport problem is solved immediately before the 2D even-parity transport equation using MOC.

5.1.3 Intermediate-Mesh MOC Solution of the Odd-Parity Equation

The third option we have for the odd-parity angular flux is to solve for it on an intermediate mesh. This intermediate mesh may have a few flat source regions (FSRs) on a pin cell that radially divides the materials, but would not have several radial divisions within a material or azimuthal divisions within the pin, as the fine mesh does. An example of the proposed mesh is given in Fig. 5.1, with hypothetical MOC rays traced through the geometry. This would require an MOC solution, although the ray spacing could be much larger than the even-parity solution because the flat source regions are much larger. It should still be much faster than the fully anisotropic MOC without polar-parity. The advantage of solving for the odd-parity angular flux on the material mesh level is that it allows for more accurate calculation of the anisotropic homogenized 1D XS. The anisotropic homogenized XS can significantly improve accuracy for certain problems [73], but most of that benefit is already realized by the method in Sec. 5.1.2, where the odd-parity flux is assumed flat over a coarse cell. This will be demonstrated in the results.

Algorithm 1 Algorithm for solving an eigenvalue problem in MPACT

```
Update macroscopic cross sections from resonance treatment (subgroup) calculations.
Guess initial source ($\phi^{(0)}$) and eigenvalue ($k_{eff}^{(0)}$).
while $\phi^{(n)}$ and $k_{eff}^{(n)}$ not converged do
    if using CMFD, then
        Generate coarse-grid quantities from the fine-grid fluxes and leakages.
        Solve the CMFD eigenvalue problem iteratively to obtain an updated eigenvalue ($k_{eff}^{(n+1)}$) and coarse-grid scalar flux
        Update the fine-grid scalar flux/fission source ($\phi^{(n+1/2)}$).
    end if
    if 2D/1D then
        Solve the 1D axial equation to update the scalar fluxes.
        Update the axial leakage with the 1D solution
    end if
    for each energy group do
        † Obtain $\psi^{-}$ by performing sweeps on the coarse-mesh 2D odd-parity transport equation, Eq. (5.21b) using $\psi^{+}$ from 1D solution
        Obtain $\psi^{+}$ and $\phi^{(n+1)}$ by performing transport sweep(s) on the 2D radial transport equations, Eq. (5.22)
        † Calculate the anisotropic homogenized $\hat{\Sigma}_t$ using Eq. (5.30)
    end for
end while
```

This option is less intruiging than the previous method because the user would likely have to specify an additional mesh for the odd-parity problem, which may require understanding of this method well beyond the scope of what should be expected from a typical user. On the other hand, the coarse-mesh method from Sec. 5.1.2 uses constructs that already exist within the code without requiring any significant additional user input. Additionally, the odd-parity MOC may have a non-negligible run time footprint, and the implementation could be complicated. The homogenized XS can have some effect, but it is typically not important, and the simpler method captures most of that effect. There is little motivation to develop this method, which would be significantly slower than the standard 2D/1D method with isotropic TL. However, it may be useful for problems where the homogenization effect is significant and it is practically necessary to correct it.

5.1.4 Full MOC Solution of the Odd Parity Equation

The final option considered involves solving the odd-parity transport equation on the fine mesh. This is potentially a very accurate (albeit expensive) way to calculate a

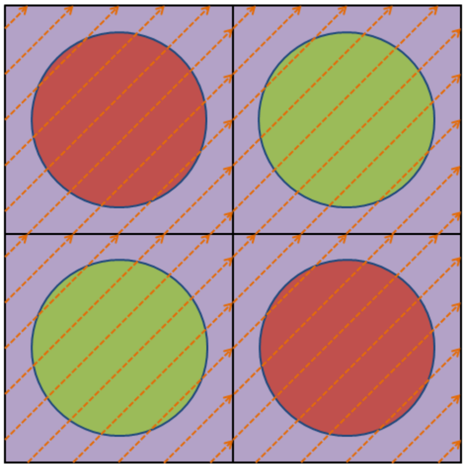

Figure 5.1: Intermediate mesh for odd-parity problem

fine-mesh axial TL shape in a 2D/1D method. However, we observed in Sec. 4.4 that the effect of the spatial shape of axial TL within a pin cell is usually negligible. This method would be expensive because it would double the time spent on MOC, and there are other potential problems without an immediately apparent solution. For example, passing ray-level data axially between processes will be, without question, prohibitively expensive. While it may be possible to develop a method of this type that has a computational cost within reason, it would likely have no tangible benefit. The MOC equations with full polar dependence can be solved without any of the complications or disadvantages of polar-parity.

5.2 2D/1D Polar-Parity Results

The method described in Section 5.1.2 was implemented in MPACT. The purpose of implementing this method is to obtain accuracy equivalent or close to the accuracy of the previously existing MPACT methods for using anisotropic TL ([9],[73]), while significantly reducing the run time. Two test cases are used to demonstrate that the accuracy of these methods is sufficient. The first case is a homogeneous fuel problem from Sec. 4.3. This problem demonstrates the validity of the 2D/1D polar parity method in the absence of pin homogenization error. In this case, the polar-parity 2D/1D method produces results close to the reference solution. The 3D C5G7 benchmark is used to demonstrate that the new method is significantly faster than the old method, and nearly as fast as the standard 2D/1D method in MPACT. The results for the 3D C5G7 benchmark are not as close to the reference solution because

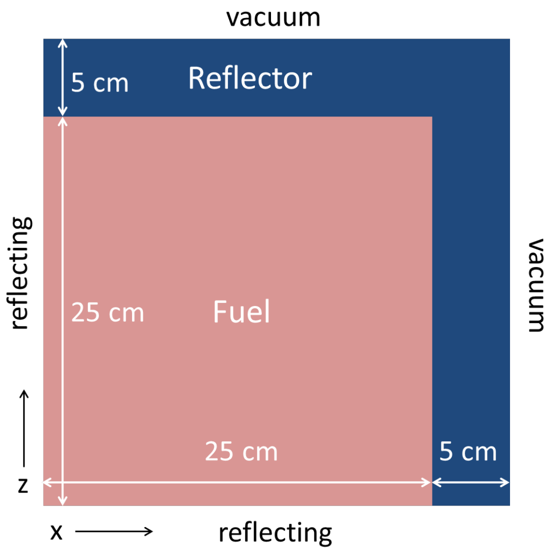

Figure 4.4: Homogeneous fuel (repeated from page 76)

the homogenization error is not being treated correctly. However, the accuracy is still improved compared to the standard isotropic TL case.

5.2.1 Homogeneous Fuel Test Problem

The homogeneous fuel problem is the same problem that was used in Sec. 4.3. It is designed to expose the fundamental deficiency in the isotropic TL approximation used by many 2D/1D codes. The problem uses 2-group fuel and reflector XS from the Takeda benchmark [31]. The geometry is given in Fig. 4.4. It is a 2D problem, with a 25 cm x 25 cm block of fuel surrounded by 5 cm of reflector on two sides. The other two sides have reflecting boundary conditions. In MPACT, this is solved using the 2D/1D method, with the MOC solver in the x direction and the 1D axial solver in the z direction. The reference solution is obtained by solving the 2D problem using 2D MOC. The problem is discretized into 1 cm square coarse cells, with a 0.5 mm fine-mesh size (i.e., flat source region size) in the x direction. Table 5.1 shows the eigenvalue, RMS power, and maximum power error for this problem using each TL method. When the old (full) anisotropic TL method is used, the eigenvalue error decreases from -156 pcm to +9 pcm, and the RMS and maximum pin power errors are both decreased by more than a factor of 2. When the new polar-parity method is used, the eigenvalue error is less than 1 pcm. The RMS and maximum pin power errors are similar to the previous method. The pin power errors using each method are given in Figs. 4.5a, 4.5b, and 5.3c. There is a clear improvement in the power

Table 5.1: Eigenvalue error and pin power errors for 1D Z, 2D X-Z problem

1D Method	P_1	P_3	P_3	P_3
TL Method	ISO	ISO	ANISO (FULL)	ANISO (PARITY)
k_{eff} error [pcm]	-454	-156	+9	0
RMS power error (%)	1.04	0.30	0.13	0.13
Max power error (%)	4.85	1.31	0.46	0.51

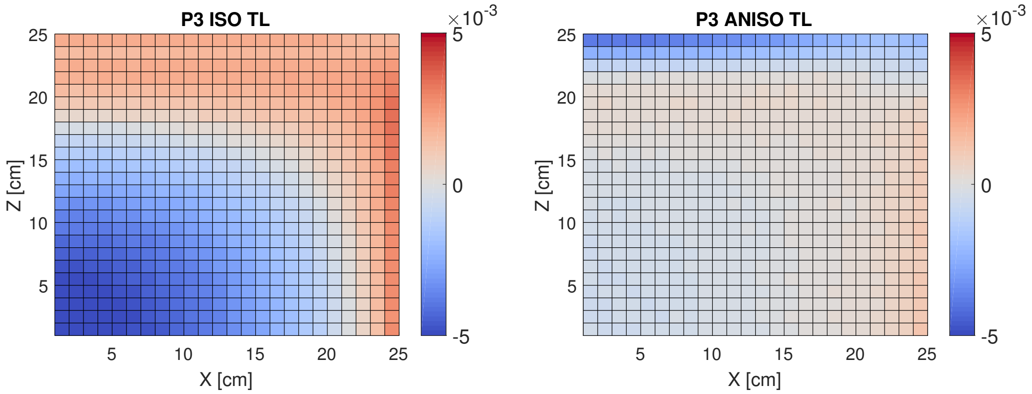

(a) P_3 with isotropic TL (repeated from page 77)

(b) P_3 with anisotropic TL (repeated from page 77)

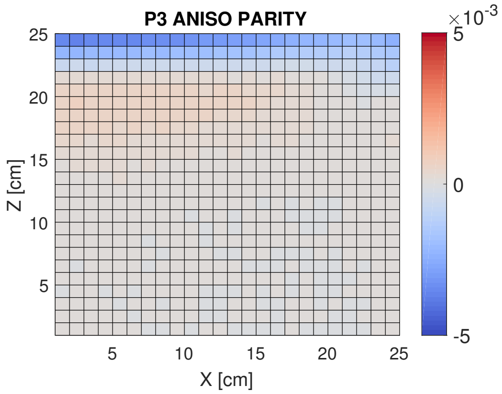

(c) P_3 with anisotropic TL (parity)

Figure 5.3: 2D homogeneous fuel problem power error (absolute)

shape when using the anisotropic TL method. With anisotropic TL, the 1D/1D P_3 method is very close to the 2D transport reference, with the only significant error occuring at the axial interface between the fuel and reflector, which is difficult for 1D P_3 to resolve. The results are similar whether the old or new method for anisotropic leakage is used.

5.2.2 3D C5G7 Benchmark

The 3D C5G7 benchmark [29] is used to demonstrate the speedup achieved by this method compared to the old method for calculating anisotropic TL. The results also show the effectiveness of the anisotropic XS homogenization. The radial geometry is repeated in Fig. 4.24.

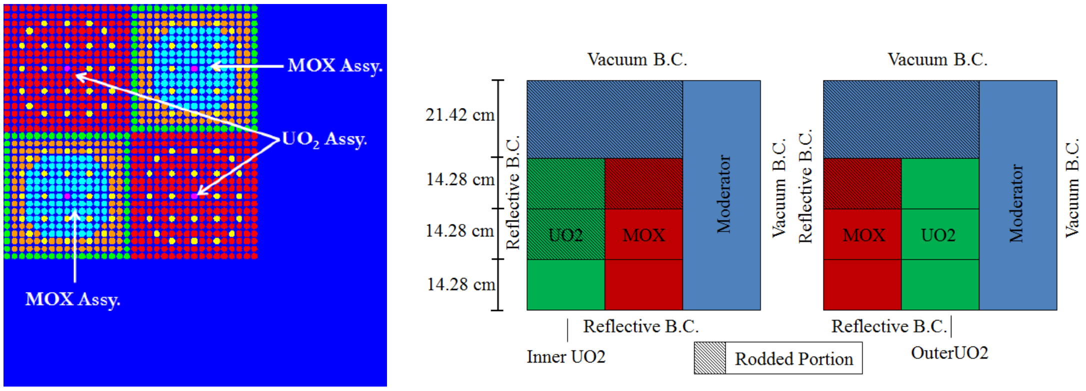

(a) C5G7 radial geometry (repeated from page 90)

(b) C5G7 axial geometry (repeated from page 90)

Figure 5.4: C5G7 benchmark problem geometry

The discretization is the same as before. Pin power and eigenvalue results, along with run times for the 3D C5G7 benchmark for the four cases are given in Tables 5.2, 5.3, and 5.4. The different transverse leakage methods are:

- ISOTL: 2D/1D with isotropic TL, the standard method in MPACT and many 2D/1D codes
- ODD-P: 2D/1D with polar-parity and 2D coarse-mesh S$_N$ for odd-parity equation
- MOM-P: 2D/1D with old anisotropic leakage method; full polar domain in MOC solution, no symmetry
- SYM-P: 2D/1D with TL that is symmetric in the polar angle, odd-parity angular flux assumed to be zero.
- -P: order P Fourier expansion in the azimuthal angle of the axial and radial TL

The goal is for the ODD-P method to produce a similar solution to the equivalent MOM-P method, but in significantly less time. The SYM-P method is the ODD-P

method without the 2D coarse-mesh S_N. SYM-P should be just as fast as ODD-P but will not give the same solution as the MOM-P method. This shows that the run time of the 2D coarse-mesh S_N is negligible, and that it has a significant effect on the accuracy of the result.

The eigenvalues improve, but the pin powers become less accurate when going from isotropic to anisotropic TL. This suggests cancellation of error, with the isotropic TL solution appearing to be more accurate than it truly is. The results in Sec. 4.3, show that the anisotropic TL performs significantly better when there is no homogenization error. To show that the anisotropic TL is truly more accurate when the homogenization error is corrected, the result using polar XS homogenization is given.

Table 5.2: 3D C5G7 unrodded benchmark results, SHIFT reference

TL	XS	k_{eff}	Error [pcm]	RMS (%)	Max (%)	Time [min]	Time [relative]
ISOTL	ISO	1.14239	-64	0.27	0.83	32.0	1.0
ODD-0	ISO	1.14241	-62	0.27	0.79	28.9	0.9
MOM-0	ISO	1.14241	-62	0.27	0.79	42.5	1.3
ODD-1	ISO	1.14307	4	0.30	0.97	37.8	1.2
MOM-1	ISO	1.14309	6	0.30	0.95	51.3	1.6
SYM-1	ISO	1.14253	-51	0.27	0.85	42.7	1.3
ODD-1	POL	1.14306	3	0.14	0.52	44.1	1.4
MOM-1	POL	1.14296	-7	0.13	0.40	104.3	3.3

Table 5.3: 3D C5G7 rodded A benchmark results, SHIFT reference

TL	XS	k_{eff}	Error [pcm]	RMS (%)	Max (%)	Time [min]	Time [relative]
ISOTL	ISO	1.12750	-62	0.25	0.71	29.1	1.0
ODD-0	ISO	1.12750	-62	0.28	0.75	29.7	1.0
MOM-0	ISO	1.12750	-62	0.28	0.76	44.7	1.5
ODD-1	ISO	1.12829	17	0.36	1.12	39.2	1.3
MOM-1	ISO	1.12831	19	0.38	1.17	51.8	1.8
SYM-1	ISO	1.12765	-47	0.28	0.74	37.6	1.3
ODD-1	POL	1.12817	5	0.21	0.68	41.4	1.4
MOM-1	POL	1.12803	-9	0.17	0.52	93.0	3.2

The magnitude of the errors is not the focus of these results. What is important is that the new parity method for anisotropic TL produces the same results as the the old method. This is clear from the similar eigenvalue, RMS, and maximum pin power errors. This is true both with azimuthally isotropic TL and the Fourier expansion

Table 5.4: 3D C5G7 rodded B benchmark results, SHIFT reference

TL	XS	k_{eff}	Error [pcm]	RMS (%)	Max (%)	Time [min]	Time [relative]
ISOTL	ISO	1.07698	-76	0.30	0.98	25.1	1.0
ODD-0	ISO	1.07699	-75	0.32	1.03	31.0	1.2
MOM-0	ISO	1.07698	-69	0.32	1.03	46.9	1.9
ODD-1	ISO	1.07798	24	0.54	2.20	39.5	1.6
MOM-1	ISO	1.07801	27	0.59	2.46	53.6	2.1
SYM-1	ISO	1.07676	-98	0.32	0.91	38.4	1.5
ODD-1	POL	1.07776	2	0.33	1.38	44.6	1.8
MOM-1	POL	1.07760	-14	0.25	0.82	93.2	3.7

azimuthal TL. With the azimuthally isotropic TL, only the polar dependence of the radial and axial TL is treated to a higher order than isotropic. This is not as accurate, but it is much faster. With the 2D coarse-mesh odd-parity S_N, the polar component of the TL can be added without any significant increase to the run time. Conversely, the old anisotropic TL method has a run time that is 30%, 50%, and 90% longer than the standard method for the three different cases.

The azimuthal TL has a longer run time because it requires more calculations to determine angular moments of surface leakage for each ray that crosses a coarse-mesh boundary. Thus, the polar-parity method is not as fast as the standard method when azimuthal moments are added to the TL, but it is still significantly faster than the old method for anisotropic TL. Compared to ISOTL, the ODD-1 run times are 20%, 30%, and 60% longer for the three cases. The MOM-1 run times for the same cases are 60%, 80%, and 110% longer. The average speedup for the ODD-1 case is 25% compared to the MOM-1 case.

We can also view the speedup from another perspective. The average slowdown using MOM-1 is 84%. With ODD-1, the average slowdown is reduced to 37%. The average slowdown when using MOM-0 is 58%. With ODD-0, that slowdown is reduced to 5% on average.

With the polar XS homogenization, the results for the ODD and MOM methods are not identical. They are similar for the unrodded case, but the ODD polar XS case has significantly greater error for the rodded B case. This makes sense, because the polar XS homogenization is more important for the rodded B case, and the spatially flat odd-parity flux approximation is more detrimental as a result. However, the polar homogenization still improves the solution significantly, and it is much faster with the polar-parity method.

Three options for approximating the spatial distribution of the odd-parity angular flux for XS homogenization are tested:

1. Flat
2. Scalar flux weighted
3. Even-parity flux weighted

The results for the rodded B case are given in Table 5.5. The flat distribution performs significantly better than the other two, which are slightly worse than using an isotropic homogenized XS. Upon closer inspection, it was discovered that scalar flux weighting and even-parity flux weighting produce algebraically equivalent anisotropic XS homogenization source terms, leading to the exact same solution. When using these weighting methods, the antisymmetric anisotropic collision terms (i.e., first and third Legendre moments) are zero, which is likely why the results are poor. Based on this, the spatially flat approximation was used for all other analysis.

Table 5.5: Polar XS homogenization weighting results, rodded B

TL	XS	Weighting	k_{eff}	Error [pcm]	RMS (%)	Max (%)
ODD-1	ISO	N/A	1.07698	-76	0.55	2.21
ODD-1	POL	FLAT	1.07776	2	0.32	1.35
ODD-1	POL	SCALAR	1.07799	25	0.60	2.57
ODD-1	POL	EVEN	1.07799	25	0.60	2.57
MOM-1	POL	MOC	1.07760	-14	0.25	0.82

The error in the axial power shape using the polar-parity method with anisotropic TL and XS is compared to that of the previous method for the three cases in Fig. 5.5. The dashed black line indicates the single standard deviation uncertainty. The uncertainty is very small because the axial power profile is determined by averaging radially over all pins. In all cases, the solution with odd-parity TL and XS is close to the full anisotropic MOC solution.

5.3 Computational and Memory Cost

The anisotropic TL and XS method described in Chapter 3 is more accurate than the isotropic TL and XS method, but it is significantly more demanding of memory and computation. The 2D/1D method with coarse-mesh odd-parity 2D S$_N$ solution is designed to significantly reduce that additional burden without sacrificing too much of the improvement in accuracy.

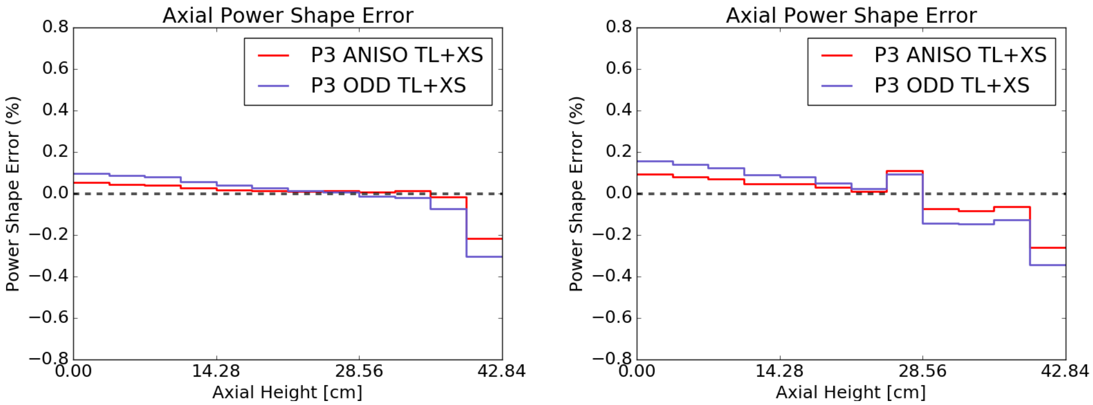

(a) Unrodded (b) Rodded A

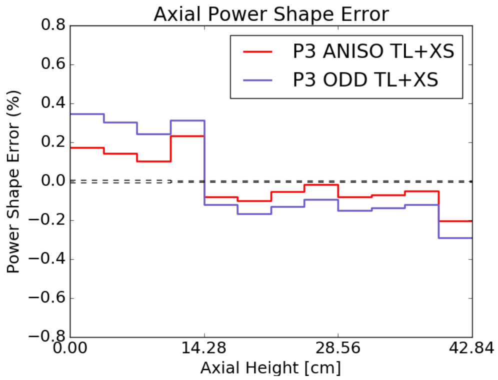

(c) Rodded B

Figure 5.5: Axial power profile errors, C5G7

To compare the memory profile and run time of the several methods, we use the radial lattice from the C5G7 benchmark problem, with 3 axial planes and one process per plane. An azimuthal expansion order of 2 is used. The required memory per process for each method is given in Table 5.6.

Any anisotropic TL method requires a significant increase in memory to store the anisotropic source. Using polar-dependent homogenization does not significantly increase the required memory. The size of the polar-dependent angular flux is only a fraction of the size of the anisotropic MOC source. For example, if 2 cosine and sine moments are used, the anisotropic source is 5 times larger than the polar-dependent angular flux. If azimuthal XS moments are used, then the angular flux storage is equivalent to the MOC source storage.

The MOC type refers to the way the inscattering source is calculated. If it is updated after each group is swept (1G), this is a Gauss-Seidel iteration. If the scattering source is not updated after each group (MG), this is a Jacobi iteration. In the case

Table 5.6: Memory requirements for 2D/1D

TL	XS	MOC Type	Memory [GB]	Memory Ratio
ISO	ISO	1G	0.544	1.00
ODD	ISO	1G	0.772	1.42
MOM	ISO	1G	0.866	1.59
ODD	POLAR	1G	0.783	1.44
MOM	POLAR	1G	0.915	1.68
ISO	ISO	MG	0.632	1.16
ODD	ISO	MG	1.470	2.70
MOM	ISO	MG	2.216	4.07
ODD	POLAR	MG	1.633	3.00
MOM	POLAR	MG	2.561	4.71

of MG, the energy group loop is performed at the ray level. The MG sweep requires the source to be stored for all groups, which is especially expensive for anisotropic TL methods. The difference between 1G and MG is much more pronounced with a larger number of energy groups. As a result, anisotropic TL methods are often memory limited to using only the 1G MOC type with the typical 51 group structure.

For any choice of MOC type and XS homogenization type, the odd parity method requires significantly less memory than the full-anisotropic moment-based equivalent.

To determine the breakdown of run times for each significant piece of the solver, a single-assembly problem was run using 3 axial planes. Only 1 process was used to eliminate communication time. For each outer iteration, the 1D nodal solver performs 5 groups sweeps with 5 inner sweeps each, the S_N solver performs 2 sweeps, and the MOC solver performs 1 sweep. These are the default options. The run times are given in Table 5.7.

Table 5.7: 2D/1D odd-parity coarse-mesh S_N run time

Calculation	Run Time [s]	Fraction
Initialization	18.5	9%
CMFD	4.1	2%
Nodal (1D)	25.7	12%
S_N	3.6	2%
MOC	155.0	75%
Total	206.9	100%

As expected, the run time for the S_N calculation is only a small fraction (2%) of the overall run time. The MOC is by far the most expensive part of the calculation. Even though the individual nodal sweeps are relatively cheap, the nodal calculation is the next most expensive component because the default setting is to perform 25 sweeps for each group in the upscattering range.

The run time for 2D/1D with full anisotropic MOC is given in Table 5.8. The MOC run time is increased by 56%, and the overall run time is increased by 41%.

Table 5.8: 2D/1D full anisotropic TL run time

Calculation	Run Time [s]	Fraction
Initialization	18.5	6%
CMFD	4.4	2%
Nodal (1D)	27.3	9%
MOC	242.4	83%
Total	292.6	100%

The run times given in Table 5.7 and Table 5.8 are for isotropic XS homogenization. With anisotropic XS homogenization, the relative cost of the MOC is greater, and the difference is more significant. These results are given in Table 5.9 and Table 5.10.

Table 5.9: 2D/1D odd-parity coarse-mesh S_N run time, polar XS

Calculation	Run Time [s]	Fraction
Initialization	18.6	8%
CMFD	4.0	2%
Nodal (1D)	25.9	11%
S_N	3.4	2%
MOC	173.8	77%
Total	225.7	100%

Table 5.10: 2D/1D full anisotropic TL run time, polar XS

Calculation	Run Time [s]	Fraction
Initialization	18.5	5%
CMFD	4.3	1%
Nodal (1D)	27.3	7%
MOC	350.8	88%
Total	400.9	100%

With anisotropic XS, the MOC run time is 2 times longer for full anisotropic MOC than for even parity MOC. As a result, the overall run time is 78% longer.

5.4 Local Refinement of TL and XS Approximation

The polar parity sweeper is a faster method than the full-polar anisotropic TL and XS 2D/1D method, but the improvement in accuracy is not quite as good. The lower degree of accuracy is especially apparent for the C5G7 rodded B case, where there are partially inserted control rods in 3 of the 4 assemblies, which leads to especially strong axial gradients. This suggests that the polar parity method may be sufficient for most of the domain, but the full-polar anisotropic treatment may be necessary to capture the 3D transport effects near axial heterogeneities with good accuracy.

Since the full-anisotropic treatment is significantly more expensive, it might be advantageous to have a 2D/1D implementation that uses approximations of varying fidelity in different regions of the core. Specifically, it may be possible to develop a method with the favorable characteristics of both the polar parity method (speed) and the full-polar anisotropic TL and XS method (accuracy) by using the higher-fidelity method only in the regions of the core where it is most important. For many problems, the regions within a few mean-free-paths of an axial transport boundary such as a rod tip is a small fraction of the overall core volume, so the vast majority of the core can be treated with the lower-fidelity method. This could theoretically eliminate most of the additional computational cost associated with the higher-fidelity method.

The concept of local refinement of the TL and XS approximations in a 2D/1D solver is much simpler on paper than in a real implementation. The choice of these approximations affects the structure of the MOC source and sweep kernel. It would be a significant coding challenge to efficiently change between two different types of approximations within a single 2D MOC solution. It would be much easier to require that the TL and XS approximation must be the same throughout each 2D MOC plane, and only allow the fidelity to vary between separate planes. This means that any 2D MOC plane that is near the tip of a control rod would require a high fidelity approximation throughout its entire radial domain. This would reduce the advantage of a local refinement method because the potential locality of the refinement is limited.

Even if an effective local refinement can be implemented, it will not be effective without proper load balancing. If the high fidelity method is used throughout an entire MOC plane, load balancing would only be achievable with a coarse spatial parallel decomposition, where multiple low-fidelity MOC planes can be assigned to a process for each high-fidelity MOC plane assigned to another. With a typical decomposition, each process has only one MOC plane, so load balancing with local refinement is impossible: the overall time is limited by the plane with the longest solve time.

There are many questions about how one would implement an effective local refinement scheme with the desired speed and accuracy properties. Solutions to these issues are outside the scope of this work. However, there is no reason to pursue a time-efficient local refinement scheme unless it is expected to have good accuracy.

To determine whether the idea is viable, a crude local refinement scheme was implemented and tested for the 3D C5G7 benchmarks. It is the 2D/1D method with polar parity, with the full-polar anisotropic TL used in MOC planes immediately above and below the control rod tips. Fig. 5.6 illustrates the idea in a simple cartoon. Fig. 5.6a is a side view of the C5G7 3D rodded B configuration. Fig. 5.6b shows where local refinement would occur with transparent boxes. The strongest leakage effects are localized to the regions around the rod tips, so most of the improvement seen with the higher-fidelity method should be captured by refining only in the vicinity of these axial heterogeneities.

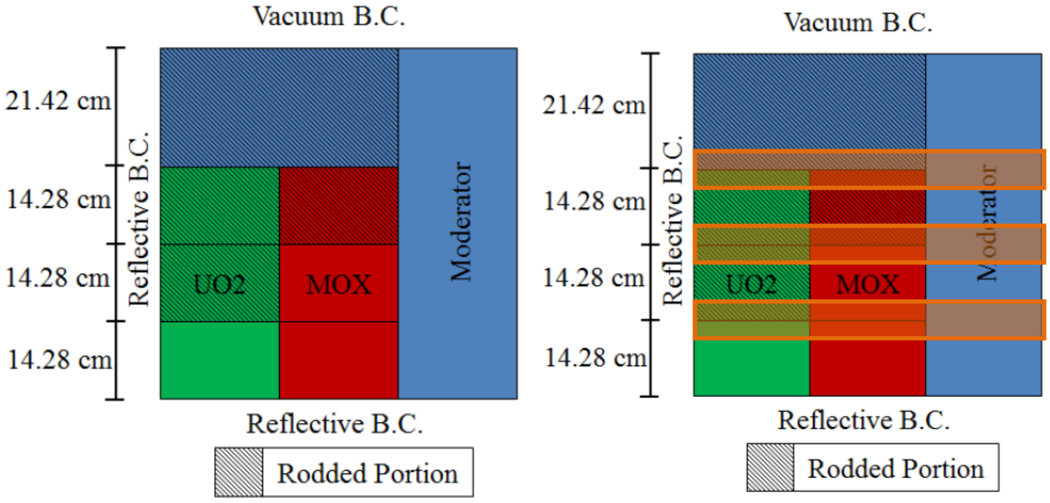

(a) C5G7 rodded B side view (b) C5G7 rodded B refinement zones

Figure 5.6: 2D/1D local refinement

The results using the local refinement are compared to isotropic TL (standard), polar parity, and full-polar anisotropic TL and XS in Table 5.11. All other parameters of the discretization are the same for all cases. The middle block, with “PAR/MOM” TL and “PAR/POL” XS, is the local refinement method using a combination of the polarity parity and full moment-based TL options. The expected accuracy is between the parity method and the full anisotropic method. This is not observed for the unrodded and rodded A cases, perhaps because the difference between the

Method (1D/TL/XS)	Case	k_{eff} [pcm]	RMS (%)	Max (%)	CPU Time [h]
1D P_3,	unrodded	-60	0.26	0.80	4.5
ISOTROPIC TL,	rodded A	-58	0.27	0.69	4.2
ISOTROPIC XS	rodded B	-71	0.29	0.95	3.2
1D P_3,	unrodded	-58	0.21	1.00	9.5
ISO / MOM TL,	rodded A	-64	0.26	1.30	10.7
ISO / POL XS	rodded B	-72	0.29	1.13	10.6
1D P_3,	unrodded	3	0.15	0.53	4.8
PARITY TL,	rodded A	5	0.21	0.68	4.8
PARITY XS	rodded B	2	0.33	1.39	5.2
1D P_3,	unrodded	2	0.16	0.58	9.6
PAR / MOM TL,	rodded A	1	0.20	0.71	9.4
PAR / POL XS	rodded B	-3	0.29	1.12	10.5
1D P_3,	unrodded	-10	0.13	0.40	8.9
POLAR / AZI TL,	rodded A	-10	0.17	0.51	8.9
POLAR XS	rodded B	-18	0.25	0.82	9.6
MONTE CARLO	unrodded	2	0.03	0.12	320.0
REFERENCE	rodded A	2	0.03	0.13	320.0
UNCERTAINTY	rodded B	2	0.03	0.13	320.0

Table 5.11: 2D/1D local refinement results

two methods is small. For the rodded B case, the RMS and maximum error is approximately halfway between the parity and full anisotropic methods. From these results, the local refinement method does not look promising. It seems that it is necessary to have the high-fidelity approximation throughout the core in order to achieve the maximum accuracy.

The local refinement method is not faster than the full anisotropic method because the load balancing is poor. The average time spent on MOC for each process (18 total) is given in Table 5.12. The overall solution time is limited by the slowest processes, so the time saved on the other processes does not reduce the overall solution time.

METHOD	Unrodded	Rodded A	Rodded B
PARITY	14	14	14
FULL ANISO	29	30	30

Table 5.12: MOC time per process, in minutes

In summary, the proposed local refinement scheme has, at best, a marginal benefit. The lower fidelity method in the scheme, which uses anisotropic TL and XS with a coarse-mesh 2D S_N odd parity solution, has accuracy that is already relatively close to the higher fidelity method. Thus, there is not much room for improvement with local refinement. A very small amount of improvement is seen with the local refinement, but it is not enough to justify the many complications and restrictions of a local refinement scheme with effective load balancing.

5.5 2D/1D Polar Parity Summary

In this chapter, a new 2D/1D method with anisotropic TL was developed. This method is cost efficient compared to the previous method for calculating anisotropic radial TL moments, which was described in Chapter 3 and used for the results in Chapter 4. The cost efficiency is achieved by splitting the angular flux into even-parity and odd-parity components, and treating the components with different levels of fidelity.

A few different ways to apply the polar parity concept to the 2D/1D method in MPACT were considered, but only one was pursued. This method was chosen because it is relatively simple, but still provides the fidelity that we seek with the anisotropic TL. In this method, the even-parity angular flux is calculated with MOC on the fine mesh, as it is in the other MPACT 2D/1D methods. The odd-parity angular flux is calculated on the coarse mesh, in a fast 2D coarse-mesh S_N solution. The even-parity [$\mathrm{P}_0(\mu)$ and $P_2(\mu)$] anisotropic radial TL moments are calculated using the MOC solution, as before. The odd-parity anisotropic radial TL moments [$P_1(\mu)$ and $P_3(\mu)$] are calculated from the coarse-mesh odd-parity solution. With this method, we can calculate the polar dependence of the radial TL while only simulating the quadrature directions in the upper half of the unit sphere ($\mu > 0$) in the MOC solver. This significantly reduces the amount of time spent on MOC, which is generally the most expensive part of the overall MPACT calculation.

The new 2D/1D method in this chapter is significantly faster than the method from Chapter 3. With respect to the anisotropic TL treatment, the new method is effectively equivalent to the previous method from Chapter 3, which was based on Stimpson's work in [8]. With respect to the anisotropic XS treatment, the new method is more accurate than assuming isotropic 1D XS, but it is not as accurate as the method from Chapter 3. The accuracy of the method from Chapter 3 demonstrated in Chapter 4 is better because the full polar distribution of the angular flux is calculated on the fine mesh. With the method in Chapter 5, the even polar-parity component of the angular flux is calculated on the fine mesh, but the odd polar-parity component is calculated on the coarse mesh. The correct fine-mesh angular flux is not known with fine enough spatial detail to accurately calculate the anisotropic homogenized 1D XS.

The accuracy improvement from using the odd polar-parity treatment for the angular flux developed in this chapter is significant, despite the relatively coarse spatial approximation used for the odd-parity angular flux. Most of the benefit from using anisotropic TL and XS that was observed in Chapter 4 was still observed with the method in Chapter 5, but the run times were reduced substantially. This new method may be more promising from a practical perspective than the previous method, because the slowdown compared to standard MPACT, at approximately 40-80%, is much more manageable than the 200-300% slowdown associated with the method from Chapter 3.

Chapter 6: SP_3 limit of the 2D/1D Equations

In this chapter, the SP_1 and SP_3 asymptotic limits of the standard 2D/1D equations with isotropic TL and the 2D/1D equations with anisotropic TL are derived and compared to the corresponding limits of the transport equation–which are the standard SP_1 and SP_3 equations. These theoretical results show that the 2D/1D equations with anisotropic TL have better accuracy than with isotropic TL. The theoretical results are confirmed numerically in Sec. 6.4.

The best application for the traditional 2D/1D method is in problems where the axial gradients are weak. In these cases, the accuracy is not severely limited by the coupling between the 2D and the 1D equations, and the accuracy of the overall solution is mostly determined by the accuracy of the 2D equation, which is transport.

In cases where gradients in all 3 dimensions are strong, the accuracy of 2D/1D is limited by the 1D solution accuracy and the fidelity of the coupling between 2D and 1D. If 1D P_1 is used with isotropic TL, the solution will be more accurate than 3D diffusion, i.e. 3D SP_1. If 1D P_3 is used with isotropic TL, the 2D/1D equations will be more accurate than with 1D P_1, but they *do not preserve* the 3D SP_3 limit. This is demonstrated theoretically in Sec. 6.2. However, with a sufficient number of anisotropic TL moments, the 2D/1D equations with 1D P_3 will preserve the SP_3 limit, and will be at least as accurate as 3D SP_3. This theoretical analysis is performed in Sec. 6.3.

The theoretical analysis in this chapter for the SP_3 approximation and the 2D/1D with isotropic TL approximation were originally done by Professor Larsen [75]. For this thesis, this line of analysis was extended to 2D/1D methods with anisotropic TL moments. This extension is the most significant original contribution in this chapter. After these theoretical results, numerical results are given to compare the 2D/1D methods to 3D diffusion and 3D SP_3 in Sec. 6.4. These numerical results corroborate the theoretical results.

6.1 Asymptotic Limit of the SP_3 Equations

As a point of reference for analysis of the 2D/1D equations, we begin by deriving the SP_3 approximation to the 3D Boltzmann Transport Equation:

$$\mathbf{\Omega}\cdot\nabla\psi(\mathbf{r},\mathbf{\Omega})+\Sigma_t\psi(\mathbf{r},\mathbf{\Omega})=\frac{1}{4\pi}\left[\Sigma_s\phi(\mathbf{r})+Q(\mathbf{r})\right]\ , \tag{6.1}$$

$$\phi(\mathbf{r})=\int\limits_{4\pi}\psi(\mathbf{r},\mathbf{\Omega}')d\Omega'\ . \tag{6.2}$$

For simplicity, we assume no energy dependence and isotropic scattering, and an infinite homogeneous medium in which $Q\to 0$ and $\psi\to 0$ as $|\mathbf{r}|\to\infty$.

We also assume that spatial derivatives are weak:

$$|\frac{1}{\Sigma_t}\mathbf{\Omega}\cdot\nabla\psi|<<\psi\ . \tag{6.3}$$

The assumption in Eq. (6.3) is the basis of the analysis in this chapter. This assumption is valid in weakly-absorbing media, sufficiently far away from material boundaries.

We define:

$$F(\mathbf{r})=\Sigma_s\phi(\mathbf{r})+Q(\mathbf{r})\ , \tag{6.4}$$

and rewrite Eq. (6.1) as:

$$\left(I+\frac{1}{\Sigma_t}\mathbf{\Omega}\cdot\nabla\right)\psi(\mathbf{r},\mathbf{\Omega})=\frac{1}{4\pi\Sigma_t}F(\mathbf{r})\ . \tag{6.5}$$

We solve for ψ and use Eq. (6.3) to formally expand the transport operator:

$$\begin{aligned}\psi(\mathbf{r},\mathbf{\Omega})&=\left(I+\frac{1}{\Sigma_t}\mathbf{\Omega}\cdot\nabla\right)^{-1}\frac{1}{4\pi\Sigma_t}F(\mathbf{r})\\&=\sum_{n=0}^{\infty}(-1)^n\left(\frac{1}{\Sigma_t}\mathbf{\Omega}\cdot\nabla\right)^n\frac{1}{4\pi\Sigma_t}F(\mathbf{r})\ .\end{aligned} \tag{6.6}$$

Next, we operate on Eq. (6.6) by $\int\limits_{4\pi}(\cdot)d\Omega$. We use the following integral properties of the unit vector Ω:

$$\frac{1}{4\pi}\int\limits_{4\pi}\left(\frac{1}{\Sigma_t}\mathbf{\Omega}\cdot\nabla\right)^n d\Omega = 0 \text{ for n odd },\tag{6.7a}$$

$$\frac{1}{4\pi}\int\limits_{4\pi}\left(\frac{1}{\Sigma_t}\mathbf{\Omega}\cdot\nabla\right)^{2n} d\Omega = \frac{1}{2n+1}\left(\frac{1}{\Sigma_t}\nabla\cdot\frac{1}{\Sigma_t}\nabla\right)^n \ .\tag{6.7b}$$

We obtain:

$$\phi = \left[I + \frac{1}{3}\left(\frac{1}{\Sigma_t}\nabla\cdot\frac{1}{\Sigma_t}\nabla\right) + \frac{1}{5}\left(\frac{1}{\Sigma_t}\nabla\cdot\frac{1}{\Sigma_t}\nabla\right)^2 + \frac{1}{7}\left(\frac{1}{\Sigma_t}\nabla\cdot\frac{1}{\Sigma_t}\nabla\right)^3 + ...\right]\frac{1}{\Sigma_t}F \ .\tag{6.8}$$

For simplicity, we define an operator $\mathscr{L}$:

$$\mathscr{L} = \left(\nabla\cdot\frac{1}{\Sigma_t}\right)\left(\nabla\cdot\frac{1}{\Sigma_t}\right) = \text{(3D diffusion operator)} \times \frac{1}{\Sigma_t} \ .\tag{6.9}$$

Using this notation, Eq. (6.8) can be written:

$$\Sigma_t\phi = \left[I + \frac{1}{3}\mathscr{L} + \frac{1}{5}\mathscr{L}^2 + \frac{1}{7}\mathscr{L}^3 + ...\right]F \ .\tag{6.10}$$

Here, we have ignored terms of order $\mathscr{O}(\mathscr{L}^4)$ and higher. We can formally solve for F:

$$F = \left[I + \frac{1}{3}\mathscr{L} + \frac{1}{5}\mathscr{L}^2 + \frac{1}{7}\mathscr{L}^3 + ...\right]^{-1}\Sigma_t\phi \ .\tag{6.11}$$

Again using an expansion for the relatively small derivative terms, we obtain:

$$\begin{aligned} F &= \left\{I - \left[\frac{1}{3}\mathscr{L} + \frac{1}{5}\mathscr{L}^2 + \frac{1}{7}\mathscr{L}^3 + ...\right] + \left[\frac{1}{3}\mathscr{L} + \frac{1}{5}\mathscr{L}^2 + ...\right]^2 - \left[\frac{1}{3}\mathscr{L} + ...\right]^3\right\}\Sigma_t\phi \ , \\ &= \left\{I - \frac{1}{3}\mathscr{L} + \left(-\frac{1}{5} + \frac{1}{9}\right)\mathscr{L}^2 + \left(-\frac{1}{7} + \frac{2}{15} - \frac{1}{27}\right)\mathscr{L}^3 + ...\right\}\Sigma_t\phi \ , \\ &= \left[I - \frac{1}{3}\mathscr{L} - \frac{4}{45}\mathscr{L}^2 - \frac{44}{945}\mathscr{L}^3 + ...\right]\Sigma_t\phi \ . \end{aligned}\tag{6.12}$$

We can write Eq. (6.12), with $\mathscr{O}(\mathscr{L}^4)$ error, as:

$$\begin{aligned} F &= \left\{ I - \frac{1}{3}\mathscr{L}\left[I + \frac{4}{15}\mathscr{L} + \frac{44}{315}\mathscr{L}^2 + ... \right] \right\}\Sigma_t\phi \ , \\ &= \left\{ I - \frac{1}{3}\mathscr{L}\left[I + \left(I + \frac{11}{21}\mathscr{L} \right) \frac{4}{15}\mathscr{L} + ... \right] \right\}\Sigma_t\phi \ , \\ &= \left\{ I - \frac{1}{3}\mathscr{L}\left[I + \left(I - \frac{11}{21}\mathscr{L} \right)^{-1} \frac{4}{15}\mathscr{L} + ... \right] \right\}\Sigma_t\phi \ , \end{aligned} \tag{6.13}$$

We now define $\phi_2(\mathbf{r})$ by:

$$2\Sigma_t\phi_2 = \left[\left(I - \frac{11}{21}\mathscr{L} \right)^{-1} \frac{4}{15}\mathscr{L} \right] \Sigma_t\phi \ , \tag{6.14}$$

allowing us to write Eq. (6.12) and Eq. (6.13) as a coupled diffusion system:

$$F = \Sigma_t\phi - \frac{1}{3}\mathscr{L}\Sigma_t\left(\phi + 2\phi_2\right) \ , \tag{6.15a}$$

$$\left(I - \frac{11}{21}\mathscr{L} \right) \Sigma_t\phi_2 = \frac{2}{15}\mathscr{L}\Sigma_t\phi \ . \tag{6.15b}$$

Equivalently, with $\mathscr{O}(\mathscr{L}^4)$ error:

$$-\frac{1}{3}\left(\nabla \cdot \frac{1}{\Sigma_t}\nabla \right)(\phi + 2\phi_2) + \Sigma_t\phi = \Sigma_s\phi + Q \ , \tag{6.16a}$$

$$-\frac{11}{21}\left(\nabla \cdot \frac{1}{\Sigma_t}\nabla \right)\phi_2 + \Sigma_t\phi_2 = \frac{2}{15}\left(\nabla \cdot \frac{1}{\Sigma_t}\nabla \right)\phi \ . \tag{6.16b}$$

Eqs. (6.16) are one form of the standard 3D SP$_3$ equations.

The 3D SP$_3$ equations agree with the 3D transport solution for terms up to $\mathscr{O}(\mathscr{L}^3)$, because they were derived from Eq. (6.12) using only approximations with $\mathscr{O}(\mathscr{L}^4)$ or higher error.

In the following sections, we perform a similar analysis for 2D/1D methods. The order of $\mathscr{L}$ to which the corresponding theoretical accuracy of each 2D/1D method agrees with Eq. (6.12) will be an indicator of how accurately we can expect that 2D/1D method to approximate the 3D transport solution. If only $\mathscr{O}(\mathscr{L})$ terms agree, then the 2D/1D method preserves the SP$_1$ limit, or diffusion. If the limit is correct for $\mathscr{O}(\mathscr{L}^2)$ terms as well, the SP$_2$ limit is preserved. If all terms up to $\mathscr{O}(\mathscr{L}^3)$ are correct, then the 2D/1D method preserves the SP$_3$ limit.

2D/1D equations that preserve high order SP$_N$ equations will have better 3D transport accuracy, especially in cases where the spatial derivatives are relatively strong in the radial and axial dimensions. It is desirable to preserve these limits exactly, but we would still expect good accuracy if the limit is approximately preserved. For example, if the coefficients of the $\mathscr{O}(\mathscr{L}^n)$ operators are within roughly 5-10% of the correct coefficients from Eq. (6.12), then we can still expect the 2D/1D method to preserve the SP$_N$ limit, for practical purposes. In practice, the 2D/1D method will often be more accurate than the corresponding SP$_N$ method that it approximately preserves, because the radial solver has transport accuracy.

6.2 2D/1D S$_N$ with Isotropic TL

In this section, we determine the theoretical accuracy of a 2D/1D method using isotropic TL. The theoretical method analyzed here assumes an exact transport solution in the axial direction. In practice, we often use a 1D P$_3$ method for the axial solver in MPACT. The results of this analysis will not be affected significantly by this difference. The difference in theoretical accuracy between a 1D P$_3$ method and 1D (exact) transport would only manifest if we were considering higher order SP$_N$ limits (i.e., including $\mathscr{O}(\mathscr{L}^4)$ and higher terms). Since we are ignoring these terms in the analysis, we can simply assume an exact 1D transport solution.

We begin by stating the 2D equation:

$$\Omega_y \frac{\partial \psi}{\partial x} + \Omega_y \frac{\partial \psi}{\partial y} + \Sigma_t \psi = \frac{1}{4\pi} \left(\Sigma_s \phi + Q - \frac{\partial \hat{J}_z}{\partial z} \right) , \tag{6.17a}$$

$$J_x = \int_{4\pi} \Omega_x \psi d\Omega , \tag{6.17b}$$

$$J_y = \int_{4\pi} \Omega_y \psi d\Omega , \tag{6.17c}$$

and the 1D equation,

$$\mu \frac{\partial \hat{\psi}}{\partial z} + \Sigma_t \hat{\psi} = \frac{1}{4\pi} \left(\Sigma_s \hat{\phi} + Q \right) - \frac{1}{4\pi} \left(\frac{\partial J_x}{\partial x} + \frac{\partial J_y}{\partial y} \right) , \tag{6.18a}$$

$$\hat{J}_z = \int_{4\pi} \Omega_z \hat{\psi} d\Omega , \tag{6.18b}$$

with

$$\phi = \int_{4\pi} \psi d\Omega \ , \ \hat{\phi} = \int_{4\pi} \hat{\psi} d\Omega \ . \tag{6.19}$$

$\frac{\partial J_z}{\partial x}$ and $\frac{\partial J_y}{\partial y}$ are the radial TL, and $\frac{\partial J_z}{\partial z}$ is the axial TL. In Eq. (6.18a), it is assumed that the axial solver of the 2D/1D coupled system is 1D transport and the transverse leakages are isotropic. Integrating Eq. (6.17a) and Eq. (6.18a) over $\mathbf{\Omega} \in 4\pi$, we obtain:

$$\left(\frac{\partial J_x}{\partial x} + \frac{\partial J_y}{\partial y}\right) + \Sigma_t \phi = \Sigma_s \phi + Q - \frac{\partial \hat{J}_z}{\partial z} \ , \tag{6.20a}$$

$$\frac{\partial \hat{J}_z}{\partial z} + \Sigma_t \hat{\phi} = \Sigma_s \hat{\phi} + Q - \left(\frac{\partial J_x}{\partial x} + \frac{\partial J_y}{\partial y}\right) \ . \tag{6.20b}$$

Eq. (6.20a) and Eq. (6.20b) imply that $\hat{\phi} = \phi$. We want to analyze these coupled equations in the same way that we analyzed Eq. (6.1). Again, we define:

$$F(\mathbf{r}) = \Sigma_s \phi(\mathbf{r}) + Q(\mathbf{r}) = \Sigma_s \hat{\phi}(\mathbf{r}) + Q(\mathbf{r}) \ , \tag{6.21}$$

and divide Eq. (6.17a) and Eq. (6.18a) by Σ_t, obtaining

$$\left[I + \frac{1}{\Sigma_t}\left(\Omega_x \frac{\partial}{\partial x} + \Omega_y \frac{\partial}{\partial y}\right)\right] \psi = \frac{1}{4\pi\Sigma_t}\left[F - \frac{\partial \hat{J}_z}{\partial z}\right] \ , \tag{6.22a}$$

$$\left[I + \frac{1}{\Sigma_t}\left(\mu \frac{\partial}{\partial z}\right)\right] \hat{\psi} = \frac{1}{4\pi\Sigma_t}\left[F - \left(\frac{\partial J_x}{\partial x} + \frac{\partial J_y}{\partial y}\right)\right] \ . \tag{6.22b}$$

Solving for ψ and $\hat{\psi}$ and expanding the inverted transport operator in an infinite series, we obtain:

$$\psi = \sum_{n=0}^{\infty} (-1)^n \left[\frac{1}{\Sigma_t}\left(\Omega_x \frac{\partial}{\partial x} + \Omega_y \frac{\partial}{\partial y}\right)\right]^n \frac{1}{4\pi\Sigma_t}\left[F - \frac{\partial \hat{J}_z}{\partial z}\right] \ , \tag{6.23a}$$

$$\hat{\psi} = \sum_{n=0}^{\infty} (-1)^n \left[\frac{1}{\Sigma_t}\left(\mu \frac{\partial}{\partial z}\right)\right]^n \frac{1}{4\pi\Sigma_t}\left[F - \left(\frac{\partial J_x}{\partial x} + \frac{\partial J_y}{\partial y}\right)\right] \ . \tag{6.23b}$$

To obtain an expression for the scalar flux, we operate on Eq. (6.23a) by $\int_{4\pi} (\cdot) d\Omega$:

$$\phi = \frac{1}{\Sigma_t}\left[I + \frac{1}{3}\mathscr{L}_r + \frac{1}{5}\mathscr{L}_r^2 + \frac{1}{7}\mathscr{L}_r^3 + \ldots\right]\left(F - \frac{\partial \hat{J}_z}{\partial z}\right) \ , \tag{6.24}$$

where:

$$\mathscr{L}_r = \nabla_r \frac{1}{\Sigma_t} \cdot \nabla_r \frac{1}{\Sigma_t} = \frac{\partial}{\partial x}\frac{1}{\Sigma_t}\frac{\partial}{\partial x}\frac{1}{\Sigma_t} + \frac{\partial}{\partial y}\frac{1}{\Sigma_t}\frac{\partial}{\partial y}\frac{1}{\Sigma_t} \tag{6.25}$$

$$= \text{“radial” diffusion operator.}$$

Hence,

$$\begin{aligned}
\left(F - \frac{\partial \hat{J}_z}{\partial z}\right) &= \left[I + \frac{1}{3}\mathscr{L}_r + \frac{1}{5}\mathscr{L}_r^2 + \frac{1}{7}\mathscr{L}_r^3 + ...\right]^{-1}\Sigma_t\phi \ , \\
&= \left\{ I - \left[\frac{1}{3}\mathscr{L}_r + \frac{1}{5}\mathscr{L}_r^2 + \frac{1}{7}\mathscr{L}_r^3 + ...\right] \right. \\
&\quad \left. + \left[\frac{1}{3}\mathscr{L}_r + \frac{1}{5}\mathscr{L}_r^2 + ...\right]^2 - \left[\frac{1}{3}\mathscr{L}_r + ...\right]^3 \right\}\Sigma_t\phi \\
&= \left\{ I - \left[\frac{1}{3}\mathscr{L}_r + \frac{1}{5}\mathscr{L}_r^2 + \frac{1}{7}\mathscr{L}_r^3 + ...\right] \right. \\
&\quad \left. + \left[\frac{1}{9}\mathscr{L}_r^2 + \frac{2}{15}\mathscr{L}_r^3 + ...\right] - \left[\frac{1}{27}\mathscr{L}_r^3 + ...\right] \right\}\Sigma_t\phi \\
&= \left[I - \frac{1}{3}\mathscr{L}_r + \left(-\frac{1}{5} + \frac{1}{9}\right)\mathscr{L}^2 + \left(-\frac{1}{7} + \frac{2}{15} - \frac{1}{27}\right)\mathscr{L}^3 + ...\right]\Sigma_t\phi \\
\left(F - \frac{\partial \hat{J}_z}{\partial z}\right) &= \left[I - \frac{1}{3}\mathscr{L}_r - \frac{4}{45}\mathscr{L}_r^2 - \frac{44}{945}\mathscr{L}_r^3 + ...\right]\Sigma_t\phi \ , \\
\Sigma_s\phi + Q - \frac{\partial \hat{J}_z}{\partial z} &= \left[I - \frac{1}{3}\mathscr{L}_r - \frac{4}{45}\mathscr{L}_r^2 - \frac{44}{945}\mathscr{L}_r^3 + ...\right]\Sigma_t\phi \ . \qquad (6.26)
\end{aligned}$$

Next, we need an equation for $\frac{\partial \hat{J}_z}{\partial z}$. We use Eq. (6.20a) to write:

$$\begin{aligned}
\Sigma_s\phi + Q - \left(\frac{\partial J_x}{\partial x} + \frac{\partial J_y}{\partial y}\right) &= F - \left(\frac{\partial J_x}{\partial x} + \frac{\partial J_y}{\partial y}\right) \ , \\
&= \Sigma_t\phi + \frac{\partial \hat{J}_z}{\partial z} \ , \qquad (6.27)
\end{aligned}$$

and rewrite Eq. (6.23b) as:

$$\hat{\psi} = \sum_{n=0}^{\infty}(-1)^n \left[\frac{1}{\Sigma_t}\left(\mu\frac{\partial}{\partial z}\right)\right]^n \frac{1}{4\pi\Sigma_t}\left[\Sigma_t\phi + \frac{\partial \hat{J}_z}{\partial z}\right] \ . \tag{6.28}$$

Operating on Eq. (6.28) by $\int\limits_{4\pi}\left(\mu\frac{\partial}{\partial z}\right)d\Omega$, we obtain an expression for the axial TL:

$$
\begin{aligned}
\frac{\partial \hat{J}_z}{\partial z} &= \sum_{n=0}^{\infty}\frac{(-1)^n}{4\pi}\int\limits_{4\pi}\left[\frac{1}{\Sigma_t}\left(\mu\frac{\partial}{\partial z}\right)\right]^{n+1} d\Omega\left(\Sigma_t\phi+\frac{\partial \hat{J}_z}{\partial z}\right) \; , \\
&= -\left[\frac{1}{3}\mathscr{L}_z+\frac{1}{5}\mathscr{L}_z^2+\frac{1}{7}\mathscr{L}_z^3+...\right]\left(\Sigma_t\phi+\frac{\partial \hat{J}_z}{\partial z}\right) \; , \qquad (6.29)
\end{aligned}
$$

where

$$
\begin{aligned}
\mathscr{L}_z &= \nabla_z\frac{1}{\Sigma_t}\cdot\nabla_z\frac{1}{\Sigma_t} = \frac{\partial}{\partial z}\frac{1}{\Sigma_t}\frac{\partial}{\partial z}\frac{1}{\Sigma_t} \qquad (6.30) \\
&= \text{“axial” diffusion operator.}
\end{aligned}
$$

Eq. (6.29) can now be written:

$$
\left[I+\frac{1}{3}\mathscr{L}_z+\frac{1}{5}\mathscr{L}_z^2+\frac{1}{7}\mathscr{L}_z^3+...\right]\frac{\partial \hat{J}_z}{\partial z} = -\left[\frac{1}{3}\mathscr{L}_z+\frac{1}{5}\mathscr{L}_z^2+\frac{1}{7}\mathscr{L}_z^3+...\right]\Sigma_t\phi \qquad (6.31)
$$

$$
\begin{aligned}
\frac{\partial \hat{J}_z}{\partial z} &= -\left[I+\frac{1}{3}\mathscr{L}_z+\frac{1}{5}\mathscr{L}_z^2+\frac{1}{7}\mathscr{L}_z^3+...\right]^{-1}\left[\frac{1}{3}\mathscr{L}_z+\frac{1}{5}\mathscr{L}_z^2+\frac{1}{7}\mathscr{L}_z^3+...\right]\Sigma_t\phi \\
&= -\left\{I-\left[\frac{1}{3}\mathscr{L}_z+\frac{1}{5}\mathscr{L}_z^2+\frac{1}{7}\mathscr{L}_z^3+...\right]+\left[\frac{1}{9}\mathscr{L}_z^2+\frac{2}{15}\mathscr{L}_z^3+...\right]+\left[\frac{1}{27}\mathscr{L}_z^3\right]\right\} \\
&\qquad \cdot\left[\frac{1}{3}\mathscr{L}_z+\frac{1}{5}\mathscr{L}_z^2+\frac{1}{7}\mathscr{L}_z^3+...\right]\Sigma_t\phi \\
&= -\left[I-\frac{1}{3}\mathscr{L}_z-\frac{4}{45}\mathscr{L}_z^2-\frac{44}{945}\mathscr{L}_z^3+...\right]\cdot\left[\frac{1}{3}\mathscr{L}_z+\frac{1}{5}\mathscr{L}_z^2+\frac{1}{7}\mathscr{L}_z^3+...\right]\Sigma_t\phi \\
&= -\left[\frac{1}{3}\mathscr{L}_z+\left(\frac{1}{5}-\frac{1}{9}\right)\mathscr{L}_z^2+\left(\frac{1}{7}-\frac{1}{15}-\frac{4}{135}\right)\mathscr{L}_z^3\right]\Sigma_t\phi+\mathscr{O}(\mathscr{L}_z^4) \\
\frac{\partial \hat{J}_z}{\partial z} &= -\left[\frac{1}{3}\mathscr{L}_z+\frac{4}{45}\mathscr{L}_z^2+\frac{44}{945}\mathscr{L}_z^3\right]\Sigma_t\phi+\mathscr{O}(\mathscr{L}_z^4) \; . \qquad (6.32)
\end{aligned}
$$

Introducing Eq. (6.32) into Eq. (6.26), we obtain:

$$
\begin{aligned}
&\left[I-\frac{1}{3}\mathscr{L}_r-\frac{4}{45}\mathscr{L}_r^2-\frac{44}{945}\mathscr{L}_r^3\right]\Sigma_t\phi+\mathscr{O}(\mathscr{L}_r^4) \\
&= \Sigma_s\phi+Q+\left[\frac{1}{3}\mathscr{L}_z+\frac{4}{45}\mathscr{L}_z^2+\frac{44}{945}\mathscr{L}_z^3\right]\Sigma_t\phi+\mathscr{O}(\mathscr{L}_z^4) \; . \qquad (6.33)
\end{aligned}
$$

Equivalently,

$$\Sigma_s\phi + Q = \tag{6.34}$$
$$\left\{I - \frac{1}{3}\left[\mathscr{L}_r + \mathscr{L}_z\right] - \frac{4}{45}\left[\mathscr{L}_r^2 + \mathscr{L}_z^2\right] - \frac{44}{945}\left[\mathscr{L}_r^3 + \mathscr{L}_z^3\right]\right\}\Sigma_t\phi + \mathscr{O}(\mathscr{L}_r^4 + \mathscr{L}_z^4)\ .$$

This result in Eq. (6.34) is similar, but not equivalent, to the result in Eq. (6.12). We note that:

$$\mathscr{L}_r + \mathscr{L}_z = \left(\frac{\partial}{\partial x}\frac{1}{\Sigma_t}\frac{\partial}{\partial x}\frac{1}{\Sigma_t} + \frac{\partial}{\partial y}\frac{1}{\Sigma_t}\frac{\partial}{\partial y}\frac{1}{\Sigma_t} + \frac{\partial}{\partial z}\frac{1}{\Sigma_t}\frac{\partial}{\partial z}\frac{1}{\Sigma_t}\right) = \mathscr{L}\ . \tag{6.35}$$

However,

$$\begin{aligned} &\mathscr{L}^2 = \mathscr{L}_r^2 + \mathscr{L}_z^2 + \mathscr{L}_r\mathscr{L}_z + \mathscr{L}_z\mathscr{L}_r\ , \\ &\mathscr{L}^2 \neq \mathscr{L}_r^2 + \mathscr{L}_z^2\ , \end{aligned} \tag{6.36}$$

and

$$\begin{aligned} &\mathscr{L}^3 = \mathscr{L}_r^3 + \mathscr{L}_z^3 + \mathscr{L}_r\mathscr{L}_z^2 + \mathscr{L}_r\mathscr{L}_z\mathscr{L}_r + \mathscr{L}_r^2\mathscr{L}_z + \mathscr{L}_z\mathscr{L}_r^2 + \mathscr{L}_z\mathscr{L}_r\mathscr{L}_z + \mathscr{L}_z^2\mathscr{L}_r\ , \\ &\mathscr{L}^3 \neq \mathscr{L}_r^3 + \mathscr{L}_z^3\ . \end{aligned} \tag{6.37}$$

Thus, the 2D/1D method with isotropic TL preserves the 3D SP_1 (diffusion) limit, but it does not preserve the 3D SP_2 limit or the 3D SP_3 limit. The correct limits for orders greater than SP_1 involve cross-derivative terms between the radial and axial spatial variables. The asymptotic limit of 2D/1D with isotropic TL has no such cross derivatives.

In order to introduce cross derivatives, we must couple the 2D and 1D equations with *anisotropic* TL terms. If the angular dependence is exact, and both the radial and axial transport solvers are exact, then that 2D/1D method would have exact 3D transport accuracy. Several codes use methods that fit this description, including CRX-2 [62], PROTEUS-MOCEX [22], and others. However, in MPACT we often use approximations to the angular dependence of the axial and radial TL. The azimuthal dependence is expanded in Fourier moments, and the polar dependence is expanded in Legendre polynomials, as described in Chapter 3. These expansions, especially the azimuthal expansion, significantly reduce the memory required to represent the anisotropic TL dependence. We know that we want to use this approximation, but we also know that we will not preserve 3D transport if the approximation is not sufficiently accuarte.

We can apply the analysis in this section to a 2D/1D method with anisotropic TL expansion in order to determine what degree of expansion is required to preserve certain levels of accuracy. In this case, we are interested in preserving the 3D SP$_3$ limit with the 2D/1D method. This type of analysis can inform us of the minimum order of Legendre and Fourier expansions required to do this.

In order to perform this analysis, we make a simplification to what we are deeming the "3D SP$_3$ limit." We do not believe that these simplifications change the results in any substantial way, qualitatively or quantitatively. First, we note that the derivative operators $\mathscr{L}_r$ and $\mathscr{L}_z$ are commutative:

$$\mathscr{L}_z\mathscr{L}_r = \mathscr{L}_r\mathscr{L}_z \ . \tag{6.38}$$

Since this analysis is being applied to an infinite medium problem, in which Σ_t has no spatial dependence, these operators commute. This allows us to reduce the number of terms we are trying to exactly preserve: For the SP$_2$ limit, we have:

$$\mathscr{L}_z\mathscr{L}_r + \mathscr{L}_r\mathscr{L}_z = 2\mathscr{L}_r\mathscr{L}_z \ , \tag{6.39}$$

For the SP$_3$ limit, we have:

$$\mathscr{L}_r\mathscr{L}_z^2+\mathscr{L}_r\mathscr{L}_z\mathscr{L}_r+\mathscr{L}_r^2\mathscr{L}_z+\mathscr{L}_z\mathscr{L}_r^2+\mathscr{L}_z\mathscr{L}_r\mathscr{L}_z+\mathscr{L}_z^2\mathscr{L}_r = 3\left(\mathscr{L}_r^2\mathscr{L}_z + \mathscr{L}_r\mathscr{L}_z^2\right) \ . \tag{6.40}$$

Now, instead of seeking 2 additional terms for the SP$_2$ limit and 6 for the SP$_3$ limit, we are only comparing to 1 for the SP$_2$ limit and 2 for the SP$_3$ limit. With this simplification, the 3D SP$_3$ limit [see Eq. (6.12)] is:

$$\begin{aligned} F = \Bigg[& I - \frac{1}{3}\left(\mathscr{L}_r + \mathscr{L}_z\right) - \frac{4}{45}\left(\mathscr{L}_r^2 + \mathscr{L}_z^2\right) - \frac{8}{45}\left(\mathscr{L}_r\mathscr{L}_z\right) \\ & -\frac{44}{945}\left(\mathscr{L}_r^3 + \mathscr{L}_z^3\right) - \frac{44}{315}\left(\mathscr{L}_r^2\mathscr{L}_z + \mathscr{L}_r\mathscr{L}_z^2\right) + ...\Bigg]\Sigma_t\phi \ . \end{aligned} \tag{6.41}$$

Thus, we seek an expression with the following form:

$$\begin{aligned} F = \Bigg[& I - \frac{1}{3}\left(\mathscr{L}_r + \mathscr{L}_z\right) - \frac{4}{45}\left(\mathscr{L}_r^2 + \mathscr{L}_z^2\right) - A\left(\mathscr{L}_r\mathscr{L}_z\right) \\ & -\frac{44}{945}\left(\mathscr{L}_r^3 + \mathscr{L}_z^3\right) - B\left(\mathscr{L}_r^2\mathscr{L}_z\right) - C\left(\mathscr{L}_r\mathscr{L}_z^2\right) + ...\Bigg]\Sigma_t\phi \ . \end{aligned} \tag{6.42}$$

We want our coefficients A, B, and C to match the SP$_3$ limit:

$$A = 2 \cdot \frac{4}{45} = \frac{8}{45} = 0.17778 \;, \tag{6.43a}$$

$$B = C = 3 \cdot \frac{44}{945} = \frac{44}{315} = 0.13968 \;. \tag{6.43b}$$

Eq. (6.42) and Eqs. (6.43) set the stage for the next step. In Sec. 6.3, we analyze 2D/1D methods with varying orders of anisotropic TL moments to obtain expressions in the form of Eq. (6.42). The accuracy of these methods are evaluated based on how closely they match the correct SP$_3$ limit.

6.3 P$_N$ Transverse Leakage dependence

In this section, we allow the axial and radial TL terms of the 2D/1D method to have higher order (non-isotropic) dependence in ω and $\Omega_z = \mu$. These anisotropic TL terms lead to cross derivatives between the radial and axial variables in the expression for the asymptotic accuracy limit. These terms are necessary to preserve SP$_N$ limits above order $N = 1$. We expect to find that the coefficients of these cross-derivative terms will approach the correct SP$_2$ and SP$_3$ limit coefficients as the number of anisotropic TL moments is increased for both the polar and azimuthal angle.

To simplify this analysis, we assume that the problem is infinite in the y direction, and all y derivatives are zero. Effectively, we are analyzing a 1D/1D method. The results of this analysis are still applicable to a 2D/1D method. A 1D/1D method has exactly the same deficiency as a 2D/1D method with respect to the order of the TL coupling.

Additionally, the results of a 1D/1D $y - z$ analysis would be exactly the same as the 1D/1D $x - z$ analysis. Since the x and y variables are coupled directly within the 2D transport solution, with no approximation, there are no $x - y$ cross derivative terms that the 2D/1D equations with isotropic TL are missing. Thus, there is no deficiency that we are failing to observe by assuming that the derivatives are zero in one of the two radial dimensions. Analysis of a 1D/1D method will produce the same results and the same information as analysis of a 2D/1D method would.

In the 2D/1D method, the azimuthal dependence of the TL is expanded in both sine and cosine moments. In the 1D/1D analysis, we expand only in cosine moments. Because of symmetry, all sine moments would be zero.

6.3.1 Analysis

First, we recall the radial and axial angular flux definitions, applying the assumption that all y derivatives are zero:

$$\psi = \sum_{n=0}^{\infty}(-1)^n \left[\frac{1}{\Sigma_t}\left(\Omega_x \frac{\partial}{\partial x}\right)\right]^n \frac{1}{\Sigma_t}\left[\frac{F}{4\pi} - TL_z\right] \ , \tag{6.44a}$$

$$\hat{\psi} = \sum_{n=0}^{\infty}(-1)^n \left[\frac{1}{\Sigma_t}\left(\mu \frac{\partial}{\partial z}\right)\right]^n \frac{1}{\Sigma_t}\left[\frac{F}{4\pi} - TL_x\right] \ . \tag{6.44b}$$

With polynomial and trigonometric expansion for the angle-dependence, the TL terms TL_z and TL_x are:

$$TL_z = \mu\frac{\partial}{\partial z}\left[\sum_{l=0}^{L}\frac{2l+1}{2}P_l(\mu)\left(\frac{f_{l,0}}{2\pi} + \frac{1}{\pi}\sum_{p=1}^{P} f_{c,l,p}\cos{(p\omega)}\right)\right] \ , \tag{6.45a}$$

$$TL_x = \frac{\partial}{\partial x}\left[\sum_{l=0}^{L}\frac{2l+1}{2}P_l(\mu)\left(\frac{g_{l,0}}{2\pi} + \frac{1}{\pi}\sum_{p=1}^{P} g_{c,l,p}\cos{(p\omega)}\right)\right] \ , \tag{6.45b}$$

$$f_{l,0} = \int_{-1}^{1} P_l(\mu)\left(\int_{0}^{2\pi}\hat{\psi}d\omega\right)d\mu \ , \tag{6.45c}$$

$$f_{c,l,p} = \int_{-1}^{1} P_l(\mu)\left(\int_{0}^{2\pi}\hat{\psi}\cos{(p\omega)}d\omega\right)d\mu \ , \tag{6.45d}$$

$$g_{l,0} = \int_{-1}^{1} \sqrt{1-\mu^2}P_l(\mu)\left(\int_{0}^{2\pi}\psi\cos\omega d\omega\right)d\mu \ , \tag{6.45e}$$

$$g_{c,l,p} = \int_{-1}^{1} \sqrt{1-\mu^2}P_l(\mu)\left(\int_{0}^{2\pi}\psi\cos\omega\cos{(p\omega)}d\omega\right)d\mu \ . \tag{6.45f}$$

Here, $f_{c,l,p}$ are the expansion coefficients of the 1D angular flux, and $g_{c,l,p}$ are the expansion coefficients of the radial TL. In MPACT, the radial TL moments (i.e., $\Omega_x \cdot \frac{\partial}{\partial x}\psi$) are expanded in Legendre and Fourier moments. However, the axial TL moments are not directly expanded. Instead, the 1D angular flux is expanded in Legendre and Fourier moments. The axial TL is calculated explicitly using the expansion of the 1D angular flux.

We need to define equations for each coefficient $f_{x,l,p}$ and $g_{x,l,p}$ and solve these equations:

$$g_{l,0} = \int\limits_{-1}^{1} P_l(\mu) \int\limits_{0}^{2\pi} \sum_{n=0}^{\infty} (-1)^n \left[\frac{\partial}{\partial x} \frac{1}{\Sigma_t} \Omega_x \right]^{n+1} \left[\frac{F}{4\pi} - TL_z \right] d\omega d\mu \ , \tag{6.46a}$$

$$\begin{aligned} g_{l,0} = & \int\limits_{-1}^{1} P_l(\mu) \int\limits_{0}^{2\pi} \sum_{n=0}^{\infty} (-1)^n \left[\frac{\partial}{\partial x} \frac{1}{\Sigma_t} \Omega_x \right]^{n+1} \\ & \cdot \left(\frac{F}{4\pi} - \mu \frac{\partial}{\partial z} \left[\sum_{l'=0}^{L} \frac{2l+1}{2} P_l'(\mu) \left(\frac{f_{l',0}}{2\pi} + \frac{1}{\pi} \sum_{p'=1}^{P} f_{c,l',p'} \cos p'\omega \right) \right] \right) d\omega d\mu \ . \end{aligned} \tag{6.46b}$$

$$\begin{aligned} g_{c,l,p} = & \int\limits_{-1}^{1} P_l(\mu) \int\limits_{0}^{2\pi} \cos p\omega \sum_{n=0}^{\infty} (-1)^n \left[\frac{\partial}{\partial x} \frac{1}{\Sigma_t} \Omega_x \right]^{n+1} \\ & \cdot \left(\frac{F}{4\pi} - \mu \frac{\partial}{\partial z} \left[\sum_{l'=0}^{L} \frac{2l+1}{2} P_l'(\mu) \left(\frac{f_{l',0}}{2\pi} + \frac{1}{\pi} \sum_{p'=1}^{P} f_{c,l',p'} \cos p'\omega \right) \right] \right) d\omega d\mu \ . \end{aligned} \tag{6.46c}$$

The moments of the axial 1D angular flux are given by:

$$f_{c,l,p} = \int\limits_{-1}^{1} P_l(\mu) \int\limits_{0}^{2\pi} \cos p\omega \sum_{n=0}^{\infty} (-1)^n \left[\frac{\partial}{\partial z} \frac{1}{\Sigma_t} \mu \right]^{n} \frac{1}{\Sigma_t} \left[\frac{F}{4\pi} - TL_x \right] d\omega d\mu \ . \tag{6.47}$$

Each azimuthal moment of the 1D axial angular flux is determined solely by the radial TL moment of the corresponding order. There is no "cross-talk" between different azimuthal moments of the radial TL and the 1D axial flux. Therefore, we have:

$$f_{l,0} = \int\limits_{-1}^{1} P_l(\mu) \sum_{n=0}^{\infty} (-1)^n \left[\frac{\partial}{\partial z} \frac{1}{\Sigma_t} \mu \right]^{n} \frac{1}{\Sigma_t} \left[\frac{F}{4\pi} - \left(\sum_{l'=0}^{L} \frac{2l+1}{2} P_l'(\mu) g_{l',0} \right) \right] d\mu \ , \tag{6.48a}$$

$$f_{c,l,p} = \int\limits_{-1}^{1} P_l(\mu) \sum_{n=0}^{\infty} (-1)^n \left[\frac{\partial}{\partial z} \frac{1}{\Sigma_t} \mu \right]^{n} \frac{1}{\Sigma_t} \left(- \sum_{l'=0}^{L} \frac{2l+1}{2} P_l(\mu) g_{c,l,p} \right) d\mu \ . \tag{6.48b}$$

The equation for the scalar flux is:

$$\begin{aligned}
\phi &= \int_{-1}^{1}\int_{0}^{2\pi} \psi d\omega d\mu \\
&= \int_{-1}^{1}\int_{0}^{2\pi} \sum_{n=0}^{\infty}(-1)^n \left[\frac{\partial}{\partial x}\frac{1}{\Sigma_t}\Omega_x\right]^n \qquad (6.49)\\
&\cdot \frac{1}{\Sigma_t}\left[\frac{F}{4\pi} - \mu\frac{\partial}{\partial z}\left[\sum_{l'=0}^{L}\frac{2l+1}{2}P_l(\mu)\left(\frac{f_{l,0}}{2\pi} + \frac{1}{\pi}\sum_{p'=1}^{P} f_{c,ll,p'}\cos p'\omega\right)\right]\right] d\omega d\mu\ .
\end{aligned}$$

The system of equations formed by Eq. (6.46) and Eq. (6.48) is a relatively dense, $[2(P+1)(L+1)]\times[2(P+1)(L+1)]$ system, where P is the number of Fourier moments and L is the number of Legendre moments in the TL expansion. This is shown in Fig. 6.1, with two additional rows and columns for the scalar flux ϕ and the total source F. Each term in the system of equations is an infinite series in derivatives (z derivatives for the axial 1D angular flux, x derivatives for the radial TL moments). In this analysis, we are specifically interested in how well the 2D/1D method preserves the asymptotic 3D SP$_3$ accuracy limit. For this limit, we are concerned only with spatial derivatives up to order 6. Consequently, we ignore the terms in the series beyond this order.

There are several aspects of this analysis that make it exceedingly difficult to perform manually. For example:

1. The system is moderately large (For $P = 3, L = 3$, it is 32x32). The density of this system is shown in Fig. 6.1.

2. The coefficients in the system of equations are not monomial, but instead consist of several derivative operators.

3. To determine the coefficients in the system, several complicated integrals in μ and ω are required.

Because of these difficulties, the analysis was performed using a Python script [1] written specifically for this application. The code is publicly available on online.[2]

The script first defines the system of equations by using a Gauss-Legendre quadrature (128 points) in the polar angle μ and a Chebyshev quadrature (64 points) in the

---

[1] Python Software Foundation, `https://www.python.org/`

[2] `https://github.com/mgjarrett/SP3_limit`

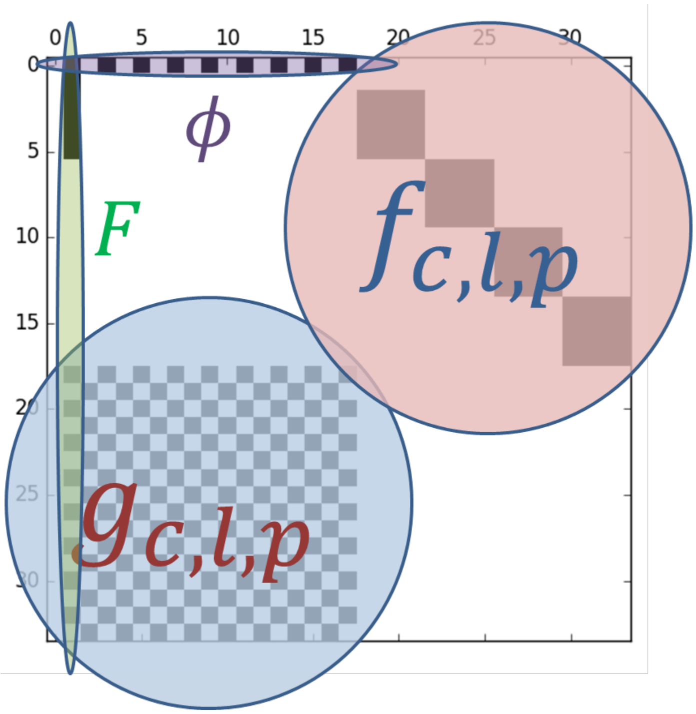

Figure 6.1: Density of SP3 limit system For $P = 3, L = 3$

azimuthal angle ω to evaluate each integral. The Chebyshev quadrature is equally-weighted, evenly spaced points around the unit circle, with weights summing up to 2π. This system of equations is then solved to obtain an expression for the scalar flux ϕ in terms of the 3D source F. First, we substitute the equations for $g_{c,l,p}$, Eq. (6.46), into Eq. (6.48). After this step, the radial TL moments $g_{c,l,p}$ are removed from the system. Then, the equations defined by Eq. (6.48) can each be solved in terms of the source F. These expressions can be substituted into the expression for the scalar flux, Eq. (6.49), and then we can solve for the expression we want, which has the form:

$$\begin{aligned} F = \Big[& I - \frac{1}{3}\left(\mathscr{L}_x + \mathscr{L}_z\right) - \frac{4}{45}\left(\mathscr{L}_x^2 + \mathscr{L}_z^2\right) - A\left(\mathscr{L}_x \mathscr{L}_z\right) \\ & - \frac{44}{945}\left(\mathscr{L}_x^3 + \mathscr{L}_z^3\right) - B\left(\mathscr{L}_x^2 \mathscr{L}_z\right) - C\left(\mathscr{L}_x \mathscr{L}_z^2\right) + \ldots \Big] \Sigma_t \phi \, . \end{aligned} \tag{6.50}$$

The analysis consists of solving these equations with varying levels of Legendre and Fourier expansion in the TL moments. For each level of angular expansion coupling, we compare the coefficients A, B, and C to the correct SP_3 limit. The expectation is that as the Legendre order L and Fourier order P become large, the coefficients will approach the correct SP_3 limit values.

6.3.2 Results

The results of the analysis for Legendre order L and Fourier order P up to 6 are given in Table 6.1 (relative to SP_3) and Table 6.2 (absolute).

Table 6.1: 2D/1D SP_3 limit coefficients (relative)

L	P	A	B	C
1	1	1.324	0.722	0.111
2	2	0.898	0.606	1.368
3	3	0.983	1.015	0.910
4	4	0.997	1.012	0.971
5	5	0.999	1.002	0.994
6	6	1.000	1.000	0.999
SP_3	SP_3	1.000	1.000	1.000

Table 6.2: 2D/1D SP_3 limit coefficients (absolute)

L	P	A	B	C
1	1	0.23538	0.10087	0.01552
2	2	0.15958	0.08465	0.19105
3	3	0.17480	0.14182	0.12713
4	4	0.17720	0.14138	0.13565
5	5	0.17763	0.14002	0.13886
6	6	0.17775	0.13972	0.13957
SP3	SP3	0.17778	0.13968	0.13968

These results are plotted in Fig. 6.2. The SP_2 cross term is at approximately 90% of the correct theoretical value with $L = 2$ and $P = 2$. All of the cross terms are within ±3% with $L = 4$ and $P = 4$. Having these coefficients within this range means that we can expect SP_3 accuracy from the 2D/1D solver.

In practice, MPACT almost always uses P_3 Legendre expansion ($L = 3$) in the polar angle. Most of the terms are very close to the SP_3 limit with $L = 3$ and $P = 3$. However, in practice we have observed that the difference in accuracy between $P = 3$ and $P = 2$ is relatively small, so $P = 2$ is usually used to minimize run time. $P = 1$ is slightly less accurate than $P = 2$ in many cases, but the difference is not severe. $P = 1$ can provide much better results than $P = 0$ for problems where axial and radial derivatives are strong.

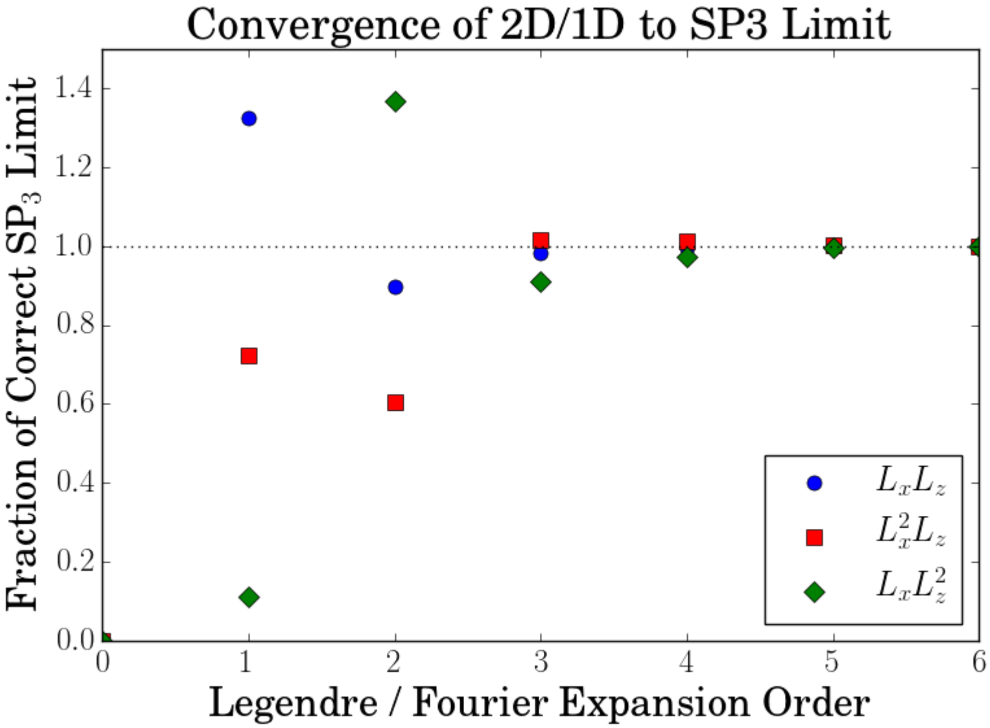

Figure 6.2: 2D/1D convergence to SP_3 limit

6.3.3 Importance of Azimuthal Moments

In MPACT, the number of azimuthal moments chosen for the TL representation is highly flexible, but the number of polar moments is essentially fixed. Because the anisotropic TL and XS method is only implemented with the 1D P_3 solver, we cannot use an expansion of higher order than P_3. There is not a good reason to use fewer than 3 moments, because it is not expensive to calculate the polar moments. The radial TL is initially calculated as discrete in the polar angle and then the moments are later calculated from this discrete representation. The cost of calculating the polar moments of the TL is negligible compared to the cost of calculating the radial TL itself.

The azimuthal dependence of the transverse leakage is treated differently. Because we do not want to store the full azimuthally dependent radial TL, we calculate the moments on the fly during the MOC sweep. Thus, it is significantly more expensive (in both memory and run time) to add more azimuthal moments. Therefore, we want to use as few azimuthal moments as possible to achieve the desired accuracy. In practice we observe that 1 or 2 azimuthal moments is sufficient. Here, we use the SP_3 limit analysis to determine how many azimuthal moments are required to retain

2D/1D accuracy that is approximately equivalent to the SP$_3$ limit. The results are given in Table 6.3.

Table 6.3: 2D/1D relative SP$_3$ limit with P$_3$ polar and varying azimuthal TL

L	P	A	B	C
3	0	-0.125	-0.091	-0.091
3	1	0.983	0.676	0.910
3	2	0.983	1.015	0.910
3	3	0.983	1.015	0.910
3	4	0.983	1.015	0.910
3	5	0.983	1.015	0.910
3	6	0.983	1.015	0.910
SP$_3$	SP$_3$	1.000	1.000	1.000

In Table 6.3, we see that even with just one azimuthal moment, the coefficient related to the SP$_2$ limit (A) is already 98.3% of the correct value. Additional azimuthal moments do not affect the SP$_2$ limit without a change in the polar TL order.

Adding a second azimuthal moment improves the B coefficient, but does not affect C. Both are relatively close to the correct SP$_3$ limit values. Beyond the second azimuthal moment, these coefficients are not affected.

Using P$_3$ expansion for the polar angle with azimuthally isotropic TL does not offer any significant benefit to the accuracy. The cross-derivative terms without azimuthal anisotropy are too small in magnitude, and of the incorrect sign.

This interesting theoretical result can inform our practical application of the anisotropic TL method. If we are interested in preserving the 3D SP$_3$ limit with the 2D/1D solver, we do not need to use any more than 2 azimuthal moments for the radial and axial TL. Using any more than 2 azimuthal moments will have no additional benefit with respect to the 3D SP$_3$ limit. Presumably, higher-order moments will affect higher-order operators, such as the SP$_4$ or SP$_5$ cross-derivative terms. While using higher-order azimuthal moments can have a marginal benefit for the overall accuracy of the 2D/1D method, we can capture most of the anisotropic TL effect with only 2 azimuthal moments. Even using just 1 azimuthal moment will capture a significant portion of the cross-derivative terms of the correct SP$_3$ limit. Using anisotropic polar TL with isotropic azimuthal TL does not improve the theoretical accuracy of the method compared to isotropic TL.

6.3.4 Modular Azimuthal Quadrature Sets

The transport solution in MPACT is obtained using discrete ordinates in both the azimuthal and polar angle, either directly (in the 2D MOC solution) or indirectly (to calculate polar integrals for the 1D axial P_N solution). The order of accuracy of these quadrature sets can affect the theoretical accuracy of the 2D/1D method. MPACT frequently uses azimuthal quadrature sets in which the directions have been adjusted to define a modular set of rays. In this section, we study the effect of that adjustment on the theoretical accuracy of the 2D/1D method.

In MPACT, the azimuthal quadrature angles are adjusted slightly to define modular rays for the MOC solution. If these adjustments are severe, it is possible that it could adversely affect the accuracy of the overall solution. An example of modularized and non-modularized MOC rays is given in Fig. 6.3.

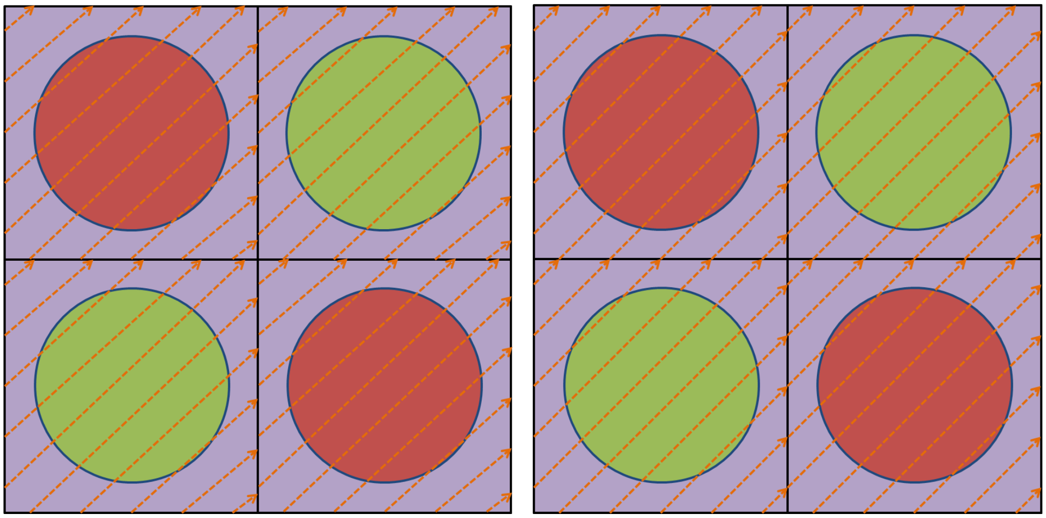
(a) Non-modularized MOC rays (b) Modular MOC rays

Figure 6.3: Modularization of angles for MOC rays

The adjustments are exaggerated in Fig. 6.3. Typically, the adjustments are relatively small (less than 1°). Additionally, the ray tracing module is typically square, which leads to a modularized quadrature set that is symmetric about $\frac{\pi}{4}$ in the first quadrant. The quadrature directions in the other quadrants are all reflections of the directions in the first quadrant over the x or y axis. As a result, the modularization of the quadrature set does not usually have a significant effect on the accuracy of the solution. We can evaluate the SP_3 limit of the 2D/1D equations with a modularized quadrature set to see if there is a significant effect on the solution.

The Chebyshev quadrature set with 16 azimuthal angles ω_n and weights w_n per octant (64 total) is given in Table 6.4, along with the modularized quadrature set (ω'_n and w'). The parameters used for this modularization are a ray tracing module dimension of 1.26 cm x 1.26 cm and a ray spacing of 0.5 mm.

Table 6.4: Modularized azimuthal quadrature set

ω_n (°)	w_n	ω'_n (°)	w'_n
2.8125	$\frac{\pi}{32}$	2.8624	0.09942
8.4375	$\frac{\pi}{32}$	8.5308	0.09751
14.0625	$\frac{\pi}{32}$	14.0362	0.09994
19.6875	$\frac{\pi}{32}$	19.9831	0.09743
25.3125	$\frac{\pi}{32}$	25.2011	0.09582
30.9375	$\frac{\pi}{32}$	30.9638	0.10183
36.5625	$\frac{\pi}{32}$	36.8699	0.09620
42.1875	$\frac{\pi}{32}$	41.9872	0.09724
47.8125	$\frac{\pi}{32}$	48.0128	0.09724
53.4375	$\frac{\pi}{32}$	53.1301	0.09620
59.0625	$\frac{\pi}{32}$	59.0362	0.10183
64.6875	$\frac{\pi}{32}$	64.7989	0.09582
70.3125	$\frac{\pi}{32}$	70.0169	0.09743
75.9375	$\frac{\pi}{32}$	75.9638	0.09994
81.5625	$\frac{\pi}{32}$	81.4692	0.09751
87.1875	$\frac{\pi}{32}$	87.1376	0.09942

Table 6.5 shows the SP_3 limit results with the original Chebyshev azimuthal quadrature, and Table 6.6 shows the results with the modularized quadrature. In both cases, an S_8 quadrature is used for the polar angle. From these results, it is clear that the effect of modularization is negligible. The only differences are very minor, in the fifth decimal place of these coefficients. The coefficients for the non-cross derivative operators are all exactly correct with both quadratures (not shown here).

Table 6.5: SP_3 Limit of 2D/1D, Chebyshev quadrature (64 azimuthal angles)

L	P	A	B	C
1	1	0.23538	0.10087	0.01552
2	2	0.15958	0.08465	0.19105
3	3	0.17480	0.14182	0.12713
4	4	0.17720	0.14138	0.13565
5	5	0.17763	0.14002	0.13886
6	6	0.17775	0.13972	0.13957
SP3	SP3	0.17778	0.13968	0.13968

Table 6.6: SP_3 Limit of 2D/1D, modularized Chebyshev quadrature (64 azimuthal angles)

L	P	$\mathscr{L}_x\mathscr{L}_z$	$\mathscr{L}_x^2\mathscr{L}_z$	$\mathscr{L}_x\mathscr{L}_z^2$
1	1	0.23538	0.10087	0.01552
2	2	0.15958	0.08465	0.19105
3	3	0.17480	0.14182	0.12713
4	4	0.17720	0.14138	0.13565
5	5	0.17763	0.14001	0.13886
6	6	0.17775	0.13971	0.13957
SP3	SP3	0.17778	0.13968	0.13968

6.3.5 Tabuchi-Yamamoto Polar Quadrature

The optimized polar quadrature developed by Tabuchi and Yamamoto [49] for MOC is widely used. In MPACT, this type of quadrature is often used when the TL is isotropic (i.e., most of the time). The goal of this quadrature set is to provide decent MOC accuracy with as few polar angles as possible. While it does provide good accuracy for the 2D MOC solution, it does not correctly integrate many functions in the polar angle that are associated with the anisotropic TL moments. As a result, anisotropic TL moments that are supposed to integrate to zero do not, and the neutron balance between the 2D and 1D solutions is disrupted, which leads to numerical instability. Thus, the Tabuchi-Yamamoto polar quadrature sets *cannot* be used with anisotropic TL.

The Tabuchi-Yamamoto quadrature with 3 polar angles in a quadrant is used for the analysis. This quadrature, given in Table 6.7, is a commonly used polar quadrature in MPACT.

Table 6.7: Optimized Tabuchi-Yamamoto polar quadrature

$\lvert\mu_n\rvert$	w_n
0.986016	0.046233
0.843132	0.283619
0.359996	0.670148

The effect of using Tabuchi-Yamamoto quadrature with anisotropic TL is demonstrated in Table 6.8. With isotropic TL, the non-cross-derivative terms are correct, and the cross-derivative terms are 0. However, if we use anisotropic TL with a Tabuchi-Yamamoto polar quadrature, all of the terms are incorrect (both non-cross and cross-derivatives).

Table 6.8: 2D/1D with Tabuchi-Yamamoto quadrature, coefficients relative to SP$_3$ limit

L	P	$\mathscr{L}_x$	$\mathscr{L}_z$	$\mathscr{L}_x^2$	$\mathscr{L}_z^2$	$\mathscr{L}_x\mathscr{L}_z$	$\mathscr{L}_x^3$	$\mathscr{L}_z^3$	$\mathscr{L}_x^2\mathscr{L}_z$	$\mathscr{L}_x\mathscr{L}_z^2$
1	1	0.99987	1.00050	0.99236	0.97999	1.33284	0.95402	1.08825	0.78943	0.09779
2	2	0.99987	1.00050	0.99236	0.97999	0.92829	0.95402	1.08825	0.75686	1.23115
3	3	0.99987	1.00089	0.99236	0.95557	1.11707	0.95402	1.07408	1.57178	0.47737
4	4	0.99987	1.00089	0.99236	0.95557	1.11015	0.95402	1.07408	1.62246	0.41666
5	5	0.99987	1.05012	0.99236	0.79549	1.76788	0.95402	1.09105	3.34351	-0.24133
6	6	0.99987	1.05012	0.99236	0.79549	2.37476	0.95402	1.09105	6.45686	-1.17073

The results in Table 6.8 show that if the 2D/1D method with anisotropic TL converged using Tabuchi-Yamamoto quadrature, the accuracy of the method would be relatively poor. While the SP$_1$ limit is approximately preserved, the agreement in higher order terms is not good, especially when a large number of polar moments is used. It is disconcerting that even the non-cross derivative term coefficients are not preserved here.

The asymptotic limit is incorrect because the Tabuchi-Yamamoto quadrature does not correctly integrate the anisotropic TL moments in the polar angle. Again, this integration error also causes particle imbalance that leads to numerical instability. As a result, Tabuchi-Yamamoto quadrature cannot be used with polar anisotropic TL moments. Instead, a quadrature that correctly integrates Legendre polynomials such as the Gauss-Legendre quadrature that is used throughout this thesis, should be used.

6.3.6 S$_4$ Quadrature

The analysis in this chapter assumes a discrete ordinates solution for the 1D transport equation with a specified quadrature order N. 1D S$_4$ is demonstrably equivalent to 1D P$_3$. Thus, if we use a Gauss-Legendre quadrature with 4 quadrature points (S$_4$), the result should be equivalent to the result of the analysis for a 1D P$_3$ solver. The results using S$_4$ polar quadrature with a 64-point Chebyshev azimuthal quadrature are given in Table 6.9.

Table 6.9: 2D/1D anisotropic TL limit, S$_4$ quadrature

L	P	A	B	C
1	1	1.367269	0.714048	0.132873
2	2	0.938756	0.583537	1.501047
3	3	1.000012	0.999982	0.999982
SP$_3$	SP$_3$	1.000000	1.000000	1.000000

The results in 6.9 are interesting. Using the S$_4$ quadrature leads to nearly perfect agreement with the correct SP$_3$ limit using only 3 polar and 3 azimuthal moments. This agreement is better than the agreement seen with a higher-order S$_8$ quadrature in Table 6.1. Although the agreement is not perfect out to machine precision, it is correct out 4 decimal places. With the S$_8$ quadrature, the C coefficient was off by 9%.

This result suggests that the 2D/1D P$_3$ method with 3 polar and 3 azimuthal moments actually has better theoretical accuracy than a 2D/1D S$_N$ method with the same number of anisotropic TL moments. However, this may not be exactly equivalent to the 2D/1D P$_3$ method implemented in MPACT. In MPACT, if we are using S$_8$ quadrature, the radial TL moments for the 1D P$_3$ solution will be calculated with the S$_8$ quadrature. In this analysis, the radial TL moments are calculated with S$_4$.

The limit with 2 polar and 2 azimuthal moments is not correct when using S$_4$ quadrature. However, it is similar to the limit when using S$_8$ quadrature. This suggests that there is no significant disadvantage to using P$_3$ as the axial solver instead of S$_N$, with respect to the SP$_3$ limit. In certain cases, the axial derivatives may be strong enough that the $\mathscr{L}_z^4$ term is important. In these problems, the 1D S$_N$ solver will be more accurate than 1D P$_3$. But with respect to the 3D SP$_3$ limit, there is no significant difference between the two axial solution methods.

6.4 Numerical Results for SP3 Limit

In this section, two problems are used to compare the traditional and new 2D/1D methods to 3D SP$_N$. First, a simple 2D problem with strong gradients in both the radial and axial directions is used to compare 2D SP$_1$, 2D SP$_3$, and 1D/1D in MPACT. The fact that there is only 1 radial dimension (x) in the 1D/1D instead of 2 (x and y) will not affect the results. The takeaway from these results is mainly the effect of the angular coupling between the radial and axial solutions, which is independent of the number of dimensions used for either solution.

Next, the 3D Takeda-Ikeda benchmark problem is used to compare the 2D/1D methods to 3D SP$_N$. The results from this probem effectively demonstrate the accuracy differences between the various methods.

To obtain results for SP_1 and SP_3, a simple finite difference code with CMFD acceleration was written in Python. The code is available online.[3] This code solves multigroup eigenvalue problems with Cartesian geometry in 1D, 2D, or 3D.

6.4.1 2D Test Problem

The test problem geometry is shown in Fig. 6.4. It is very similar to the problem from Sec. 4.3, but the fuel region is smaller here to increase the gradients and accentuate any deficiencies in the methods.

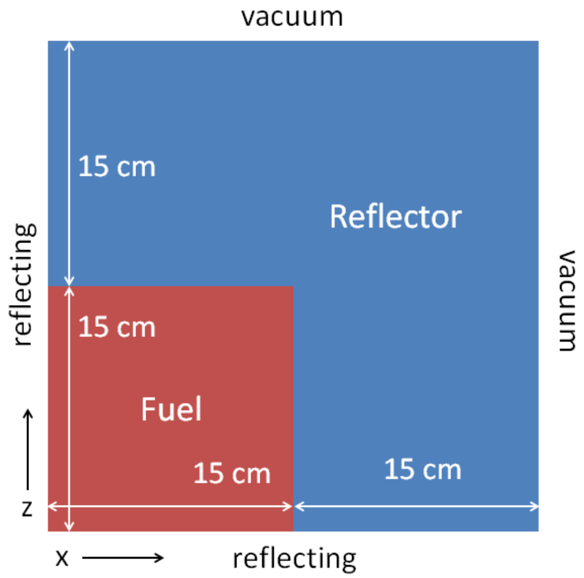

Figure 6.4: 2D problem geometry

The SP_1 and SP_3 discretization is finite difference with 1 mm square cells. For the 1D/1D cases, the coarse cells are 1 cm square, and the MOC uses 32 azimuthal angles and 12 polar angles per octant, with 0.2 mm ray spacing and 1 mm flat source regions in the x direction. The results are given in Table 6.10. There are several takeaways from the results in Table 6.10. First, the 2D SP_1 (diffusion) performs poorly. The standard 1D/1D with isotropic TL (0.38% RMS, 1.43% max, -379 pcm) is significantly

Table 6.10: 2D homogeneous fuel results

	ISO TL	ODD TL	MOM TL	1D S_{24}	SP_3	SP_1
k_{eff} [pcm]	-379	+1	-2	+2	+31	-1665
RMS error (%)	0.48	0.18	0.18	0.02	0.29	2.44
Max. error (%)	1.43	0.53	0.54	0.10	1.08	7.54

---

[3] `https://github.com/mgjarrett/SP3_solver_FD`

better than diffusion, but is also significantly worse than 2D SP_3 (0.29% RMS, 1.08% max, +31 pcm). This indicates that the standard 1D/1D method does not preserve the SP_3 limit. With ansiotropic TL, the accuracy of 1D/1D is better than SP_3. The difference between the reference solution and 1D/1D with anisotropic TL are relatively small (0.18% RMS and 0.53% max, +1 pcm), and mostly attributable to the error from the 1D P_3 solution. When using 1D S_{24}, the errors are very small (0.02% RMS and 0.10% max).

From these results, an approximate hierarchy of accuracy can be established, beginning with the least accurate:

1. 3D SP_1 (diffusion)
2. 2D/1D with isotropic TL
3. 3D SP_3
4. 2D/1D P_3 with anisotropic TL
5. 2D/1D S_N with anisotropic TL

In this case, the difference between (3) and (4) was relatively small compared to the difference between (1) and (2) or (2) and (3). While the magnitude of the differences may change in other cases, the relative order should remain the same.

The power shape error for each method is given next. The standard 1D/1D with isotropic TL pin power errors are given in Fig. 6.5a. The parity TL method errors are given in Fig. 6.5b. The 2D SP_3 errors are given in Fig. 6.5c. The errors for the 1D/1D S_N method are given in Fig. 6.5d. We see that the magnitude of the error for 1D/1D with isotropic TL is greater than that for 2D SP_3. 1D/1D P_3 with anisotropic (odd-parity) TL is more accurate than 2D SP_3. 1D/1D S_N is more accurate than 1D/1D P_3.

Next, the axially integrated radial power shape error is shown in Fig. 6.6, and the radially integrated axial power shape is shown in Fig. 6.7. This helps to highlight the accuracy of the 1D/1D method with respect to strong gradients in the radial and axial directions, individually.

In Fig. 6.6, the isotropic TL method and the 2D SP_3 method have some error in the radial power shape. The anisotropic TL method has better accuracy. In Fig. 6.7, the isotropic TL method has significant error in the axial power shape. The 2D SP_3 method and the anisotropic TL method (with axial 1D P_3) have nearly identical axial power shape errors. Thus, the 1D/1D P_3 method with anisotropic TL is limited in the

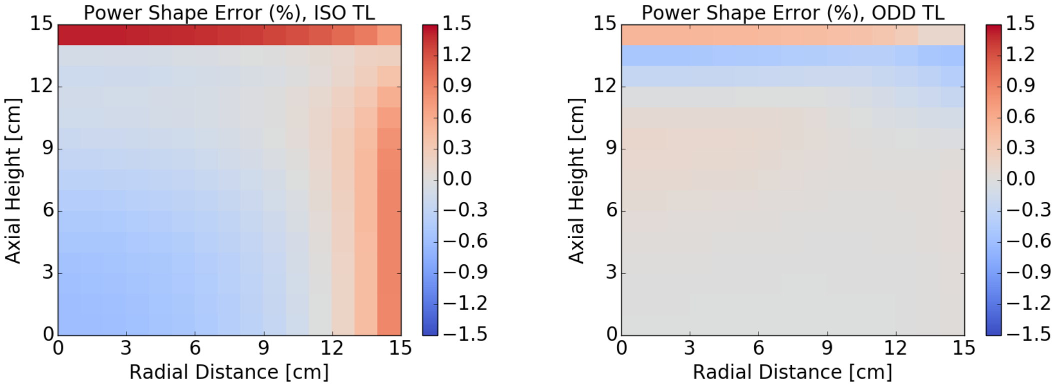

(a) 1D/1D, isotropic TL

(b) 1D/1D, parity TL

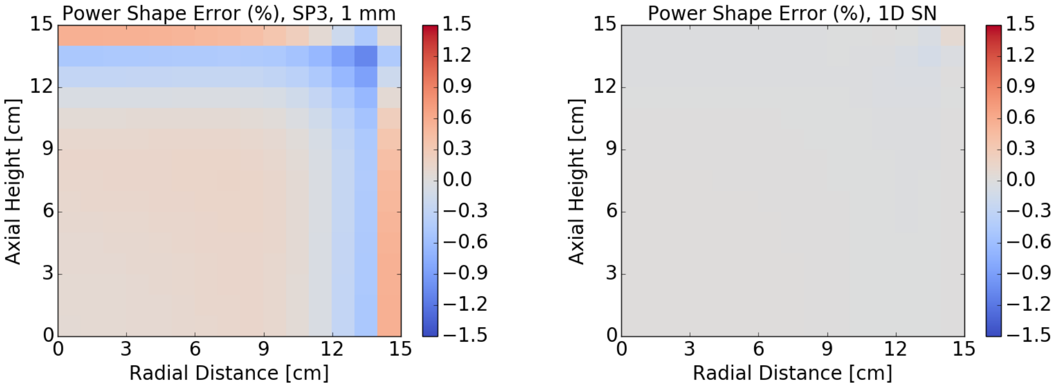

(c) 2D SP_3

(d) 1D/1D S_N, anisotropic TL

Figure 6.5: 2D homogeneous fuel problem power error

axial direction by the accuracy of the 1D solution. With isotropic TL, the accuracy is limited by the low-fidelity isotropic TL.

6.4.2 Takeda-Ikeda Benchmark Problem

The Takeda-Ikeda LWR benchmark [31] is a good test problem to compare 2D/1D to 3D SP_3 because it can be exactly modeled by a structured Cartesian 3D mesh. This allows the use of the finite difference 3D SP_3 solver from the previous section.

The problem geometry is a 25 cm cube with a 15 cm cubic core surrounded by a reflector region. Immediately adjacent to the core is a 5 cm × 5 cm × 25 cm control rod. The top view of the geometry is shown in Fig. 6.8 and the side view is shown in Fig. 6.9.

An unrodded problem also exists, where the control rod is replaced by void. The 2D/1D solvers do not converge for the voided case. In this work, only the rodded Takeda-Ikeda benchmark problem is studied.

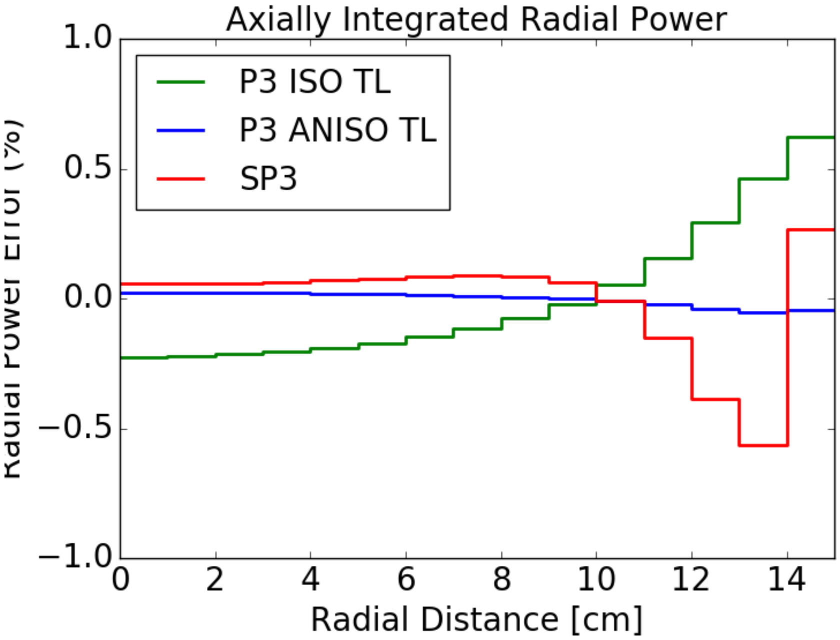

Figure 6.6: Axially integrated radial power shape error

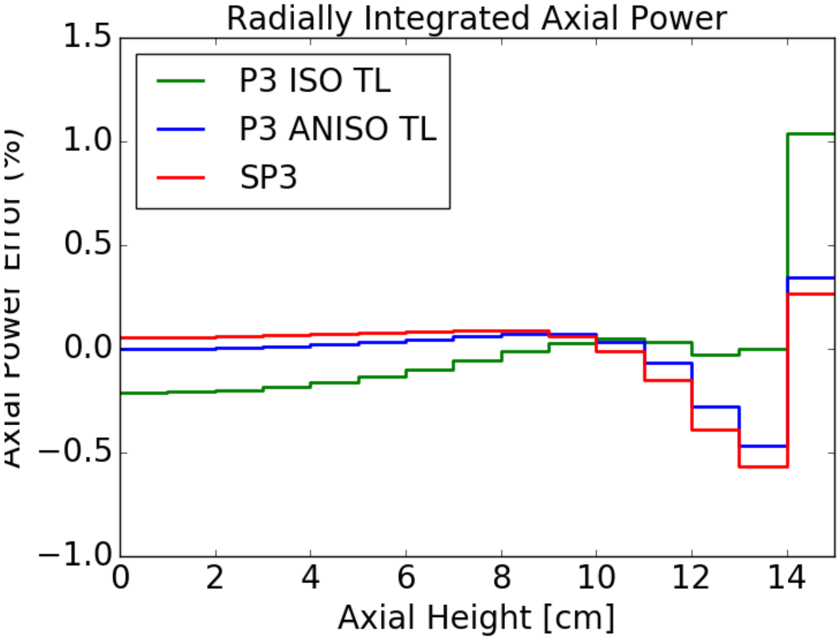

Figure 6.7: Radially integrated axial power shape error

Table 6.11 shows the two group XS data for the three different materials in the rodded benchmark problem.

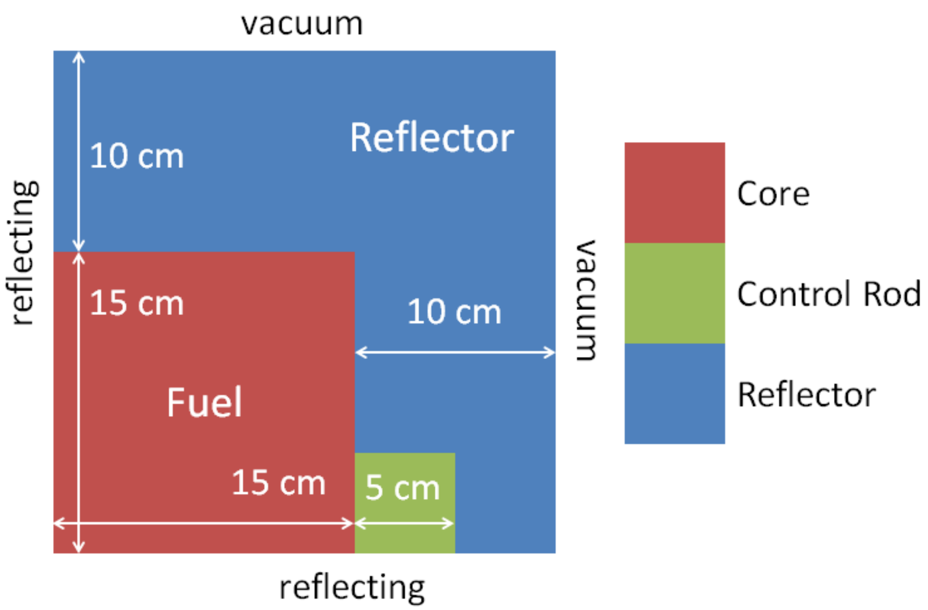

Figure 6.8: Takeda-Ikeda geometry - top view

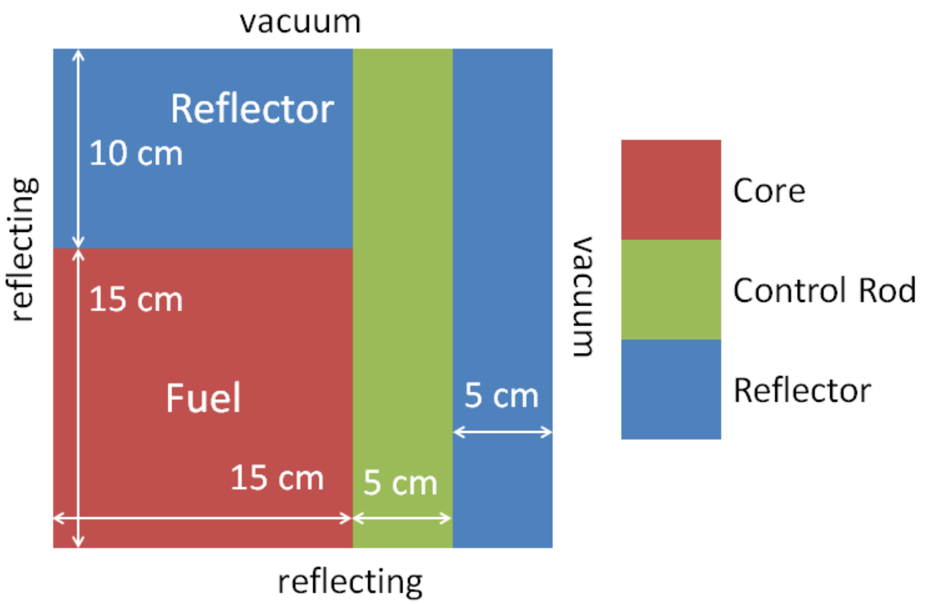

Figure 6.9: Takeda-Ikeda geometry - side view

In MPACT, the radial discretization consists of 1 cm cube coarse cells, with 1 mm square FSRs. The angular quadrature has 16 azimuthal and 4 polar angles per octant. The ray spacing is 0.02 cm. The eigenvalue results are given in Table 6.12. We see the same trend as in the previous section. Of all the methods, 3D SP_1 has the largest error. 3D SP_3 is significantly better than 2D/1D with isotropic TL. The eigenvalue error for the 2D/1D isotropic TL method with 1D P_3 is 500 pcm less than

Table 6.11: Takeda-Ikeda cross section data

Region	g	$\Sigma_{tr,g}$	$\nu\Sigma_{f,g}$	χ_g	$\Sigma_{s0,1\rightarrow g}$	$\Sigma_{s0,2\rightarrow g}$
Core	1	2.23775E-01	9.09319E-03	1.0	1.92423E-01	0.00000E+00
	2	1.03864E+00	2.90183E-01	0.0	2.28253E-02	8.80439E-01
Reflector	1	8.52325E-02	0.0000E+00	0.0	6.77241E-02	0.00000E+00
	2	2.17460E-01	0.0000E+00	0.0	6.45461E-05	3.52358E-02
Control Rod	1	2.50367E-01	0.0000E+00	0.0	1.93446E-01	0.00000E+00
	2	1.64482E+00	0.0000E+00	0.0	5.65042E-02	1.62452E+00

with 1D P_1. 2D/1D P_3 is significantly more accurate than with 1D P_1, but it does *not* have 3D SP_3 accuracy. 2D/1D P_3 (or S_N) with anisotropic TL is significantly more accurate than 3D SP_3, and within uncertainty of the Monte Carlo transport solution. It is important to note that the uncertainty given with the Monte Carlo reference is relatively large (60 pcm). The errors in the flux for group 1 and group 2, integrated over each material region, are also given.

Table 6.12: Takeda-Ikeda rodded k_{eff} results

Method	k_{eff}	error	FUEL	(%)	REFL	(%)	CTRL	(%)
		[pcm]	1	2	1	2	1	2
Reference	0.96240	± 60	(0.10)	(0.13)	(0.21)	(0.23)	(0.48)	(0.72)
3D SP_1	0.93265	-2975	-3.08	0.31	12.69	12.32	8.51	15.75
3D SP_3	0.95981	-259	-0.93	-0.07	1.20	1.99	0.36	-1.64
2D/1D P_1 ISO TL	0.95014	-1226	-1.55	0.03	4.74	4.58	-0.06	1.53
2D/1D P_3 ISO TL	0.95523	-717	-0.85	-0.09	1.82	1.96	-0.29	0.43
2D/1D P_3 ODD TL	0.96244	+4	-0.46	-0.16	0.00	0.20	-0.12	-0.06
2D/1D S_N	0.96250	+10	-0.35	-0.18	-0.14	0.13	0.01	-0.08

The results in Table 6.12 are obtained with the control rod oriented along the z axis. This configuration has stronger radial TL than axial, because the interface between core and control rod is on a lateral face. This geometry can be rotated so that the control rod is oriented along the x or y axis. This case will have stronger axial TL than radial TL, because the interface between control rod and fuel is on an axial boundary. The eigenvalue results for 2D/1D with the rotated geometry are given in Table 6.13. As expected, 2D/1D with isotropic TL does not perform as well when the strongest gradients are treated by the 1D solver instead of the 2D. The difference with 1D P_1 is more significant than the difference with 1D P_3. When using 1D S_N, the 3D transport accuracy is maintained. Although it seems that the anisotropic TL methods are also slightly less accurate, it is difficult to determine the significance of the results because the statistical uncertainty in the Monte Carlo solution is much larger than the errors.

Table 6.13: Takeda-Ikeda rodded k_{eff} results, rotated

Method	k_{eff}	Difference [pcm]
Reference	0.96240	± 60
2D/1D P1 ISO TL	0.94612	-1628
2D/1D P3 ISO TL	0.95393	-847
2D/1D P3 ODD TL	0.96219	-21
2D/1D S_N	0.96256	+16

6.5 Summary

In this section, the asymptotic accuracy limit was determined for 2D/1D methods with varying orders of anisotropic TL coupling. These theoretical results show that the 2D/1D method with isotropic TL preserves the 3D SP_1 limit, but it does not preserve the 3D SP_3 limit. Using higher-order anisotropic TL moments improves the accuracy of 2D/1D. With 3 polar and 3 azimuthal moments, the 2D/1D method approximately preserves the 3D SP_3 limit. The modularization of the azimuthal quadrature has little effect on the accuracy of 2D/1D, but the Tabuchi-Yamamoto polar quadrature is insufficient when using anisotropic TL moments. For 2D/1D with anisotropic TL, Gauss-Legendre quadrature should be used.

A finite-difference 3D diffusion and SP_3 solver was developed in Python to provide numerical results against which the 2D/1D methods in MPACT could be compared. The comparison was done using the Takeda-Ikeda benchmark. The results show that the 2D/1D method with isotropic TL is more accurate than 3D SP_1, but less accurate than 3D SP_3. This provides numerical verification for the results of the theoretical analysis in this chapter.

The results also show that the 2D/1D method with sufficiently accurate anisotropic TL treatment preserves the 3D SP_3 limit, and is actually more accurate than the 3D SP_3 equations. The 2D/1D method with anisotropic TL is more accurate than 3D SP_3 because it has transport accuracy for the radial solver, which is important when the radial gradients are large.

In this chapter, we have shown that the 2D/1D P_3 method with anisotropic TL preserves the 3D SP_3 limit, both theoretically and numerically. This is an important result, because SP_3 is a commonly used method, and some other codes that are used in the same realm as MPACT (LWR analysis) do preserve the 3D SP_3 limit. Any 3D Monte Carlo or deterministic 3D transport method will have better than 3D SP_3 accuracy. Pin-by-pin SP_3 [76, 77] is a tool that has been developed and used for LWR analysis lately that also has SP_3 accuracy. This would be an advantage of these methods over 2D/1D with isotropic TL. With anisotropic TL, 2D/1D has SP_3 accuracy, and does not suffer from the same homogenization problems as pin-by-pin SP_3. The analysis here has shown that the anisotropic TL removes this one possibly significant disadvantage of 2D/1D compared to other contemporary methods.

Chapter 7: Conclusion

7.1 Summary

The objective of this thesis is to advance the theory behind the 2D/1D methods used in MPACT and develop new 2D/1D methods with improved accuracy, especially for LWR problems that have heterogeneity within the coarse cell. Previous work had improved 2D/1D accuracy significantly for problems without this pin heterogeneity by using anisotropic TL [9]. For problems with the pin heterogeneity, a non-negligible error in the 2D/1D solution still existed. The anisotropic 1D XS homogenization method developed in Chapter 3 addresses this error. The 2D/1D P_3 method with anisotropic 1D XS homogenization, using a polar-dependent homogenized 1D XS for the axial solution, has significantly improved transport accuracy compared to any previous pin-homogenized 2D/1D method. The 2D/1D P_3 method developed in this thesis is a significant and novel contribution to the theory of 2D/1D methods and the capabilities of the 2D/1D neutron transport solution implemented in MPACT.

The transport accuracy of the method developed in Chapter 3 is demonstrated using several different test problems in Chapter 4. The most significant test case is the 3D C5G7 benchmark, where the new 2D/1D method shows good agreement with the 3D multigroup Monte Carlo reference solution. With a very fine spatial and angular mesh, the 2D/1D method is within ±3 pcm of the Monte Carlo solution for all three C5G7 benchmark cases, and the maximum power error is less than 1%. For several other smaller cases, the 2D/1D P_3 method with anisotropic 1D XS shows almost perfect agreement with a 3D transport or near-3D transport solution.

The 2D/1D P_3 method with anisotropic 1D XS homogenization is a high-fidelity approximation to the 3D transport equations. It makes use of several approximations to the angular variable:

1. The polar dependence of the radial TL, axial TL, and homogenized 1D total XS, is expanded in Legendre polynomials.

2. The azimuthal dependence of the radial and axial TL is expanded in Fourier moments.

3. The azimuthal dependence of the homogenized 1D total XS is ignored.

These approximations drastically reduce the memory and run-time required compared to a similar 2D/1D method with exact representation in angle for the TL and XS. The numerical results in this thesis demonstrate that these approximations, compared to exact representations of the TL and XS, do not degrade the accuracy in a significant way. A good example of this is Table 3.1 in Sec. 3.3, where the 2D/1D P_3 method using the above approximations agrees almost exactly with a 2D/1D S_N method with exact angular representation of the TL and XS. Although there are still some small errors in the 2D/1D P_3 method, they generally do not arise from the approximations enumerated above.

The 2D/1D P_3 method with full anisotropic TL and polar-dependent homogenized 1D XS developed in Chapter 3 is significantly more burdensome than the standard 2D/1D method with isotropic TL used in MPACT. The anisotropic TL leads to a source for the 2D MOC problem that is not symmetric in the polar angle, and requires that the 2D MOC simulate angles over the full unit sphere (4π). With isotropic TL, the MOC could simulate only half of the unit sphere, with the other half being defined by polar symmetry. The additional MOC requirement is a significant computational cost. Also, calculating the polar-angular flux on the fine mesh during MOC sweeps for the polar-dependent homogenized 1D XS requires additional computation for each MOC sweep. These two requirements, along with calculation of radial TL moments on the coarse surface boundaries during MOC sweeps, combine to significantly increase the run time of 2D/1D with anisotropic TL and XS. While the desired accuracy improvement is attained by this method, the associated slowdown makes it less attractive for practical use.

To avoid the cost of performing MOC over 4π instead of 2π, a 2D/1D method with polar-angle parity was developed in Chapter 5. This method splits the 2D angular flux into a symmetric (even-parity) component and an antisymmetric (odd-parity) component. The even-parity angular flux is calculated using the fine-mesh 2D MOC, which is similar to the standard isotropic TL 2D/1D method in MPACT. The odd-parity angular flux is calculated on the coarse mesh using a Cartesian 2D S_N. The run time for the 2D S_N solution is fast (approximately 5% of the run time for MOC). The accuracy of this method for modeling the anisotropic TL is nearly equivalent to the fully anisotropic MOC method, but significantly faster. The 2D/1D method with coarse-mesh odd-parity 2D S_N is not as accurate for calculating the anisotropic homogenized 1D XS because the odd-parity angular flux is not calculated on the fine mesh. However, the anisotropic 1D XS can still be calculated by assuming a spatially flat odd-parity angular flux over the coarse cell. Even using this crude approximation, the accuracy of the 2D/1D method is improved by using the polar-dependent 1D XS. This 2D/1D method with fast calculation of the anisotropic TL is another novel contribution to the field of 2D/1D computational neutron transport methods.

It is clear that 2D/1D with anisotropic TL should be more accurate than 2D/1D with isotropic TL. This is intuitive, and it is borne out in numerical results, both in this work and several previous works on this topic [8, 9, 11, 67, 68]. In some of these cases, an explicit angular representation of the TL is used [11, 67]. The explicit representation is accurate, but it is relatively expensive and can be overkill in many cases. In MPACT, functional expansion of the angular dependence is used to significantly decrease the burden of using anisotropic TL [8, 9].

When choosing to make this approximation to the anisotropic TL in MPACT, one must select the appropriate number of moments to use. One should strive for the fewest number of moments required to achieve the desired accuracy in order to keep run times (and memory) to a minimum. Initially, the preferred number of moments was determined empirically in Stimpson's thesis [8], where results show that the solution with second-order azimuthal moments is close to the solution with an explicit representation, and using any more azimuthal moments does not significantly affect the solution. In the present thesis, numerical results show that the 1D P_3 solver (with P_3 polar TL dependence) provides similar solutions to the 1D S_N with explicit polar representation.

While this simple experimentation provides some guidance, it is beneficial to have a theoretical basis for choosing the optimal order of expansion used for the TL. In Chapter 6, we compare the theoretical asymptotic accuracy of the 2D/1D equations with anisotropic TL to the SP_3 limit of the 3D transport equations to determine the number of anisotropic TL moments required to preserve the 3D SP_3 limit. This is a good measuring stick for the 2D/1D method, because SP_3 is a commonly used method that is often considered to have sufficient accuracy for a wide range of practical problems. 2D/1D with isotropic TL does not preserve the 3D SP_3 limit.

The theoretical analysis, which involved an unwieldy amount of integration and algebra, was performed using a Python script. The results of this analysis in Sec. 6.3.2 show that as the number of anisotropic TL moments is increased, the limit of the 2D/1D equations converges to the exact 3D SP_3 limit. The analysis also showed that using P_3 polar dependence with 2 azimuthal moments provides good accuracy in Sec. 6.3.3. The 2D/1D limit agrees well with the SP_3 limit using this configuration $(L = 3, P = 2)$; the largest discrepancy is 9% for the $\mathscr{L}_r\mathscr{L}_z^2$ term. Using an additional azimuthal moment $(P = 3)$ does not improve the 2D/1D accuracy with respect to the SP_3 limit. Thus, $L = 3$ and $P = 2$ are a good choice for the accuracy and efficiency of the 2D/1D method with anisotropic TL. These are exactly the parameters that were used for most of the numerical results in this thesis, including the 3D C5G7 benchmark in Sec. 4.6. Thus, the theoretical analysis has provided more support for what we have already inferred through numerical testing. The theoretical foundation gives us confidence that the 2D/1D P_3 method will be at least as accurate as 3D SP_3 when a sufficient number of anisotropic TL moments are used.

The 2D/1D P_3 method was compared directly to a 3D SP_3 solution using the Takeda-Ikeda benchmark in Sec. 6.4. The results for this benchmark corroborate the theoretical analysis. The 2D/1D method with isotropic TL is more accurate than 3D SP_1 (diffusion), but less accurate than 3D SP_3. The 2D/1D method with anisotropic TL is more accurate than 3D SP_3. 2D/1D P_3 with anisotropic TL is more accurate than 3D SP_3 because, in addition to preserving the 3D SP_3 limit, it has transport accuracy in the radial directions.

The theoretical and numerical comparison of 2D/1D with anisotropic TL to 3D SP_3 is a significant result that can inform our choice of the polar and azimuthal angle treatment for the 2D/1D method. This result also establishes and contextualizes the theoretical accuracy of the 2D/1D method with approximate anisotropic TL. It is an analogue to an analysis performed in Kelley's thesis [63], which compared the 2D/1D method with isotropic TL to 3D SP_1. In [63], it was shown that 2D/1D P_1 with isotropic TL was more accurate than 3D SP_1. The analysis in the present thesis shows that 2D/1D P_3 with isotropic TL is *not* as accurate as 3D SP_3, but 2D/1D P_3 with a sufficient number of anisotropic TL moments preserves the 3D SP_3 limit, and is more accurate than 3D SP_3 in some cases.

7.2 Future Work

Several remaining aspects of the 2D/1D method in MPACT are either not fully developed or not fully understood. Thus, there are many possible avenues of further research that are at least loosely related to some of the work contained in this thesis. Here, we focus on those that are most promising or most directly related to the present work.

7.2.1 More Applications to Real LWR Problems

While the methods developed in this thesis generally had excellent results for some benchmark problems, the results for the one realistic PWR model in Sec. 4.7 (VERA Problem 4) were underwhelming. This is a problem where the standard MPACT solution has large error due to partially inserted control rods. Unfortunately, the differences between the standard MPACT 2D/1D solution and the higher-fidelity 2D/1D solution developed in this thesis were barely perceptible. While the anisotropic TL and XS were effective for the C5G7 benchmark in Sec. 4.6, they were much less effective for VERA Problem 4. The smearing of the control rod axially within the MOC plane into which it is partially inserted generates a large error. We do not expect the method developed in this thesis to do anything to treat that error, but we might still expect it to reduce other errors in the 2D/1D solution. Instead, the change in the solution when using the new method is relatively small. Because it is so small, we cannot tell whether the solution is being improved.

There has been work in MPACT to develop improved control rod decusping methods [30]. These other methods are mostly focused on using an axial sub-mesh within the standard MPACT MOC slice, and an additional solver (1D collision probabilities method or subray MOC) to model the physics near a control rod tip. These methods perform significantly better than the polynomial decusping that was used in Sec. 4.7. However, the new anisotropic TL and XS methods developed in this thesis are not yet implemented together with the advanced decusping methods. Implementing these improvements to the 2D/1D methods side-by-side may be important for problems with partially inserted control rods.

There may be other target problems for MPACT, such as full core PWR analysis, where these methods are important, but none have been identified yet. It is also possible that the errors addressed by the methods developed in this thesis are not practically important for MPACT target problems, and whatever small effect these methods have is not worth the significant computational cost of using them. If this were the case, it would likely not be that the LWR problems are "easy" for 2D/1D and do not require 3D transport, but rather that the errors associated with the standard 2D/1D approximation are small enough that they are not limiting for any of the simulation, design, verification, or other analysis an MPACT user would be conducting.

BWRs have much stronger axial streaming than PWRs, large water rods, and partially inserted control rods. Because of this, we expect that BWRs will be more difficult for the standard 2D/1D method and will require methods with better transport accuracy, such as the 2D/1D P_3 method with anisotropic TL and XS developed in this thesis. Preliminary testing on 3D BWR assemblies with MPACT has commenced, but we have not yet identified any case where the method developed in this thesis provides a clear and significant benefit. Further testing is required to determine where there is a need for the "high-fidelity" 2D/1D methods and what role they could perform in LWR analysis.

7.2.2 Extension to P_N Scattering

MPACT frequently uses TCP0 scattering, because it is efficient and usually effective for PWR problems. However, P_N scattering should be more accurate in some cases. For reactors with a fast neutron spectrum, P_N scattering up to order 2 or 3 is absolutely necessary. If we want a high-fidelity 2D/1D solution, the separate high-fidelity methods should all be capable of working simultaneously. The anisotropic TL and XS methods developed in this thesis have not yet been implemented with P_N scattering in MPACT. This work would include not just coding and implementation, but also theoretical development for the correct homogenization of the anisotropic scattering moments. It may be possible to use some of the same anisotropic moment information for the scattering source and the XS homogenization. If so, it could save run time and memory, which would make the anisotropic XS homogenization relatively more attractive with anisotropic scattering.

One possibly significant difficulty in using the anisotropic TL formulation that we currently have with P_N scattering is that the TL and scattering moments are expanded differently. The TL is expanded in separate Legendre polar and Fourier azimuthal moments, but the scattering moments are expanded in spherical harmonics. While these moments are loosely related, they are not the same. The storage and calculation of the anisotropic MOC source may be complicated with different angular expansions of the TL and scattering. Storing the TL in spherical harmonics is not conducive to efficient 1D axial solutions, but storing the scattering moments like the TL would have a significantly higher memory footprint and computation requirement.

7.2.3 2D/1D Convergence and Transverse Leakage Splitting

The standard 2D/1D method in MPACT usually converges for the problems of interest, and failure to converge due to negative source sensitivity is not a major concern. If the 2D/1D iteration does fail to converge due to nonlinear negative source instability, it can often be fixed by splitting the axial or radial TL. However, this splitting can degrade the accuracy.

When using anisotropic TL, this negative source sensitivity is much more likely. This is because the maximum anisotropic TL is often several times greater in magnitude than the isotropized TL. Because the axial TL magnitude is larger, negative sources, and in turn, negative fluxes, are more likely. Homogenizing with negative fluxes for the 1D solution can cause numerical instability. This makes it more difficult to apply the 2D/1D method with anisotropic TL to real problems, since the negative sources are more likely with narrower energy groups. While the C5G7 benchmark cross sections used in this thesis have only 7 groups, MPACT often uses a 51-group structure, and the TCP0 approximation reduces the scattering source, which makes the situation ripe for a negative total source.

TL splitting can sometimes alleviate the sensitivity, but the degradation in accuracy defeats the purpose of using anisotropic TL and XS in the first place. A more accurate, angle-dependent TL splitting has been recently developed [66], but it is computationally expensive. There is a significant amount of room for further research into causes and modes of 2D/1D convergence issues, and ways to address the negative source sensitivity without sacrificing too much run time or accuracy. Any method that could substantially improve stability without perturbing the solution would be a significant development in 2D/1D neutron transport.

Possible avenues of future research could include formal analysis of the stability and accuracy consequences of transverse leakage splitting. Proper under-relaxation factors for 2D/1D with one-node axial solvers are also a potential topic for future research. The under-relaxation method that was originally developed to achieve stability for 2D/1D was specific to two-node 1D solvers. Some work in this area has indicated that under-relaxation is not necessary for one-node 1D solvers, but the work is not complete. The hybrid one-node/two-node P_3 solver previously developed in [17] could also be converted to a full two-node solver by using the polar-dependent angular flux that is necessary for the polar-dependent XS homogenization to calculate the pin-averaged $P_2(\mu)$ moment of the angular flux.

The need for TL splitting arises because the 2D/1D iteration has negative flux sensitivity caused by the nonlinearity in the 2D/1D iteration, which was mentioned in Sec. 3.2.1. If the 2D/1D method is defined without nonlinearity, the iteration should be much more robust and would not fail to converge when negative solutions are encountered during the iteration. Removing the sensitivity would require:

1. Using a linear acceleration scheme.

2. Avoiding homogenization or modifying the homogenization so that it is less sensitivie to the presence of negative fluxes.

If future work were to successfully remove the negative source sensitivity in MPACT, the need for TL splitting would be eliminated. In turn, the need for all the aforementioned TL splitting study, analysis, and improvements would be removed. Addressing the negative source sensitivity directly by removing the nonlinearity is likely a more robust way to resolve the convergence failure problem than to develop more advanced, but still ad hoc, TL splitting methods. If the negative source sensitivity can be addressed without TL splitting, MPACT will have an improved capability to converge to an accurate solution for difficult and realistic neutron transport problems.

7.2.4 Intermediate-Mesh Odd-Parity 2D/1D

In Chapter 5, we chose to use a coarse-mesh 2D S_N solution to calculate the odd-parity angular flux for the 2D/1D method with polar parity. The odd-parity coarse-mesh 2D S_N solver uses pin-homogenized XS. This method is simple to implement, efficient, and effective for calculating the odd-parity angular flux on the coarse-mesh boundaries. However, it does not provide the within-pin spatial distribution of the odd-parity angular flux that would be necessary to calculate the anisotropic homogenized 1D XS. In order to do this, the spatial mesh of the odd-parity 2D solution should be no coarser than what is necessary to faithfully model the material distribution in the pin cell without smearing or homogenization of dissimilar materials such as fuel and moderator.

In Sec. 5.1.3, a polar-parity 2D/1D method is roughly outlined in which the odd-parity transport equation is solved using MOC on an "intermediate" mesh. This intermediate mesh is finer than the pin mesh, but not as fine as the even-parity MOC FSR mesh. This intermediate mesh would allow for coarser ray spacing than what is used in the fine-mesh MOC solution. Between the coarser FSR mesh and coarser ray spacing, the intermediate-mesh MOC run time should still be relatively small compared to the fine-mesh MOC for the even-parity solution.

A method such as the one just described, or one that otherwise utilizes the polar parity concept for 2D/1D, is a potentially fruitful topic for future research. The key facet that makes the polar-parity 2D/1D concept attractive is the treatment of the TL with less fidelity than the scattering and fission source. This separation of TL from scattering and fission allows for the 2D/1D method to account for TL effects without sacrificing too much speed.

Appendix A: 1D/1D S$_N$ Demonstration Results

This appendix contains extended results from Section 4.1. While a simplified single pin cell case was presented in the main text, these results serve to demonstrate that the method also works when there is non-zero radial TL in the transverse "axial" solution. The MOX pin results are shown to demonstrate the increased severity of the anisotropic XS effect with MOX fuel.

The angular fluxes in groups 1, 4, 6, and 7 for a MOX pin cell are given in Fig. A.1. The thermal anisotropy effect is stronger in the MOX pin than it was in UO2. The errors in the transverse 1D angular fluxes are given in Tables A.1. Again, the angular flux homogenization exactly reproduces the group-wise angular flux distribution from the original 1D S$_N$ solution. The scalar flux homogenization has larger errors in the

Table A.1: Transverse 1D angular flux error, MOX pin

(a) Scalar flux homogenization

	Group 1	**Group 2**	**Group 3**	**Group 4**	**Group 5**	**Group 6**	**Group 7**
Angle 1	-0.05%	0.11%	-0.07%	0.06%	-0.97%	-2.73%	-9.13%
Angle 2	-0.05%	0.10%	-0.07%	0.06%	-0.90%	-2.46%	-7.85%
Angle 3	-0.04%	0.08%	-0.05%	0.04%	-0.66%	-1.47%	-3.56%
Angle 4	0.08%	-0.16%	0.11%	-0.09%	1.43%	3.75%	12.64%
Total	0.01%	-0.02%	0.02%	-0.01%	0.22%	0.61%	2.06%

(b) Angular flux homogenization

	Group 1	**Group 2**	**Group 3**	**Group 4**	**Group 5**	**Group 6**	**Group 7**
Angle 1	-2.3E-09	-2.8E-10	1.3E-10	1.1E-10	8.7E-11	1.6E-10	4.1E-10
Angle 2	-2.3E-09	-2.8E-10	1.3E-10	1.1E-10	8.7E-11	1.6E-10	4.1E-10
Angle 3	-2.3E-09	-2.8E-10	1.3E-10	1.1E-10	8.7E-11	1.6E-10	4.1E-10
Angle 4	-2.3E-09	-2.8E-10	1.3E-10	1.1E-10	8.7E-11	1.6E-10	4.1E-10
Total	-2.3E-09	-2.6E-10	1.7E-10	1.6E-10	1.4E-10	2.1E-10	4.7E-10

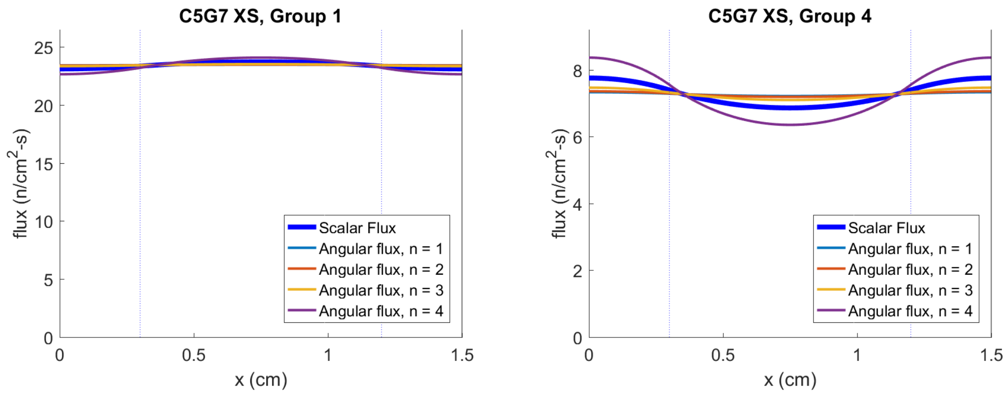

(a) Group 1 (b) Group 4

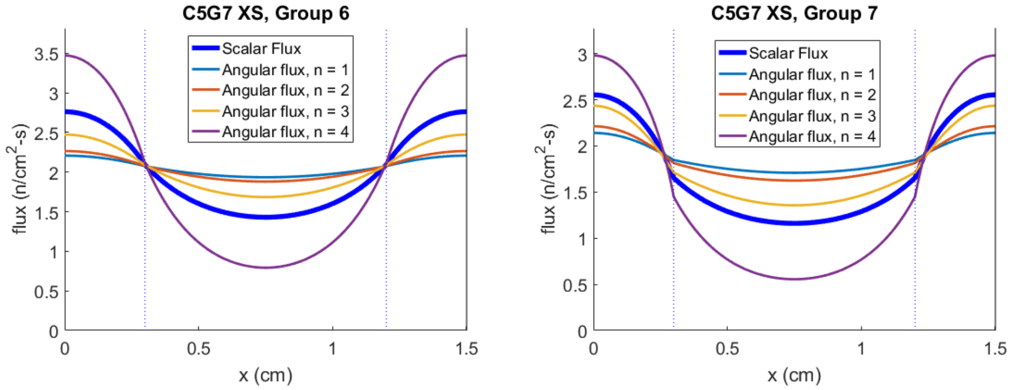

(c) Group 6 (d) Group 7

Figure A.1: C5G7 MOX pin cell group angular fluxes

thermal groups than in the UO2 pin cell case. Here, the maximum individual angle error is 12.6% for group 7, angle 4, and the total partial current error for group 7 is 2.0%.

The control cell is a control pin with a fuel pin on either side, with reflective boundaries on the outside. A simple diagram is given in Fig. A.2. The angular fluxes in groups 1, 4, 6, and 7 for a control cell are given in Fig. A.3. As expected, the anisotropy effect is even stronger in control cell than in the MOX pin. The errors in the transverse 1D angular fluxes for the control pin are given in Tables A.2. Here, there are non-negligible errors in all 7 energy groups, with the total errors reaching 2-3% in the thermal groups and the max errors peaking near 20%. Again, the angular flux homogenization exactly reproduces the group-wise angular flux distribution from the original 1D S$_N$ solution. This case is more complicated because there is radial TL between the adjacent pin cells in the transverse 1D problem. However, the angular flux is still reproduced exactly when the correct anisotropic TL and anisotropic XS

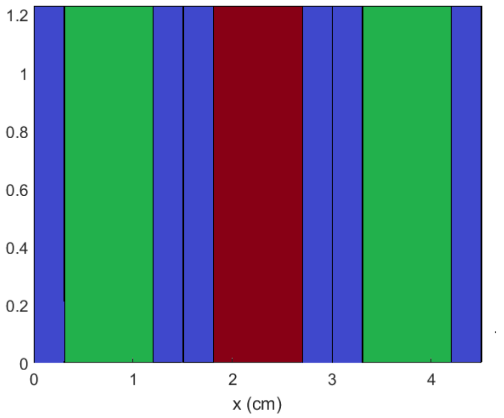

Figure A.2: Geometry for 3-pin control cell

Table A.2: Transverse 1D angular flux error, control pin

(a) Scalar flux homogenization

	Group 1	Group 2	Group 3	Group 4	Group 5	Group 6	Group 7
Angle 1	-4.53%	-2.14%	-1.67%	-5.94%	-13.56%	-16.60%	-13.89%
Angle 2	-4.27%	-1.91%	-1.35%	-4.71%	-11.38%	-12.96%	-9.44%
Angle 3	-3.22%	-1.11%	-0.40%	-1.09%	-4.18%	-2.58%	-0.16%
Angle 4	7.45%	2.85%	1.68%	6.10%	19.09%	20.45%	12.40%
Total	1.10%	0.47%	0.32%	1.17%	3.12%	3.67%	2.66%

(b) Angular flux homogenization

	Group 1	Group 2	Group 3	Group 4	Group 5	Group 6	Group 7
Angle 1	1.7E-12	5.2E-11	1.1E-10	6.5E-11	3.1E-11	1.7E-10	6.1E-10
Angle 2	1.7E-12	5.2E-11	1.1E-10	6.6E-11	3.2E-11	1.7E-10	6.4E-10
Angle 3	1.7E-12	5.2E-11	1.1E-10	6.9E-11	3.5E-11	1.9E-10	6.9E-10
Angle 4	1.9E-12	5.4E-11	1.2E-10	7.8E-11	4.5E-11	2.4E-10	7.3E-10
Total	1.8E-12	5.3E-11	1.1E-10	7.2E-11	3.8E-11	2.0E-10	6.9E-10

are used. The scalar flux homogenization has very large errors in the thermal groups because of the strong thermal flux anisotropy.

The assembly model is a 17-pin “lattice” with reflective boundaries on either end. There are control rods at positions 3, 6, 9, 12, and 15; all fuel pins are UO2. This is like a 1D slice through the exact center of a 2D C5G7 assembly with the control rods inserted, but with the instrumentation chamber in the center replaced by a control rod.

The angular fluxes in groups 1, 4, 6, and 7 for the assembly are given in Fig. A.4. The angular flux variation is very strong along the length of the assembly. Because

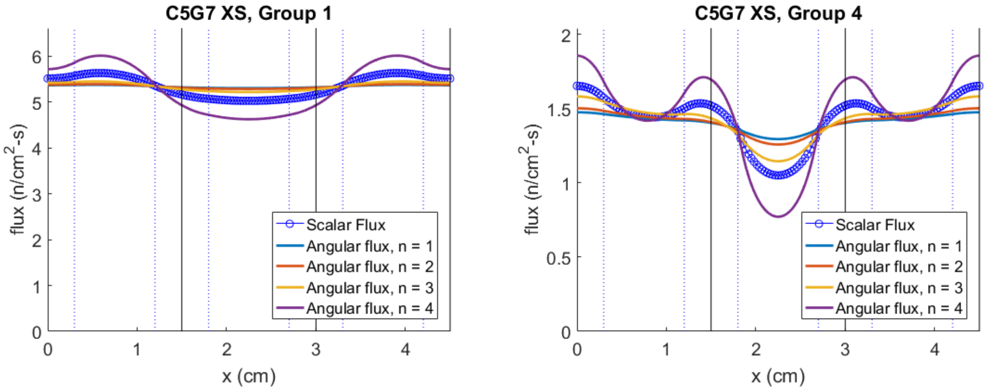

(a) Group 1 (b) Group 4

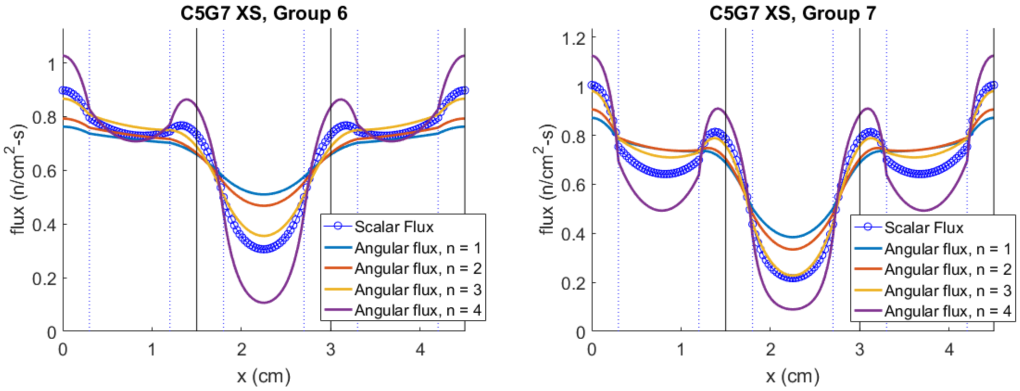

(c) Group 6 (d) Group 7

Figure A.3: C5G7 control cell group angular fluxes

of the rapid variation between sinks and sources of thermal and fast neutrons (fuel, moderator, control), there is strong variation and strong anisotropy in the angular flux. The errors in the transverse 1D angular fluxes for the 4^{th} pin (fuel) are given in Tables A.3a and A.3b. The errors in the 9^{th} pin (center control rod) are given in Tables A.3c and A.3d.

Again, the angular flux homogenization exactly reproduces the group-wise angular flux distribution from the original 1D S_N solution. This is true for all 17 pins in the problem (not shown here). The magnitude of the transverse angular flux errors in this problem is similar to that of the fuel and control pins in the other problems. This gives us confidence that the angle-dependent XS homogenization will produce the desired, accurate results when implemented in a full 2D/1D solver.

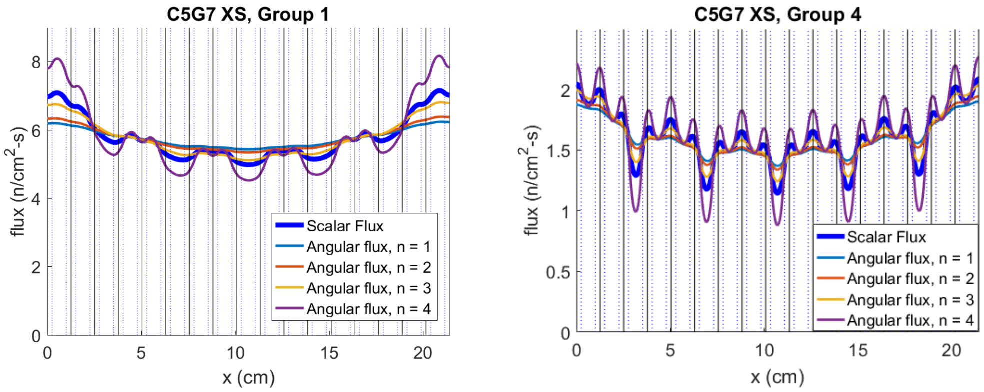

(a) Group 1 (b) Group 4

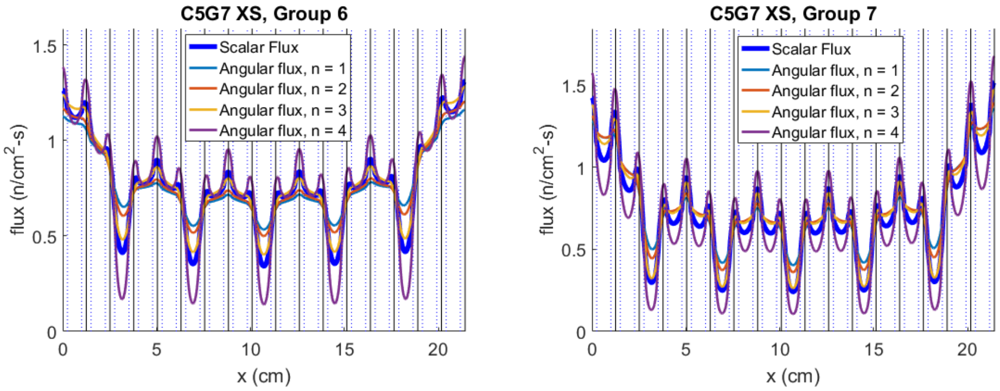

(c) Group 6 (d) Group 7

Figure A.4: C5G7 assembly group angular fluxes

Table A.3: Transverse 1D angular flux error, assembly

(a) Pin 4 (fuel), scalar flux homogenization

	Group 1	**Group 2**	**Group 3**	**Group 4**	**Group 5**	**Group 6**	**Group 7**
Angle 1	4.48%	2.96%	2.40%	5.49%	10.92%	6.16%	-3.86%
Angle 2	4.56%	2.37%	1.71%	3.86%	7.84%	3.20%	-4.80%
Angle 3	3.30%	0.78%	0.21%	0.31%	0.91%	-1.94%	-4.46%
Angle 4	-6.21%	-2.82%	-1.83%	-3.85%	-7.35%	-2.18%	7.44%
Total	0.06%	-0.07%	-0.16%	-0.77%	-1.57%	-1.07%	0.46%

(b) Pin 4 (fuel), angular flux homogenization

	Group 1	**Group 2**	**Group 3**	**Group 4**	**Group 5**	**Group 6**	**Group 7**
Angle 1	6.6E-11	9.5E-11	8.9E-11	6.2E-11	5.4E-11	8.2E-11	1.1E-10
Angle 2	6.6E-11	9.4E-11	8.8E-11	6.1E-11	5.2E-11	7.9E-11	1.1E-10
Angle 3	6.5E-11	9.3E-11	8.7E-11	5.9E-11	4.9E-11	7.5E-11	1.1E-10
Angle 4	5.9E-11	8.9E-11	8.5E-11	5.6E-11	4.4E-11	7.2E-11	1.1E-10
Total	6.2E-11	9.0E-11	8.6E-11	6.0E-11	5.0E-11	7.9E-11	1.1E-10

(c) Pin 9 (control), scalar flux homogenization

	Group 1	**Group 2**	**Group 3**	**Group 4**	**Group 5**	**Group 6**	**Group 7**
Angle 1	-7.97%	-3.01%	-2.04%	-5.90%	-12.60%	-15.48%	-13.83%
Angle 2	-6.42%	-2.18%	-1.49%	-4.70%	-10.57%	-12.38%	-9.59%
Angle 3	-2.34%	-0.68%	-0.36%	-1.39%	-4.34%	-3.06%	0.06%
Angle 4	9.37%	2.85%	1.96%	6.79%	19.74%	22.43%	14.91%
Total	1.65%	0.55%	0.37%	1.20%	2.98%	3.59%	2.82%

(d) Pin 9 (control), angular flux homogenization

	Group 1	**Group 2**	**Group 3**	**Group 4**	**Group 5**	**Group 6**	**Group 7**
Angle 1	-1.3E-12	-7.5E-14	5.1E-13	4.3E-13	2.2E-13	2.4E-13	3.5E-13
Angle 2	-1.4E-12	-7.6E-14	5.2E-13	4.3E-13	2.2E-13	2.5E-13	3.6E-13
Angle 3	-1.4E-12	-8.1E-14	5.2E-13	4.5E-13	2.4E-13	2.8E-13	3.9E-13
Angle 4	-1.6E-12	-8.0E-14	5.4E-13	5.1E-13	3.1E-13	3.4E-13	4.2E-13
Total	-1.5E-12	-8.0E-14	5.3E-13	4.7E-13	2.7E-13	3.0E-13	4.0E-13

Bibliography

[1] J.J. DUDERSTADT and L.J. HAMILTON, *Nuclear Reactor Analysis*, John Wiley & Sons, Inc., New York, NY, USA (2016).

[2] J.R. ASKEW, "A Characteristics formulation of the Neutron Transport Equation in Complicated Geometry," AEEW-M 1108, UKAEA, Winfirth, UK (1972).

[3] K. KOEBKE, "Advances in Homogenization and Dehomogenization," *Proc. M&C 1981, Munich, Germany* (1981).

[4] K.S. SMITH, "Assembly Homogenization Techniques for Light Water Reactor Analysis," *Prog. Nucl. Energ.*, **17**, *3*, 303 (1986).

[5] R. SANCHEZ, "Assembly homogenization techniques for core calculations," *Prog. Nucl. Energ.*, **51**, *1*, 14 (2009).

[6] M.T.H. YOUNG, "Orthogonal-Mesh, 3-D Sn with Embedded 2-D Method of Characteristics for Whole-Core, Pin-Resolved Reactor Analysis," PhD Thesis, University of Michigan (2016).

[7] J.Y. CHO, H.G. JOO, K.S. KIM, and S.Q. ZEE, "Three-Dimensional Heterogeneous Whole Core Transport Calculation Employing Planar MOC Solutions," *Trans. Am. Nucl. Soc.*, vol. 87, 234–236 (2002).

[8] S.G. STIMPSON, "An Azimuthal, Fourier Moment-Based Axial S_N Solver for the 2D/1D Scheme," PhD Thesis, University of Michigan (2015).

[9] S.G. STIMPSON, B.S. COLLINS, and T.J. DOWNAR, "A 2-D/1-D Transverse Leakage Approximation Based on Azimuthal, Fourier Moments," *Nucl. Sci. Eng.*, **185** (2017).

[10] D.W. PEACEMAN and H.H. RADFORD, "The Numerical Solution of Parabolic and Elliptic Differential Equations," *J. Soc. Indust. Appl. Math.*, **3**, *1*, 28 (1955).

[11] N.Z. CHO, G.S. LEE, and C.J. PARK, "Fusion of Method of Characteristics and Nodal Method for 3-D Whole-Core Transport Calculation," *Trans. Am. Nucl. Soc.*, vol. 86, 322 (2002).

[12] H.G. Joo, J.Y. Cho, K.S. Kim, C.C. Lee, and S.Q. Zee, “Methods and Performance of a Three-Dimensional Whole Core Transport Code DeCART,” *Proc. PHYSOR 2004, Chicago, IL, USA* (2004).

[13] J.Y. Cho, K.S. Kim, C.C. Lee, S.Q. Zee, and H.G. Joo, “Axial SPN and Radial MOC Coupled Whole Core Transport Calculation,” *J. Nuc. Sci. Tech.*, **44**, 1156 (2007).

[14] Y.S. Jung and H.G. Joo, “Decoupled planar MOC solution for dynamic group constant generation in direct three-dimensional core calculations,” *Proc. M&C 2009, Saratoga Srpings, NY, US*, vol. 44 (2009).

[15] T.J. Downar, B.M. Kochunas, and B.S. Collins, “Validation and Verification of the MPACT Code,” *Proc. PHYSOR 2016, Sun Valley, ID, USA* (2016).

[16] Y.S. Jung et al., “Practical numerical reactor employing direct whole core neutron transport and subchannel thermal/hydraulic solvers,” *Annals of Nuclear Energy*, **62**, 357 (2013).

[17] S.G. Stimpson, B.S. Collins, and T.J. Downar, “Axial Transport Solvers for the 2D/1D Scheme in MPACT,” *Proc. PHYSOR 2014, Kyoto, Japan* (2014).

[18] M. Hursin, B.S. Collins, Y. Xu, and T. Downar, “The Development and Implementation of a One-Dimensional S_N Method in the 2D-1D Integral Transport Solution,” *Nucl. Sci. and Eng.*, **176**, 186 (2014).

[19] B.W. Kelley and E.W. Larsen, “2D/1D Approximations to the 3D Neutron Transport Equation. I: Theory,” *Proc. M&C 2013, Sun Valley, ID, USA* (2013).

[20] B.W. Kelley, B.S. Collins, and E.W. Larsen, “2D/1D Approximations to the 3D Neutron Transport Equation. II: Numerical Results,” *Proc. M&C 2013, Sun Valley, ID, USA* (2013).

[21] B.M. Kochunas, Z. Liu, and T.J. Downar, “Parallel 3-D Method of Characteristics in MPACT,” *Proc. M&C 2013, Sun Valley, ID, USA* (2013).

[22] A. Marin-Lafleche, M.A. Smith, and C.H. Lee, “PROTEUS-MOC: A 3D Deterministic Solver Incorporating 2D Method of Characteristics,” *Proc. M&C 2013, Sun Valley, ID, USA* (2013).

[23] C.H. Lee, E.R. Shemon, M.A. Smith, and Y.S. Jung, “FY16 Status Report on NEAMS Neutronics Activities,” ANL/NE-16/23, Argonne National Laboratory (2016).

[24] T. Zhang, Y. Wang, E.E. Lewis, M.A. Smith, W.S. Yang, and H. Wu, “Assessment of 2D-Transport/1D-Diffusion Approximations in a Pin Resolved Variational Nodal Method for PWR Calculations,” *these proceedings* (2017).

[25] T. Zhang, E.E. Lewis, M.A. Smith, W.S. Yang, and H. Wu, "A Variational Nodal Approach to 2D/1D Pin Resolved Neutron Transport for Pressurized Water Reactors," *Nucl. Sci. Eng.*, **186** (2017).

[26] Y.Q. Zheng, S.Y. Choi, and D.J. Lee, "A new approach to three-dimensional neutron transport solution based on the method of characteristics and linear axial approximation," *Journal of Computational Physics*, **350** (2017).

[27] B. Faure, P. Archier, J.F. Vidal, and L. Buiron, "A 2D/1D Algorithm for Effective Cross-Section Generation in Fast Reactor Neutronic Transport Calculations," *Nuclear Science and Engineering*, **0**, *0*, 1 (2018); 10.1080/00295639.2018.1480190., URL `https://doi.org/10.1080/00295639.2018.1480190`.

[28] J.Y. Cho, K.S. Kim, and C.C. Lee, "Error Quantification of the Axial Nodal Diffusion Kernel of the DeCART Code," *Proc. PHYSOR 2006, Vancouver, BC, Canada* (2006).

[29] E.E. Lewis, M.A. Smith, and B.C. Na, "Benchmark on Deterministic 3-D MOX Fuel Assembly Transport Calculations Without Spatial Homogenization," *Prog. Nucl. Energy*, **48**, 381 (2006).

[30] A.M. Graham, "Subgrid Methods for Resolving Axial Heterogeneity in Planar Synthesis Solutions for the Boltzmann Transport Equation," PhD Thesis, University of Michigan (2017).

[31] T. Takeda and H. Ikeda, "Final Report on the 3-D Neutron Transport Benchmarks," AEEW-M 1008, Nuclear Energy Agency Organisation for Economic Cooperation and Development (NEA-OECD) (1991).

[32] G. Bell and S. Glasstone, *Nuclear Reactor Theory*, Van Nostrand Reinhold Company (1970).

[33] A.K. Prinja and E.W. Larsen, "Principles of Neutron Transport," D.G. Cacuci (Editor), *Nuclear Engineering Handbook*, 427–542, Springer.

[34] E.E. Lewis and W.F. Miller Jr., *Computational Methods in Neutron Transport*, Wiley, New York, New York (1984).

[35] N.Z. Cho, "Fundamentals and Recent Developments of Reactor Physics Methods," *Nuclear Engineering and Technology*, **47**, 25 (2005).

[36] A. Zhu, "Transient Methods for Pin-Resolved Whole-Core Neutron Transport," PhD Thesis, University of Michigan (2016).

[37] T.M. Pandya, S.R. Johnson, G.G. Davidson, T.M. Evans, and S.P. Hamilton, "SHIFT: A Massively Parallel Monte Carlo Radiation Transport Package," *Proc. M&C 2015, Nashville, TN, USA* (2015).

[38] P.K. Romano, B. Herman, N. Horelik, A. Nelson, B. Forget, and K. Smith, “OpenMC: A State-of-the-Art Monte Carlo Code for Research and Development,” *Ann. Nucl. Energy*, **82**, 90 (2015).

[39] Y. Liu, “A Full Core Resonance Self-shielding Method Accounting for Temperature-dependent Fuel Subregions and Resonance Interference,” PhD Thesis, University of Michigan (2015).

[40] A.T. Till, M.L. Adams, and J.E. Morel, “The finite element with discontiguous support multigroup method: Theory,” *Proc. M&C 2015, Nashville, TN, USA* (2015).

[41] A.T. Till, “Finite Elements with Discontiguous Support for Energy Discretization in Particle Transport,” PhD Thesis, Texas A&M University (2015).

[42] Lei Zhu and Benoit Forget, “A discrete generalized multigroup energy expansion theory,” *Nuclear Science and Engineering*, **166**, 239 (2010).

[43] A. Yamamoto et al., “Derivation of Optimum Polar Angle Quadrature Set for the Method of Characteristics Based on Approximation Error for the Bickley Function,” *Journal of Nuclear Science and Technology*, **4**, *2*, 129 (2007).

[44] E.W. Larsen, “Lecture Notes for NERS 543: Nuclear Reactor Theory II,” (2013).

[45] E.M. Gelbard, “Simplified Spherical Harmonics equations and their use in shielding problems,” WAPD-T-1182, Bettis Atomic Power Laboratory (1961).

[46] R.G. McClarren, “Theoretical Aspects of the Simplified P_N Equations,” *Transport Theory and Statistical Physics*, **39**, 73 (2011).

[47] E.W. Larsen, J.E. Morel, and J. McGhee, “Asymptotic derivation of the multigroup P_1 and simplified P_N equations with anisotropic scattering,” *Nuclear Science and Engineering*, **123**, 328 (1996).

[48] P. Brantley and E. Larsen, “A variational derivation of the simplified P_3 approximation,” *Proceedings of ANS Topical Meeting on Mathematical Models and Supercomputing for Nuclear Applications*, Saratoga Springs, New York (1997).

[49] A. Yamamoto, Y. Kitamura, and Y. Yamane, “Simplified treatments of anisotropic scattering in LWR core calculations,” *Nuclear Science and Technology*, **45**, 217 (2008)URL `http://dx.doi.org/10.1080/18811248.2008.9711430`.

[50] B.R. Herman et al., “Improved diffusion coefficients generated from Monte Carlo codes,” *Proc. M&C 2013, Sun Valley, ID, USA* (2013).

[51] K.S. Kim et al., “Development of a new 47-group library for the CASL neutronics simulators,” *Proc. M&C 2015, Nashville, TN, USA* (2015).

[52] B.C. Yee, E.W. Larsen, and B.M. Kochunas, “An Analytical Derivation of Transport-Corrected P_0 Cross Sections and Diffusion Coefficients,” *Proc. PHYSOR 2016, Sun Valley, ID, USA* (2016).

[53] E.R. Shemon, C.H. Lee, M.A. Smith, and A Marin-Lafleche, “NEAMS neutronics: Development and validation status,” *International Congress on Advances in Nuclear Power Plants, ICAPP 2014*, vol. 1, 686–693 (2014).

[54] J.J. Jarrell, T.M. Evans, G.G. Davidson, and A.T. Godfrey, “Full Core Reactor Analysis: Running Denovo on Jaguar,” *Nuclear Science and Engineering*, **175**, 283 (2013).

[55] M.T.H. Young, J.J. Jarrell, and Tom Evans, “Method of Characteristics assisted cross section homogenization for Denovo,” , Oak Ridge National Laboratory (2012).

[56] S. Shaner, G. Gunow, K.S. Smith, and B. Forget, “Verification of the 3D Method of Characteristics Solver in OpenMOC,” *Proc. PHYSOR 2016, Sun Valley, ID, USA.* (2016).

[57] R. Ferrer, J. Rhodes, and K.S. Smith, “Linear Source Approximation in CASMO5,” *Proc. PHYSOR 2012, Knoxville, TN* (2012).

[58] K.S. Smith, “Nodal Method Storage Reduction by Nonlinear Iteration,” *Transactions of the American Nuclear Society*, vol. 44, 265 (1983).

[59] B.C. Yee, B.M. Kochunas, and E.W. Larsen, “A multilevel in space and energy solver for multigroup diffusion eigenvalue probelms,” *Nuclear Engineering and Technology*, **49**, 1125 (2017).

[60] F. Finnemann and M. Wagner, “Interface nodal current technique for multidimensional reactor calculation,” *Atomkernenergie*, **30**, 123 (1977).

[61] S.G. Stimpson, B.S. Collins, A. Zhu, and Y. Xu, “A Hybrid Nodal P3/SP3 Axial Transport Solver for the MPACT 2D/1D Scheme,” *Proc. PHYSOR 2016, Sun Valley, ID, USA* (2016).

[62] Seungsu Yuk and Nam Zin Cho, “Whole-Core Transport Solutions with 2-D/1-D Fusion Kernel via p-CMFD Acceleration and p-CMFD Embedding of Nonoverlapping Local/Global Iterations,” *Nuclear Science and Engineering*, **181**, *1*, 1 (2015); 10.13182/NSE14-88., URL `https://doi.org/10.13182/NSE14-88`.

[63] B.W. Kelley, “An Investigation of 2D/1D Approximations to the 3D Boltzmann Transport Equation,” PhD Thesis, University of Michigan (2015).

[64] M. Jarrett, B. Kochunas, E. Larsen, and T. Downar, “Progress in Characterizing 2D/1D Accuracy in MPACT,” *Proc. M&C 2017, Jeju, Korea* (2017).

[65] R. Alcouffe, "Diffusion Synthetic Acceleration Methods for the Diamond-Differenced Discrete-Ordinates Equations," *Nuclear Science and Engineering*, **64**, 344 (1977); 10.13182/NSE77-1., URL `https://doi.org/10.13182/NSE77-1`.

[66] C. Zhao, Z. Liu, L. Cao, and H. Wu, "Improved Leakage Splitting Method for the 2D/1D Transport Calculation," *Proc. PHYSOR 2018, Cancun, MX* (2018).

[67] G.S. Lee and N.Z. Cho, "2D/1D Fusion method solutions of the three-dimensional transport OECD benchmark problem C5G7 MOX," *Prog. in Nucl. Energy*, **48**, 410 (2006).

[68] S. Yuk and N.Z. Cho, "Comparison of 1-D/1-D Fusion Method and 1-D/1-D Hybrid Method in Two-Dimensional Neutron Transport Problems: Convergence Analysis and Numerical Results," *Nucl. Sci. Eng.*, **184**, 151 (2016).

[69] N.Z. Cho, G.S. Lee, and C.J. Park, "Refinement of the 2-D/1-D Fusion Method for 3-D Whole-Core Transport Calculation," *Trans. Am. Nucl. Soc.*, vol. 87, 417–420 (2002).

[70] K.S. Smith and B. Forget, "Challenges in the Development of High-Fidelity LWR Core Neutronics Tools," *Proc. M&C 2013, Sun Valley, ID, USA* (2013).

[71] S. Goluoghlu et al., "Monte Carlo Criticality Methods and Analysis Capabilities in SCALE," *Nuclear Technology*, **174**, *2*, 214 (2011).

[72] K.D. Lathrop, "Spatial Differencing of the Transport Equation: Positivity vs. Accuracy," *J. Comp. Physics*, **4**, 475 (1969).

[73] M. Jarrett, B.M. Kochunas, E.W. Larsen, and T.J. Downar, "An Improved 2D/1D P_3 Method with Angle-Dependent Leakage and Pin Homogenization," *Proc. PHYSOR 2018, Cancun, Mexico* (2018).

[74] B.M. Kochunas, B.S. Collins, and S.G. Stimpson, *MPACT Theory Manual*, University of Michigan, Oak Ridge National Laboratory (2017).

[75] E. Larsen, "SP3 Approximations to the 3D Boltzmann Transport Equation and the 2D/1D Equations," unpublished (private communication) (2016).

[76] T. Kozlowski, Y. Xu, T. Downar, and D.J. Lee, "Cell homogenization method for pin-by-pin neutron transport calculations," *Nuclear Science and Engineering*, **169**, *1*, 1 (2011); 10.13182/NSE08-85.

[77] D. Litskevich and B. Merk, "SP3 Solution versus Diffusion Solution in Pin-by-Pin Calculations and Conclusions Concerning Advanced Methods," *Journal of Computational and Theoretical Transport*, **43**, *1-7*, 214 (2014); 10.1080/00411450.2014.913184., URL `https://doi.org/10.1080/00411450.2014.913184`.